Delft University of Technology

Analysis of nitric oxide emissions from anode baking furnace through numerical modeling

Nakate, P.A.

DOI
10.4233/uuid:5073b4ad-86ed-4cd9-b1dd-66f4bc5588e5

Publication date
2022

Document Version
Final published version

Citation (APA)
Nakate, P. A. (2022). *Analysis of nitric oxide emissions from anode baking furnace through numerical modeling*. https://doi.org/10.4233/uuid:5073b4ad-86ed-4cd9-b1dd-66f4bc5588e5

Important note
To cite this publication, please use the final published version (if applicable).
Please check the document version above.

Copyright
Other than for strictly personal use, it is not permitted to download, forward or distribute the text or part of it, without the consent of the author(s) and/or copyright holder(s), unless the work is under an open content license such as Creative Commons.

Takedown policy
Please contact us and provide details if you believe this document breaches copyrights.
We will remove access to the work immediately and investigate your claim.

This work is downloaded from Delft University of Technology.
For technical reasons the number of authors shown on this cover page is limited to a maximum of 10.

ANALYSIS OF NITRIC OXIDE EMISSIONS FROM ANODE BAKING FURNACE THROUGH NUMERICAL MODELING

ANALYSIS OF NITRIC OXIDE EMISSIONS FROM ANODE BAKING FURNACE THROUGH NUMERICAL MODELING

Dissertation

for the purpose of obtaining the degree of doctor
at Delft University of Technology,
by the authority of the Rector Magnificus Prof. dr. ir. T.H.J.J. van der Hagen;
Chair of the board for Doctorates,
to be defended publicly on
Wednesday 11 May 2022 at 17:30 o'clock

by

Prajakta NAKATE

Master of science in Chemical Engineering,
Delft University of Technology, The Netherlands,
born in Aurangabad, India.

This dissertation has been approved by the promotors:

Promotor: Prof. dr. ir. C. Vuik
Copromotor: Dr. D.J.P. Lahaye

Composition of the doctoral committee:

Rector Magnificus,	Chairperson
Prof. dr. ir. C. Vuik,	Delft University of Technology, promotor
Dr. D.J.P Lahaye,	Delft University of Technology, copromotor
Independent member:	
Prof. dr. B. Cuenot	Eindhoven University of Technology
Prof. dr. C. Budd	University of Bath
Prof. dr. A. Gangoli Rao,	Delft University of Technology
Prof. dr. D.J.E.M. Roekaerts,	Delft University of Technology
Prof. dr. ir. A.W. Heemink,	Delft University of Technology

Keywords: Anode baking furnace, CFD, Combustion, Radiation, NOx analysis, COMSOL Multiphysics software

Copyright © 2021 by P. Nakate

ISBN 978-94-6384-334-8

An electronic version of this dissertation is available at
`http://repository.tudelft.nl/`.

To my beloved family and friends without whom achieving this was not possible…

CONTENTS

SUMMARY

Industrial emissions are discussed worldwide for their adverse effects on the global climate change. Nitric oxide (NOx) emissions are harmful among the various flue gases emitted in the atmosphere. There are multiple routes of formation of NOx in industry. The formation of NOx due to local overheating in fuel lean conditions is the most common way. The heavy industries such as aluminium consists of various intermediate processes. Anode baking is one such important process. The anode baking process comprises of a combustion chamber in which natural gas is fired for generating heat. The temperature in the furnace due to the combustion process is as high as 2000^{o}C. This leads to formation of NOx in the anode baking furnace. The Aluminium and Chemie B.V. (Aluchemie) operates industrial anode baking furnaces situated in Rotterdam, The Netherlands. The problems of NOx formation in anode baking furnace of Aluchemie are discussed in this thesis.

Aluchemie has challenges in understanding the optimum operating condition for reducing NOx emissions. Trial and error approach to understand the NOx formation often fails. A more sophisticated approach to gain insights on NOx formation involves developing a multi-physics model of the furnace. The computation of mass fractions of chemical species and temperature can provide better understanding on the NOx formation. This can further help in formulating optimum operating conditions. Therefore, in this thesis, a multi-physics model of the furnace is developed. The anode baking process involves several physical phenomena such as turbulent flow, combustion, heat transfer by radiation and conduction through walls. In Chapter 2, the evaluation of these phenomena is carried out in terms of selecting models for each of the physics. The choices of the models are based on their reasonable accuracy as well as simplicity in implementation for a complex geometry. The mathematical approach for solving the model equations is discussed in Chapter 3. The finite element based COMSOL Multiphysics software package is chosen as a simulator. We motivate the choice for the COMSOL Multiphysics simulation software and describe the algorithms that this package implements.

The anode baking furnace consists of multiple sections namely preheating, heating, blowing and cooling section. Each of this section is distinguished based on the direction of heat transfer either from the hot gas side or from hot anodes side. The conditions in all these sections differ and only the heating section has temperatures amenable to the formation of NOx. Therefore, the model is restricted to a single section of the furnace that mimics the operating conditions in heating section as presented in Chapter 4. The geometrical representation of the heating section of anode baking furnace along with the burner design is explained in Chapter 4. The bottle neck in meshing the model with detailed burner geometry is presented. The external meshing software cfMesh is tested against the default meshing tools of COMSOL Multiphysics software. A conversion tool is developed for obtaining FOAM mesh in Nastran format so as to import in the COMSOL software. The comparison of meshes obtained in two software packages is based on the average element quality computed using skewness parameter. The superiority of cfMesh software with higher average element quality is suppressed by few elements with negative skewness parameter. The occurrence of such low quality elements is due to the disparity in computation of skewness. Various approaches for aligning the computation of skewness with two packages are explained and needs further research. This leads to changing the burner geometry to a simple pipe. The different meshing techniques for the simple pipe burner geometry are explained in Chapter 4.

The aerodynamics in the furnace is an important physical phenomenon. Chapter 5 provides results of the turbulent flow modeling in the heating section of the furnace. The requirement of boundary layers is justified by analysing the boundary layer refinement. The meshing of the geometry is crucial for obtaining the reasonable results. The initial results generated with the COMSOL default meshing tool provide non-physical results of turbulent viscosity ratio near the fuel injection. Whereas, the mesh generated by the cfMesh softwares provide valuable results even with 15% of the number of elements. Further analysis such as local mesh refinement in the region of fuel jet injection shows improved flow behaviour.

The modeling of the combustion process is added after the development of reasonable aerodynamics. The combustion process is assumed to be mixing dominated. The combustion model available in COMSOL Multiphysics software i.e. eddy dissipation model is deployed in Chapter 6. The variations in the distribution of chemical species are compared with operational conditions such as air flow velocity, fuel flow velocity and fuel pipe diameter. The behaviour of the streams changes with changing these conditions. Further addition of radiation and conjugate heat transfer has impact on the temperature distribution. The effect of the radiation absorption coefficient is studied and differences in temperature at two burners is observed due to varying amount of radiation absorbing species. Since the modeling of all physical phenomena is coupled, the change in temperature also changes the distribution of flow and chemical species. The NOx computations are carried out on the coupled model. The variations in operational conditions is reflected on the NOx as discussed in Chapter 6. The eddy dissipation model has limited accuracy and can not be used for multiple reaction mechanism. Therefore, the mixture fraction/beta PDF model is implemented in Chapter 6. The adiabatic model of the developed workflow shows improved results compared to eddy dissipation model.

A measurement campaign is carried out in Aluchemie furnace. The measured values of chemical species and temperature at accessible locations are compared with the values from model. This comparison is elaborated in Chapter 7. The values of chemical species such as O_2 and CO_2 provides reasonable comparison with the measurement. The temperature is over predicted by approximately 10%. The NOx values are significantly overpredicted by model, approximately by 300%, showcasing the high sensitivity towards temperature. This motivates to develop more accurate mixture fraction/beta-PDF model. The mixture fraction/beta-PDF model reduces peak temperatures by 15% in case that only a single burner is activated and brings NOx concentrations close to measured values.

In conclusion, the multi-physics model of the heating section of anode baking furnace is developed in COMSOL Multiphysics software. The trends of NOx are studied with varying operational conditions. The results are compared with the measured values from

the Aluchemie furnace.

SAMENVATTING

Wereldwijd worden industriële emissies besproken vanwege hun nadelige effecten op de klimaatsverandering. Emissies van stikstofmonoxide (NOx) zijn schadelijke rookgassen die in de atmosfeer worden uitgestoten. Er zijn meerdere routes voor de vorming van NOx in de industrie. De vorming van NOx door plaatselijke oververhitting in brandstofarme omstandigheden is de meest voorkomende manier. De zware industrie zoals aluminium productie bestaat uit verschillende processen. Het bakken anode is een belangrijk tussenproces. Het anodebakproces bestaat uit een verbrandingskamer waarin aardgas wordt gestookt om warmte op te wekken. De temperatuur in de oven als gevolg van het verbrandingsproces bereikt tweeduizend graden Celcius. Dit leidt tot vorming van NOx in de anodebakoven. Aluminium en Chemie B.V. (Aluchemie B.V.) heeft industriële anodebakovens in Rotterdam, Nederland. De NOx-vorming in de anodebakoven van Aluchemie worden in dit proefschrift besproken.

Aluchemie B.V. heeft uitdagingen bij het begrijpen van de optimale bedrijfsomstandigheden voor het verminderen van de NOx-emissies. De trial-and-error-methode om de NOx-vorming te begrijpen faalt vaak. Een meer geavanceerde benadering om inzicht te krijgen in de vorming van NOx omvat het ontwikkelen van een multifysisch model van de oven. De berekening van massafracties van chemische soorten en temperatuur geeft een beter inzicht geven in NOx-vorming. Dit helpt bij het formuleren van optimale bedrijfsomstandigheden. Daarom wordt in dit proefschrift een multifysisch model van de oven ontwikkeld. Het anodebakproces omvat verschillende fysische verschijnselen zoals turbulente stroming, verbranding, warmteoverdracht door straling en geleiding door muren. In Hoofdstuk 2 wordt de evaluatie van deze verschijnselen uitgevoerd in termen van het selecteren van modellen voor elk van de fysica. De keuzes van de modellen zijn gebaseerd op hun redelijke nauwkeurigheid en eenvoud in implementatie voor een complexe geometrie. De wiskundige benadering voor het oplossen van de modelvergelijkingen wordt besproken in Hoofdstuk 3. Het op eindige elementen gebaseerde COMSOL Multiphysics softwarepakket is gekozen als een simulator. We motiveren de keuze voor dit pakket en beschrijven de beschikbare algorithmen.

De anodebakoven bestaat uit meerdere secties. Op basis van de richting van de warmteoverdracht, maakt men onderscheid tussen de voorverwarming-, verwarmings-, blaas- en koelsectie. In bepaalde secties stroomt de warmte van het hete gas naar de anodes. In andere secties gebeurt de warmteoverdracht in de andere richting. De omstandigheden in de secties verschillen. Alleen in de verwarmingssectie is de temperatuur hoog genoeg voor de vorming van thermische NOx. Daarom is het model dat wordt voorgesteld in Hoofdstuk 4 beperkt tot de verwarmingssectie. In dit hoofdstuk wordt de geometrische weergave van de verwarmingssectie van de oven en het branderontwerp uitgelegd. De bottleneck bij het uitwerken van het model met gedetailleerde brandergeometrie wordt gepresenteerd. De externe roostergeneratiesoftware cfMesh wordt vergeleken met de roostergeneratietools beschikbaar binnen de COMSOL Multiphysics

software. Er wordt een tool ontwikkeld voor de conversie van het FOAM roosterformaat naar het NASTRAN roosterformaat. Dit laatste maakt het mogelijk om het rooster te importeren in de COMSOL Multiphysics software. De vergelijking van meshes verkregen in twee softwarepakketten is gebaseerd op de gemiddelde elementkwaliteit berekend met behulp van de scheefheidsparameter. De superioriteit van cfMesh-software met een hogere gemiddelde elementkwaliteit wordt onderdrukt door enkele elementen met een negatieve scheefheidsparameter. Het voorkomen van dergelijke elementen van lage kwaliteit is te wijten aan de ongelijkheid in de berekening van scheefheid in de twee softwarepaketten. Verschillende benaderingen voor het afstemmen van de berekening van scheefheid met twee pakketten worden uitgelegd en vereisen verder onderzoek. Dit leidt tot het veranderen van de brandergeometrie naar een eenvoudige pijp. De verschillende roostergeneratietechnieken voor de eenvoudige pijpbrandergeometrie worden uitgelegd in Hoofdstuk 4.

De stromingsdynamiek in de oven is een belangrijk natuurkundig fenomeen. Hoofdstuk 5 geeft resultaten van de turbulente stromingsmodellering in de verwarmingssectie van de oven. De noodzaak om de stroming in de grenslagen te discretizeren motiveert de analyze van de roosterafstand bij de muur. Een gepaste roostergeneratie is daarom cruciaal voor het verkrijgen van de goede resultaten. De eerste resultaten die zijn gegenereerd met de standaard meshing-tool roostergeneratietools beschikbaar binnen de COMSOL Multiphysics software. Deze resultaten tonen een niet-fysisch gedrag van de turbulente viscositeitsverhouding nabij de brandstofinjectie. De roosters gegeneerd met de cfMesh-software laten toe om waardevolle resultaten te genereren met één-achtste van het aantal elementen. Een verdere analyse, zoals adaptieve roosterverfijning in het gebied van brandstofstraalinjectie, laat een verbeterd stromingsgedrag zien.

De modellering van het verbrandingsproces wordt toegevoegd na de ontwikkeling van een voldoende nauwkeurig stromingsstromings. Het verbrandingsproces wordt verondersteld te worden gedomineerd door turbulente menging. Het verbrandingsmodel dat beschikbaar is in COMSOL Multiphysics-software, d.w.z. het werveldissipatiemodel, wordt toegepast in Hoofdstuk 6. De variaties in de distributie van chemische stoffen worden vergeleken met operationele instellingen zoals luchtstroomsnelheid, brandstofstroomsnelheid en brandstofleidingdiameter. Het gedrag van de stromen verandert met veranderende dergelijke omstandigheden. Het toevoegen van straling en warmteoverdracht naar de vaste stoffen heeft een significante invloed op de temperatuurverdeling. Het effect van de stralingsabsorptiecoëfficiënt wordt bestudeerd en er wordt een verschil in temperatuur bij twee branders waargenomen als gevolg van een variërende hoeveelheid stralingsabsorberende soorten. Omdat alle fysische verschijnselen zijn gekoppeld, weerspiegelt de verandering in temperatuur zich in een herverdeling van stroming en chemische soorten. De NOx-berekeningen worden uitgevoerd op het gekoppelde model. De variaties in operationele omstandigheden worden weerspiegeld op de NOx en worden besproken in Hoofdstuk 6. Het werveldissipatiemodel heeft een beperkte nauwkeurigheid en kan niet worden gebruikt voor meervoudige reactiemechanismen. Daarom wordt in Hoofdstuk 6 een workflow van een mengselfractie/beta-PDF-model voor de implementatie in COMSOL Multiphysics software gegeven. Het adiabatische model van de ontwikkelde workflow laat verbeterde resultaten zien in vergelijking met het werveldissipatiemodel.

Meetcampagnes worden uitgevoerd in de oven van AluChemie. De gemeten waarden van chemische soorten en temperatuur op bereikbare locaties worden vergeleken met de waarden uit het model. Deze vergelijking is uitgewerkt in Hoofdstuk 7. De waarden van chemische soorten zoals O_2 en CO_2 geven een redelijke vergelijking met de meetwaarden. De temperatuur is ongeveer 10% te hoog voorspeld. De NOx-waarden worden door het model aanzienlijk overschat, ongeveer 300%, wat de hoge gevoeligheid voor temperatuur aantoont. Dit motiveert om een nauwkeuriger mengselfractie/beta-PDF-model te ontwikkelen. Het mengfractie/beta-PDF-model verlaagt de piektemperaturen met 15% in het geval dat slechts een enkele brander wordt geactiveerd en brengt de NOx-concentraties in de buurt van de gemeten waarden.

Concluderend wordt een multifysisch model van de verwarmingssectie van de anodebakoven in de COMSOL Multiphysics software ontwikkeld. De trends van NOx worden bestudeerd met wisselende operationele omstandigheden. De resultaten worden vergeleken met de meetwaarden in de ovens van AluChemie B.V.

1

INTRODUCTION

Heavy industries are gaining attention due to the widespread awareness with respect to climate change. The global energy demand of heavy industries is as large as 40%. Moreover, these industries contribute to almost one-fifth to a quarter of emissions [1]. Due to their significant share, these industries are investigating routes to optimize their process in order to have lower energy demand and lower emissions. The ongoing research involves various options such as finding efficient design and operational conditions to lower the generation of emissions at the source, incorporating greener fuels, capturing carbon and sequester, performing heat integration to lower energy demands, and many more. Among various industries, aluminium has a large environmental impact and shares approximately 3% of the sector's emissions [1, 2]. The anodes used for the extraction of aluminium are pre-baked. The baking process has an important role in industry's energy demand and emissions. In this thesis, the anode baking process is examined to reduce its environmental impact.

1.1. ANODE BAKING PROCESS

Aluminium industries heavily rely on the Hall-Héroult process for the extraction of aluminium from the bauxite ore. The electrolysis process requires the carbon anodes as one of the important components. During the electrolysis process, the anodes are continuously consumed.

The anodes form the important component in the electrolysis cell (right most picture in Figure 1.1) at which the electrons are discharged by the reaction of carbon material with oxygen. The anodes need to be replaced regularly since they are continuously consumed in the process. The anodes that are utilized in the extraction process need to have certain properties to be efficient in the electrolysis process. The anodes should be homogeneous to have the required mechanical properties. Furthermore, the anodes should be conductive and have minimal interaction in the chemical reaction during the reduction process. These properties can be achieved by the baking process. The ideal anodes after the baking process have lower reactivity towards CO_2, lower electrical resistivity, lower reactivity with air, lower air permeability, and lower surface oxidation.

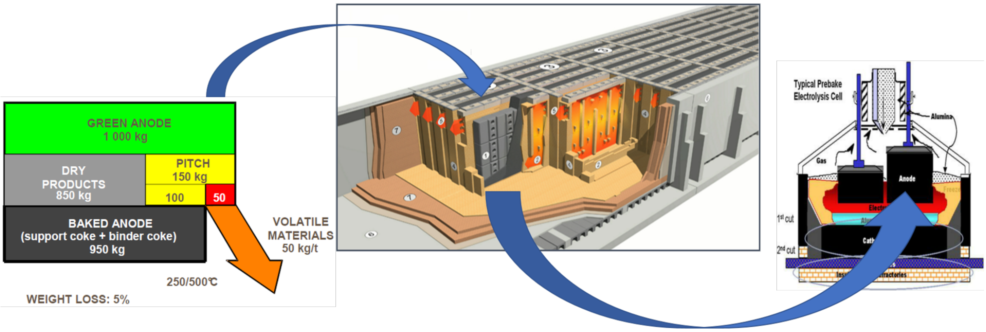

Figure 1.1: The leftmost picture represents the composition of raw anodes (Source: Rio Tinto Alcan Inc., Primary Metal, 2011). The middle picture shows a schematic representation of anode baking furnace (Source: Rio Tinto Alcan Inc., Primary Metal, 2011). The rightmost picture shows the use of baked anodes in electrolysis process. (Source: Parhi, Sidharth Sankar. "Gainful utilization of spent pot lining–A hazardous waste from aluminum industry." PhD diss., 2014.)

Whereas the baked anodes should have higher thermal conductivity, higher crack resistance, and higher resistance to mechanical stress.

The raw anodes, also known as 'green anodes,' consists 85% of dry matter and 15% of the pitch as shown in leftmost picture of Figure 1.1. The pitch component of the green anodes does not conduct the electric current. Therefore, the green anodes are inefficient in the electrolysis process. There are two main stages of the transition in the anode baking. In the first stage of the anode baking process, the coking of the binder pitch occurs with the release of volatile matter. In the second stage, the binder coke is calcined so that a more organised coke structure is formed. Therefore, the overall objective of baking anodes is to calcine the binder pitch so that anodes are more efficient in the Hall-Héroult process.

The anode baking process is carried out in an industrial furnace. Depending on their geometry, there are two main types of anode baking furnaces, namely, horizontal ring furnaces and vertical ring furnaces. In this work, the horizontal open ring furnace is studied. The middle picture of Figure 1.1 shows a typical horizontal anode baking ring furnace. There are two prime components of the furnace. The heat is generated by the combustion process of natural gas in the first component. This component is referred to as the flue wall. The second component is the pit in which the green anodes are placed. The heat generated in the flue wall is conducted through the wall to the anodes in the pits. As can be observed from Figure 1.1, the flue wall consists of baffles that redirect the flow in the desired U-shape directions. The orange arrow shown in the middle picture of Figure 1.1, presents the direction in which the flue gases are transported. The heat transfer, whereas, occurs both in the direction of flow and perpendicular to the flow across the walls.

There are various zones in the anode baking furnace depending on the direction of heat transfer, either from flue gases to anodes or from anodes to flue gases. Figure 1.2 shows a schematic representation of the various zones in the anode baking furnace. Based on the transfer of heat, the anode baking furnace is divided into zones such as preheating, heating, blowing, and cooling zone. Each zone consists of three or four sections.

In the preheating zone, the raw anodes are loaded in the pits. Whereas, the adjacent flue wall contains a flow of the hot gas coming from the heating section. The transfer of heat in this section occurs from the flue to the anodes. The temperature of the anodes is increased to approximately 550 °C in this section. In the heating section, the fuel (natural gas) is injected from the top. Figure 1.2 shows a total of three ramps (one for each section) with two burners on each ramp. In the heating section, the combustion of natural gas is carried out due to the contact with air at ignition temperature. The transfer of heat occurs from the flue gas to the anodes. As a result, the temperature of anodes further increases to approximately 1100 °C. In the third zone, that is, the blowing zone, the air is injected using the blowing ramp. In this zone, the anodes are already heated. Therefore, the transfer of heat occurs from the anodes to the cold air. This results in an increase of gas temperature to 1150 °C. The last zone is the cooling zone in which the anodes are further cooled using external fans so as to post-process.

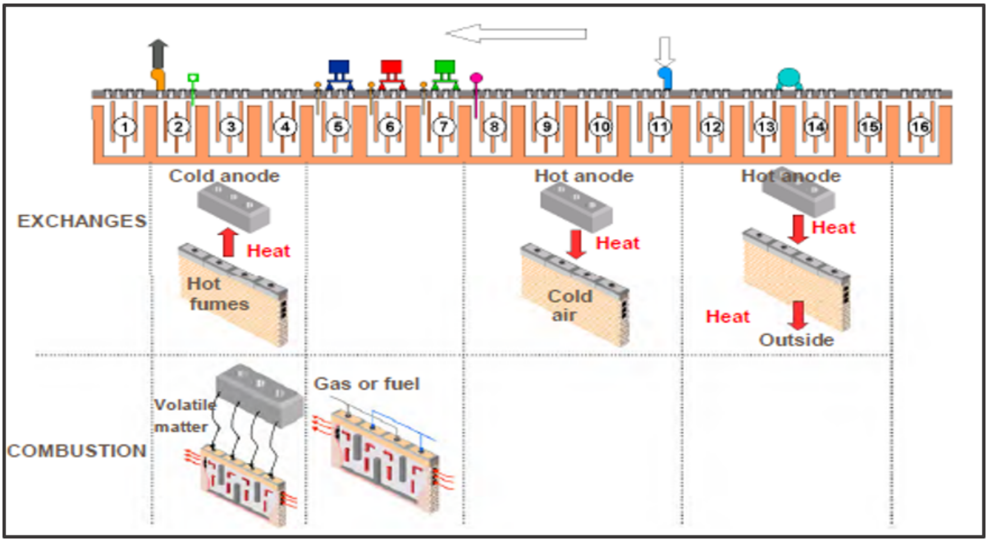

Figure 1.2: The schematic representation of the various sections of anode baking furnace. (Source: Rio Tinto Alcan Inc., Primary Metal, 2011)

1.2. PROBLEM DESCRIPTION

The anode baking process accounts for 15% of the costs in the aluminium production. Due to the significant costs involved in the process, it is important to understand and thereby minimise the challenges involved in the process. The major challenges involved in the process are the high energy consumption, soot formation, nitric oxide emissions, wall deformations, and maintaining the uniform quality of anodes. There are multiple other companies working on resolving these challenges. However, addressing all these issues together can be difficult. Some of the goals even contradict each other. Therefore, defining the problem statement for the work is important.

The problem statement for this thesis work is defined as the unavailability of a definite understanding of the NOx formation in the anode baking furnace. In order to address this problem, a literature study is carried out. Based on the literature, the objectives of the study are defined.

1.3. LITERATURE REVIEW

The modeling of the anode baking process started gaining attention since the early 80s. During this time, Bui. et. al. proposed a simple simulation scheme that assumes a process similar to semi-continuous counter-flow heat exchanger [3–5]. This one-dimensional model was developed by considering sub-models for infiltration, draft, and convection-radiation equation in the flue, micro model for the conduction in solid parts, and macro model to describe overall counter-flow heat exchange. The models developed during this early period were relatively simple but formed the basis of the models that were developed at the later stage. In the mid-90s, the models of vertical anode baking furnaces were in focus [6–8]. The fundamental idea of this modeling was similar to the horizontal anode baking models. Though it proved to be useful for preliminary analysis, these models also failed to give more specific details on emissions. During this time, Jacobsen and Melaaen [8] used Fluent code to study the effect of heating rate and geometry on anode properties in vertical flue ring furnace. However, the model needed further validation and improvement in the combustion model.

A more detailed 3D modeling of the flue of an anode baking furnace started in the mid-90s. Kocaefe et. al. presented a model in which a commercial CFD code CFD S-FLOW3D was used for solving the governing differential equations [9]. The model presents the details of the effect of geometry on the gas flow in the flue and temperature distribution in anodes. However, this model used simplified combustion and radiation models, failing to comment on the pollutants. Much later, Zhang et. al. developed a 2D transient model to evaluate the thermal phenomena [10]. This model does not solve detailed flow fields in the flue; rather, it solves it approximately based on the mass, pressure, and temperature. Therefore, though the results were in good agreement with measured data, the complete overview of the anode baking process was not considered in the model, which limited the optimization of different factors. During this time, Johnson et. al. from Rusal engineering and technical center, Russia, investigated a simplified baking furnace model on the STAR-CD platform to improve flue wall design [11]. In this model, they defined a strategy to deal with different scales in the flue gas and flue wall, packing coke and anode material. This reduced the complexity of the baking model by reducing the high degrees of freedom in the computational domain. The model provided results that predict the heating up process in anodes which is based on the flue gas temperature. However, the model can only provide an overall picture of the heat-up cycle in the anode baking process. The model fails to deal with more specific problems, such as dealing with NOx reduction.

Severo et. al. from PCE Engineering made significant progress in the modeling of anode baking furnaces. A 3D transient model was developed using the commercial code CFX 5.6, in which differential equations were solved using a finite volume method [12]. The model took into account all physical phenomena occurring in preheating and heating sections, as well as the specific burner geometry. The effect of tie bricks and baffle positions was studied by considering two cases. The validation suggests that the model is in good agreement with the industrial furnaces. However, the model only considers single-step combustion reactions failing to provide information on soot and NOx formation. Also, simulating the entire fire cycle with this model was not possible. Therefore, in their subsequent work, an approach to design a furnace was developed by solving mass and energy balances globally in 2D [13]. A 3D model developed in previous work for one section was used as input data. The 2D global model consisted of balance equations for heat transfer, species concentration, and distribution of pressure and was solved by software built-in Fortran. Here, the furnace was considered to behave as a counterflow heat exchanger in which anode movement is discrete. In this model, the heat balance, oxygen concentration inside the flue was calculated in one-dimensional form whereas, only the heat conduction in solids is considered in 2D. However, later by Oumarau et. al. [14], it was shown that the one-dimensional form of heat balance and oxygen concentration was not accurate. However, based on this modeling approach, Severo and Gusberti developed user-friendly software to analyze furnace energy efficiency, minimum oxygen concentration in different sections [15]. This model captures the real transient effect. It was a useful simplified tool for optimizing an anode baking furnace. However, for obtaining more specific data related to soot or NOx formation with higher accuracy, the tool cannot be considered.

The work at the Quebec university in Canada includes both design models (3D) and process models (2D) of horizontal anode baking furnace [14, 16–21]. The design models which are mainly used for optimizing furnace design need more details of the geometry and physical phenomena, and therefore, the models are 3D. Whereas process models are simplified as 2D and are mainly useful for predicting operational parameters. The process models mainly developed by Oumarau et. al. [14] consisted of two separate sub-models for flue and pit due to different time constants in the two domains. They were coupled via an interface at the bricklayer from the flue side. For both flue and pit sub-model, equations were solved using the explicit Euler finite difference method on a Fortran platform. The vertical motion of the gas in the flue was considered as opposed to most of the previous works, where only unidirectional flow in the flue along the furnace length was considered. This allows the 2D temperature distribution boundary condition for the pit sub-model. As the flue wall and pit are symmetric, the domain of the model covers half of the flue wall, brick wall, layer of packed coke, and half of the pit. In their work, the coke layers at the top and bottom of the anodes were also considered so as to account for the heat loss through these layers. In this work, a pit submodel was developed for both constant (at 400° C) and variable properties for refractory wall, filler coke, and anode material layer. It was observed that, with the constant properties, some information is lost, and the temperature is underpredicted. Also, the gradients are higher with constant properties. In the subsequent work of Kocaefe et. al. [17], a 3D transient design model was developed with ANSYS 12. The effect of flue geometry on the flow field was studied on the basis of a number of tie brick layers between two baffles. It was observed that the geometry with two bricklayers is the best configuration as it gives similar velocity for the highest volume fraction of the flue, dispersed flow field, and reasonable pressure drop. The model also presents the anode surface temperatures with respect to time. In the same publication, the continuation results of the process model developed in [14] were presented. It shows that the impact of variable properties on average anode temperature for a given gas temperature profile is not significant. The more detailed results of the process model were presented in their further work [19]. Here, the 2D gas temperature distribution in preheating, heating, and cooling sections after 8 hours of permutation and complete fire cycle are presented along with the 2D distribution of solid temperatures on the vertical place covering the refractory wall coke layer and anode material. The temperature distribution in all sections provides reasonable values, and the pseudo tridimensional temperature distribution in the solid material is predicted. In this model, the impact of the amount of volatiles released was also studied by considering two cases with varying percentages of released volatiles. The mass fraction of O_2 in all sections is decreased for the case where a higher volatile release is assumed. Parallelly, the mass fraction of CO_2 and H_2O in all sections is increased for the case with the higher volatile release. Therefore, this model provides a reasonable tool to study the impact of the amount of volatiles released. However, the exact validation of these results was not provided in these previous publications. Furthermore, the effect of wall deformation on the anode temperature was studied [20]. It was observed that when the pit width is decreased, the anode center temperature is increased, while for an increase in pit width, this temperature is lowered. Also, the gradient of temperature decreases when the pit width is decreased and vice versa. This model also shows the effect of the brick refractory material. The effect is more prominent at the end of a baking cycle as compared to the initial time. The volatile released is measured in terms of tar, hydrogen, and methane release, and the temperature at which this release happens is as per the expectations confirming the model reliability. The effect of airflow at the inlet was studied in this model, and the adverse effect of a lower inlet airflow rate was confirmed. The validation of these results by comparing with experimental data was carried out and provided a good agreement. In the subsequent work, [21], the effect of increasing anode height by keeping pit height constant was explained. The increase in the anode height increases the maximum anode temperature reached due to enhanced heat transfer by reducing the packing coke thermal barrier. Baiteche et. al. from the same research group developed a 3D design model in ANSYS CFX commercial code [17]. In this model, the different radiation models were compared, and the Monte Carlo model was chosen to carry out the simulations. The results were validated by comparing with the measured values and were observed to be in agreement with the measured values. The effect of wall deformation was also studied with this 3D model, and it was found that for the deformed pit and flue, the anodes are not heated uniformly from both sides. The design and process model developed in this research group provides significant information as described above. However, the model lacks the study of the effect of burner geometry. The NOx prediction is mainly in the region of the burner. Also, in the model, only a combustion chemical reaction is considered. The model needs further development in order to predict NOx.

More recently, modeling of anode baking furnace was developed by a group at Khalifa University of science and technology [22–27]. Zaidani et. al. developed a 3D model in COMSOL Multiphysics to study the effect of flue wall deformation on the anode baking [25, 27]. These 3D models are simplified geometries without tie-bricks. The combustion process is simplified by considering the hot jet approach. The model presents the dependence of flow on baffle positions. The model is validated by comparing with measured values, and some differences in the values are observed. Further, the effect of flue wall deformation on anode temperature is investigated, and it is observed that the maximum temperature increases with the increase in the flue wall deformation. This study also shows that the temperature-dependent properties of the material are required for a more realistic picture. The effect of operational parameters such as hot jet speed and mainstream velocity also have a significant impact on the anode temperature distribution in both straight and deformed flue walls. However, the model does not consider the position of tie bricks, which also affects the flow field in the flue as well as the structural stability. Tajik et. al. in their work, develops a 2D steady-state model of anode baking by using ANSYS Fluent to study the effect of operational parameters on the distribution of gas temperature [26]. The flow and temperature homogeneity are studied based on the flow and temperature uniformity index that is calculated from mass and area-weighted averages. The work suggests that more uniformity is achieved by closing the top of the baffles space. However, the bypass is needed for the safety of the furnace operation. The effect on safety is not mentioned in this work. In the subsequent work [22], the flow blockages due to packing coke infiltration are also studied, and design modifications are proposed that provide a more uniform flow and temperature field. Though the suggested modifications sound promising, the pilot run is needed to analyze the possible problems that might affect the safety of the furnaces. Later, Tajik et. al. also developed a 2D steady-state model in ANSYS Fluent that investigates two combustion models, eddy dissipation model and presumed PDF model [24]. The results are obtained for the average temperature of the combustion flame, mixture fraction, soot volume fraction, and NO concentration. The validation is performed by comparing these results with another confined flame model. The presumed PDF model provides results that agree with experimental results. However, the validation process is obscure in this work. This model is also used to predict the effect of flue design modification on soot and NOx formation. The paper suggests that the flue wall modification by closing the top of baffles can result in a significant decrease in the global equivalence ratio, which results in lower CO, NOx, and soot concentration. However, the calculation of this reduced global equivalence ratio is not clear from the paper. The most recent work on NOx modeling provides changes in the NOx generation with respect to the inlet oxygen concentration at elevated oxidizer temperature. The work shows that by diluting the inlet oxygen concentration, pollutant formation can be decreased [28]. Recently, a work by Bourgier et. al. from Rio Tinto also provides insights on the 3D transient model of the entire fireline developed in ANSYS Fluent software by taking into account all important physical phenomena [29]. The developed model can be used for the modification of existing furnace designs. However, improvements in the model are needed to implement control strategies, predict soot and NOx formation. The continuous prediction of flow in the flue wall is still a challenge.

For the optimization of NOx, the chemistry near the burner plays an important role. This also includes focusing on combustion models that are used in the modeling of flue gas. For simplicity, the eddy dissipation model proves to be useful. However, this model does not provide an accurate prediction of chemical kinetics. Gregoire and Gosselin compared two modeling approaches of combustion in an anode baking furnace [30]. In this paper, two cases were considered. The first case mimicked the burner flame by introducing a hot stream of air, whereas, in the second case non-premixed mixture fraction approach was used. A detailed 3D model was developed focusing on the heating section of the furnace in ANSYS Fluent. The two approaches were compared with respect to the combustion flame shape, hot spots in the furnace, and maximum and minimum temperatures attained in the anodes. It was observed that the mixture fraction model provides more detailing of the overall temperature distribution with one third more computational time. The model provides good preliminary results. However, development in terms of combustion of volatiles, infiltration at the top, and control strategy of fuel gas was lacking in this model. In their further work, Gregoire and Gosselin compared three combustion models, namely, eddy dissipation, mixture fraction/PDF, and simplified approach of mimicking burner flame by a hot stream of air from the previous paper [31]. Even in this work, a 3D model was simulated using ANSYS Fluent. The results suggest that all three approaches provide similar final anode temperatures. However, a hot jet flame model needs some adjustments to reproduce the flame shape and flame temperature. Also, the mixture fraction model should be used to predict the maximum flame temperature. Moreover, the effect of radiation seems to be important with all combustion models, whereas the effect of buoyancy can be neglected. This work provides important information regarding the use of a combustion model.

A literature study shows that there have been enormous efforts to develop an understanding of anode baking furnaces. The objectives of all these studies vary with respect to addressing different challenges of the anode baking process. As illustrated in the problem statement, the challenge of NOx reduction has been a focus of this study. There have been modeling studies for the reduction of NOx in literature. However, these models lack validation by comparing NOx from the furnace. Keeping this limitation in mind, the objective of this thesis is determined.

1.4. OBJECTIVES

In this work, the anode baking furnace of Aluminium and Chemie Rotterdam B.V. (Aluchemie) is studied. Along with the other challenges, Aluchemie has difficulties in maintaining their nitric oxide (NOx) emission as per the regulations. Therefore, the goal of the project is to understand the NOx formation in the furnace and thereby, providing strategies to reduce the emissions. As the maximum NOx generation occurs in the heating zones, the section of the heating zone is selected for the examination.

The general objective of the study is to obtain a mathematical model of a single section from the heating zone of an anode baking furnace. The heating section has overhead burners through which the natural gas is injected into the flue walls. The important physical phenomena in the furnace are turbulent flow, combustion of natural gas, radiation, and conjugate heat transfer through walls. Therefore, the present study aims to couple multi-physics models in COMSOL multi-physics software. The structured meshing of the flue wall is difficult to obtain due to the internal complexities. Therefore, one of the objectives is to investigate the external dedicated meshing tool.

The NOx generation strongly depends on the temperature distribution in the furnace. The temperature distribution can be obtained by coupling the turbulent flow, combustion process, radiation, and conjugate heat transfer. The choice of appropriate turbulent, combustion, and radiation model depends highly on the application. In this work, the objective is to compare models with varying operating conditions and check their effect on the NOx generation. The final aim of the work is to compare the model with measured values at the furnace to check if the model values are within the range of measured values.

1.5. SCIENTIFIC CONTRIBUTIONS

The scientific contribution expected from the thesis work more specifically are as follows:

- Numerical model of realistic representation of furnace by industrial partner and comparison with measurements
- Mesh generation by external software (cfMesh) and the conversion tool to convert mesh from FOAM to Nastran format
- Development of mixture fraction beta-pdf combustion model in COMSOL Multiphysics software

1.6. THESIS OUTLINE

In this thesis, a numerical model of the heating section of an anode baking furnace is developed. Chapter 2 provides an overview of the multiphysics phenomena occurring in the heating section of the furnace. The chapter describes the modeling approach used for each of the physics. After establishing the modeling approach for each of the physics, the mathematical techniques implemented for solving model equations are described in Chapter 3. The accuracy of the finite element method described in chapter 3 is dependent on the meshing of the model geometry. Chapter 4 describes the meshing techniques applied in this work. Chapter 4 also describes the workflow for obtaining the mesh by the cfMesh meshing software and the conversion tool required for converting the mesh into Nastran format. The aerodynamics of the flue gases is an important physical phenomenon in the furnace. Chapter 5 describes the turbulent flow modeling executed in the furnace section. In chapter 6, the results of combustion and heat transfer modeling are examined. The radiation and conjugate heat transfer through walls are described under the section of heat transfer modeling. In chapter 7, the model is validated by comparing values with the measurement carried out in the furnace. Finally, the conclusions of the work are presented in chapter 8.

2

MULTI-PHYSICS EVALUATION

The anode baking process is a typical example of an industrial furnace that comprises multiple physical phenomena occurring simultaneously. These physical phenomena are highly dependent on each other. For accurate prediction of emissions from the furnace, all these phenomena need to be considered. One way to inter-relate these phenomena is through numerical modeling. The modeling requires describing these physical phenomena in the form of mathematical expressions. These expressions are further simplified based on the underlying assumptions.

In this chapter, all underlying physics of the anode baking process are described. The mathematical expressions governing the physical phenomena are simplified using numerical models. The relevant numerical models for various physical phenomena are analyzed for a given application of the anode baking process. The motivation for using these numerical models is elaborated.

2.1. CONSERVATION EQUATION FOR FLUID FLOW

Fluid flow is of primary importance in the anode baking process. The heat generated in the furnace results from the combustion process governed by the mixing of two streams, namely, air and fuel. The flow of these streams determines the extent of mixing and thus the combustion in the process. Therefore, modeling the fluid flow is the primary step for modeling the anode baking process.

The governing equations of fluid flow are derived by the fundamental laws of continuum physics, i.e., the law of mass and momentum conservation. The law of conservation of mass states that, 'in an isolated system, mass can neither be created nor be destroyed by chemical reactions or physical transformation' [32]. The mathematical transformation of this law is known as the continuity equation and is given by Equation 2.1. The first term of the equation determines the net rate of density change with time and is zero for the steady-state assumption. The second term represents the convective term and is the net flow of mass across boundaries. The continuity equation in the incompressible form is the basis of all fluid flow problems.

$$\frac{\partial \rho}{\partial t} + \nabla \cdot (\rho \mathbf{u}) = 0 \tag{2.1}$$

The second critical equation for the fluid flow is based on the conservation law of momentum. The conservation law of momentum is derived from Newton's second law of motion. Equation 2.2 provides the mathematical form of the law of conservation of momentum. The first term of the equation represents the accumulation of momentum with respect to time in the control volume, the second term represents the net flux of momentum through the control volume, the third term is the pressure and viscous stresses applied to the control volume, and the fourth term represents the external body forces (such as gravity) acting on the control volume.

$$\rho \frac{\partial \mathbf{u}}{\partial t} + \rho(\mathbf{u} \cdot \nabla)\mathbf{u} = \nabla \cdot [-p\mathbf{I} + \tau] + \mathbf{F} \tag{2.2}$$

For a Newtonian fluid, the viscous stresses are proportional to the deformation rate. Equation 2.3, known as Navier-Stokes equation, is obtained by substituting the viscous stress term of 2.2 by a proportionality constant and the deformation rate term for a Newtonian fluid. The proportionality constant is known as the dynamic viscosity.

$$\rho \frac{\partial \mathbf{u}}{\partial t} + \rho(\mathbf{u} \cdot \nabla)\mathbf{u} = \nabla \cdot [-p\mathbf{I} + \mu(\nabla \mathbf{u} + (\nabla \mathbf{u})^T)] + \mathbf{F} \tag{2.3}$$

The Reynolds number is the crucial parameter to determine whether the flow is laminar, transitional, or turbulent. The Reynolds number is given by Equation 2.4. Based on the calculation, it will be explained in later sections that the flow dynamics in an anode baking furnace are turbulent.

$$Re = \frac{\rho U_{\text{ref}} D}{\mu}. \tag{2.4}$$

Here, ρ , U_{ref}, D and μ are the density, reference velocity, reference diameter and dynamics viscosity, respectively.

2.2. TURBULENT FLOW

As in most industrial applications, the flow in the anode baking furnace is turbulent. The modeling of turbulent flow is challenging due to the presence of spatial and temporal fluctuations. These fluctuations give rise to the swirling of fluids known as eddies. The length of these eddies is of a wide range, and therefore, modeling turbulent flow is challenging [33]. Among the various computational approaches for modeling turbulent flow, RANS, LES, and DNS are the most popular. These are discussed in the following sections.

DIRECT NUMERICAL SIMULATION (DNS)

In the direct numerical simulation approach, no modeling or closure equations are needed for resolving the spectrum of eddies. The Navier-Stokes equation presented in Equation 2.3 is solved numerically to a complete extent up to a Kolmogorov scale. The Kolmogorov scale is given by $\eta = (\frac{\nu^3}{\epsilon})^{1/4}$ where ν is the kinematic viscosity and ϵ is the turbulent dissipation rate [34]. The dissipation rate ϵ can be scaled as $\epsilon \sim \frac{u'^3}{l}$, where u' is the RMS fluctuation velocity. The integral scale l is characterized by turbulent kinetic energy k and dissipation rate ϵ as $l = \frac{k^{3/2}}{\epsilon}$. Based on these relations, it was estimated that, for a three-dimensional domain with $Re_l = 6000$, the minimum number of grid points required is as high as 2×10^9 [34]. Therefore, though the calculations can resolve the smallest length scales of eddies and time scales, they demand high computational power. The computational power further increases exponentially with the Reynolds number. This implies that using DNS calculations for complex geometry with a high Reynolds number is practically impossible in terms of the required computational power available to date. Moreover, the need for an accurate solution is less of a priority compared to the time required to achieve that solution. Therefore, in most engineering applications, the DNS approach is omitted.

LARGE EDDY SIMULATION (LES)

Large-eddy simulation is another modeling approach for turbulent flows. In the LES approach, the large length scale eddies are resolved while the small eddies are modeled with subgrid-scale (SGS) models [35]. The larger eddies consist of the maximum of the turbulent kinetic energy. Therefore, the assumption of resolving only larger-scale eddies is practical. The larger eddies are separated with spatial filters, and Navier-Stokes equation is solved for determining the flow field. In comparison, the SGS modeling for the small-scale eddies is implemented. Most of the SGS models use Boussinesq's hypothesis in which the eddy viscosity defines the SGS stress tensor. The eddy viscosity is further computed using closure models such as the Smagorinsky model [35].

The LES approach has developed significantly in the last few years. Similar to DNS, the approach was initially limited to simple geometries with low Reynolds numbers. With the improvement in computational power, the approach has started gaining attention for more complex geometries. However, the method still needs further improvement in terms of the required computational power to be used in industrial applications.

REYNOLDS AVERAGE NAVIER-STOKES APPROACH

The most common approach for solving turbulent flows in industrial applications is Reynolds average Navier-Stokes (RANS) approach [36]. In most industrial applications, steady state flow conditions are desired. In such cases, the averaged quantity of variables as a solution is a good approximation. In the RANS approach, the Navier-Stokes equation is averaged over time. In this way, the mean flow, i.e., mean values of the variables, is calculated while the instantaneous scales of turbulent flow are modeled. Though the transitional changes are ignored while averaging the equation of flow motion, the approach provides good enough output with the minimum required computational power. Therefore, in this study, the RANS approach is utilized for modeling the turbulent flow.

The time-averaging of the Navier-Stokes equation is carried out by decomposing the instantaneous variable into the mean and fluctuating part as given in Equation 2.5. Here, ϕ is the instantaneous quantity, $\overline{\phi}$ is the mean of the quantity, and ϕ' is the fluctuating part of the quantity.

$$\phi = \overline{\phi} + \phi' \tag{2.5}$$

For compressible flow, further averaging, known as Favre averaging, is required for obtaining the RANS equation. The density-based Favre averaging is represented by Equation 2.6.

$$\overline{u} = \frac{1}{\overline{\rho}} \lim_{t_1 \to \infty} \int_{t_0}^{t_0+t_1} \rho(x,\tau)u(x,\tau), d\tau \tag{2.6}$$

Applying the time and Favre averaging to Equation 2.1 and 2.3, the RANS form of the continuity and NS equations for the compressible flow can be obtained as presented in Equation 2.7 and 2.8.

$$\frac{\partial \overline{\rho}}{\partial t} + \frac{\partial(\overline{\rho u_{\mathrm{i}}})}{\partial x_{\mathrm{j}}} = 0 \tag{2.7}$$

$$\overline{\rho}\frac{\partial \overline{u_{\mathrm{i}}}}{\partial t} + \overline{\rho u_{\mathrm{j}}}\frac{\partial \overline{u_{\mathrm{i}}}}{\partial x_{\mathrm{j}}} = -\frac{\partial \overline{p}}{\partial x_{\mathrm{j}}} + \frac{\partial}{\partial x_{\mathrm{j}}}\left(\mu\left(\frac{\partial \overline{u_{\mathrm{i}}}}{\partial x_{\mathrm{j}}} + \frac{\partial \overline{u_{\mathrm{j}}}}{\partial x_{\mathrm{i}}}\right) - \frac{2}{3}\mu\frac{\partial \overline{u_{\mathrm{k}}}}{\partial x_{\mathrm{k}}}\delta_{\mathrm{ij}} - \overline{\rho u_{\mathrm{j}}' u_{\mathrm{i}}'}\right) + \overline{F_{\mathrm{i}}} \tag{2.8}$$

Where, μ is the dynamic viscosity. Equation 2.8 has a Favre averaged Reynolds stress term which needs further modeling for closure. The Reynolds stress term can be defined with the Boussinesq's approximation in terms of the eddy viscosity as shown in Equation 2.9.

$$-\overline{\rho u_{\mathrm{j}}' u_{\mathrm{i}}'}) = \mu_{\mathrm{T}}\left(\frac{\partial \overline{u_{\mathrm{i}}}}{\partial x_{\mathrm{j}}} + \frac{\partial \overline{u_{\mathrm{j}}}}{\partial x_{\mathrm{i}}}\right) - \frac{2}{3}\left(\mu_{\mathrm{T}}\frac{\partial \overline{u_{\mathrm{k}}}}{\partial x_{\mathrm{k}}} + \overline{\rho k}\right)\delta_{\mathrm{ij}} \tag{2.9}$$

Here, the μ_{T} is the turbulent viscosity. The variable k is the turbulent kinetic energy which can be modeled with various turbulent models described in the following sections. Moreover, in the subsequent equations the overbar, which represents that the quantity is averaged, has been removed for simplicity. Following is a list of some of the relevant turbulence models that can be used to model the eddy viscosity term from Equation 2.9. These models differ in the number of variables for which an additional transport equation is solved, the variable itself and the treatment carried out at the walls accounting for the high gradients. The brief introduction of all the models is presented below [37]. The detailed explanation of all these models can be found in [38].

- L-VEL - In this model, no additional transport equations are solved. The eddy viscosity is obtained by the algebraic expression that is derived by extending the logarithmic wall function. Though the model is computationally inexpensive, it does not provide the required level of accuracy [37].

- yPlus - The yPlus model is similar to L-VEL model and the eddy viscosity is not based on any additional transport equation. The model is based on the Prandtl-mixing length theory which accounts for the nearest distance to the wall. Similar to the L-VEL model, the solution does not provide the desired level of accuracy if the turbulent flow is the dominant phenomenon.

- Spalart- Allmaras - The turbulent eddy viscosity is defined in terms of undamped turbulent kinematic viscosity which is computed by solving its transport equation.

The model is suitable for the flow over external bodies, especially in aerodynamics. There have been numerous validation studies for the SA model in aerodynamic applications [37].

- k-ϵ - The k-ϵ model is a two equation model, i.e., it solves two transport equations of turbulent kinetic energy and turbulent dissipation rate. The turbulent eddy viscosity is defined based on these two equations. The model has two variations, namely standard k-ϵ model and realizable k-ϵ model, based on the relation of eddy viscosity with turbulent kinetic energy and turbulent dissipation rate [37]. The model is prevalent in industrial applications due to its robustness and sufficient accuracy of solution. Moreover, the model is preferable in the case of flows over bluff bodies. In the anode baking section, there are large number of tie-bricks as well as baffles over which the flow occurs. Therefore, both versions of the model are a good choice for solving the turbulent flow in the anode baking furnace and are discussed in detail in the following section.

- k-ω - The k-ω model involves solving two transport equations for turbulent kinetic energy and turbulent specific dissipation rate. The eddy viscosity in this model is defined based on these two variables. The k-ω model provides a more accurate solution near the walls as compared to the k-ϵ model since it does not always use wall functions. In specific cases, the wall functions can be added. However, the model is highly non-linear and sensitive towards the initial guess of the solution [37]. The anode baking furnace geometry is quite complex and obtaining mesh and initial guess for such a sensitive turbulent model is challenging. Moreover, Tajik et.al. have shown in their study of confined turbulent diffusion flame that the realizable k-ϵ model performs better than k-ω model with respect to the experimental data of Brooks and Moss [22].

- SST - SST model is a combination of k-ϵ model and k-ω model. The model uses k-ϵ model in the bulk flow and k-ω model near the walls. The model essentially performs better that the individual k-ϵ and k-ω models. The model needs similar resolution of mesh to that which is required for the k-ω model [37]. Therefore, the disadvantages of applying k-ω turbulent model for the anode baking furnace model continues for this model as well.

- v2-f - The anisotropic behaviour of the velocity fluctuations are accounted in the v2-f model by solving two more equations apart from the turbulent kinetic energy and turbulent dissipation rate of the k-ϵ model. The third equation is solved for the transport of normalized velocity fluctuations whereas the fourth equation accounts for the non-local pressure-strain effect [37]. This model is effective for the enclosed flows and could be a good option for the anode baking model. However, the additional transport equations as compared to the k-ϵ model for a complex geometry such as an anode baking furnace makes it unattractive.

The description of the turbulent flow models studied in this work are described in detail in the next subsection.

2.2.1. STANDARD K-ϵ MODEL

The standard k-ϵ model is formulated based on the two transport equations, namely for turbulent kinetic energy and the turbulent dissipation rate presented by Equation 2.10 and 2.11, respectively. The terms on the right-hand side represent the conservative diffusion, turbulent production and dissipation, respectively. Both of these equations can be obtained by the time averaging of Navier-Stokes equation. Further treatment such as multiplying by mean velocity is required followed by some algebraic operations. The flows where the convection and diffusion are responsible for production and dissipation of turbulence are modeled well by the standard k-ϵ model. The model proves helpful in the applications where the internal flow with low pressure gradients is observed.

$$\rho(\mathbf{u}\cdot\nabla)k = \nabla\cdot\left[\left(\mu+\frac{\mu_t}{\sigma_k}\right)\nabla k\right] + P_k - \rho\epsilon \tag{2.10}$$

$$\rho(\mathbf{u}\cdot\nabla)\epsilon = \nabla\cdot\left[\left(\mu+\frac{\mu_t}{\sigma_\epsilon}\right)\nabla\epsilon\right] + C_{\epsilon 1}\frac{\epsilon}{k}P_k - C_{\epsilon 2}\rho\frac{\epsilon^2}{k} \tag{2.11}$$

The turbulent viscosity in the standard k-ϵ model is defined by Equation 2.12.

$$\mu_t = \rho C_\mu \frac{k^2}{\epsilon} \tag{2.12}$$

where, C_μ is constant. The production term in Equation 2.10 and 2.11 is defined by Equation 2.13.

$$P_k = \mu_t[\nabla\mathbf{u} : (\nabla\mathbf{u} + (\nabla\mathbf{u})^T) - \frac{2}{3}(\nabla\cdot\mathbf{u})^2] - \frac{2}{3}\rho k\nabla\cdot\mathbf{u} \tag{2.13}$$

In all these equations μ and μ_T are the dynamics and turbulent viscosity, respectively. The values of the constant parameters for Equations (2.10) and (2.11) are given in Table 2.1.

Table 2.1: Values of the constants for the standard k-ϵ model.

Constant	Value
C_μ	0.09
$C_{\epsilon 1}$	1.44
$C_{\epsilon 2}$	1.92
σ_k	1.00
σ_ϵ	1.30

2.2.2. REALIZABLE K-ϵ MODEL

The formulation of the realizable k-ϵ model is similar to the standard k-ϵ model. This model also consists of two transport equations for turbulent kinetic energy and turbulent dissipation rate. The turbulent kinetic energy equation is precisely the same as Equation 2.10. However, the transport equation of the turbulent dissipation rate is improved by accounting for the mean flow distortion [38]. The equation for the turbulent dissipation rate for the realizable k-ϵ model is given by Equation 2.14.

$$\rho(\mathbf{u}\cdot\nabla)\epsilon = \nabla\cdot\left[\left(\mu+\frac{\mu_t}{\sigma_\epsilon}\right)\nabla\epsilon\right] + C_1\rho S\epsilon - C_{\epsilon 2}\frac{\rho\epsilon^2}{k+\sqrt{\nu\epsilon}} \tag{2.14}$$

The turbulent viscosity in the realizable k-ϵ model is also defined by Equation 2.12. But C_μ is not constant and is defined by the series of equations from Equation 2.15 to 2.20.

$$C_\mu = \frac{1}{A_0 + A_s U^{(*)} \frac{k}{\epsilon}} \tag{2.15}$$

$$A_s = \sqrt{6}\cos(\frac{1}{3}\arccos(\sqrt{6}W)) \tag{2.16}$$

$$W = \frac{2\sqrt{2}\mathbf{S}:(\mathbf{S}\cdot\mathbf{S})}{|\mathbf{S}|^3} \tag{2.17}$$

$$U^{(*)} = \sqrt{\mathbf{S}:\mathbf{S}+\omega:\omega} \tag{2.18}$$

$$\mathbf{S} = \frac{1}{2}(\nabla\mathbf{u}+(\nabla\mathbf{u})^T) \tag{2.19}$$

$$\Omega = \frac{1}{2}(\nabla\mathbf{u}-(\nabla\mathbf{u})^T) \tag{2.20}$$

The values of the constant parameters for Equation (2.14) are given in Table 2.2.

Table 2.2: Values of the constants for the realizable k-ϵ model.

Constant	**Value**
$C_{\epsilon 2}$	1.90
σ_k	1.00
σ_ϵ	1.20
A_0	4.00

The boundary conditions for both standard and realizable k-ϵ model are the same. The k and ϵ at the inlet of air and fuel are defined based on the reference velocity, turbulent length scale, and turbulent intensity as presented in Equations (2.21) and (2.22).

$$k = \frac{3}{2}(U_{ref} I_T)^2 \tag{2.21}$$

$$\epsilon = C_\mu^{(3/4)} \frac{k^{(3/2)}}{L_T}. \tag{2.22}$$

The analytical expression known as wall function is used to describe the flow near walls. The domain of computation is considered located at a distance δ_w such that the δ_w^+ computed by Equation (2.23) is close to the value 11.06. The δ_w^+ distance represents the location at which the logarithmic layer meets the viscous sublayer. The value 11.06 is explained in the work of Grotjans and Menter [39]. At this distance both linear relations given in Equations (2.24) and (2.25) hold. The value 11.06 is the optimized solution for these two relations solved at default values of κ and β. The δ_w is adjusted such that its value is not less than half of the cell size near the boundary mesh cell.

$$\delta_w^+ = \rho u_\tau \delta_w / \mu \tag{2.23}$$

$$y^+ = \frac{1}{\kappa} log y^+ + \beta \tag{2.24}$$

$$y^+ = \frac{|u|}{u_\tau}. \tag{2.25}$$

As will be discussed in the next chapter, COMSOL Multiphysics software is used for the modeling in this work. There have been test cases that have validated the standard and realizable k-ϵ model in COMSOL Multiphysics software [40]. It has been verified that these models provide good results for anode baking furnace modeling [22]. Therefore, in this work, these two models have been studied.

2.3. COMBUSTION

The combustion process is practically the most important process to extract energy from the fossil fuels. The burning of fossil fuels accounts for 87% of the electrical and heat energy [41, 42]. There are numerous industries such as chemical, steel, aluminium, glass, mining etc. which are based on the combustion as the energy source. The typical conventional fuels that undergo combustion for producing the energy are coal, diesel, gasoline, natural gas etc. The combustion of these sources of energy poses various challenges. Some of these challenges include efficient burning of fuels and reducing emissions of gases such as CO_2. The combustion industry has been investigating into addressing such challenges by studying the fundamental science behind the combustion phenomena [43–47]. The developments in the combustion industry with respect to the efficiency, productivity, safety and environmental performance are based on the optimization of the combustion process [48]. The combustion modeling of the system plays an important role in the optimization process. There are numerous combustion models with varying complexities that can be used for finding an optimal solution in the system [49]. In the present energy transition scenario where the decarbonization or reducing emissions is at the center of energy industries, the combustion modeling of industrial furnaces is at the forefront. The combustion models can be examined to understand the performance of different fuels or fuel blends with the existing design of the furnace.

The heat required for the baking of anodes is generated by the combustion process of natural gas. Therefore, combustion is another critical phenomenon in anode baking furnace modeling. The following reaction provides a simple representation of the one-step combustion reaction of methane.

$CH_4 + 2\,(O_2 + 3.76\,N_2) \longrightarrow CO_2 + 2\,H_2O + 7.52\,N_2$

In reality, there exist many intermediate and side reactions. The chemical reaction mechanism is a combination of reactions, species and intermediate radicals that are considered in the process. Therefore, the thermodynamic data, chemical equilibrium and chemical kinetics follows from the chemical reaction mechanism [44]. There are various chemical reaction mechanisms established in the literature for accounting the combustion reaction of methane [50]. Table 2.3 presents a summary of a number of involved chemical species and reactions for chemical reaction mechanisms studied in this work.

Table 2.3: Summary of chemical reaction mechanisms

Mechanism	**Number of chemical species**	**Number of chemical reactions**
1 step	5	1
2 step BFER	6	2
GRI 3.0	325	53

The thermodynamics in the system are dependent on the choice of chemical reaction mechanism. Figure 2.1 shows the adiabatic flame temperature for various mechanisms with respect to the equivalence ratio. The equivalence ratio provides the indication of the ratio of air to fuel in the system. If the value is less than 1 then the mixture is lean while if the value is higher than 1 then it is a rich mixture. The system with an equivalence ratio of 1 represents the stoichiometric mixture [33]. It can be observed that the adiabatic flame temperature changes as the chemical reaction mechanisms are varied. For a given stoichiometric ratio, the adiabatic flame temperature for a 1 step mechanism is higher than for two mechanisms. With the increase in the chemical reactions, the heat released is absorbed by the other reactions in the mechanisms. This leads to lower adiabatic flame temperature with increased chemical reactions.

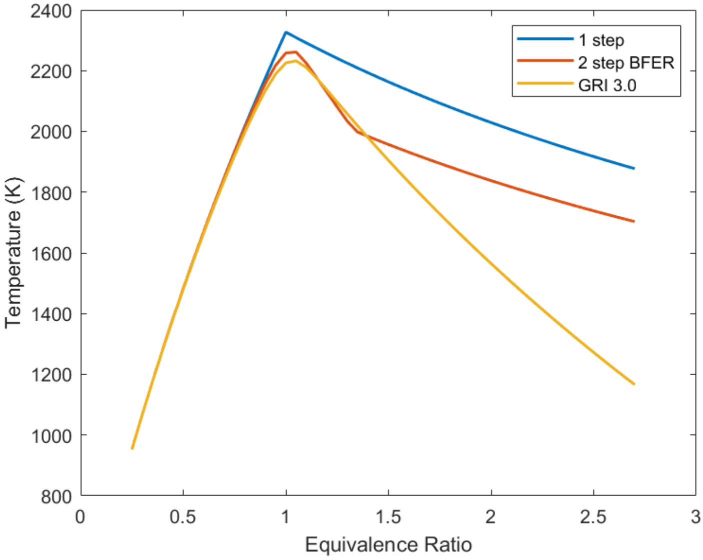

Figure 2.1: The adiabatic flame temperature as a function of equivalence ratio for different chemical mechanisms.

In the anode baking furnace the combustion reaction occurs when the two flow streams, i.e., fuel and oxidizer streams, are mixed. This is a classic example of reactive flow. Therefore, the transport equation of the mass fraction of the individual species needs to be solved for obtaining the final mass fraction distribution across the furnace. Moreover, as discussed in the previous section, Favre averaging of the transport equation is carried out so that it can be coupled with the Favre averaged turbulent flow. Equation 2.26 presents the Favre averaged transport equation of i'th chemical species.

$$\frac{\partial(\overline{\rho w_i})}{\partial t} + \frac{\partial(\overline{\rho w_i u_j})}{\partial x_j} = \frac{\partial}{\partial x_j}(\tau_i \frac{\partial \overline{w_i}}{\partial x_j}) + \overline{R_i} \tag{2.26}$$

The first term on the right-hand side represents the diffusion of the species where $\tau_i = \frac{\mu+\mu_T}{Sc_i}$. Here, the Sc_i is the Schmidt number of species i. μ and μ_T represents the dynamic and turbulent viscosity, respectively. The Schmidt number is calculated by the Kays-Crawford model. According to this model, turbulent Schmidt number is derived from the turbulent Peclet number as per Equation 2.27.

$$Sc_T = \left(\frac{1}{2Sc_{T\infty}} + \frac{0.3Pe_T}{\sqrt{Sc_{T\infty}}} - (0.3Pe_T)^2[1 - e^{-1/0.3\,\mathrm{Pe_T}\sqrt{Sc_{T\infty}}}]\right) \tag{2.27}$$

The turbulent Schmidt number at infinity is $SC_{T\infty} = 0.85$ and turbulent Peclet number is defined as per the Equation 2.28.

$$Pe_T = \frac{\nu_T}{\nu} Sc \tag{2.28}$$

The term $\overline{R_i}$ in Equation 2.26 is the reaction source term and depends on the formation or consumption of species i. In the following section the methods that can be used for the computation of this source term are elaborated.

2.3.1. CHEMICAL KINETICS

The formation or consumption of a particular chemical species in a given reaction set is dependent on the chemical kinetics. The reaction source term R_i for species i contributing in j reactions is given by Equation 2.29.

$$R_i = M_i \sum_{j=1}^{n} \frac{d[i]}{dt} \tag{2.29}$$

In general, the rate of formation/consumption of a chemical species is defined by the rate constants. These rate constants can be further determined based on the activation energy and the pre-exponential factor as given by Equation 2.30. This formulation is known as the Arrhenius law.

$$k = Ae^{\frac{-Ea}{RT}} \tag{2.30}$$

where, Ea is the activation energy of the reaction, R is the universal gas constant and T is the temperature. Let us consider a two step BFER reaction mechanism as given by Westbrook and Dryer [51] presented by the following two reactions.

$$\mathrm{CH_4 + 1.5\,O_2 \xrightarrow{kf_1} CO + 2\,H_2O}$$

$$\mathrm{CO + 0.5\,O_2 \xrightleftharpoons[kr_2]{kf_2} CO_2}$$

Based on the chemical kinetics, the rate of change of concentration of CO is given by the following equation [52].

$$\frac{d[CO]}{dt} = (kf_1[CH_4]^1[O_2]^{1.5}) - (kf_2[CO]^1[O_2]^{0.5} - kr_2[CO_2]^1) \tag{2.31}$$

Similarly, the rate of change of concentration for all other species can be represented by the following equations.

$$\frac{d[CH4]}{dt} = -(kf_1[CH_4]^1[O_2]^{1.5}) \tag{2.32}$$

$$\frac{d[O2]}{dt} = -1.5(kf_1[CH_4]^1[O_2]^{1.5}) - 0.5(kf_2[CO]^1[O_2]^{0.5} - kr_2[CO_2]^1) \tag{2.33}$$

$$\frac{d[H_2O]}{dt} = 2(kf_1[CH_4]^1[O_2]^{1.5}) \tag{2.34}$$

$$\frac{d[CO_2]}{dt} = 1(kf_2[CO]^1[O_2]^{0.5} - kr_2[CO_2]^1) \tag{2.35}$$

The non-linear ODEs presented by Equation 2.31 to 2.35 are solved by integrating over time to obtain the reaction source term R_i in Equation 2.26. For a single step or two step reactions, calculating the rate of formation or consumption by considering the chemical kinetics might be feasible. However, for a complex reaction mechanism, calculating this term for all species is difficult [53]. With a larger number of chemical species, the system of equations becomes too large. Moreover, the time scale of reaction for different reactions can vary significantly. In such cases, the system of equations is stiff and difficult to solve. Therefore, calculating reaction source terms for a laminar system itself is difficult.

In the present application of an anode baking furnace, the flow is turbulent. In the turbulent reactive flow, the Favre averaged reaction source term $\overline{R_\mathrm{i}}$ is required. This further leads to the calculation of Favre-averaged rate of change of concentration of species. Due to a highly non-linear Arrhenius equation, it is challenging to express the Favre-averaged mean reaction source term. The other routes in which the mean reaction source term is written by expanding a Taylor series also requires correlations and models to solve the unknowns [33, 52]. The complexity in defining these correlations further increases with increasing the complexity in the reaction mechanisms.

There are different modeling techniques that are used to compute the mean reaction source term. These techniques represent the turbulent chemistry interactions in different ways. The assumptions and the formulation of these modeling techniques are such that they sufficiently describe the solution in the given application.

2.3.2. EDDY DISSIPATION MODEL

Eddy dissipation is a turbulent-chemistry model that provides reaction source term based on the turbulent mixing. The model assumes an infinitely fast chemical reaction and therefore, the mixing time scale is larger than the chemical time scale. In other words, the Damkohler number is high enough (>10) that it can be assumed that the the reaction is controlled by the mixing parameters [52]. Therefore, the reaction source term in the eddy dissipation model is governed by k and ϵ.

Equation 2.36 presents the reaction term, from Equation (2.26) which is modeled by the eddy dissipation model [54, 55]. The treatment on the reaction source term such as the regularization, is implemented to ensure that the reactant is consumed only when its mass fraction value is higher than zero [55]. Moreover, the mass fraction of product is restricted to take the maximum value of 1. The eddy dissipation model equations are given by Equation (2.36) to (2.40).

$$\overline{R_i} = \frac{1}{2}\frac{R_i^c - |R_i^c|}{\max(w_i, w_i^{dl})}\max(w_i, 0) + \frac{1}{2}\frac{R_i^c + |R_i^c|}{\max(1 - w_i, w_i^{dl})}\max(1 - w_i, 0) \tag{2.36}$$

$$R_i^c = \nu_i M_i[\min(r^{for}_{MV,i}, r^{for}_{ED,i}) - \min(r^{rev}_{MV,i}, r^{rev}_{ED,i})] \tag{2.37}$$

$$r^{for}_{MV,i} = k^{for}\prod_r(\frac{\rho w_r}{M_r})^{-\nu_{i,r}}, \qquad r^{rev}_{MV,i} = k^{rev}\prod_p(\frac{\rho w_p}{M_p})^{-\nu_{i,p}} \tag{2.38}$$

$$r^{for}_{ED,i} = \frac{\alpha\epsilon}{k}\rho\min\left[\min\left(\frac{w_r}{\nu_r M_r}\right), \beta\sum_p\left(\frac{w_p}{\nu_p M_p}\right)\right] \tag{2.39}$$

$$r^{rev}_{ED,i} = \frac{\alpha\epsilon}{k}\rho\min\left[\min\left(\frac{w_p}{\nu_p M_p}\right), \beta\sum_r(\frac{w_r}{\nu_r M_r}\right) \tag{2.40}$$

The eddy dissipation model is computationally cheap and provides reasonable results. Since the non-linear Arrhenius equation is avoided for the calculation of the reaction source term, the model is easy to implement. However, there are certain limitations of this model [36]. The eddy dissipation model is limited by the choice of reaction mechanism. Since every reaction would have the same turbulent parameters, the multiple reaction step mechanism provides inaccurate results. With the eddy dissipation model, the reaction would occur whenever there is a turbulent flow. This might not be the case in every application. The model can be used only in the non-premixed set up. Since, for the premixed case the combustion will be predicted as soon as it is mixed before entering the system by this model, which is not correct. Irrespective of these limitations, the model has been studied in this work due to its simple implementation. Moreover, the COMSOL Multiphysics software used in this work allows for turbulent-chemistry interactions by the eddy dissipation model. The module has been validated with test cases [56, 57].

2.3.3. MIXTURE FRACTION/PDF MODEL

Mixture fraction modeling theory developed by Bilger in 1980 provides another way to define turbulent chemistry interaction. The mixture fraction modeling technique is formulated based on three components. The first component is based on the canonical description presented in the form of mixture fraction. With the assumption of equal diffusivity all conserved scalars can be linearly related to a scalar quantity called mixture fraction. For rapid reactions chemical equilibrium is achieved in all parts of the domain.

Therefore, for rapid reactions if the instantaneous mixture fraction is known corresponding state variables can be calculated. The second component deals with computing the statistical average values of state variables. This is generally carried out using the probability density functions (PDF). The PDF can either be determined by solving it differentially or by assigning a general shape. The first approach has difficulties in the closure approximations and is computationally expensive. The second approach provides flexibility and can be computed with defining number of parameters. The beta function proves to provide remarkable flexibility with only two number of parameters. The beta function is given by Equation 2.41.

$$\tilde{P}(Z) = Z^{\mathrm{a}\text{-}1}(1-Z)^{\mathrm{b}\text{-}1}\frac{\Gamma(a+b)}{\Gamma(a)\Gamma(b)} \tag{2.41}$$

In this equation, a and b are the nonnegative parameters and is the gamma function. Based on the $\tilde{P}(Z)$, these parameters can be calculated from mixture fraction and its variance. The density incorporated in the function is favre averaged and therefore the function is called favre PDF. The third component in the modeling of mixture fraction is the formulation of mixture fraction and its variance. The RANS formulation of the mixture fraction and variance equation needs closure approximations of Reynolds flux terms. This is carried out through gradient transport. The numerical equation of the mixture fraction and its variance after closure of Reynolds flux terms and Favre-averaged scalar dissipation rate are given by Equation 2.42 and 2.43, respectively.

$$\frac{\partial}{\partial t}(\overline{\rho}\overline{f}) + \nabla\cdot(\overline{\rho u}\overline{f}) = \nabla\cdot(\frac{\mu_l+\mu_t}{\sigma_t}\nabla\overline{f}) \tag{2.42}$$

$$\frac{\partial}{\partial t}(\overline{\rho}\overline{f'^2}) + \nabla\cdot\left(\overline{\rho u}\overline{f'^2}\right) = \nabla\cdot\left(\frac{\mu_l+\mu_t}{\sigma_t}\nabla\overline{f'^2}\right) + C_g\mu_t\cdot(\nabla\overline{f})^2 - C_d\rho\frac{\epsilon}{k}\overline{f'^2} \tag{2.43}$$

The closure approximations introduce two constants namely C_g and C_d in Equation 2.43. The most common values of these constants used in applied CFD literature are $C_\mathrm{g} = 2.86$ and $C_\mathrm{d} = 2.0$. The same values are used in this work as well. The Dirichlet boundary conditions for the mixture fraction variable are specified at the air and fuel inlet. The mixture fraction variable is zero at the air inlet and one at the fuel inlet. At the outlet, the diffusion flux is zero whereas at all other boundaries, the net flux is defined to be zero. The variance at both air and fuel inlets is defined as zero whereas at all other boundaries the net flux is defined to be zero.

The chemistry tables are obtained for the desired chemical mechanism assuming chemical equilibrium as a function of mixture fraction. However, these values provide instantaneous quantities. To compute the mean average quantity the instantaneous values are convoluted by the probability density function. The workflow of this model is explained in detail in Chapter 6. Gosselin et.al. have demonstrated the advantage of mixture fraction/PDF model in their study of anode baking furnaces [31]. The model shows significant benefits in the accurate computation of temperature. Therefore, the model is considered for this study as well. However, COMSOL Multiphysics software does not provide the default module of this model. Therefore, the model is developed and validated in this work.

There are many other advanced combustion models that provide a good estimation of species mass fraction and temperature in the furnace. Some of these models are: flamelet generated manifold [58–61], thickened flamelet model, etc. COMSOL Multiphysics does not provide default modules of these models. Therefore, implementation of these advanced models is difficult for this work.

2.4. TRANSPORT EQUATION OF HEAT TRANSFER

The combustion process explained in the earlier section leads to a generation of energy. The temperature distribution across the system depends on the transport of the energy. The two important modes of transport of heat energy are conduction and convection. As discussed in the earlier section, the RANS approach is utilised for modeling the turbulent flow. The energy equation can be expanded to obtain the temperature transport equation. The temperature is split into a mean and fluctuating part. The Favre averaging of temperature is carried out as shown in Equation 2.44 for considering the effect of compressible turbulence [62]. Equation 2.45 presents the Favre averaged temperature transport equation. The detailed derivation with accompanied assumptions of the equation is presented in the book by Moukalled, Mangani and Darwish [63]. The term Q represents the source term due to the combustion.

$$\widetilde{T} = \frac{\overline{\rho T}}{\overline{\rho}} \tag{2.44}$$

$$\overline{\rho} C_{\mathrm{p}} \left(\frac{\partial \widetilde{T}}{\partial t} + \widetilde{u}_{\mathrm{j}} \frac{\partial \widetilde{T}}{\partial x_{\mathrm{j}}} \right) = \frac{\partial}{\partial x_{\mathrm{j}}} \left((\lambda + \lambda_{\mathrm{T}}) \frac{\partial \widetilde{T}}{\partial x_{\mathrm{j}}} \right) + \widetilde{\tau_{\mathrm{ij}} S_{\mathrm{ij}}} - \left(\frac{\partial (\ln \rho)}{\partial (\ln T)} \right)_{\mathrm{P}} \frac{Dp}{Dt} + Q \tag{2.45}$$

The turbulent thermal conductivity in Equation 2.45 is defined by the turbulent Prandtl number. The Kays-Crawford model is used for determining the turbulent Prandtl number [62, 64]. Equation 2.46 presents the equation of turbulent Prandtl number computed by Kays-Crawford model [62].

$$\mathrm{Pr_T} = \left(\frac{1}{2\mathrm{Pr_{T\infty}}} + \frac{0.3\mathrm{C_P}\mu_{\mathrm{T}}}{\lambda\sqrt{\mathrm{Pr_{T\infty}}}} - \left(\frac{0.3\mathrm{C_P}\mu_{\mathrm{T}}}{\lambda} \right)^2 \left(1 - \exp\left(- \frac{\lambda}{0.3\mathrm{C_P}\mu_{\mathrm{T}}\sqrt{\mathrm{Pr_{T\infty}}}} \right) \right) \right)^{-1} \tag{2.46}$$

2.4.1. RADIATION

The heat energy generated by the combustion reaction in an anode baking furnace is high. This leads to a high temperature in the furnace. The radiation heat transfer involves the transport of thermal rays in the form of electromagnetic waves. All matter that is at a temperature higher than absolute zero emits these waves. The radiation energy transported by these wide ranges of wavelengths is proportional to the fourth power of the temperature [52]. The well-known Stefan-Boltzmann law provides this relation between the radiation energy and the temperature [65]. Therefore, as the temperature increases, radiation heat transfer becomes significant. At temperatures as high as $2000^{\mathrm{o}}C$, radiation heat transfer proves to be an essential mode of transport of heat. Therefore, radiation modeling is a fundamental physical phenomenon in an anode baking furnace. The radiation is accounted for by the source term in the energy equation. There are two classifications of radiation heat transfer [62]. The first type of radiation involves radiation from one surface to another without the involvement of the participating media. This type of radiation occurs in most applications. The second type of radiation involves absorption, emission and scattering of the radiation of the participating media. For example, in the gaseous phase participating media, if chemical species such as CO_2 and H_2O are present, these species absorb radiation [66]. In the anode baking furnace, the combustion products consist of these species. Therefore, radiation in participating media has to be considered. The more advanced concepts such as turbulent radiation interaction (TRI) are out of scope for this work [67]. The overall equation with radiation is specified by Equation 2.47 [62]. Note that the temperature in Equation 2.47 is Favre averaged. However, for simplicity, the overbar that represents the Favre averaging has been removed from Equation 2.47.

$$\overline{\rho} C_{\mathrm{p}} \left(\frac{\partial \widetilde{T}}{\partial t} + \widetilde{u}_{\mathrm{j}} \frac{\partial \widetilde{T}}{\partial x_{\mathrm{j}}} \right) = \frac{\partial}{\partial x_{\mathrm{j}}} \left((\lambda + \lambda_{\mathrm{T}}) \frac{\partial \widetilde{T}}{\partial x_{\mathrm{j}}} \right) + \widetilde{\tau_{\mathrm{ij}}} \widetilde{S_{\mathrm{ij}}} - \left(\frac{\partial (\ln \rho)}{\partial (\ln T)} \right)_{\mathrm{P}} \frac{Dp}{Dt} + Q + Q_{\mathrm{r}} \tag{2.47}$$

The radiation in participating media is accounted by the divergence of the radiative heat flux as given by Equation 2.48. It can be observed that the radiation source term is independent of the scattering term. The scattering phenomena merely redistributes the radiation energy intensity in different directions [52]. Therefore, the radiation source term does not constitute to the scattering term.

$$Q_{\mathrm{r}} = \nabla \cdot \mathbf{q_r} = \kappa (G - 4\pi I_{\mathrm{b}}(T)) \tag{2.48}$$

The incident radiation term G from Equation 2.48 is defined as given in Equation 2.49 based on the radiation intensity.

$$G = \int_{4\pi} I(\Omega) d\Omega \tag{2.49}$$

The quantity radiation intensity is solved by the overall radiative heat transfer equation as given by Equation 2.50 in its general form. The terms on the right-hand side represents absorption, emission and scattering, respectively.

$$s \cdot \nabla I(r,s) = \kappa I_b(r) - \beta I(r,s) + \frac{\sigma_s}{4\pi} \int_{4\pi} I(r,s) \phi(s,s') d\Omega' \tag{2.50}$$

The radiation intensity transport equation suggests that the equation needs discretization in angular space. The computation of the incident radiation term G based on the discretization of the radiative transfer equation can be carried out by considering different models. These models differ from each other with respect to the way they handle the directional dependence of the radiation intensity [22]. The first method is known as the spherical harmonics method, in which a set of simultaneous partial differential equations is formed by expressing radiation intensity by a series of directional dependent spherical harmonics [68]. This approach yields only one differential equation in terms of the incident radiation G and is known as the P1 approximation model. This model is explained in detail in the following section. Another approach is by solving the radiative transport equation for a finite number of solid angles. This approach is known as the discrete ordinate method. In this approach, the isotropic radiation intensity assumption of the P1 approximation model is improved by considering variations in a finite set of directions. This increases the required computational power. For a complex geometry such as an anode baking furnace, solving such an extensive system of equations poses challenges of computational cost and convergence. Therefore, in this work, the P1 approximation model is used for modeling the radiation source term.

2.4.2. P1 APPROXIMATION MODEL

The P1 approximation model is based on the spherical harmonics method. The model assumes linear isotropic scattering and medium to be optically thick [62]. The simplistic P1 approximation formulation is based on the transport equation of incident radiation given by Equation 2.51. The diffusion coefficient is defined by Equation 2.52. The absorption coefficient κ in Equation 2.52 is calculated based on the Planck mean absorption coefficient, explained in a later section.

$$-\nabla\cdot(D_{P1}\nabla G) = Q_r \tag{2.51}$$

$$D_{P1} = \frac{1}{3\kappa + \sigma_s(3-a_1)} \tag{2.52}$$

The boundary condition at the boundaries is given by Equation 2.53. The ϵ at the inlet and outlet is defined as the black wall (ϵ=1). Other boundaries are treated as gray walls, and ϵ depends on the temperature as shown in Figure 2.2.

$$q_{r,net} = \frac{\epsilon}{2(2-\epsilon)}(4\pi I_{b,w} - G) \tag{2.53}$$

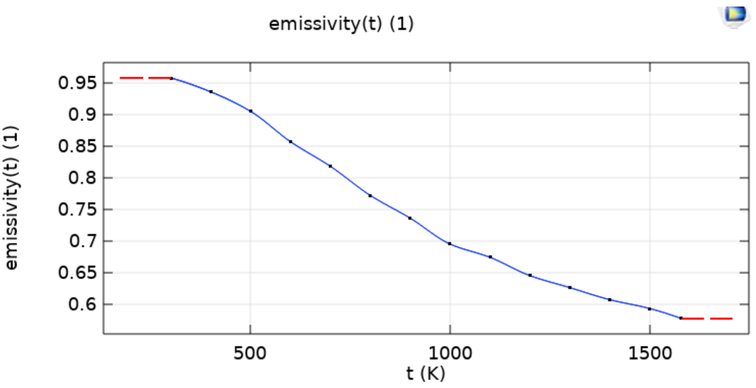

Figure 2.2: The emissivity dependence on temperature for the anode baking refractory

The optically thin medium assumption is not reasonable for the anode baking furnace geometry. This implies that the assumption that all surfaces reflect the incident radiation isotropically is not valid. Therefore, the radiative fluxes are over-predicted by the P1 approximation model. However, the alternative of the P1 approximation model is computationally way more expensive. With the P1 approximation model, the intuition on the radiation source term can be established with reasonable computational power.

2.4.3. PLANCK MEAN ABSORPTION COEFFICIENT (PMAC)

There are various methods to compute the radiation absorption coefficient of the participating media. The PMAC is a promising approach to calculate the absorption coefficient as it provides a better fitting with the experiment [66]. In this approach, each computational cell is assumed to be a combustion chamber. The radiation path lengths of the individual components are proportional to the partial pressure of the component in the cell. The Planck mean absorption coefficient for individual gases is given by the following Equation 2.54 developed in [66].

$$\kappa_{\mathrm{i}} = \frac{\pi}{\sigma T^4} \int_0^\infty I_{\mathrm{b}\eta} \sum_j \kappa_{\eta \mathrm{j}} d\eta = \sum_j \left(\frac{\pi I_{\mathrm{b}\eta 0}}{\sigma T^4}\right) S_{\mathrm{j}} \tag{2.54}$$

The κ_{i} presented in Equation 2.54 can be fitted by functions. The fitting can further be analyzed based on the sum of squares due to error (SSE) and R^2 values. The literature shows that for the fourth-order Gaussian function, the fitting is represented well. Therefore, the Plank mean absorption coefficient is calculated by fitting the parameters to a Gaussian fourth-degree function. The fitting parameters are computed using comparison with the experimental data [66]. Figure 2.3 shows the absorption coefficient of CO_2 and H_2O as a function of temperature calculated based on the Gaussian function. The fitting parameters for the Gaussian function are taken from the literature [66].

The total absorption coefficient can then be calculated using the partial pressures of individual species as given in Equation 2.55. In the current model, there are only two species, namely, CO_2 and H_2O that are radiation absorbing species. Therefore, only these species contribute in Equation 2.55.

$$\kappa_{mix} = \sum_{i=1}^{N} \frac{n_i}{n_{tot}} p_{tot} \kappa_i \tag{2.55}$$

The other well-known method of calculating the radiation absorption coefficient is the Weighted-sum-of-gray-gas (WSGG) model. The COMSOL Multiphysics software does not have built-in modules for the implementation of the models of the absorption coefficient. The implementation of the PMAC approach is easy to implement and thus used in this thesis.

2.5. NOx FORMATION MECHANISMS

The NOx emissions from industrial furnaces are responsible for air pollution. Therefore, industries are trying to find solutions to minimize NOx emissions. This work aims to analyze the NOx formation in anode baking furnace. The NOx formation is primarily due to either the nitrogen present in the air used as an oxidizer or nitrogen-based fuels [33]. The influence of NOx formation on the variables of the flow field, density, temperature, etc., can be assumed to be negligible due to its lower concentration [36]. Therefore, in most cases, the computations of the NOx formation are carried out in the

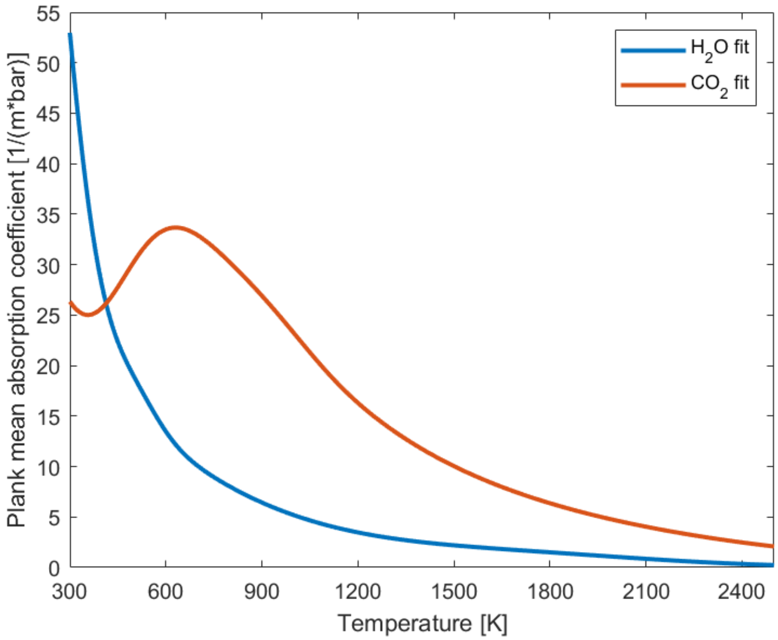

Figure 2.3: The Plank mean absorption coefficient of H_2O and CO_2 computed by Gaussian 4th degree polynomial function

post-processing stage by solving a passive scalar transport equation of mass fraction of NOx. To understand the formation of NOx, it is vital to enlist the possible routes of NOx formation. NOx is a combined term for the species NO and NO$_2$. However, due to the higher concentration of formation of NO in the combustion process, looking into the routes of formation of NO suffices for the study of overall NOx formation. There are four main ways with which NOx is formed. The detailed mechanisms of these four ways are explained in [36].

- **Thermal NOx formation**: The thermal NOx formation mechanism converts the nitrogen in the combustion air (used as an oxidizer) stream into nitrogen oxides at high temperatures. The combustion process is accompanied by the release of high heat energy. In other words, the temperature in the combustion process system is always high. If nitrogen from the oxidizer stream resides in the high-temperature zone for longer, the NOx is generated in the system [36]. It has been observed that the thermal NOx formation is susceptible to temperature rise. In most of the combustion processes, both conditions are satisfied. Therefore, the thermal NOx formation is the most widespread source of NOx formation. In an anode baking furnace, the thermal NOx formation is the most significant source, and its details are discussed in the following section.

- **Prompt NOx formation**: Prompt NOx formation occurs primarily in rich flames due to the high-speed reactions at the front flame [36]. In the fuel-rich region at low temperature where the residence time is short, the hydrocarbon fuel is fragmented into intermediate species such as C, CH, and CH_2. These species react with nitrogen from the combustion air to form NO via the formation of HCN or CN. The formation of NOx does not depend on the type of hydrocarbon. The only significant quantity that determines the appearance of NOx is the number of carbon atoms per unit volume [36]. In the anode baking furnace, the fuel-rich conditions with low temperatures are not prominent. Therefore, the formation of prompt NOx is not significant.

- **Fuel NOx formation**: The NOx formation mechanism is associated with the oxidation of nitrogen contained in the fuel. Approximately 0.3-2% nitrogen is present in the residual fuel, oil, and coal [36]. The amount of NOx formation with this mechanism depends mainly on the composition of nitrogen in the fuel and the local combustion characteristics. The nitrogen in the fuel is first converted into the intermediate radicals such as HCN, N, CN, and NH, which are further converted into NO [36]. There are various reaction mechanisms based on the intermediate radicals formed from the nitrogen-based fuel. In the anode baking process, natural gas is used as the fuel source. The nitrogen contained in the natural gas is negligible. Therefore, the NOx formation with this mechanism can be neglected in the modeling.

- **NOx formation via intermediate N_2O**: The NOx formation via intermediate N_2O formation occurs at elevated pressure conditions in the oxygen-rich zone [36]. Though there are exceptions to this. The N2O route can also be important at standard pressure, especially in flameless or MILD combustion [69]. Moreover, this mechanism is significant in combustion systems where the elevated temperature decreases to avoid thermal NOx. Some of the examples of these systems are gas turbines and compression-ignition engines [36]. In the anode furnace, elevated pressure conditions are not observed. Therefore, the formation of intermediate N_2O is not significant.

To summarise, the only NOx formation mechanism that is significant in the anode baking furnace is the thermal NOx mechanism. This is elaborated further in the following section.

2.5.1. THERMAL NOx BY ZELDOVICH MECHANISM

The Zeldovich mechanism provides the governing reactions for the formation of thermal NOx from molecular nitrogen. The three reactions involved under the Zeldovich mechanism are provided from Equation 2.56 to 2.58 [36]. The third reaction represented by Equation 2.58 contributes only when the mixture is fuel-rich. In the anode baking furnace, the system is fuel-lean, and therefore, only the first two reactions are considered.

$$O + N_2 <=> N + NO \tag{2.56}$$

$$N + O_2 <=> O + NO \tag{2.57}$$

$$N + OH <=> H + NO \tag{2.58}$$

The thermal NOx reaction rate with the above reactions can be written as shown in Equation 2.59.

$$\frac{d[NO]}{dt} = k_{f,1}[O][N_2]+k_{f,2}[N][O_2]+k_{f,3}[N][OH]-k_{r,1}[NO][N]-k_{r,2}[NO][O]-k_{r,3}[NO][H] \tag{2.59}$$

The reaction constants used in Equation 2.59 are as presented in Equation 2.60 to 2.65.

$$k_{f,1} = 1.8 * 10^8 \exp(\frac{-38370}{T}) \tag{2.60}$$

$$k_{f,2} = 1.8 * 10^4 T \exp(\frac{-4680}{T}) \tag{2.61}$$

$$k_{f,3} = 7.1 * 10^7 \exp(\frac{-450}{T}) \tag{2.62}$$

$$k_{r,1} = 3.8 * 10^7 \exp(\frac{-425}{T}) \tag{2.63}$$

$$k_{r,2} = 3.81 * 10^3 T \exp(\frac{-20820}{T}) \tag{2.64}$$

$$k_{r,3} = 1.7 * 10^8 \exp(\frac{-24560}{T}) \tag{2.65}$$

Equation 2.59 contains the concentration of [N], [O] and [OH]. Since the temperature in the system is very high, the concentration of [OH] is considered to be negligible. The concentration of [O] is given by Equation 2.66 considering the equilibrium approach [36].

$$[O] = 3.97 * 10^5 T^{-1/2} [O_2]^{1/2} \exp\frac{-31090}{T} \tag{2.66}$$

Assuming the quasi-steady assumption for [N], the rate of formation of NO is given by Equation 2.67 [36].

$$\frac{d[NO]}{dt} = 2k_{f,1}[O][N_2]\frac{1-\frac{k_{r,1}k_{r,2}[NO]^2}{k_{f,1}[N_2]k_{f,2}[O_2]}}{1+\frac{k_{r,1}[NO]}{k_{f,2}[O_2]+k_{f,3}[OH]}} \tag{2.67}$$

NO is assumed to be the major component of NOx. The transport equation of the NO is given by Equation 2.68. It consists of the convection, diffusion, production and consumption of NO. The Zeldovich mechanism of NOx formation is implemented in COMSOL Multiphysics by solving the stabilized convection diffusion equation.

$$\frac{\partial(\bar{\rho}\widetilde{Y}_{\mathrm{NO}})}{\partial t} + \nabla\cdot(\bar{\rho}\tilde{\mathbf{u}}\widetilde{Y}_{\mathrm{NO}}) = \nabla\cdot(\bar{\rho}\mathbf{D}\nabla\widetilde{Y}_{\mathrm{NO}}) + S_{NO} \tag{2.68}$$

The production/consumption term from Equation 2.68 is computed by the Zeldovich mechanism. The term depends on the rate of formation of NO as given in Equation 2.69.

$$S_{NO} = M_{w,NO}\frac{d[NO]}{dt} \tag{2.69}$$

The temperature distribution is obtained by coupling the equations of turbulent flow, combustion reaction and radiation. The transport equation of NO formation is solved with reaction source term from the Zeldovich mechanism in post-processing. The values of variables are then taken from the solutions of the coupled equations.

The aim of this study is restricted to gaining insights on NOx formation in the anode baking furnace. Such insights can further be extended to understand possibilities to implement techniques such as flameless combustion to reduce NOx formation in the furnace [70].

2.6. CONCLUSION

The anode baking process consists of multiple physical phenomena that are highly dependent on each other. The physical phenomena are translated into mathematical expressions based on the laws of physics. For the engineering applications such as an anode baking furnace, the implementation of the mathematical expressions has to be simplified to be able to solve them with computational algorithms. In this chapter, the models used for the closure and simplification of the terms in the mathematical equations are discussed. The models suitable for the modeling of anode baking process are identified. These models are further judged based on their performance and simplicity of implementation in COMSOL Multiphysics software.

3

MATHEMATICAL APPROACH

Mathematics forms the backbone of the established physical phenomena in all applications. The conversion of qualitative knowledge of physics to quantitative computations is carried out by implementing mathematical approaches. Like many other applications, the anode baking process involves an understanding of multiple physical phenomena, which is translated into transport equations. All these transport equations are partial differential equations in time and space. Therefore, a mathematical approach is needed to approximate the required quantities. In this chapter, the numerical technique chosen for solving the associated transport equations is described. The choice of the numerical simulation package is established, followed by the discussion of numerical implementations corresponding to the package. At the end of the chapter, the solver flowcharts for the various steps of the anode baking furnace model are described.

3.1. NUMERICAL METHODS

Numerical analysis is a branch of mathematics that allows approximating a solution of partial differential equations by converting them into finite-dimensional subspace approximations. The conversion allows solving the problem relatively faster with the use of computational resources. In many engineering problems, finding an analytical solution to the differential equations is almost impossible. In such cases, the numerical methods provide a reasonably good approximate solution that is close to the actual solution.

In the previous chapter, the underlying equations defining the physical phenomena in the anode baking furnace are elaborated. For all physical phenomena, the equations are partial differential equations (PDE). Solving these PDE's for the desired application is possible through numerical methods. With these methods, the numerical approximations of the PDE's are calculated in order to further compute the approximate solutions of the desired quantities. There are various discretization methods that convert the PDE's into discretized equations that can be solved with computational algorithms. The commonly used methods to treat PDE's numerically are the finite volume method and the finite element method. These methods are evaluated based on stability, consistency, and convergence.

3.1.1. NUMERICAL SIMULATION SOFTWARE

There is a variety of software packages that adopt numerical methods to solve PDE's associated with a number of physical phenomena. These packages differ in various ways, such as the discretization method, coupling of equations, treating non-linearity of equations, and solver algorithms. Furthermore, there are software packages that are specially calibrated with respect to certain physics or applications. Therefore, the choice of numerical simulation software is complicated.

In this work, the COMSOL Multiphysics software package is used for the modeling of anode baking furnace. The COMSOL Multiphysics software is widely used in academia. The expertise related to the usage of the software is exercised in the research group for a significant time. The package provides a good balance between usability and customization based on the requirements of the application. Moreover, the existing modules of the package for the desired physical phenomena are explored by taking advantage of embedded functionalities. The user-friendly interface of the software helps in accelerating the learning curve. The customer support of the package is readily available to get more insights on the available tools and the embedded coding of the software. The possibility of using the software is tested on a small domain and proves to be promising for further use [71].

The anode baking application demands for coupling multiple physics. The modules such as 'Turbulent flow', 'Transport of concentrated species', 'Heat transfer in solids and fluids', 'Radiation in participating media' and, 'stabilized convection-diffusion equation' are employed in this work. The coupling interfaces such as 'Non-isothermal flow', 'Reacting flow' and 'Heat transfer with radiation in participating media' are used for coupling the various physics.

Despite the advantages of using COMSOL Multiphysics software, the package also imposes some challenges. The complex geometry of anode baking furnaces requires advanced meshing techniques. The meshing capabilities of the COMSOL software are limited for the given application. Therefore, an external mesh generation tool is needed for a satisfactory mesh. This further enforces challenges for importing this mesh into a COMSOL supported format. The external meshing adds to the restriction of solver usage. For example, due to the external meshing, the geometric multigrid pre-conditioners can not be used, leading to the usage of algebraic multigrid solvers that are less efficient as compared to geometric multigrid pre-conditioners. The challenges with the convergence of the realizable k-ϵ model and higher memory requirements of the discrete ordinate method for radiation heat transfer are encountered in the study. Furthermore, the software is not advanced in combustion modeling and provides only one basic implementation. These challenges are identified as opportunities to increase the knowledge base in the research group and are discussed in later chapters.

The alternative software packages such as Ansys Fluent and OpenFOAM are explored to some extent in this work. These packages are based on the finite volume discretization method and have different implementation algorithms. Due to the lack of a commercial Ansys Fluent package in the research group and the less user-friendly OpenFOAM interface, these packages are not chosen for the primary study in this work. Nonetheless, these packages are used for the validation purpose of some of the sub-models studied in this work.

Figure 3.1 shows a block diagram of various components utilized by the COMSOL Multiphysics software for solving a multi-physics model of this work. The COMSOL Multiphysics software employs the Galerkin finite element spatial discretization method. The steady-state stabilization for the non-linear method is provided by pseudo-time stepping. The COMSOL Multiphysics software is widely known for its performance concerning the coupling of physics. This coupling is carried out either by considering a fully coupled or segregated approach in the software. The software treats the non-linear equations using the Newton-Raphson method with the possibility of several damping approaches. In COMSOL Multiphysics software, there is a number of direct and iterative solver algorithms to compute the approximate solution of a linear system of equations. The iterative solvers can further be customized with various options of pre-conditioners.

In the following sections of this chapter, the concepts of each of these components are explained by taking general simple examples. The specific details used in different modeling steps carried out in this work are elaborated after establishing the general understanding of these concepts.

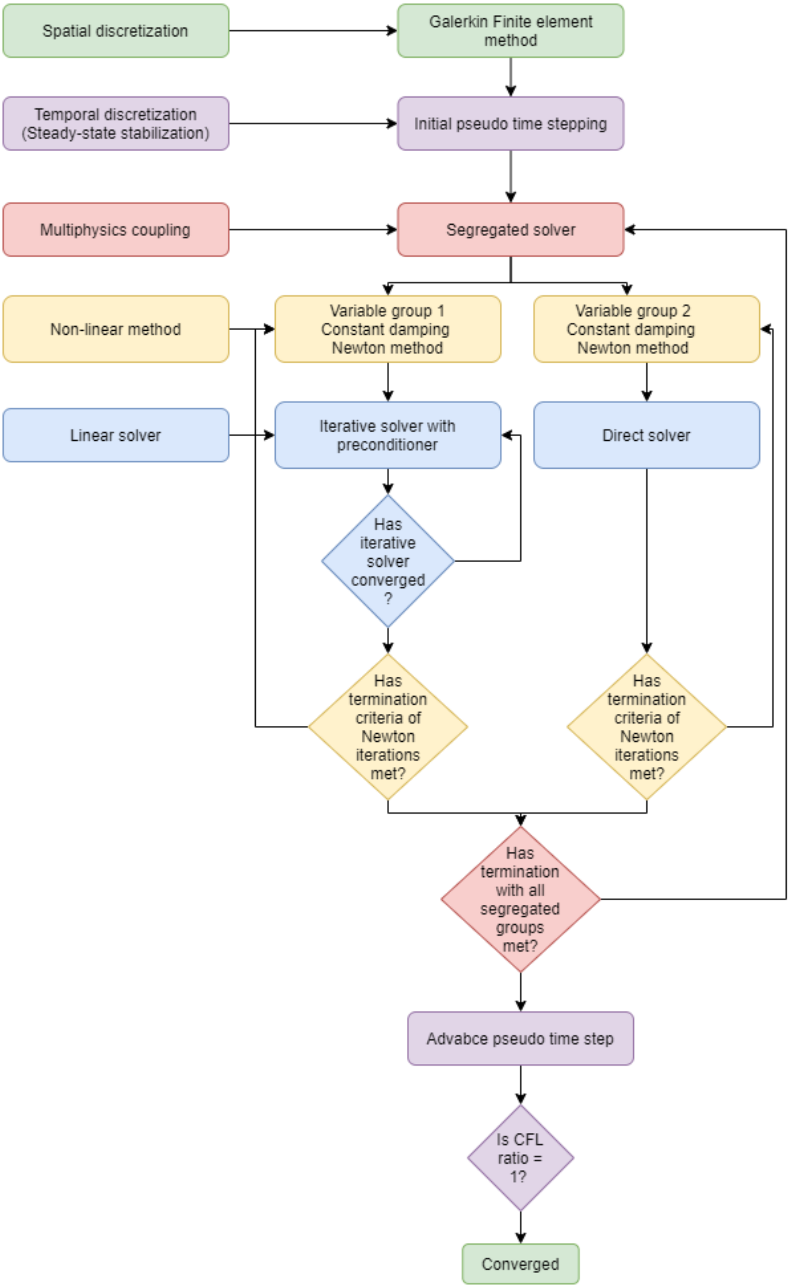

Figure 3.1: The general flowchart structure of COMSOL Multiphysics software utilized in this work.

3.2. FINITE ELEMENT DISCRETIZATION

In this section, the comprehension of the component on the spatial discretization (Figure 3.2) is gained. The finite element method is one of the discretization techniques of partial differential equations [72]. The method is the special case of the Galerkin method and reduces the complexity of the original equation by converting it into a simpler equation, known as the weak form of the equation.

Figure 3.2: The spatial discretization by FEM component of general flowchart structure.

In the finite element method, the domain of interest is converted into smaller parts by generating a mesh. These smaller sub-domains of the mesh are known as finite elements. The meshing process is carried out as a pre-processing step. There are different programs available for the meshing process. The details of these programs have been explained in Chapter 4. The mesh provides information on the coordinates of the nodes of the elements and the neighboring elements. For each of the finite elements, the approximate functions of the desired physical variables are calculated at the nodes of the element. The approximate functions are defined using the basis functions as represented by Equation 3.1. The basis functions are primarily polynomial functions. The degree of these polynomial functions is based on the number of nodes of the elements.

$$\phi \approx \phi_{\mathrm{h}} = \sum_i \phi_i \psi_i \tag{3.1}$$

where ψ is the basis function and ϕ_{h} is the approximation of ϕ. In the next step, the weak form is obtained by multiplying the partial differential equation by a test function on both sides and integrating it over the entire domain. The requirement for the test function is such that it should belong to the same Hilbert space as the physical variable function. With this step, the matrix equation is established that has unknowns as the parameters related to the approximated nodal functions. The global matrix system is then formed by combining the equations for all the elements. Here the information of the neighboring elements from the mesh is used. The global system of equations is solved using a suitable solver.

The finite element discretization is implemented in COMSOL Multiphysics software [73, 74]. Here, the treatment carried out to a partial differential equation for the discretization is elaborated with an example. Let's consider time-dependent heat transfer in the solid object, which is represented by the Equation 3.2 in the domain Ω. The first term represents the increase in temperature of the solid as a function of time. The second term on the left side of the Equation 3.2 represents the heat conduction through solid while the right-hand side term accounts for the heat sink or source in the solid domain Ω.

$$\rho c_{\mathrm{p}} \partial_{\mathrm{t}} T + \nabla \cdot (-k \nabla T) = g(T, x, t) \qquad \text{in } \Omega \tag{3.2}$$

The boundary conditions needed to solve the above differential equation are given by Equations 3.3 to 3.5. Dirichlet and Neumann boundary conditions are specified on boundaries $\partial\Omega_1$, $\partial\Omega_2$, and $\partial\Omega_3$, respectively.

$$T = T_0 \qquad \text{on } \partial\Omega_1 \text{ at time t} \tag{3.3}$$

$$(-k\nabla T)\cdot\mathbf{n} = h(T - T_{\mathrm{amb}}) \qquad \text{on } \partial\Omega_2 \text{ at time t} \tag{3.4}$$

$$(-k\nabla T)\cdot\mathbf{n} = 0 \qquad \text{on } \partial\Omega_3 \text{ at time t} \tag{3.5}$$

The time-dependent equation needs an additional information on the initial condition of the equation with respect to time as given by Equation 3.6.

$$T = T_0 \qquad \text{on } \Omega \text{ at t=t}_0 \tag{3.6}$$

In order to spatially discretize the above problem with the finite element method, it is multiplied by the test function on both sides and is integrated over the entire domain Ω as shown in Equation 3.7. The test function ϕ should be such that the Equation 3.7 should be always true in the given Hilbert space in which variable T lies as well, i.e., $T \epsilon H$ and $\phi \epsilon H$ [74]. The Hilbert spaces have suitable properties such that the vector algebra and calculus can be extended to three-dimensional spaces with the required number of dimensions [75]. Therefore, the multiplication with the test function allows to treat it as a vector.

$$\int_\Omega \rho c_{\mathrm{p}} \partial_{\mathrm{t}} T \phi dV + \int_\Omega \nabla\cdot(-k\nabla T)\phi dV = \int_\Omega g\phi dV \tag{3.7}$$

In the next step, Equation 3.7 is expanded by using integration by parts as shown in Equation 3.8. This form of the equation is known as the ‘Weak formulation’. There are various methods with which the weak form of the equation is discretized with the finite element method. COMSOL Multiphysics software applies the Galerkin method for discretization.

$$\int_\Omega \rho c_{\mathrm{p}} \partial_{\mathrm{t}} T \phi dV + \int_\Omega k\nabla T\cdot\nabla\phi dV + \int_{\partial\Omega} (-k\nabla T)\cdot\mathbf{n}\phi dS = \int_\Omega g\phi dV \tag{3.8}$$

Further, the variable T is approximated as shown in Equation 3.9. The function ψ, known as the basis function, is chosen such that the variable T is expressed as a linear combination of the basis functions. The basis function also belongs to the same subspace as variable T. The unknown variables are translated from T to coefficient T_{i}.

$$T_{\mathrm{h}}(x,t) = \sum_i T_{\mathrm{i,t}}(t)\psi_{\mathrm{i}}(x) \tag{3.9}$$

By substituting expression 3.9 into the Equation 3.8, the equation for the j’th test function ψ_{j} is written as shown in Equation 3.10. The Galerkin method employs the same set of test and basis functions.

$$\rho c_{\mathrm{p}} \partial_{\mathrm{t}} T_{\mathrm{i,t}} \sum_i \int_\Omega \psi_{\mathrm{i}} \psi_{\mathrm{j}} dV + \sum_i T_{\mathrm{i,t}} \int_\Omega k \nabla \psi_{\mathrm{i}} \cdot \nabla \psi_{\mathrm{j}} dV + \sum_i \int_{\partial\Omega} (-k T_{\mathrm{i,t}} \nabla \psi_{\mathrm{i}}) \cdot \mathbf{n} \psi_{\mathrm{j}} dS = \int_\Omega g \psi_{\mathrm{j}} dV \tag{3.10}$$

The choice of the test and basis functions depends on the chosen finite elements and shape functions of the elements. There are various types of shape functions for the elements. Some of the examples are Lagrange elements, Serendipity elements, Hermite elements, etc. These shape functions differ in the way they define the degree of freedom for a particular variable in a given element. The functions can be of different orders, which further changes the approximation of the variable that is obtained from the combination of these functions.

The most commonly used shape function in this work is the linear order Lagrange elements. The Lagrange elements of the linear order include a minimum number of degrees of freedom for a given mesh. For the multi-physics application of an anode baking furnace, the computational costs increases exponentially if the quadratic order of elements is used. The Lagrange elements are available in linear order while the order of other elements is higher, starting from quadratic order. The mesh refinement for increasing the accuracy of the solution is more viable in terms of computational requirements as compared to increasing the order of elements. Therefore, all variables are approximated with the linear test and basis functions.

After the choice of the function is established, the weak formulation is further simplified by assuming ψ such that the value of the function at the boundary is always zero. This eliminates the term that involves integration over the boundary and changes to Equation 3.11.

$$\rho c_{\mathrm{p}} \partial_{\mathrm{t}} T_{\mathrm{i,t}} \sum_i \int_\Omega \psi_{\mathrm{i}} \psi_{\mathrm{j}} dV + \sum_i T_{\mathrm{i,t}} \int_\Omega k \nabla \psi_{\mathrm{i}} \cdot \nabla \psi_{\mathrm{j}} dV = \int_\Omega g \psi_{\mathrm{j}} dV \qquad \text{such that } \psi = 0 \text{ at } \partial\Omega \tag{3.11}$$

The problem statement changes to finding the coefficients $T = [T_1, ..., T_{\mathrm{N}}] \in \mathbb{R}^{\mathrm{N}}$ such that Equation 3.11 holds for all $j = 1, ..., N$. The local matrices are formed by the Lagrangian condition for all finite elements. The transformation into the global matrix is then carried out by sharing the information with the neighbouring element. The resulting global matrices are called mass matrix, stiffness matrix and load matrix as represented by Equation 3.12, 3.13 and, 3.14, respectively.

$$\rho c_{\mathrm{p}} \sum_i \int_\Omega \psi_{\mathrm{i}} \psi_{\mathrm{j}} dV = M_{\mathrm{ij}} \tag{3.12}$$

$$\int_\Omega k \nabla \psi_{\mathrm{i}} \cdot \nabla \psi_{\mathrm{j}} dV = A_{\mathrm{ij}} \tag{3.13}$$

$$\int_\Omega g \psi_{\mathrm{j}} dV = b_{\mathrm{j}} \tag{3.14}$$

The final finite element discretized equation is transformed into system of differential equations in time as given by Equation 3.15.

$$M_{\mathrm{ij}} \partial_{\mathrm{t}} T_{\mathrm{h}}(t) + A_{\mathrm{ij}} T_{\mathrm{h}}(t) = b_{\mathrm{j}}(T_{\mathrm{h}}, t) \tag{3.15}$$

Equation 3.15 is such that there are no terms that depend on a spatial coordinate, x. The equation is in the form that can be solved numerically with computational algorithms.

3.3. PSEUDO TIME STEPPING

The time-dependent heat transfer problem discretized by the finite element method results in an equation that needs further simplification in terms of the time derivative. For the steady-state problem, the time derivative term is equal to zero and does not appear in the equation. In this work, the steady-state is assumed for all models. However, if the steady-state equation is non-linear, the so-called Newton-Raphson method is used for converting the equations into a system of linear equations. The stabilization with the constant damped Newton method is required. Such stabilization is carried out by assuming pseudo time stepping. Therefore, the next component in the overall solver flowchart (Figure 3.3) includes calculating a pseudo-time step.

Figure 3.3: The temporal discretization by pseudo time stepping component of the general flowchart structure.

The damped Newton method with a constant damping factor often needs a stabilization method towards a steady state. To drive the convergence towards steady-state while using constant a damping factor, COMSOL provides a stabilization method called pseudo-time stepping. In this method, a pseudo time step $\tilde{\Delta} t$ is introduced as shown in Equation (3.16). The first term from Equation (3.16) is always zero and does not affect the solution. However, it helps to convert the non-linear iteration into a step size of $\tilde{\Delta} t$. This method speeds up the convergence of the model towards a steady state.

$$M_{\mathrm{ij}} \frac{T_h^n - nojac(T_h^n)}{\tilde{\Delta} t} + A_{\mathrm{ij}} T_h^n = b_{\mathrm{j}}(T_h) \tag{3.16}$$

The *nojac* function in COMSOL excludes the expression under operation from the Jacobian computation. The step size is related to the local CFL number, which is controlled by the PID controller as per Equation 3.17.

$$\mathrm{CFL}_{\mathrm{n+1}} = \left(\frac{e_{\mathrm{n\text{-}1}}}{e_{\mathrm{n}}}\right)^{k_{\mathrm{P}}} \left(\frac{tol}{e_{\mathrm{n}}}\right)^{k_{\mathrm{I}}} \left(\frac{e_{\mathrm{n\text{-}1}}/e_{\mathrm{n}}}{e_{\mathrm{n\text{-}2}}/e_{\mathrm{n\text{-}1}}}\right)^{k_{\mathrm{D}}} \mathrm{CFL}_{\mathrm{n}} \tag{3.17}$$

where the e is the non-linear error estimate at a given step n and k_{p}, k_{I} and k_{D} are positive constants controlling the PID controller [38].

3.4. MULTIPHYSICS COUPLING SOLVER

As discussed in the previous chapter, the modeling of the anode baking furnace involves solving multiple physical phenomena. Moreover, these phenomena have a strong dependence on each other, and thus, the coupling of these phenomena is necessary. Depending on the complexity of the domain, available computational power, and the involved physical phenomena, the solvers for the coupled system of equations may vary. In the COMSOL Multiphysics software, the different physical phenomena can be coupled by two techniques as described in the following sub-sections.

3.4.1. FULLY COUPLED SOLVER

In the fully coupled solver, as the name suggests, a large system of equations with all unknown physical fields is solved in a single iteration. Since all field variables are fully coupled, the solver is more robust. The solver converges in a fewer number of iterations. However, each iteration is computationally expensive and takes a longer time. In order to achieve convergence, memory-intensive direct solvers are needed for solving the linear system. This approach can be good for smaller systems where strong coupling is desired. However, a fully coupled approach is not preferable for complex computational domain with multiple physical phenomena as it is memory and time-intensive.

3.4.2. SEGREGATED SOLVER

For complex engineering problems a segregated solving approach is used. In this work, the hybrid of coupled and segregated approaches is utilized. For example, the pressure and velocity variables are solved in a fully coupled manner in a single segregated group, while the turbulent quantities are solved in a different segregated group. In the segregated solver, the field variables are divided into a number of sub-steps. Figure 3.4 represents the step at which the multi-physics coupling is accounted in the general solver flowchart.

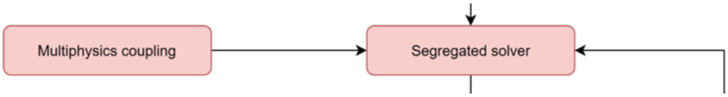

Figure 3.4: The multi-physics coupling component of the general flowchart structure.

These sub-steps are sequentially solved within a single iteration. The variables solved in one segregated group are fully coupled. Generally, each step solves for field variables belonging to the same physics. Sometimes there is more than one step for single physics. The system of equations for the segregated solver for each step is smaller, and thus, the time required for solving individual steps is smaller and consumes less memory. The following algorithm explains the segregated approach.

1. Initialise the physical field variables from all physics
2. Initialise the counter of the number of segregated iterations
3. Solve the variables from the first sub-step by using the values of other field variables (that are not solved in the first sub-step) from the previous segregated iteration

4. Solve the variables from the second sub-step using updated values of the variables from the first sub-steps while, the variables from the third sub-step are used from the previous segregated iteration

5. Solve the variables from the n'th sub-step using the updated values of variables solved till this point (n-1'th sub-step)

6. Repeat the process 3-5 until convergence is reached or the maximum number of segregated iterations are reached

The convergence criteria for the segregated solver can be defined based on the estimated error in a solution or the residual norm. The convergence of the segregated solver is achieved when the error estimate (computed either as estimated error in the solution or the residual norm) for all segregated groups is less than the corresponding tolerance for the segregated group. The estimated error in the solution is calculated by Equation 3.18 [38].

$$e_{\mathrm{j,k}}{}^{\mathrm{N}} = \max_{\mathrm{l}}(1-\alpha_{\mathrm{l,j}}) \left[\frac{1}{M} \sum_{p=1}^{M} \frac{1}{N_{\mathrm{j,p}}} \sum_{i=1}^{N_{\mathrm{j,p}}} \left(\frac{|\Delta U_{\mathrm{i}}{}^{\mathrm{l,j,k,p}}|}{W_{\mathrm{i}}{}^{\mathrm{j,p}}} \right)^2 \right]^{1/2} \tag{3.18}$$

where l is the total number of iterations in each of the segregated step, j is the total segregated groups, $\alpha_{\mathrm{l,j}}$ is the damping factor, N is the number of degrees of freedom for variable field p with total number of field variables M, W is the weight factors and, $|\Delta U_{\mathrm{i}}{}^{\mathrm{l,j,k,p}}|$ is the Newton increment vector [38].

3.5. NEWTON-RAPHSON METHOD

The Newton-Raphson method (commonly known as the Newton method) is a widely used technique to find the roots of a real-valued function. The Newton method enables us to find solutions to non-linear equations. Therefore, the discretized transport equations that are non-linear in nature can be linearised using the Newton method as the next step of solver structure (Figure 3.5). In this work, the Newton method is used for the purpose of linearization of non-linear equations.

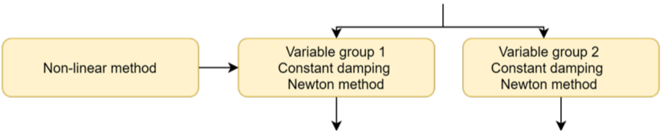

Figure 3.5: The non-linear solver component of the general flowchart structure.

The load vector of the spatial and temporal discretized equation of the heat transfer problem is temperature-dependent, as can be seen in Equation 3.16. The temperature dependence can invoke non-linearity in the equation. The Newton-Raphson algorithm for the continuous and differential function $f(T)$ as given by Equation 3.19 is elaborated as following.

$$f(T) = M_{\mathrm{ij}} \frac{T - nojac(T)}{\tilde{\Delta} t} + A_{\mathrm{ij}} T - b_{\mathrm{j}}(T) \tag{3.19}$$

1. An initial guess T_0 is defined
2. A tangent to the function $f(T) = 0$ at the T_0 is computed by finding a derivative to the function at T_0
3. The intersection point of the tangent and x axis is computed to get the value of T_1
4. The new tangent is computed at T_1
5. The process is continued till the T_{n} value is computed such that $f(T_{\mathrm{n}}) \approx 0$

In summary, the method involves solving the following Equation 3.20.

$$T_{\mathrm{n+1}} = T_{\mathrm{n}} - |f'(T_{\mathrm{n}})|^{-1} f(T_{\mathrm{n}}) \tag{3.20}$$

The termination criteria for the Newton step are decided either by specifying the number of maximum iterations within each segregated iteration or by defining the tolerance for the solution or residual norm.

It should be noted that the Newton method demands the calculation of the inverse of a derivative matrix. The calculation of the inverse matrix is expensive. Moreover, there might be some regions where the solution can not be calculated. In order to avoid that, the damped Newton method is used [76]. The damping modifies the values of $T_{\mathrm{n+1}}$ as shown by Equation 3.21. The values of the damping parameter α vary between 0 to 1. The value of 1 represents that the equation is not damped, while as the value approaches 0, the damping increases.

$$T_{\mathrm{damped}} = T_{\mathrm{n}} + \alpha(T_{\mathrm{n+1}} - T_{\mathrm{n}}) \tag{3.21}$$

There are some cases where the Newton method might fail. If the initial values are far from the actual solution or if the problem does not have a solution, or if the problem is not smooth and, differentiable the Newton solver fails. The method to stabilize the damped Newton has been discussed earlier in section 3.3.

3.6. LINEAR SOLVERS

At each iteration of the Newton method, a system of linear equations needs to be solved. Therefore, the solver algorithm contains the linear equation of the form $AT = b$ in the innermost loop, as can be seen in Figure 3.6. There are two types of solvers that can be used to solve the linear system of equations. The choice of the solver depends on the type, size of the system matrix, and available computational power. The two types of linear solvers, namely, direct and iterative, will be explained in the following subsections.

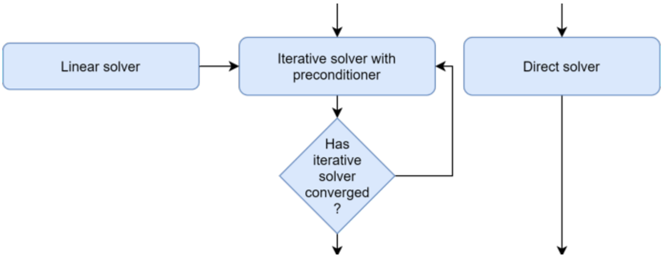

Figure 3.6: The linear solver component of general flowchart structure.

3.6.1. DIRECT SOLVER

The direct solver algorithm is based on the LU Decomposition of matrix A. The pre-ordering algorithms are used to permute rows and columns of matrix A in such a way that the L and U factors of matrix A have a minimum number of non-zero elements. The different types of direct solver algorithms available in COMSOL Multiphysics software are PARDISO, MUMPS, SPOOLES, and Dense Matrix solvers. The details of the version of algorithms implemented in COMSOL Multiphysics are explained in the manual in detail [77]. The speed and the required memory vary for these solvers. The PARDISO and MUMPS solvers can reuse the pre-ordering and, therefore, are the fastest. In this work, either PARDISO or MUMPS solvers are used when the direct linear solver is chosen for the segregated step.

3.6.2. ITERATIVE SOLVER

The iterative solver method is another technique to solve a linear system of equations. Unlike direct solvers, the solution is gradually approached with the iterative solver. The solution is approached from the initial guess. The direction of the approach towards the solution depends on the type of iterative solver. The major difference of iterative solvers as compared to the direct solver is that the iterative solvers are computationally less memory intensive. Therefore, for the majority of engineering applications where the computational domain is large, iterative solvers are used. Though the iterative solvers have the advantage of the low memory requirement, a good initial guess with appropriate conditioning is needed for getting a converged solution. The different types of iterative solvers are the Conjugate gradient method, Generalized minimum residual method (GMRES), Flexible generalized minimum residual method (FGMRES), and the biconjugate gradient stabilized method. In this work, the GMRES iterative solvers are used when the iterative solver is chosen.

The pre-conditioning of the stiffness matrix is required in the case of iterative solvers. There are multiple pre-conditioning techniques available that work well with the Krylov iterative solver. The choice of the iterative solver and the efficient pre-conditioner depends on the model being studied. In this work, Smoothed Aggregated Algebraic Multigrid (SAAMG) is used as a pre-conditioner. The choice of SAAMG over geometric multigrid pre-conditioner is due to the external mesh generation process.

The termination criterion for iterative solvers is given by Equation 3.22. For iterative solvers with left preconditioning, M is the pre-conditioned matrix, while for other iterative solvers, M is the identity matrix [38].

$$\rho|M^{-1}(b - AT)| < \text{tol} \cdot |M^{-1}(b)| \tag{3.22}$$

where ρ is the factor, tol is the tolerance, and the definition of M depends on the solver. The factor ρ can be tuned if the system matrix A or the pre-conditioner is not well-conditioned. The tuning is carried out based on the condition number of the matrix $M^{-1}A$. Therefore, the convergence criteria depend on the relative value of factor ρ compared to the condition number.

3.7. SOLVER STRATEGY FOR ANODE BAKING FURNACE MODEL

As discussed in the previous chapter, the anode baking furnace modeling consists of multiple physical phenomena. The coupling of all physical phenomena together in a solver algorithm is challenging and can lead to non-convergence. Therefore, the complexity of the model is increased step by step. The choice of solver strategy and the linear solvers depend on the number of physical phenomena solved in a coupled manner. In this section, the solver algorithms used for the different models are explained.

3.7.1. NON-ISOTHERMAL TURBULENT FLOW

The non-isothermal turbulent flow model is developed as a first step. The overall flowchart of the solver settings is represented in Figure 3.7. As described in the previous section of the numerical model, the non-isothermal turbulent flow consists of a system of equations that includes Navier-Stokes (RANS), turbulent transport equation, and the heat equation [78]. For the fluid flow, P1-P1 discretization is applied, which means that for both velocity and pressure, piecewise linear interpolation shape functions are used [77]. The linear shape functions are used for the turbulent kinetic energy, turbulent dissipation rate, and temperature variables as well. COMSOL® Multiphysics applies the Galerkin finite element method to solve highly non-linear equations such as the Navier-Stokes equation. These equations can become unstable, especially if the flow is convection-dominated. Therefore, three types of stabilizations, namely streamline diffusion, crosswind diffusion, and isotropic diffusion, are applied [79, 80]. The Babuska-Brezzi condition, that is, the requirement of higher-order shape function of velocity than pressure, is circumvented using the streamline diffusion as described by Hughes et.al.[81]. Streamline diffusion also stabilizes the flow if it is dominated by convection. The streamline diffusion formulation in COMSOL Multiphysics recovers either streamline upwind Petrov-Galerkin formulation or Galerkin least-squares formulation for Navier-Stokes equation. The basic idea behind these formulations is the addition of a perturbation term in the weighting functions [81]. The streamline diffusion obtains a smooth numerical solution if the exact solution is smooth. The solution deviates from the exact solution at the boundaries. In order to reduce the spurious oscillations at the boundaries, a weak term is added to the transport equation, which is termed as crosswind stabilization. In the case of discontinuities at sharp gradients, the crosswind diffusion is added orthogonal to the streamline diffusion. In other words, crosswind diffusion introduces extra diffusion in boundary layers and shear layers.

In order to avoid the ill-conditioning of the system, a segregated approach is adopted.

The system of equations is distributed in three segregated steps, first for velocity and pressure, second for turbulent quantities, and third for temperature. A damped Newton method with a constant damping factor is used to linearize the non-linear equations. To drive the convergence towards steady-state while using constant damping factor, a pseudo-time stepping described in the earlier section is used. To balance the highly non-linear source terms of turbulence transport equations, three iterations of the turbulent transport equation are carried out before proceeding to the next Navier-Stokes iteration. In the linearized equations of the turbulent flow, variable groups are solved using the GMRES iterative solver due to their lower requirement of memory with Smoothed Aggregated Algebraic Multigrid (SAAMG) as a preconditioner. The SOR line method is used as smoother. A coarse mesh is prepared algebraically in SAAMG as opposed to the Geometric Multigrid (GMG) approach in which actual additional meshes are required. Since the external meshes are imported into COMSOL® Multiphysics software, additional meshes for GMG have to be provided externally as well. Therefore, though GMG is computationally faster, SAAMG is a better choice for the current study. Five Multigrid levels with coarse level matrices prepared using the Galerkin projection method are used. The V-cycle algorithm is implemented for each multigrid cycle. The MUMPS direct solver is used on the coarsest level [38]. The linear equation of the temperature equation is solved using the PARDISO direct solver. The coupling of turbulent flow equations and temperature are strongly coupled in such a way that the turbulent viscosity governs the diffusivity of the temperature transport equation. Solving the linear equation of the temperature by the direct solver introduces robustness in the solving procedure. Introducing a direct solver for all segregated groups is not practical due to their huge memory requirement. Using a direct solver for only one segregated group facilitates the convergence with only a little increase in the memory requirement. The tolerance for the segregated solver is set at 0.001. The simulation is converged when the estimated error in solution for each of the segregated groups is less than the tolerance.

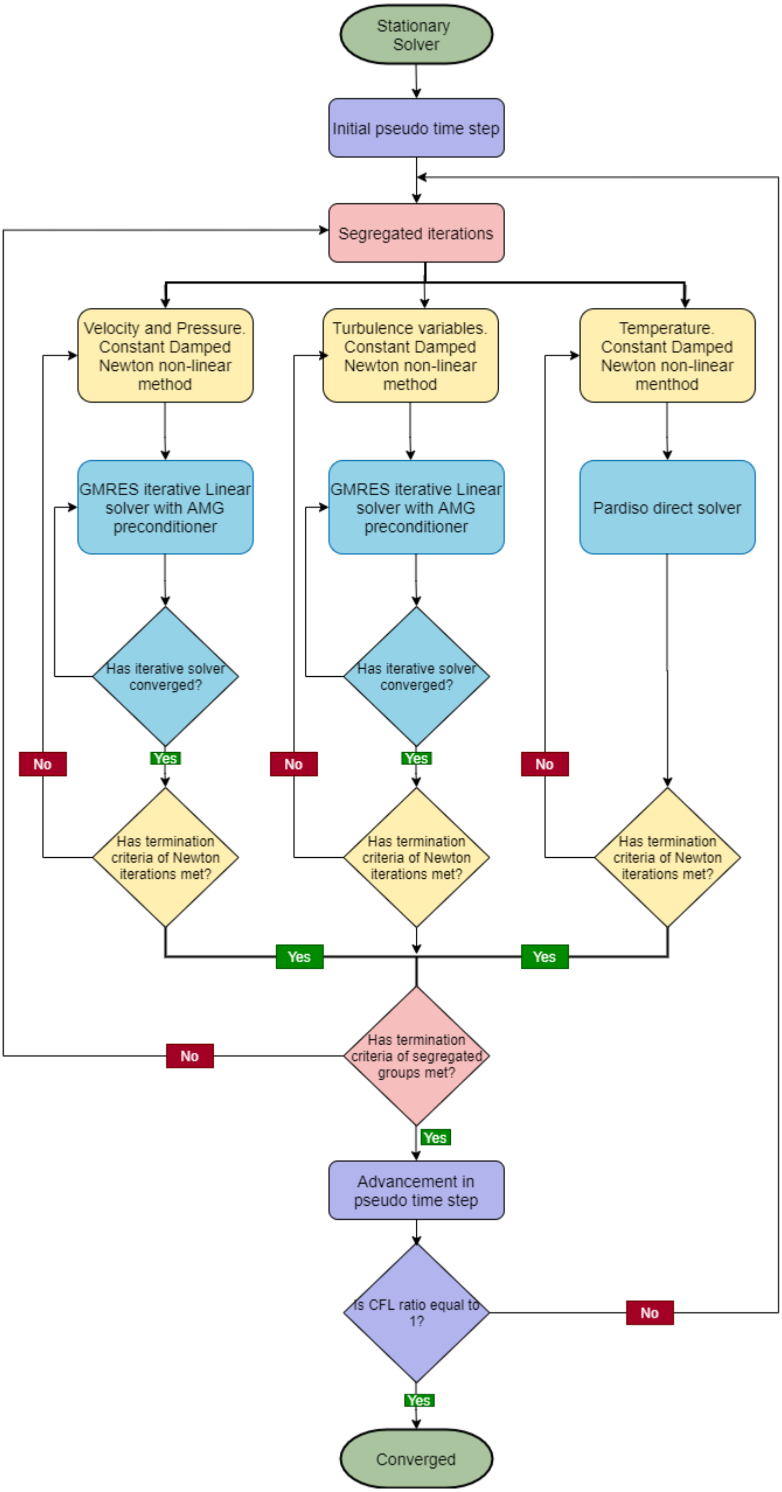

Figure 3.7: The flowchart of non-isothermal non-linear flow solver in COMSOL Multiphysics.

3.7.2. REACTIVE NON-ISOTHERMAL TURBULENT FLOW

In the second step of modeling, the transport equation of chemical species is added to the model. The coupling of reactive flow with the non-isothermal effect is explained next. Figure 3.8 shows the updated solver algorithm for the reactive non-isothermal model with eddy dissipation combustion model. Mass fraction variables for all species are grouped together and are solved in a single segregated step. As shown in Figure 3.8, there are four segregated steps for the reactive non-isothermal turbulent flow. The linearisation of the discretized equations is carried out by the constant damped Newton method. The linear shape functions are used for finite element discretization. The GMRES iterative solver with Smoothed Aggregated Algebraic Multigrid (SAAMG) as a preconditioner is used for solving the linear discretized equation of the transport equation of individual chemical species. The choice of the preconditioner is due to the external importing of the mesh in COMSOL Multiphysics software, as discussed in the above section. Similar to the turbulent flow variables, V-cycle algorithm is applied to each of the five multigrid cycles. The coarse level cycle is solved by either the MUMPS or PARDISO direct solver. The solver settings for the non-isothermal turbulent flow variables remain the same. The tolerance for the reactive model is set at 0.001, and therefore, convergence is achieved when the error for all the segregated groups is less than this tolerance.

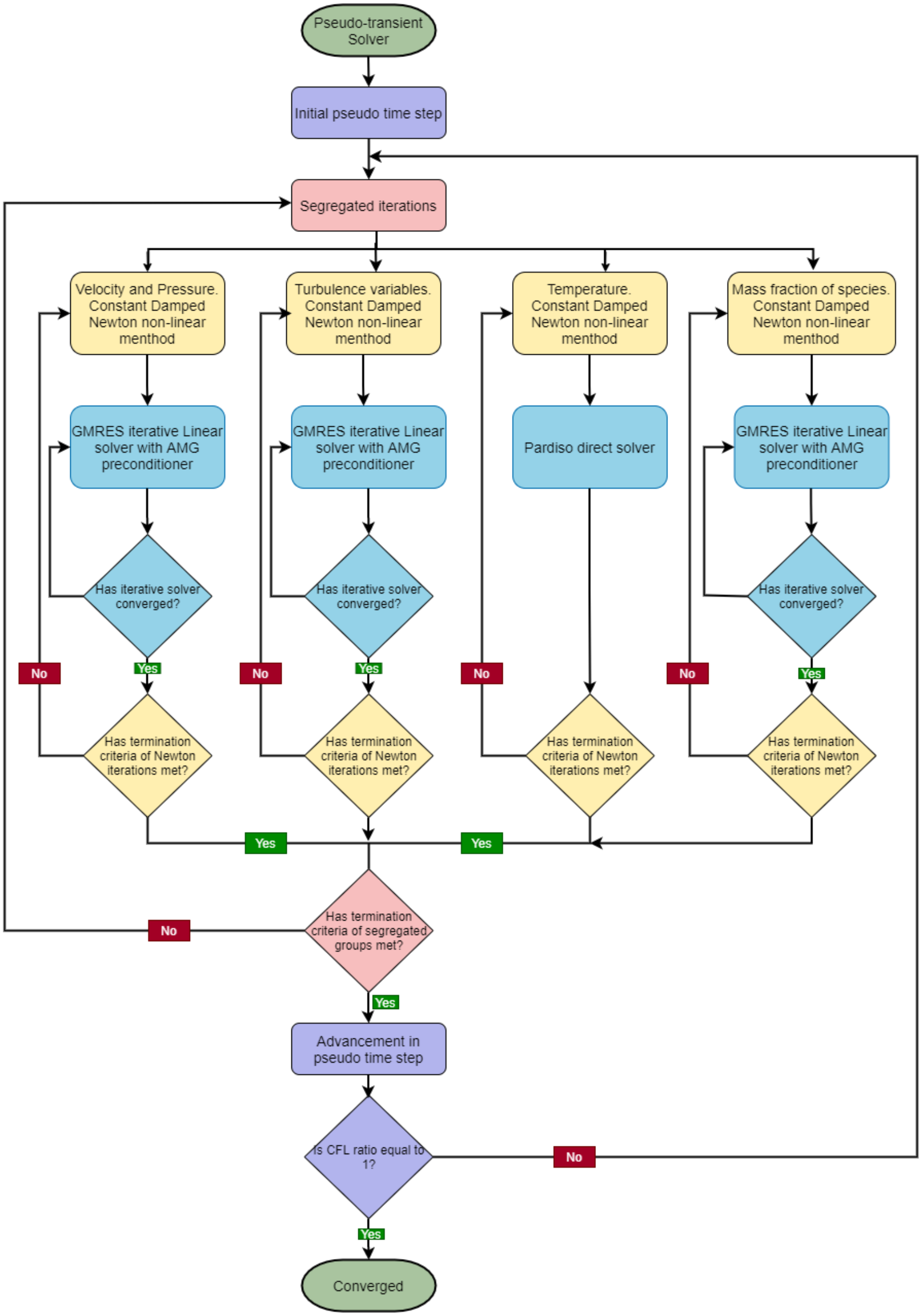

Figure 3.8: The flowchart of reactive non-isothermal non-linear flow solver in COMSOL Multiphysics.

3.7.3. Reactive non-isothermal turbulent flow with radiation

The reactive non-isothermal model is further improved by adding radiation into the model. As discussed in the previous chapter, the addition of radiation modeling demands solving additional transport equations. The number of equations depends on the choice of the radiation model. Figure 3.10 shows the solver algorithm for the P1 approximation radiation model added to a reactive non-isothermal model. COMSOL Multiphysics solves the discrete ordinate method for radiative heat transfer by grouping a number of rays in segregated groups. This grouping is likely the main contribution to the large memory requirements for the discrete ordinate method. The way that COMSOL solves the discrete ordinate method motivated the choice for a P1 radiation model in this thesis. The P1 approximation model introduces a single field (first-order spherical approximation) of the total incidence. The transport equation of the incident radiation variable is discretized with a linear shape function using the finite element method. The Newton Raphson method linearizes the equation with constant damping. The direct linear solver is used for the temperature and incident radiation variable to improve the robustness of the system. Figure 3.9 shows the convergence plot of variables for two sets of solver schemes. It can be observed that convergence is achieved when the direct solvers are used for the temperature and incident radiation variable. On the other hand, the scheme with GMRES iterative solver with SAAMG multigrid pre-conditioner for temperature and incident radiation leads to divergence.

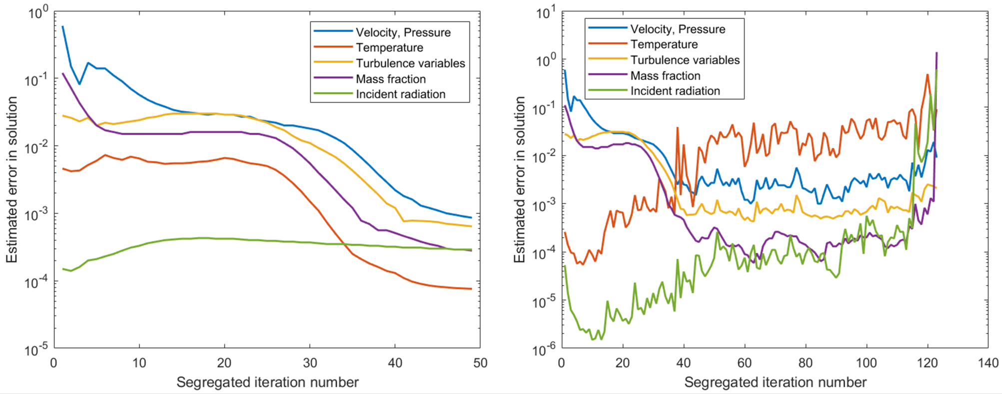

(a) (b)

Figure 3.9: The convergence plots for the reactive non-isothermal turbulent flow radiation model in which temperature and incident radiation are solved by (a) PARDISO direct solver and (b) GMRES iterative solver with SA-AMG pre-conditioner.

As the previous models, this model is solved with a tolerance of 0.001 for the segregated groups. The estimated error in solution for each of the segregated groups is calculated after every segregated iteration. The simulation is converged when all the groups have estimated errors in solution less than the prescribed tolerance.

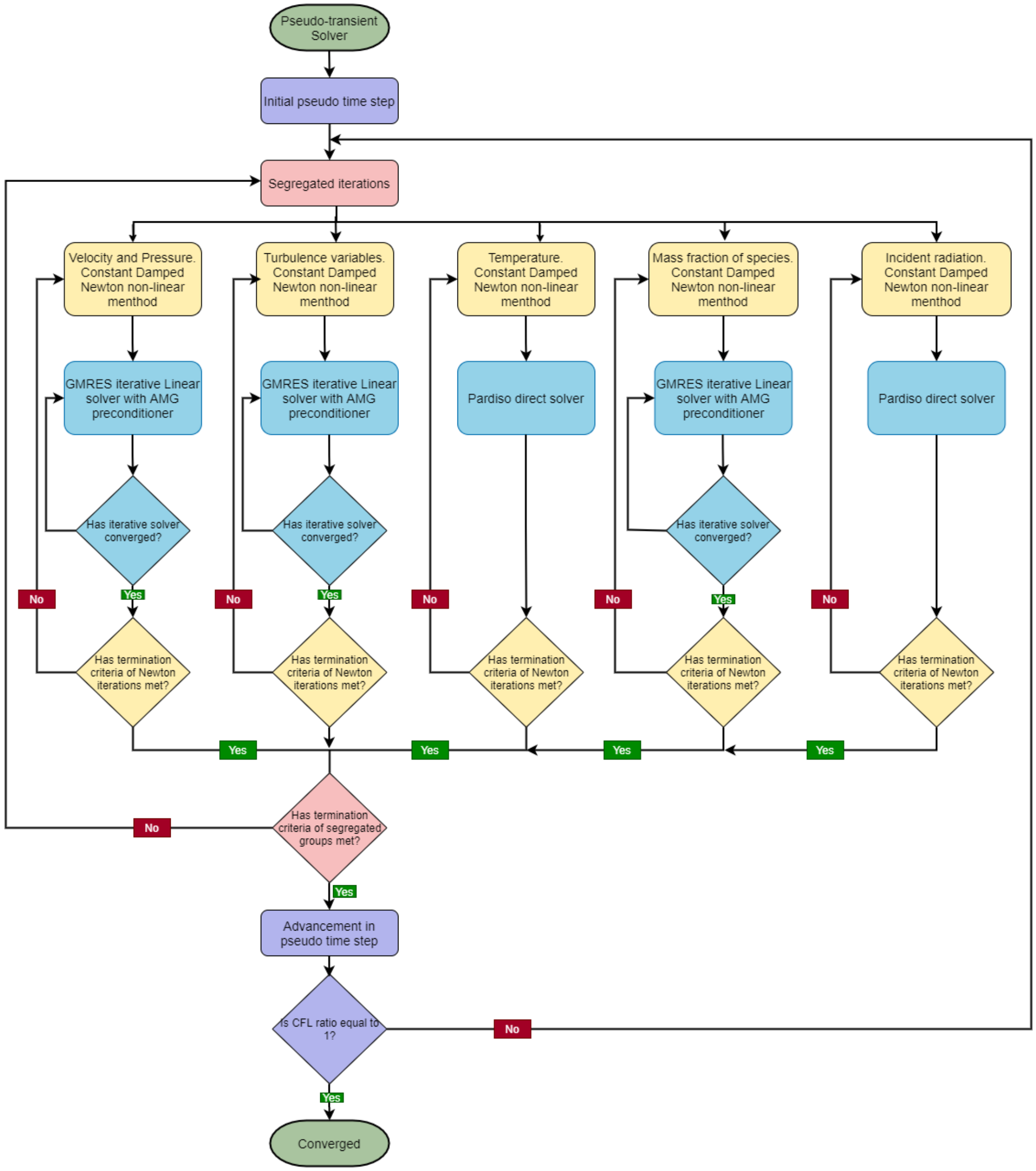

Figure 3.10: The flowchart of reactive non-isothermal non-linear flow solver with radiation in COMSOL Multiphysics.

3.8. CONCLUSION

The transport equation derived in the earlier chapter requires a mathematical approach to obtain the desired solution. In this chapter, the implementation of this approach for a steady-state assumption is described. The COMSOL Multiphysics software package of version 5.4 is used as a simulator. The finite element discretization method is applied with linear shape functions. The different physics are coupled in a segregated manner with field variables of one physics grouped in one segregated step. The linearization of the non-linear equations is carried out using the Newton Raphson method with a constant damping factor. The pseudo time stepping is implemented for accelerating convergence towards a steady state. The linear solvers are either GMRES iterative or direct depending on the field variables in the segregated group. For temperature and incident radiation field direct solver, while for all other field variables, GMRES iterative solver with Algebraic multigrid pre-conditioner is used as a linear solver. The solver algorithms for the different models are presented.

4

MESHING TECHNIQUES

The mesh of a computational domain is an integral part of the numerical simulation. The discretization followed by the assembly of linear system of equations is dependent on the type and size of the mesh elements. In other words, the accuracy of the solution of the numerical simulation relies heavily on the quality of the mesh. In simple words, meshing is the subdivision of the domain under consideration. The levels of the subdivisions should be so small that the simplifications can be made with respect to physical equations. Generating an appropriate mesh for the complex geometries such as an anode baking furnace is complicated. The difficulties further increase when the computational domain considers the burner, since that introduces length scales ranging from mm to m. Therefore, a detailed study is required for obtaining the satisfactory mesh for the furnace. In this chapter, the meshing techniques for the anode baking furnace geometry with varying complexities are studied.

4.1. FURNACE WITH DETAILED BURNER MODEL

The process in the anode baking furnace is such that there is a continuous exchange of heat either from the hot gases to the wall or from the walls to the gases. Based on the transfer of heat, the anode baking furnace is divided into zones such as preheating, heating, blowing, and cooling zone. Each zone consists of three or four sections. In this thesis, the focus is on understanding the NOx generation in the furnace. It has been observed that the majority of the NOx generation occurs in the heating section. Therefore, the geometry of the numerical model is based on only the heating section of the furnace. The heating section of anode baking furnace consists majorly of two parts. The first part is the furnace domain where the preheated air mixes with the fuel. While, the second part is the burner through which fuel is injected into the furnace domain.

The thermal NOx in the furnace is dependent on the temperature as well as the air-fuel ratio in the furnace. In the fuel-rich zone, the NOx generation is less due to the absence of oxygen. If fuel is partially burnt before introducing it in the bulk of oxidizer, the fuel can be burned at lower temperatures. In this way, generation of NOx can be lowered in the fuel-lean zone. Therefore, the transition from fuel-rich zone to fuel-lean zone has a significant effect on the NOx generation. This suggests that studying the design of the burner is equally important for lowering the NOx generation since it governs the local mixing of the two streams.

4.1.1. GEOMETRICAL REPRESENTATION OF FURNACE WITH DETAILED BURNER

The source of the NOx formation in the anode baking furnace is in the heating sections. In other sections of the furnace high temperature zones required for the formation of NOx are not observed. Therefore, the model is confined to the heating section of the furnace in this study. Figure 4.1 shows the geometry of the complete heating section along with the detailed geometry of the burner. The geometry of the domain mimics the actual Aluchemie furnace. As can be seen from the figure, there are three air inlets at the side. The pre-heated air enters the domain which mixes with the fuel injected from top through the burners. There are two burners placed on alternate top sections. The flue gas exits at the opposite end of the air inlet through three pipes as shown in the figure. The flow is directed in U-shape by three baffles. The tie-bricks that provide structural strength to the furnace also affects the flow and aids in mixing of air and fuel.

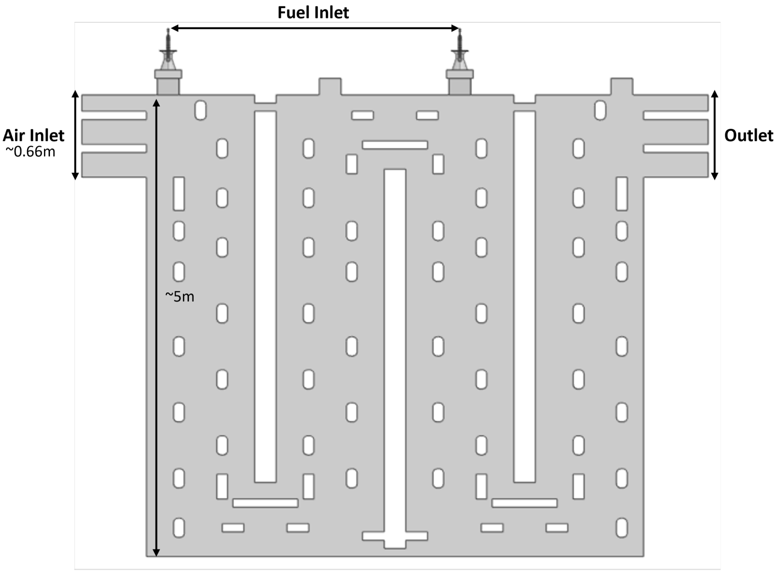

Figure 4.1: A 3D geometry of the heating section of the anode baking furnace model with simplified burner

The geometry shown in Figure 4.1, consists of the design of the detailed burner geometry. Figure 4.2 shows the existing burner geometry of Aluchemie furnace. The geometry consists of two important sections, one for the fuel flow and the other for the air flow. The fuel is injected from the top boundary. The fuel flows through the innermost pipe. The diameter of the fuel pipe varies in such a way that the pressure drop requirements are met. Finally, the fuel passes through a nozzle to a last leg of the fuel pipe that co-axially injects the fuel into air. The second important section of the burner design is the air pipe. The partial premixing of the fuel with air is carried out inside the burner to create local air-fuel mixing. Such partial premixing is beneficial to avoid high temperature in the bulk of air. Therefore, the air is injected in the burner through 8 circular holes as shown in Figure 4.2. The air flows through a pipe that is co-axial to a fuel pipe. Both fuel and air pipes are protected by annular tubes. The local mixing of fuel and air occurs in the region downstream to fuel pipe.

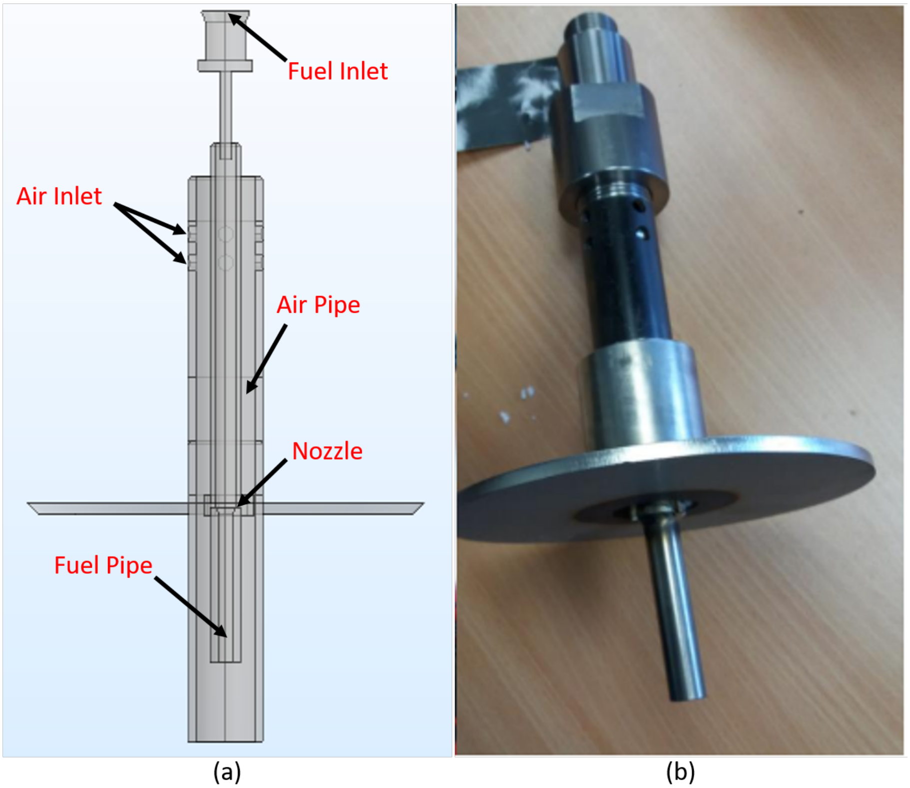

Figure 4.2: (a) Schematic representation of the detailed burner geometry (b) Real picture of the burner used in Aluchemie furnace

4.1.2. DESIGN PARAMETERS

It is important to identify the design parameters that affect the formation of NOx. The variation in these design parameters and their subsequent effect on the NOx generation can provide insights on lowering the NOx. In this section, the potential burner design parameters important for lowering the NOx from anode baking process are shortlisted. The local mixing of air and fuel inside the burner significantly affects the NOx generation. Therefore, the parameters that changes the nature of the air and fuel mixing in the burner needs to be studied. It has been observed that the burner should account for the following factors to be efficient towards lowering NOx [82–84].

- Burner should allow higher residence time in the fuel-rich zone so that maximum oxygen is utilized for fuel combustion
- Burner should have lower mixing rate as compared to the chemical reaction rate in the fuel rich zone so that turbulent mixing governs the overall rate of combustion
- The premixed fuel should be injected in the bulk of oxidizer in such a way that the combustion occurs uniformly in the fuel lean zone.

The current design of the burner from Aluchemie furnace generates fuel-rich region with induced airflow from the small air inlets of the burner. Whereas, the fuel-lean region is created when the partially premixed fuel meets the preheated air in the flue-wall. The above mentioned factors can be controlled with different design parameters of the burner. These parameters are listed as following [85].

- Number of air-inlets- The air-fuel ratio of the partially premixed fuel can be controlled by the number and position of air-inlets of the burner.
- Nozzle diameter of fuel pipe- The nozzle diameter of the pipe changes the magnitude of the velocity at which fuel is injected. This leads to changes in the mixing of air and fuel and therefore, an important parameter to be studied for NOx generation.
- Length of mixing zone between fuel and air- The length of the mixing zone between fuel and air injected through burner can be varied by changing the length of air pipe. With this the residence time of the premixing with air is controlled which can have an impact on NOx generation.

Apart from these parameter, the choice of type of burner and fuel injection depth are other significant parameters. The study by Bessen et.al. [86] shows that the injection depth does not help in reducing NOx emission but reduces the life of burner. The choice of burner type is vast study in itself and is out of scope for this work.

The design of the furnace can be varied by changing the position of the tie-bricks and baffles. Such change might lead to different mixing patterns resulting in the reduction of NOx formation. It has been observed that only the local mixing pattern downstream of the burner has major impact on the NOx formation. To study the optimized design, it is important to generate a workflow to easily create models with varying design parameters. The main obstruction in generating such workflows is obtaining satisfactory meshes.

4.2. COMSOL MESHING TEHNIQUES

Mesh generation is the crucial step in the numerical modeling especially for the complex geometries. The anode baking furnace consists of length scale ranging from mm to m. This leads to the requirement of different refinement across the domain. The presence of tie-bricks and baffles has many curved surfaces that impose further challenges in the meshing process. The boundary layers around the tie-bricks and baffles along with the outer wall are required which increases the necessity of more refinement levels. The refinements are also needed in the region of sharp corners present in the furnace domain.

The COMSOL Multiphysics software utilized in this thesis for the modeling is based on the finite element method (FEM). Figure 4.3 (a) shows the mesh generated by the COMSOL default mesher near the region of first burner. The details of the mesh are also presented in Figure 4.3. As can be observed from the figure, the 88% of the mesh elements (8.8M) are tetrahedral. The tool is insufficient to obtain the hexahedral mesh of the geometry. The mesh quality is measured in terms of the skewness of the elements. Figure 4.3 (b) shows the histogram of mesh quality based on the skewness parameter. The skewness of 1 signifies that the mesh element is perfect while the skewness of 0 means a bad quality element. It can be observed that even with the number of elements as high as 9.9M, the average mesh quality is limited to 0.67.

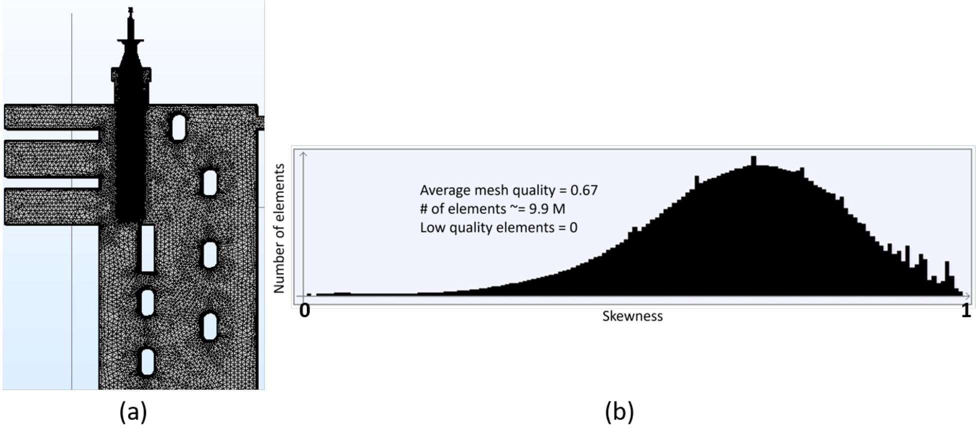

Figure 4.3: (a) The mesh near the first burner obtained by the COMSOL default mesher with detailed burner geometry (b) Histogram of the mesh quality based on skewness over the entire domain

Jeong and Seong [87] have observed that the CFD solvers based on finite element modeling are more sensitive to mesh quality than that of the finite volume modeling. The default meshing techniques available in COMSOL Multiphysics software are limited. It is extremely difficult to control the type of elements while meshing the complex geometry such as anode baking furnace with COMSOL meshing tools. The default meshing tool generates many of tetrahedral elements. The attempts of making hexahedral mesh show difficulties due to the presence of obstacles in the furnace such as tie-bricks and baffles. Biswas and Strawn [88] have shown that a significantly higher number of elements are required to obtain the equivalent level of accuracy with tetrahedral elements as compared to hexahedral elements. Similar results are obtained in this thesis work as well as explained in the Chapter 5. Moreover, the study of Biswas and Strawn [88] also conveys that the isotropic refinement necessary for maintaining the mesh quality is difficult to obtain with a tetrahedral mesh. In order to study the mesh sensitivity, it is important to have a refined mesh that has the same mesh quality as their coarser counterpart. Since the large number of tetrahedral elements are required for the desired accuracy, the storage and CPU time are almost double as compared to a hexahedral mesh.

4.3. CFMESH MESHING TECHNIQUES

In the earlier section, the limitations of the mesh generated using COMSOL default mesher are summarised. Among the various meshing tools, cfMesh meshing software, a dedicated meshing tool provided by the Creative Fields [1] is chosen. The cfMesh meshing tool provides a library such that the limitations encountered with the COMSOL default mesher can be overruled. Moreover, the support and expertise available from the cfMesh software provide favorable conditions to evaluate this customised tool.

cfMesh is a collection of mesh generation tools distributed as a library [89]. This library is designed to provide customizable meshing workflows for automatic generation of meshes with various cell types in complex geometries of industrial interest. cfMesh generates hex-dominant meshes, tetrahedral meshes, meshes consisting of arbitrary polyhedra, and 2D quad-dominant meshes. The library uses both shared-memory with OpenMP and distributed-memory parallelization with MPI. Parallelization is encapsulated inside the meshing algorithms. Hence, it allows customization of meshing process while preserving the benefits of the code executing in parallel. The output of the software is suitable for the OpenFOAM software and can be converted to formats that are supported by many other commercial softwares such as Ansys Fluent. Furthermore, the software provides support to obtain tools to convert the mesh into other formats.

4.3.1. WORKFLOW

The meshing process in cfMesh software is controlled by a geometry file given as a surface triangulation, most often as a STL (Surface Triangle Language) file, and a dictionary containing the parameters provided by the user. Once the geometry and the settings are given, the mesher generates the mesh automatically without any user intervention. The dictionary allows the user to specify the global cell size in the domain and local refinement zones. The latter can be specified via subsets, surface meshes, edges mesh, as well as via objects such as cylinders, boxes, spheres and lines. The dictionary also allows to control the number of boundary layers at each boundary of the domain, their number and their thickness ratio. Dictionary settings allow mesh-sensitivity studies by changing a single parameter. The algorithms used by cfMesh are described in reference [89].

The workflow implemented in this thesis for the generation of mesh through cfMesh software is presented in Figure 4.4. It can be observed that the generation of the mesh and importing it into COMSOL software requires interference of other tools such as Salome and MeshMixer.

---

[1] https://cfmesh.com/

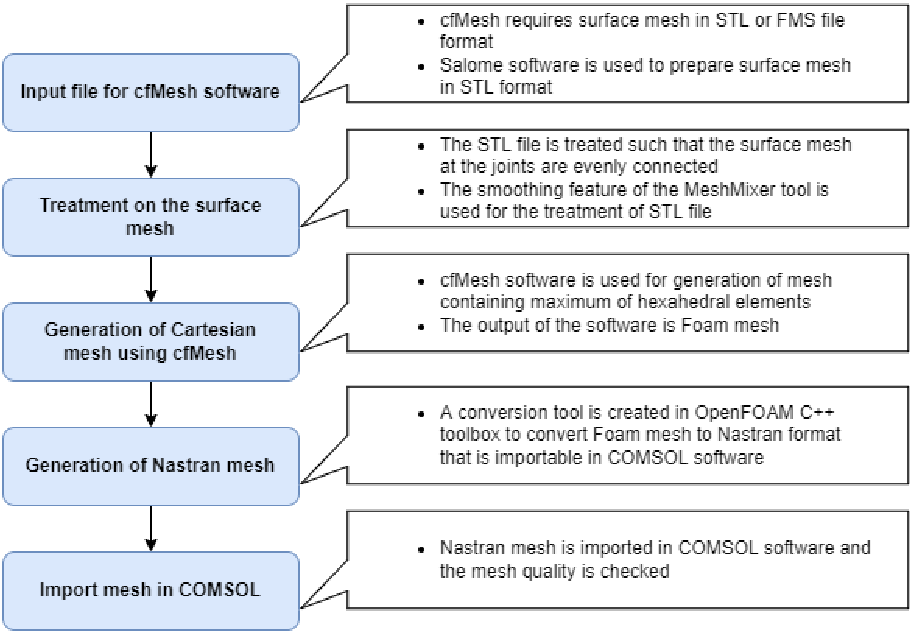

Figure 4.4: The workflow of integrating meshing of cfMesh software in the COMSOL software

4.3.2. CONVERSION TOOL

The output of the cfMesh software is in the OpenFOAM compatible format. To import this mesh in COMSOL, it needs to be converted in the Nastran format supported by COMSOL Multiphysics software. In this work, a conversion tool for a three dimensional mesh is developed as the OpenFOAM utility. The OpenFOAM utilities are established using the C++ toolbox and can be modified as per the requirement of the application.

The Nastran format is classified into two sections, namely Grid data section and Element data section. In the first section, all vertices are numbered and their corresponding X, Y and Z coordinates are assigned. The column width, alignment and the precision of the numbers needs to be adjusted according to the requirement of COMSOL. In the Element data section, the cells are numbered and their corresponding vertices are enumerated. Initially, the shape of each element is matched with already existing functions for various cell shapes such as hex, pyramid, prism, tetrahedron etc. After identifying the cell shape, it is important to arrange the vertices as per the prerequisites of COMSOL software. Similar to the Grid data section, the column width and alignment needs to be adjusted. The mapping of vertices for the Nastran format can further be explained with the help of Figure 4.5. The numbering of the Nastran format needs to be in an order as shown in Figure 4.5 (b) if the default numbering is as given in 4.5 (a).

Figure 4.5 shows the example of hexahedron element. Such mapping of the numbering needs to be carried out for other cell shapes as well. Table 4.1 shows the default numbering and the corresponding mapping required while converting the elements into Nastran format. This conversion tool which is a source code of the OpenFOAM utility is

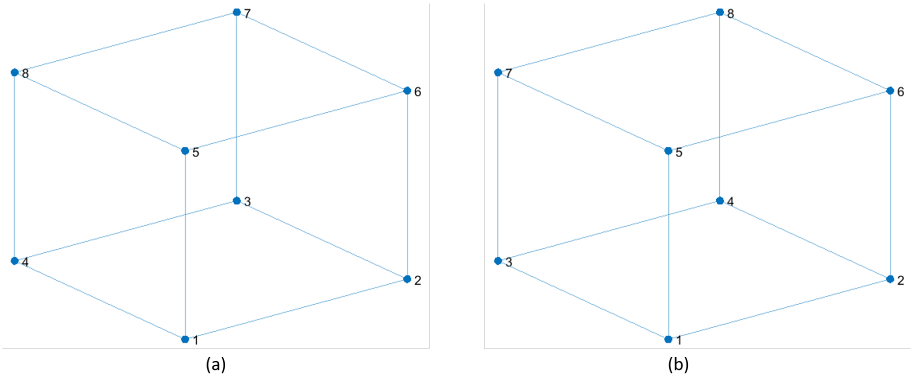

(a) (b)

Figure 4.5: (a) The default numbering of vertices (b) The Nastran numbering of vertices in COMSOL

available for download. The tool can be downloaded with this link https://doi.org/10.4121/13522691.v2.

Table 4.1: The details of the mapping of vertices for 3D Nastran format in COMSOL

Element shape	Tag	Default numbering	Nastran format numbering
Hexahedral	CHEXA	1,2,3,4,5,6,7,8	1,2,4,3,5,6,8,7
Tetrahedral	CTETRA	1,2,3,4	1,2,3,4
Pyramid	CPYRAM	1,2,3,4,5	1,2,4,3,5
Prism	CPENTA	1,2,3,4,5,6	1,2,4,3,5,6

The development of the workflow and the conversion tool is tested on simple geometries. The performance of the cfMesh is found to be better as compared to the COMSOL mesh for these test cases. Therefore, the workflow is implemented to the anode baking furnace geometry with detailed burner design.

4.4. CHALLENGES WITH A FURNACE WITH DETAILED BURNER

The mesh generated by cfMesh is controlled by the various parameters that govern the local refinement. cfMesh provides checks on the quality of the mesh and optimizes the mesh so as to improve this quality. The STL files of the different patches of the geometry are imported in the cfMesh software. The software also allows to internally group different patches for controlling the refinement. For example, the boundary layers for the burner walls and the walls of the furnace certainly need different refinement of the first layer as well as a distinct number of layers. In these cases, the wall faces of the burner are assembled as one group while the faces of the furnace walls are collected in a separate group. The refinement of the boundary layers for these two separate groups can then be controlled individually. The COMSOL default meshing tool also allows grouping such patches. However, control on the structure of the mesh is unclear. In other words, obtaining a mesh that aligns with the flow dynamics is difficult in COMSOL compared to the cfMesh software.

4.4.1. PERFORMANCE OF CFMESH COMPARED TO THE COMSOL MESH

The mesh equivalent to the most refined mesh from the COMSOL default meshing tool is generated with cfMesh software. Figure 4.6 shows the comparison of the meshing carried out by the two software packages. It can be observed that though the refinement level for both meshes is compatible, the mesh generated with cfMesh is more aligned with the flow and therefore, is characterized as more structured compared to the mesh obtained in the COMSOL default meshing tool.

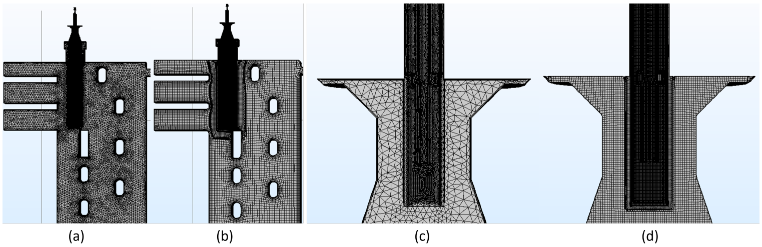

Figure 4.6: The mesh near the first burner at the symmetry plane generated by (a) COMSOL default meshing tool and (b) cfMesh software

The mesh quality for both meshes obtained in COMSOL and cfMesh softwares are compared in Figure 4.7. The mesh quality for both meshes is calculated based on the skewness parameter. It can be observed that the average mesh quality of the mesh obtained by the cfMesh software is significantly higher as compared to the COMSOL mesh. However the mesh statistics show that there are certain elements in the mesh prepared by cfMesh that have negative skewness and therefore are of low quality. When the mesh obtained in cfMesh is imported in COMSOL, the software complains about such low quality elements. It has been observed that the convergence of the model with even a couple of such low quality elements in the mesh is problematic. Therefore, though the average quality of the mesh generated in cfMesh is higher, the presence of few low quality elements makes it undesirable.

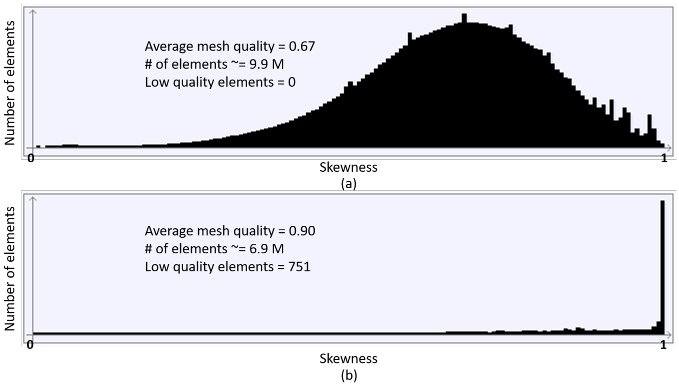

Figure 4.7: The mesh quality based on skewness parameter for meshes generated by (a) COMSOL default meshing tool and (b) cfMesh software

4.4.2. ELEMENTS WITH CURVED FACED AND LOW SKEWNESS IN CFMESH

The low quality elements complained by the COMSOL software on importing the cfMesh mesh is assessed. The majority of these elements are in the vicinity of the burner and around the edges of the tie-bricks in the furnace. The different tests are carried out to identify the reason of occurrence of such elements [85]. The important observations of these tests are summarised below.

- Edge refinement - In order to improve these elements, additional edge refinement is carried out. The observation suggests that refining these regions worsen the quality of the mesh. This might be due to the insufficient optimization of cfMesh for sharp corners and curved surfaces.

- Burner refinement - Tests on meshing of only the burner part (detached from the main furnace) are carried out in order to have more control on the refinement. The burner geometry is simplified to a 2D geometry by removing the air inlets of the burner. The low quality elements are not observed in the 2D mesh. However, the low quality elements appears by extruding the 2D mesh to 180^0.

- Decomposition of polyhedral cells - The cfMesh introduces polyhedral cells as the default setting. Since the conversion tool to Nastran format fails to convert these elements, the decomposition of polyhedral cells is activated while meshing in cfMesh. The tests are carried out to inspect whether these decomposed elements are problematic. It has been observed that even without the decomposition of polyhedral cells, the low quality elements exist.

- Different skewness computation procedure - The mesh quality of the low quality elements is analysed in the cfMesh software. The optimization of the mesh is carried out such that the mesh does not have elements below a certain skewness. It has been observed that the low quality elements complained by the COMSOL software have different skewness computed in cfMesh.

The analysis on the low quality element suggests that changes in the skewness computation and the optimization procedure in the cfMesh software is needed to obtain compatible mesh for the detailed burner geometry.

4.4.3. CHANGES IN CFMESH TO DEAL WITH LOW SKEWNESS ELEMENTS

The support from cfMesh software allows the customization of the algorithms. The mesh obtained by the cfMesh software is promising due to its high average mesh quality. Moreover, the structure of the mesh aligns with the flow dynamics making it favorable for the flow simulations. The only disadvantage of the mesh is the presence of the low quality elements which are as low as 0.01% of total elements in number. Therefore, the attempts to optimize the cfMesh algorithm to align the mesh for COMSOL software is reasonable.

SKEWNESS COMPUTATION IN COMSOL MULTIPHYSICS

The skewness is the important metric for judging the quality of the mesh. It has been observed that the mesh imported in COMSOL multi-physics software in the Nastran format has low quality elements. This can be attributed to the difference in the calculation of skewness by cfMesh and COMSOL Multi-physics software. Therefore, it is important to study the skewness in order to align the calculations with the two software packages.

The skewness in COMSOL is calculated based on the ideal element. An ideal element is defined as the one that has equal angles. The skewness is therefore, the deviation from the ideal element. The skewness in COMSOL is calculated according to Equation 4.1. The θ_i is the dihedral angle over an edge while θ_e is the ideal dihedral angle.

$$S = \min\left(1 - \max\left(\frac{\theta_\mathrm{i} - \theta_\mathrm{e}}{180 - \theta_\mathrm{e}}, \frac{\theta_\mathrm{e} - \theta_\mathrm{i}}{\theta_\mathrm{e}}\right)\right) \tag{4.1}$$

Further, it is important to understand the calculation of the dihedral angle between planar as well as non-planar faces of elements. Let us consider the element as shown in Figure 4.8. Each edge of interest has two adjacent faces. Therefore, for each edge of interest, four triangles can be formed by joining the two nodes of the edge with the opposite node of each adjacent face. Moreover, for each triangle, a normal can be calculated based on taking the vector product. This results in four normals corresponding to each triangle associated with a given edge of interest. The dihedral angles for the edge of interest can be calculated based on the four possible pairs such as n1-n3, n1-n4, n2-n3 and n2-n4. If the face is planar, the two normals corresponding to two triangles on the face are equal.The maximum of the four angles is considered for a given edge as the dihedral angle in Equation 4.1.

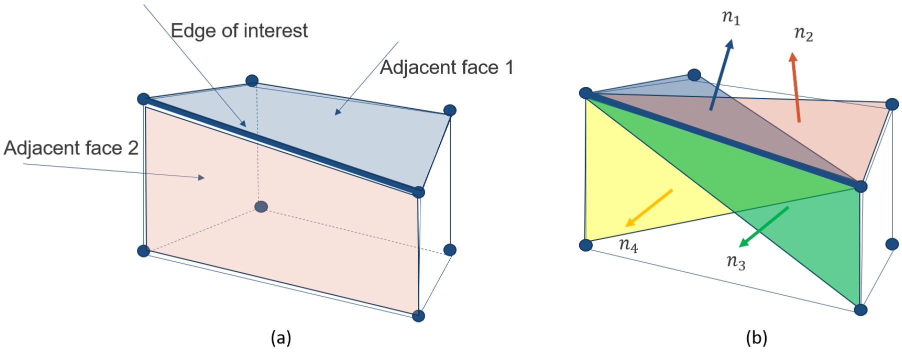

(a)

(b)

Figure 4.8: (a) The edge of interest with corresponding adjacent faces (b) The four normals corresponding to four triangles for a given edge of interest

SKEWNESS COMPUTATION IN CFMESH

In this section the additions and modifications in the cfMesh software library to be able to compute the skewness of the elements in a given mesh is described. The target is to obtain the same values in cfMesh as provided in Comsol Multiphysics. The code is developed for the cfMesh tool by accounting the skewness calculations in the Comsol Multiphysics software as described in the previous subsection.

The decomposition of hexahedral cells into tetrahedra raises complexities. This ambiguity has thus far impeded obtaining the same values of skewness in both software packages.

MESH SMOOTHING TO OPTIMIZE SKEWNESS IN CFMESH

The decomposition of cells into tetrahedral cells creates a problem in the computation of the skewness similar to Comsol Multiphysics software. The investigation is conducted to improve the mesh in terms of skewness in the cfMesh code. The process is iterative and in each iteration the following process is carried out.

1. Find cells/faces in the mesh failing active checks
2. Select vertices that shall be moved by searching the faces/cells detected above
3. For each vertex, the cells adjacent to the vertex are decomposed into tetrahedra, each tetrahedron consists of an edge containing the optimized vertex, face centre and cell centre. So far this is detected as the cause of problem because these tetrahedra can all have a positive volume, even though some of the cells used for the decomposition are failing the skewness check. As a consequence, the point does not move to rectify the problem.

The difficulties of obtaining a mesh of the detailed burner geometry for COMSOL software without low quality elements are not resolved. The cfMesh software is designed for the generation of the mesh that are compatible for softwares based on finite volume method. Further study is needed to make cfMesh software compatible with finite element based solver such as COMSOL software.

4.5. FURNACE WITH SIMPLIFIED BURNER MODEL

The low quality elements observed in the detailed burner furnace geometry are located majorly in the burner domain. The dimensions in the burner are as small as mm while the furnace dimensions range to m. The size of cells in the burner domain should be at least one order of magnitude smaller than mm. As the size of the elements decrease, the possibility of the lower skewness parameter increases.

The anode baking furnace consists majorly of two domains namely: furnace domain and burner domain. As discussed in earlier sections, the modeling of the burner domain has limitations due to challenges in obtaining a suitable mesh. The meshing of the furnace domain is relatively easy due to its larger size. The modeling of the furnace domain is equally important to understand the overall mixing behaviour of the different streams. Therefore, the model of the anode baking furnace is simplified by replacing the detailed burner geometry by a simple pipe.

4.5.1. SIMPLIFICATION OF GEOMETRICAL REPRESENTATION

The geometry of the model with simplified burner geometry is shown in Figure 4.9. The major difference between this geometry and the geometry of the detailed burner is that the burner is replaced by a simple pipe. The diameter of this pipe is equivalent to the outlet pipe of the detailed burner. To study the effect of the design parameters, there have been various flue designs modeled in the literature [22, 86]. The geometry of the model studied in this thesis is based on the existing furnace design from the Aluchemie factory. The geometry consists of three air inlet pipes, three outlet pipes and two fuel inlets as shown in Figure 4.9. The length of the outlet pipes is such that the backflow is suppressed and uniform pressure distribution is ensured at the outlet. The typical bypass dimensions at top and bottom are 0.084 [m] in y direction. The rectangular obstacles with smoothed corners are the tie-bricks required for the structural strength of the furnace and also aids in providing turbulence. The three baffles directs the flow in the desired direction. Symmetry in the flue wall is assumed.

4.5.2. MESH GENERATION USING COMSOL AND CFMESH

The meshing of the simplified burner geometry is less complicated than the detailed burner geometry. The challenges of the varying length scales are significantly reduced by removing the exact geometry of the burner. The problems of the meshing are restricted to refinement around tie-bricks, baffles and sharp corners. The mesh being an important step in numerical modeling, the attention on obtaining a satisfactory mesh is required despite the simplifications in the burner geometry. The analysis of different meshing techniques is carried out by closely investigating properties that are more sensitive to the mesh. The variations in meshing techniques are introduced by varying the meshing tool and the local refinement in the region of interest.

COMPARISON OF DIFFERENT MESHING TOOLS

The limitations of the COMSOL default meshing tool are described in the discussion of meshing of the detailed burner geometry. Due to insufficient quality of few elements with the cfMesh meshing tool the simulations of the detailed burner geometry model fails to converge. In general the analysis of results with both meshing tools for the de-

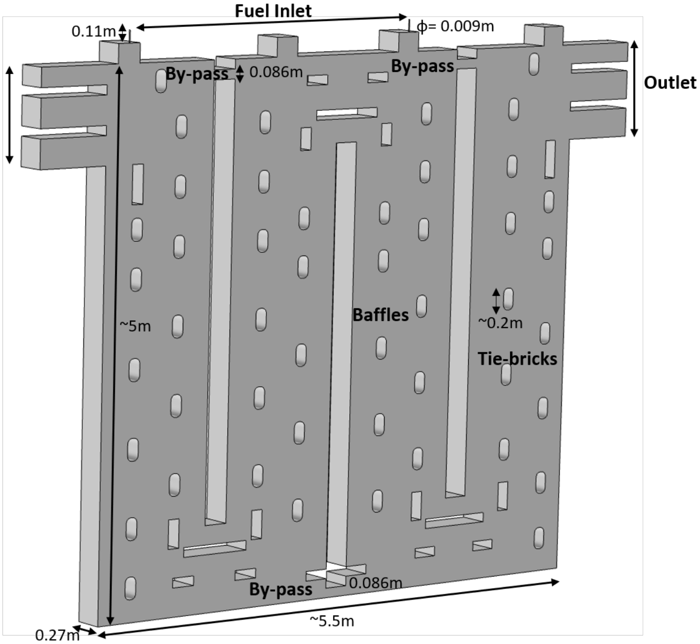

Figure 4.9: A 3D geometry of the heating section of the anode baking furnace model with simplified burner

tailed burner geometry remains a challenge. The geometry with simplified burner pipe is meshed with both meshing tools such that the low quality elements are absent. Therefore, the results of the aerodynamics in the furnace are obtained with both meshing tools. This gives us the opportunity to analyse the performance of these meshes.

Figure 4.10 shows the difference between the mesh generated by cfMesh (Mesh 1) and COMSOL Multiphysics software (Mesh 2) at the symmetry plane near the fuel inlet and at the YZ plane cut through jet region. It can be observed that even though with both meshing softwares, the mesh is refined near the fuel inlet, the mesh generated by cfMesh is more aligned with flow dynamics. The nomenclature ‘Mesh 1’ and ‘Mesh 2’ are utilized in later chapters.

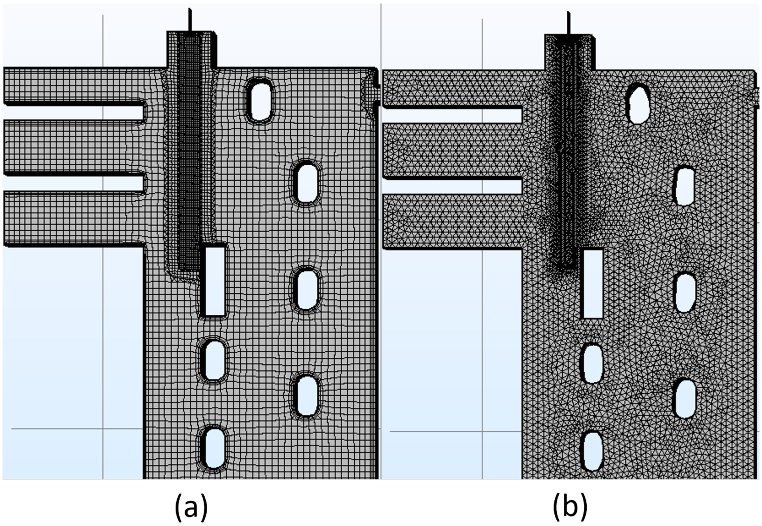

Figure 4.10: Mesh at the symmetry plane of the flue wall prepared in cfMesh (Mesh 1) and COMSOL (Mesh 2) software respectively

Figure 4.11 shows the histogram of the mesh quality of the two meshes along with the number of elements and the average mesh quality based on the skewness parameter. Even with the higher number of elements with the COMSOL mesh, the quality of the elements remains low. Moreover, the low quality elements observed for the mesh of the detailed burner geometry with cfMesh is absent for the simplified burner geometry.

'Mesh 1' generated by the cfMesh software contains approximately 2-10 times of mesh elements as compared to the finer meshes of the literature models on anode baking furnace for an equivalent geometry. This suggests that the numerical solution is computed more accurately by decreasing the numerical error with 'Mesh 1'.

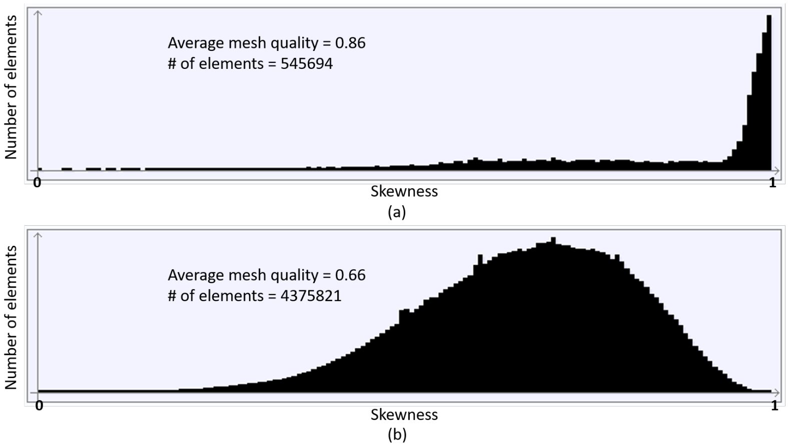

Figure 4.11: Mesh at the symmetry plane of the flue wall prepared in cfMesh (Mesh 1) and COMSOL (Mesh 2) software respectively

EFFECT OF THE LOCAL REFINEMENT ZONE

The importance of mesh refinement has been discussed in the research field [90]. The trade-off between the accuracy of solution and the required computational power can be achieved by local refinement. The region of interest or the region with higher gradients are identified and the mesh is refined in those regions. The regions in which the gradients are not so crucial have coarser refinement. For models such as an industrial furnace, identifying such regions is important to generate more accurate solution. In the present study, such region lies beneath the fuel outlet. Therefore, in this section the mesh with varying local refinement is examined. The nomenclature used for the mesh without local refinement obtained in the cfMesh software is referred as ‘Mesh 3’.

Figure 4.12 shows the mesh obtained by the cfMesh software with and without the local refinement underneath the fuel outlet. The mesh in the other parts of the domain is equivalent for both models. The analysis of the mesh quality is presented in Figure 4.13. The number of elements decreases while the average mesh quality increases for the mesh without local refinement. The local refinement introduces decomposition of cells in refined region. Such decomposition often results in mesh elements with lower quality. This justifies the slightly higher average mesh quality of the mesh without local refinement. Despite the higher mesh quality, the results of the more sensitive variables such as turbulent viscosity are not accurately predicted for the mesh without local refinement as discussed in the later chapters.

Further comparison of ‘Mesh 1’ with meshes used in the literature suggests that the local refinement under the fuel outlet is absent in literature models. The introduction of this local refinement decreases the numerical error in this region and resolves variable fields more accurately. The decrease in the numerical diffusion due to finer mesh poses challenges in achieving the convergence. The compromise between accuracy and convergence is another factor along with the computational power that discourages addition of such finer refinement.

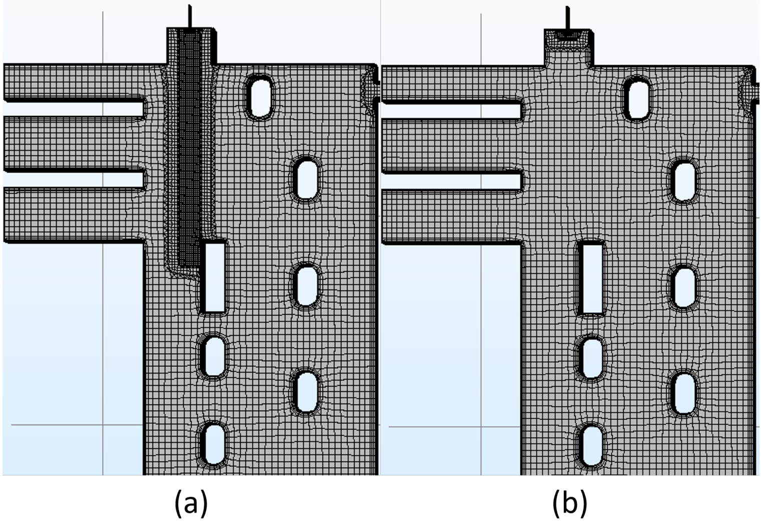

Figure 4.12: Mesh at the symmetry plane in the heating section prepared in cfMesh a) with jet refinement (Mesh 1) and b) without jet refinement (Mesh 3)

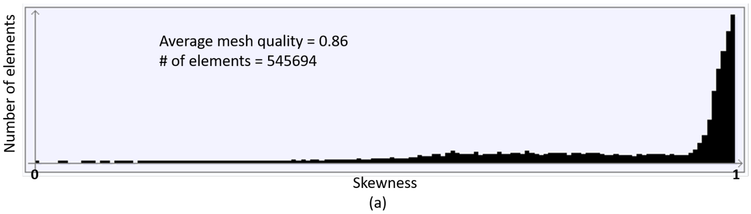

(a)

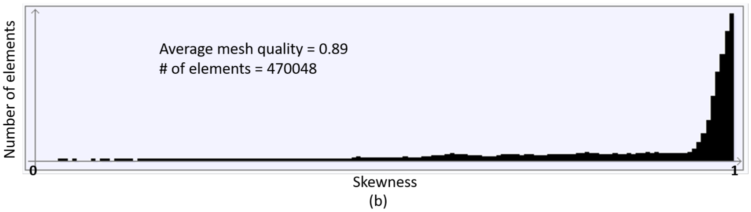

(b)

Figure 4.13: Mesh at the symmetry plane in the heating section prepared in cfMesh a) with jet refinement (Mesh 1) and b) without jet refinement (Mesh 3)

In all meshes, the boundary layer refinement is introduced. This refinement is important near the walls where the no-slip boundary condition is employed. The number of boundary layers, refinement of the first layer thickness, and the growth rate of the layers are decided by analyzing the y+ values. These values should be close to 11.06.

EFFECT OF DIFFERENT FUEL PIPE DIAMETER

In the Aluchemie factory the different diameters of the fuel inlet pipe have been investigated. It is interesting to understand the overall physical phenomena with different fuel pipe diameters for the calculation of NOx formation. Therefore, in this study, two geometry models with different fuel pipe diameters have been studied. Figure 4.14 shows the difference between the two fuel pipes for the model. The only difference between these models is the diameter of the fuel pipe. The remaining geometry of the furnace is exactly equal for both cases.

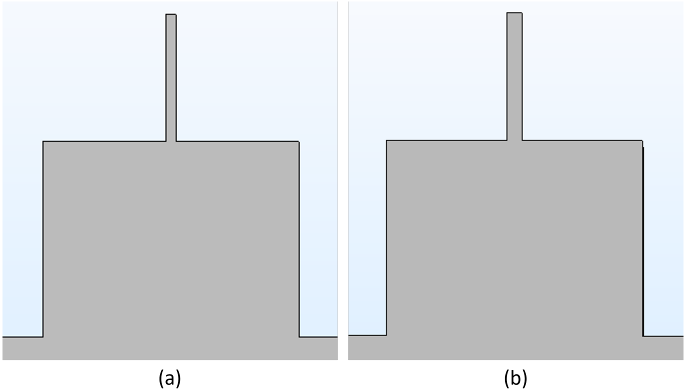

Figure 4.14: The geometry of the models with fuel pipe diameter of (a) 9 mm and (b) 13 mm

The difference in the fuel pipe diameter induces the variation in the flow dynamics due to different fuel jet outlet velocity. The meshing for both models is carried out using the cfMesh meshing tool as shown in Figure 4.15. The refinement in the fuel injection pipe is equivalent for both models. The refinement is such that the mesh elements at the attachment of pipe are smoothly merged with relatively coarser mesh elements in the furnace.

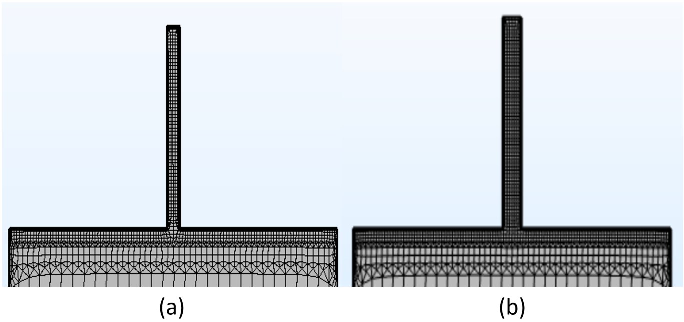

Figure 4.15: The mesh of the models with fuel pipe diameter of (a) 9 mm and (b) 13 mm

4.5.3. REMAINING CHALLENGES IN MESHING TECHNIQUES

The cfMesh meshing tool generates high quality meshes for the simplified burner geometry of the anode baking furnace as compared to the COMSOL default meshing tool. Moreover, unlike the detailed burner geometry, the cfMesh tool is able to obtain meshes compatible for the COMSOL software without a complaint of low quality element. Despite the promising meshes, the cfMesh tool imposes a few challenges while meshing the simplified burner geometry as well.

The difference in the skewness computation by the two algorithms lead to formation of low quality elements when the mesh is refined further. Therefore, a lot of trial and error experiments are required to obtain a mesh which upon importing in COMSOL is without low quality elements. Another major challenge is the difference in the two software packages to handle elements which have a Z coordinate slightly out of the symmetry plane. The results in the COMSOL software for such meshes seem to have voids. Therefore, the mesh should not have such elements that have out of plane Z coordinate. Obtaining such mesh again needs an extensive trial and error. Due to these two challenges, the satisfactory mesh for the simplistic burner model with lower pipe diameter is difficult to obtain. For example, the Aluchemie also has a burner with 6.5 mm fuel pipe diameter. However, the study of this model was challenging due to unavailability of appropriate meshing technique.

4.6. CONCLUSION

In this chapter, the meshing techniques for the anode baking furnace with various geometries of burners are discussed. The importance of the mesh in the numerical modeling with finite element method is realized. A detailed investigation on the requirement of appropriate meshing is carried out. The COMSOL Multiphysics software is excellent for the numerical modeling of the multiple physical phenomena. However, the meshing techniques available in the software are limited. Moreover, the mesh elements generated by the software are majorly tetrahedral. The control on obtaining a mesh with hexahedral elements, that are known to provide less numerical diffusion, is limited for complex geometries. Therefore, an external mesh generation tool namely cfMesh software is tested.

The cfMesh software provides excellent control over obtaining hexahedral mesh. The workflow for generating a mesh and converting into a Nastran format is developed in this thesis. The comparison of the mesh quality generated by two softwares suggests that the mesh obtained by the cfMesh software has higher average mesh quality with lower number of elements. However, the skewness computation with the two softwares differ. This leads to generation of few low quality elements in cfMesh mesh as per the COMSOL criteria. The customization of skewness with cfMesh based on the COMSOL software has been challenging but has provided immense opportunity to learn about the skewness computation. The disparity of skewness computation is majorly problematic for extremely small elements (present in the burner geometry). Therefore, the burner geometry simplified as a single pipe can be meshed with cfMesh without having such low quality elements.

The analysis of meshes for simplified burner geometry concludes that the cfMesh mesh has the high average quality as compared to COMSOL mesh. The mesh also performs better for the mesh sensitive variables. cfMesh also allows to control the local mesh refinement which proves to provide more accurate results in the region of interest. Therefore, despite the challenges posed by cfMesh, it proves to be a better meshing tool as compared to COMSOL for this thesis work.

5

TURBULENT FLOW MODELING

The combustion process is often the energy generation source in most of the industries. The combustion process is governed by the flow patterns inside the furnace. It is common practice to study the aerodynamics of the furnace before proceeding to modeling the combustion. The anode baking process consists of a combustion chamber in which heat required for the baking process is generated. The combustion of gaseous fuel i.e. methane occurs when it is mixed with air at ignition temperature. The mixing of the methane and air is controlled by the turbulent flow in the furnace. In this chapter, the turbulent flow modeling in the anode baking section is described. The description of the mixing pattern is dominated by the turbulence induced through obstacles such as baffles and tie-bricks. Due to the large number of such obstacles, the flow over the external surface is an important feature to be considered. The evaluation of the standard and realizable k-ϵ turbulence models for the anode baking furnace is carried out. The finite element solver of COMSOL Multiphysics software is used for the simulation of all the models. The mesh elements are of primary importance for the finite element modeling. In this chapter, the turbulent flow modeling with various meshing techniques are discussed for the anode baking section.

5.1. CROSS-FLOW MIXING OF FUEL-AIR JETS

The overall anode baking furnace modeling consists of various phases namely a gas phase on the flue side and a solid phase on the wall, anodes, and packing coke. In this chapter, the focus is only on the gas phase in the furnace. The flow in the heating section of an anode baking furnace is characterized by the air from the side inlets and fuel flow from the top inlets. The outlet is on the other side in the perpendicular direction to the fuel inlet as shown in Figure 5.1. The air and fuel interact in a cross-flow manner. Apart from providing structural strength, the tie-bricks also aids in the aerodynamics of the flow. The small openings at the top of the furnace are required to avoid the dead flow and the associated hot spots at the corners. The presence of baffles directs the flow

---

Parts of this chapter have been published in [91–93] in the U-shape providing maximum mixing of air and fuel and assure overall heating of the wall. Aluchemie furnaces have by-passes to avoid hot spots in the dead zones and thereby, ensuring safety in the furnace. The flue wall is symmetric and therefore, the half-flue model is developed defining symmetry at the XY plane.

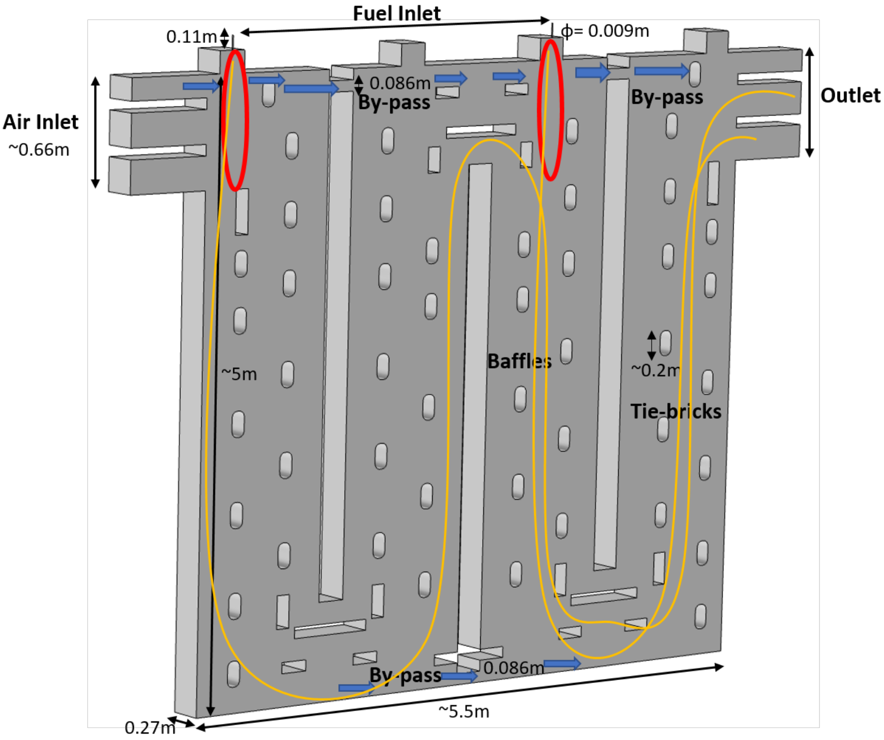

Figure 5.1: The geometry of the turbulent flow model of the heating section of anode baking furnace

The next important component following the understanding of the geometry and flow behaviour for developing a model is boundary condition. The baseline model is defined such that the boundary conditions are assumed from the existing conditions of the furnace. The Reynolds number at the fuel inlet and air inlet for the baseline model is around 13,000 and 8500, respectively. The Reynolds number is calculated based on Equation (5.1). The parameter values are mentioned in Tables 5.1 and 5.2. The diameter for the air and fuel inlets are mentioned in Figure 5.1. Table 5.1 provides the fuel inlet and air inlet boundary conditions. Due to the high velocity of the fuel, the jet is expected to penetrate deeper and provide higher turbulent mixing. The presence of tie-bricks generates backflow due to the adverse pressure gradient. The effects of the backflow are highly dependent on the velocity of the jet.

$$Re = \frac{\rho U_{ref} D_h}{\mu}. \tag{5.1}$$

Where, Re is the Reynolds number, U_{ref} is the reference velocity, D_h is the hydraulic diameter and μ is the dynamic viscosity.

Table 5.1: Inflow conditions at fuel and air inlets for the baseline model.

Property	Symbol	Air Inlet	Fuel Inlets	Initial Condition
Velocity [m/s]	U_{ref}	1.45	74	0
Temperature [K]	T	1050	300	300
Re [-]	Re	8500	13,000	-
Turbulent length scale [m]	L_T	0.01	0.01	-
Turbulent intensity [%]	I_T	0.05	0.05	-

The air and fuel streams are injected at different temperatures. The effect of temperature variations on the flow is considered by taking into account the variation of density with respect to the temperature. The representative values of the physical properties of the gas in the flue are as mentioned in Table 5.2. The ideal gas behaviour is assumed to compute the relation of density with pressure and temperature. The non-isothermal turbulent flow couples the turbulent flow module with the heat transfer in fluids module in such a way that the density for the flow dynamics is computed based on the updated temperatures of the heat transfer in fluids.

Table 5.2: Representative values of the physical properties of the gas.

Physical Property	Symbol	Values
Specific heat capacity [J/(kg×K)]	Cp	1004.5
Ratio of specific heats [-]	γ	1.4
Prandtl number [-]	Pr	0.73
Molecular viscosity [kg/(m×s)]	μ	1.8×10^{-5}

With the physical conditions established in this section, results of the non-isothermal turbulent flow models are analysed in the following sections.

5.1.1. TURBULENT BOUNDARY LAYER AND WALL TREATMENT

The computation of the turbulent flow field near the walls is complex. The region near walls is divided into four sub-regions depending on the relation of flow field with respect to the distance from the wall. The points that are in contact with the wall have zero velocity. In the next sub-region, the velocity is linearly proportional to the distance from the wall. This sub-region is known as the viscous sublayer since the viscous forces dominate in this region. In the next sub-region, the turbulent effects starts appearing. This region is known as buffer layer. In this region the turbulent forces starts to dominate over viscous forces. Finally, the fourth region is the fully turbulent dominated region in which the flow field is logarithmically proportional to the distance from the wall. This region is known as log-law region. In general, the buffer layer is significantly smaller than the log-law region. Moreover, resolving flow in this region requires extremely fine mesh closer to the walls. Therefore, in turbulent flow models such as k-ϵ model, the flow fields in these regions are approximated by considering the so called wall functions. Wall functions simplify the flow in this region by assuming analytical formulations.

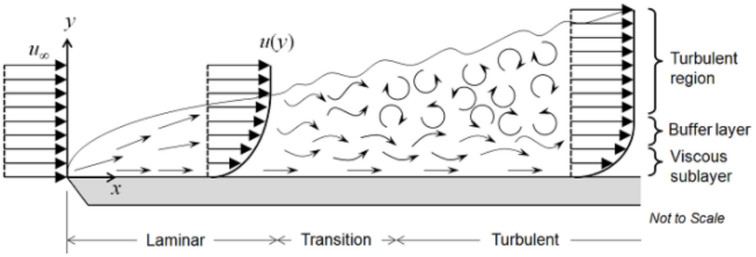

Figure 5.2: The schematic representation of different sub-regions in boundary layers. (Source: https://www.comsol.com/blogs/which-turbulence-model-should-choose-cfd-application/)

In the chapter Multi-physics evaluation (Chapter 2), the formulation of wall functions in COMSOL Multiphysics software is explained. In this software, a quantity ${\delta_w}^+$, wall lift-off viscous units is defined in such a way that the mesh is assumed to provide satisfactory results if the value of ${\delta_w}^+$ is close to 11.06. The appropriate boundary layers are added to the mesh in each case to have the ${\delta_w}^+$ value close to 11.06. Simplified 2D test cases are studied to analyse the effect of different turbulent flow models with and without adding boundary layers. Figure 5.3 shows the ${\delta_w}^+$ plot for the simplified 2D test case model with and without boundary layers [91]. It has been observed that the addition of boundary layers results in the ${\delta_w}^+$ being closer to 11.06. This suggests that in order to have satisfactory flow results near walls, the addition of boundary layers in the mesh is important.

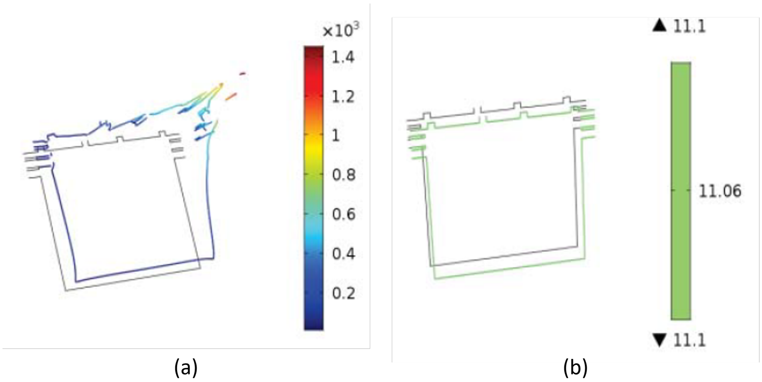

Figure 5.3: The wall lift off in viscous units plot $\delta_w{}^+$ for the 2D test case model (a) without boundary layer and (b) with boundary layers.

5.2. 3D SIMPLIFIED BURNER GEOMETRY MODEL

The meshing of the geometry with all the burner details is complex. Moreover, understanding the distribution of flow and temperature in the furnace geometry is equally important for an overall analysis of emissions. Therefore, the geometry of the burner is simplified to a simple pipe and a non-isothermal turbulent flow model of the furnace is developed. In this section, the results of the model with simplified burner geometry are discussed. Initially, the meshing of the geometry is carried out using the default meshing tool of COMSOL® Multiphysics software. It is difficult to affirm the adequacy of the mesh due to the complexity and the size of the furnace geometry. To surpass this difficulty, the approach taken in this work is to validate the results of primary meshes by comparing the results with another dedicated flow solver that generates a mesh with relative ease. The requirement of the improved mesh is realized with these results. Therefore, further improvement in the meshing with cfMesh meshing tool is carried out.

5.2.1. ANALYSIS OF FLOW DYNAMICS RESULTS WITH COMSOL MESHING TOOL

A 3D non-isothermal turbulent flow model is developed with three levels of refinement of the mesh generated by COMSOL® Multiphysics software. The details of the statistics of the meshes are given in Table 5.3. The mesh is finer near the fuel inlet pipe as compared to the bulk domain in all three cases. In this model the symmetry of the flue is not taken into account.

Table 5.3: Statistics of refinement levels of mesh implemented in 3D non-isothermal flow model.

Refinement level	**Number of elements**	**Average element quality**
Mesh Coarse (C)	850777	0.659
Mesh Medium (M)	1086068	0.662
Mesh Fine (F)	1400584	0.666

The temperature and velocity results are analysed with these three refinement levels on one horizontal line located near the fuel inlet on the XY center plane of the full flue model. Figure 5.4 (a) and (b) show the comparison of temperature and velocity on the above mentioned line for the different mesh levels. It can be observed from these comparisons that the maximum difference between the temperatures and velocities with the three refinements levels is approximately 42 K (difference of 5%) and 4 m/s (difference of 25%), respectively. The differences are significant mostly in the region where the fuel pipe is located. A consistent trend of decreasing temperature or increasing velocity is not observed while increasing the refinement level. This might be due to the inconsistent refinement factor in the bulk domain and the domain near fuel inlet. In other words, the factor with which the mesh is refined in the bulk domain is different from the refinement factor in the region of fuel pipe. The improvement in the mesh and consistency of refinement is needed. However, from an industrial perspective, these first results can be claimed to be satisfactory to progress towards a more developed mesh for the model.

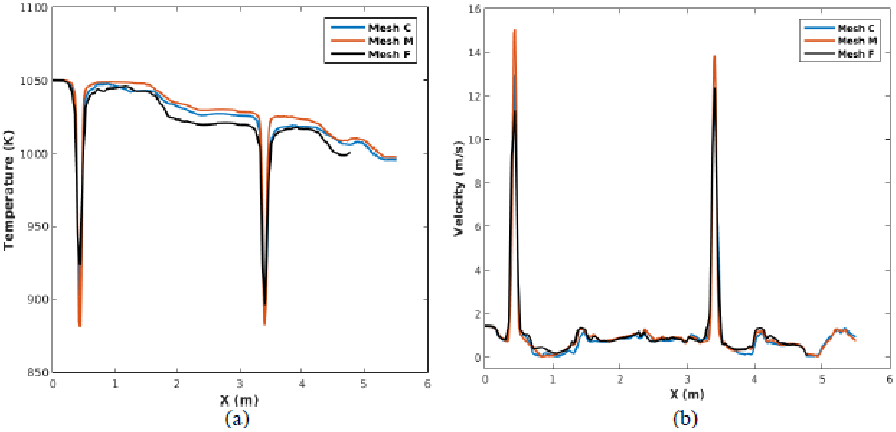

(a)

(b)

Figure 5.4: (a) Comparison of temperature [K] on line Y=4.55m of XY center plane for three mesh refinement levels (b) Comparison of velocity [m/s] on line Y=4.55m of XY center plane for three mesh refinement levels.

The results obtained by COMSOL® Multiphysics are compared with another simulation environment to validate the results. The numerical simulation results for the 3D non-reactive turbulent flow model with the given boundary conditions are provided by PM2ENGINEERING with their IB-Raptor code. The solver of the code is based on a cell-centered finite volume discretization of the equations. The code utilizes the IB-REX mesh generator which is based on immersed boundary conditions [94]. The implementation of the immersed boundary method results in a consistent Cartesian mesh as shown later in Figure 5.9. Figure 5.5 shows the comparison of temperature on the XY center plane simulated by the IB-Raptor code and COMSOL® Multiphysics. The preliminary observation shows that the temperature distribution in the bulk domain is comparable. For a precise comparison, the temperatures on the horizontal line (Y=4.5) is plotted as a function of geometrical coordinates. It can be observed from Figure 5.6 that the temperature estimated by COMSOL® Multiphysics is approximately 9% higher as compared to the IB-Raptor code at the X coordinate where the burner pipe is located.

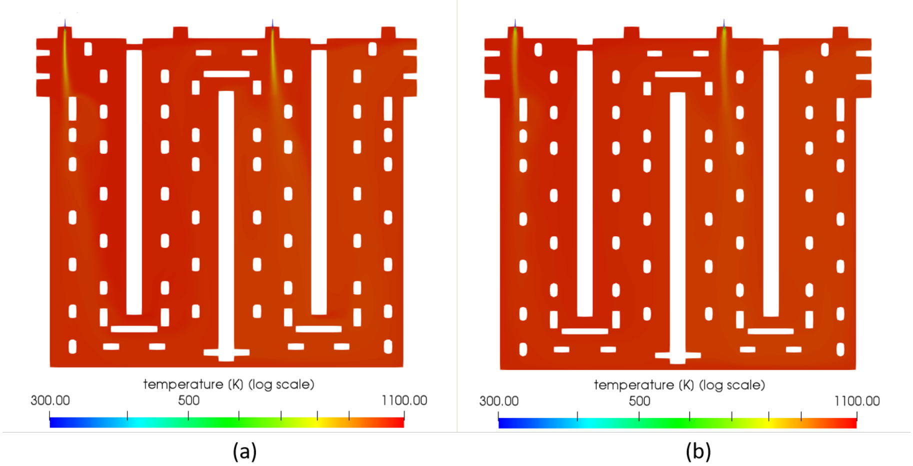

Figure 5.5: Color plot of the temperature distribution [K] obtained on XY center plane by (a) IB-Raptor code (b) COMSOL® Multiphysics

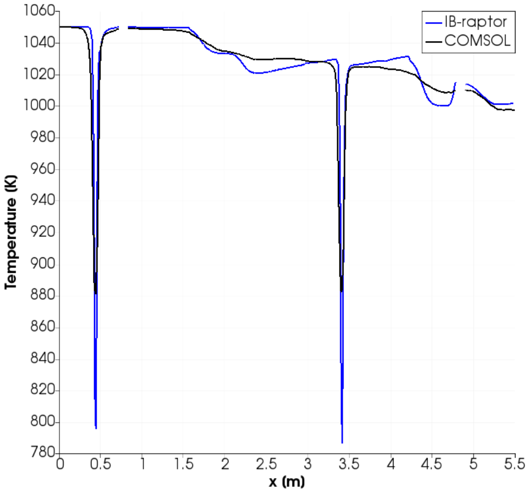

Figure 5.6: Plot of the temperature distribution [K] obtained on XY center plane by (a) IB-Raptor code (b) COMSOL® Multiphysics

The density of the gas is modeled by employing the equation of state, i.e., the density is defined as a function of temperature. Therefore, the differences observed in Figure 5.6, between the temperatures calculated by the two codes are translated into the density as well. The density near the jet location is observed to be lower with COMSOL® Multiphysics as compared to the IB-Raptor code. The velocities depend on the density of the gas. Figure 5.7 shows a comparison of the velocity magnitude with COMSOL® Multiphysics and IB-Raptor code. The spreading of the jet is observed with COMSOL® Multiphysics near the outlet of the fuel pipe as opposed to the IB-Raptor code. A slight difference in the penetration of the jet in the furnace is also observed. The occurrence of low-velocity zones is observed with both codes. However, the position of these zones does not overlap completely. Similar to the temperature, velocities are also compared on the same line for more accurate comparison (Figure 5.8). It can be observed that the peak velocity near the location of fuel pipe obtained by COMSOL® Multiphysics differs by a magnitude of 3-4 m/s as compared to IB-Raptor code. The differences observed in the bulk domain are comparatively less significant.

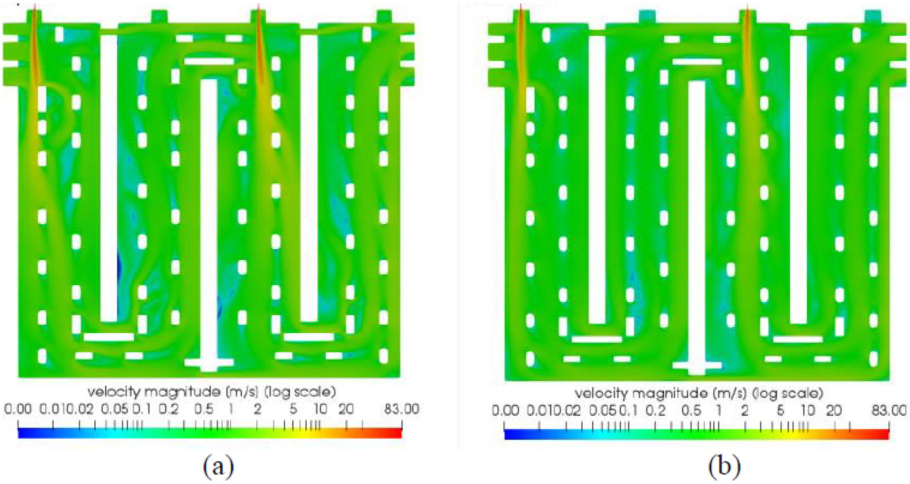

(a) (b)

Figure 5.7: The Color plot of velocity distribution [m/s] obtained on XY center plane by (a) IB-Raptor code (b) COMSOL® Multiphysics

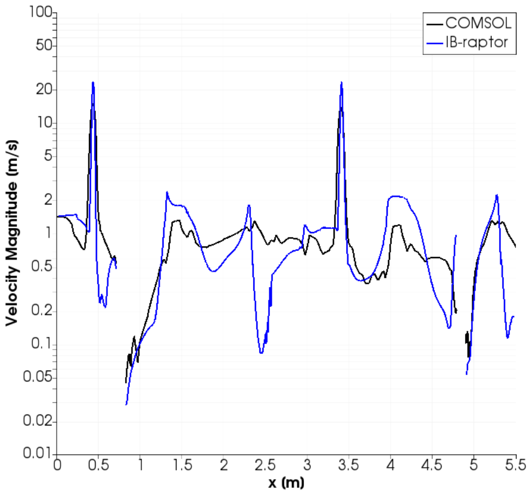

Figure 5.8: The Color plot of velocity distribution [m/s] obtained on XY center plane by (a) IB-Raptor code (b) COMSOL® Multiphysics

The differences in the numerical results generated by the COMSOL® Multiphysics and IB-Raptor code are within 10-15% for the variables such as temperature and velocity near the fuel inlet pipe. Note that these differences are lower in the bulk flow region and the flow patterns observed by the two codes are comparable. These differences in the numerical results can be attributed to the dissimilarities in the discretization, type of solvers and wall treatments to some extent. However, a detailed analysis shows that the disparity in the size and structure of the mesh has a major influence on the differences in the results.

Figure 5.9 shows the differences in the mesh implemented by COMSOL® Multiphysics and IB-Raptor code near the location of fuel pipe. The mesh in the COMSOL® Multiphysics numerical model is tetrahedral whereas, the mesh in the model of IB-Raptor code is Cartesian. The Cartesian mesh is numerically less dissipative than a tetrahedral mesh with analogous characteristics. Moreover, the Cartesian mesh is more consistently refined in the region near the fuel inlet as compared to tetrahedral mesh. The boundary layer mesh in the XZ section of COMSOL® Multiphysics is finer as compared to the bulk region. Whereas, in IB-Raptor code, the difference in the refinement of the bulk region and boundary layers is negligible in XZ plane (Figure 5.9 (b)). The mesh sensitivity study described in the first subsection of the 3D non-reactive flow results shows a non-uniformity in the refinement while moving from coarser to finer mesh. In the case of IB-Raptor code the refinement while moving from coarser to finer mesh is more consistent. In summary, to have a closer comparison of both codes, the uniformity in the mesh refinement of the two models is required.

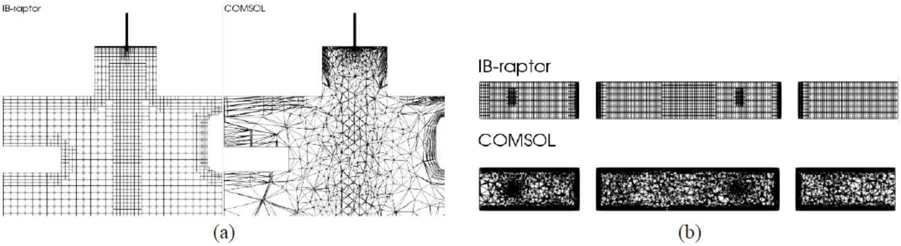

(a) (b)

Figure 5.9: (a) Comparison of mesh near fuel inlet on XY center plane with IB-Raptor code and COMSOL® Multiphysics (b) Comparison of mesh on XZ plane near fuel inlet with IB-Raptor code and COMSOL® Multiphysics

INCONSISTENCY IN THE RESULTS WITH COMSOL MESH

In the above section the comparison of velocity and temperature for the two models simulated in COMSOL® Multiphysics software and IB Raptor code is studied. The results seem to compare well for these properties. In this section, a further analysis of the comparison of turbulent kinetic energy and turbulent dissipation rate for the two models is carried out. Figure 5.10 and 5.11 show the comparison at the XY center plane with IB Raptor and COMSOL model for turbulent kinetic energy and turbulent dissipation rate, respectively. It can be observed that for both variables, the results calculated by COMSOL® Multiphysics software are not physical. The turbulent kinetic energy at the fuel injection should be higher at the fuel outlet. This is observed in the results of IB Raptor code but not with the COMSOL® Multiphysics software. The inconsistency in the results is observed for the finer mesh as well. The nonphysical results might be due to the unstructured meshing carried out by default meshing tool of COMSOL® Multiphysics software. The turbulent kinetic energy and dissipation rate are sensitive to a mesh as compared to velocity and temperature. This leads to a significant difference in the results for the turbulent kinetic energy and dissipation rate.

The difference in results motivates to opt for the better meshing tools in COMSOL® Multiphysics software model. In the following section, results of the new meshing technique with cfMesh software are discussed. Later, it is seen that to obtain comparable results with COMSOL meshing tool, the number of elements required are approximately 8 times higher than cfMesh software.

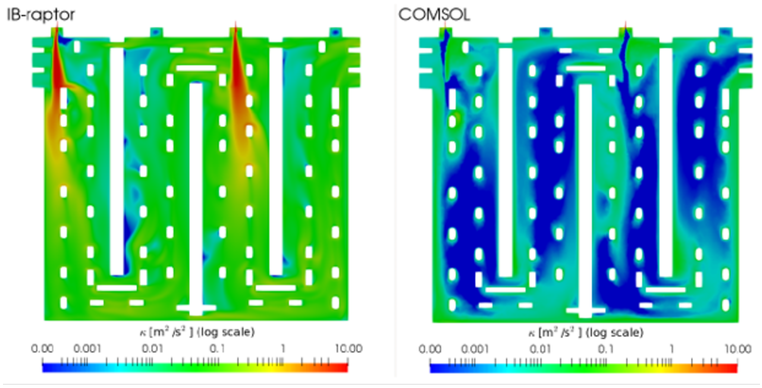

(a) (b)

Figure 5.10: The color plot of turbulent kinetic energy $[m^2/s^2]$ at XY center plane with (a) IB Raptor code and (b) COMSOL® Multiphysics software

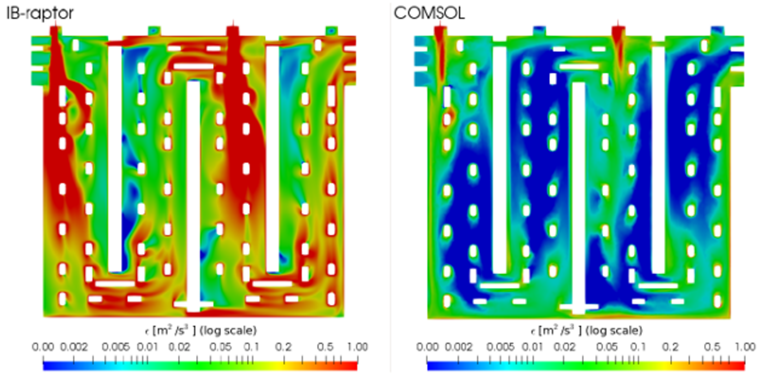

(a) (b)

Figure 5.11: The color plot of turbulent dissipation rate $[m^2/s^3]$ at XY center plane with (a) IB Raptor code and (b) COMSOL® Multiphysics software

5.2.2. ANALYSIS OF FLOW DYNAMICS RESULTS WITH CFMESH MESHING TOOL

In this section, results of the flow modelling in the heating section of the anode baking furnace with cfMesh meshing tool are discussed. As compared to the previous section, the geometry is modified in such a way that the symmetry of the flue model is taken into account. In the first part of the section, the results of the 'Baseline model' with Mesh 1 (elaborated in Chapter 4) are presented. Further, the non-isothermal results with the standard k-ϵ model are compared for two meshing types namely with cfmesh (Mesh 1) and the COMSOL default mesher (Mesh 2) (elaborated in Chapter 4). The mesh prepared by the COMSOL default mesher in this case is finer than the one studied in the previous section. Here, the COMSOL mesh (Mesh 2) is improved by considering the size of elements compatible with the mesh generated by the cfMesh software. The NOx formation is typically in the region of jet development which is the region of interest for this work. Therefore, the sensitivity of refinement in the region of jet development is studied by comparing Mesh 1 and Mesh 3. The geometry and meshes for all these models are described in the previous chapter.

BASELINE MODEL WITH MESH 1

The models are systematically developed by solving isothermal air flow (step 1) at first instance. The solution is used as the initial condition for the model in which fuel is added starting from low velocity to high (step 2). The isothermal model is used as an initial guess for the further non-isothermal flow model (step 3). As a next step, the artificial stabilization parameter is removed (step 4) to improve accuracy of the results. The Intel(R) Xeon(R) Gold 6152 CPU with 22 cores is used to simulate the models. The approximate CPU time required for the simulations of standard k-ϵ model is provided in Table 5.4. To summerize, each line from Table 5.4 generates the initial guess for the next line.

Table 5.4: CPU time required for the simulation steps for baseline model with Mesh 1.

Simulation Step	**CPU Time**	**Newton Iterations**	**GMRES Iterations (v,p)**	**GMRES Iterations (k,ϵ)**
step 1	1 h 35 min	22	478	1674
step 2	2 h 11 min	25	479	1812
step 3	1 h 6 min	48	222	710
step 4	2 h 33 min	121	1027	699

The non-isothermal results of the baseline model with Mesh 1 are presented in Figure 5.13. As explained earlier, the $\delta_w{}^+$ values provide estimate of the refinement at the boundary layers. Figure 5.12 shows the $\delta_w{}^+$ plot for the baseline model. As can be seen from the figure, the $\delta_w{}^+$ values for the model range from 11.1 to 93. However, the $\delta_w{}^+$ values are close to 11.06 in most of the region.

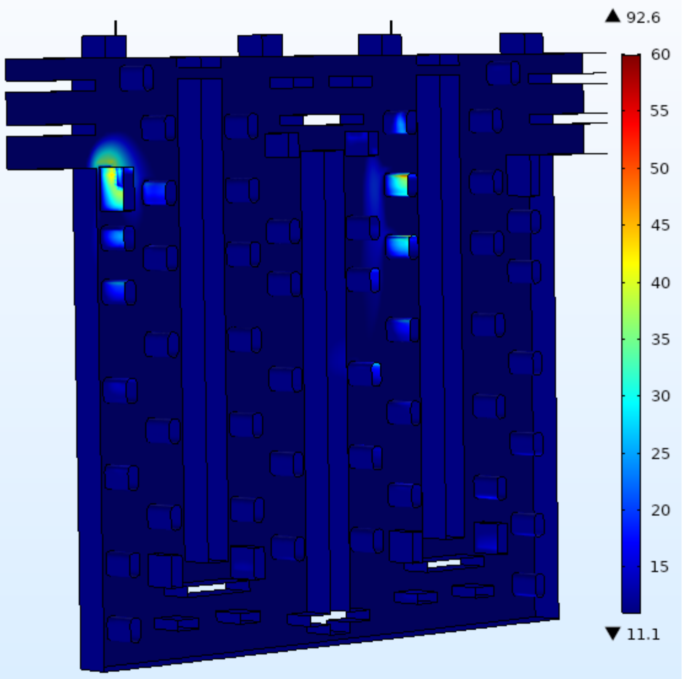

Figure 5.12: The wall lift off in viscous units plot $\delta_w{}^+$ for the baseline model

The baseline model is judged on the basis of the qualitative behaviour of the expected solution. The solution of this model for velocity, turbulent viscosity ratio, and temperature are as shown in Figure 5.13 (a–c) respectively, aligns with the expected physical behaviour. The baseline model serves as the reference for the analysis of the other meshes studied in this work.

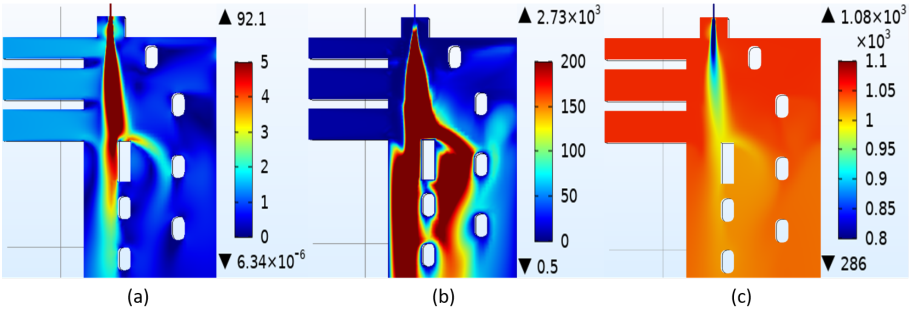

Figure 5.13: The color plots of (a) velocity (b) turbulent viscosity ratio and (c) temperature at the symmetry plane of baseline model with Mesh 1

The non-isothermal model is solved by segregating physics in three different groups. The convergence behaviour of the three segregated groups is as shown in Figure 5.14.

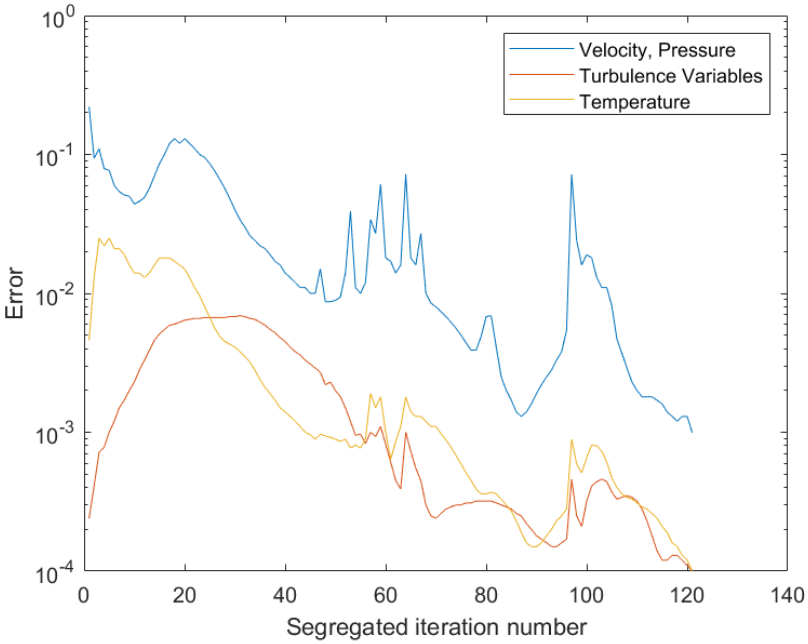

Figure 5.14: The convergence plot for the three segregated groups of different physics for baseline model with Mesh 1. The convergence is plotted for the last step from Table 5.4

NON-ISOTHERMAL EFFECT ON BASELINE MODEL WITH MESH 1

The non-isothermal effect on the velocity and the turbulent viscosity ratio is shown in Figure 5.15. Due to the varying density, the jet has penetrated further in the furnace. The temperature coupling steadily increases the temperature of the jet reducing the density. This results in the deeper penetration of the jet. The effect of the obstacle by the tie brick is more significant and changes the flow dynamics in the furnace for the coupled equations. Therefore, while studying aerodynamics in the anode baking furnace, it is important to consider the non-isothermal flow model.

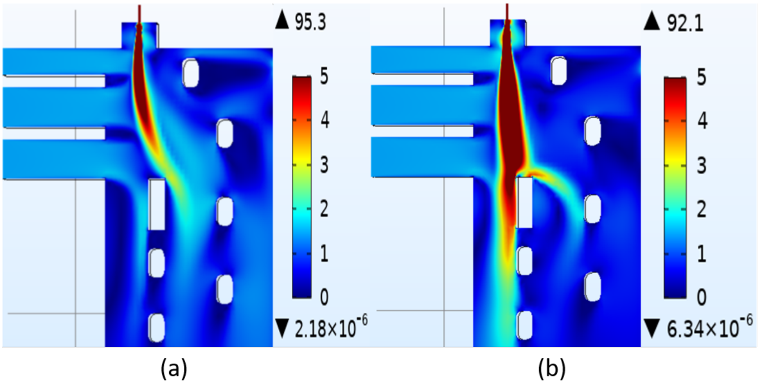

(a) (b)

Figure 5.15: The color plots of the velocity magnitude [m/s] at the symmetry plane for a) uncoupled and b) coupled flow and energy equations for baseline model with Mesh 1

COMPARISON OF MESH 1 AND MESH 2

In the previous section, the results with the relatively coarser meshing carried out by COMSOL are discussed. Due to the physically unrealistic computation of turbulent viscosity ratio with the COMSOL mesh, the alternate meshing tool, cfmesh, is considered for the study. After confirming the precise turbulent viscosity ratio with this meshing tool, the mesh with comparable element sizes is prepared with the default mesher from COMSOL. The details of these meshes are discussed in the earlier chapter (Figure 4.10) on Mesh. The comparison of the velocity with the two meshing techniques, namely, by COMSOL (Mesh 2) and cfmesh (Mesh 1) are provided in Figure 5.16 (a) and (b), respectively. It can be observed that a comparable velocity magnitude is obtained with the cfmesh and COMSOL mesh. However, it should be noted that the number of elements required to obtain such comparable results with COMSOL are approximately 8 times larger as compared to cfmesh.

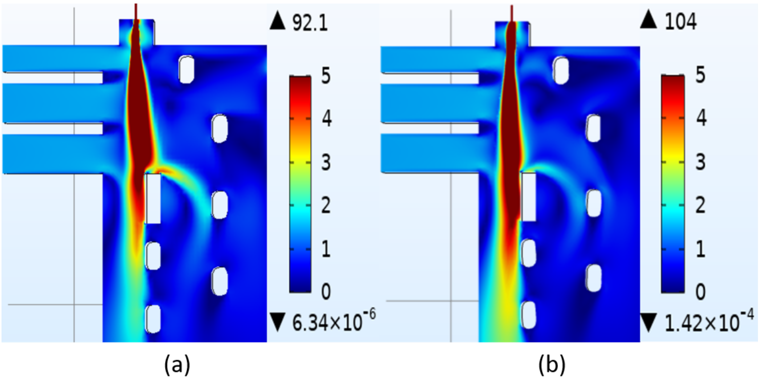

(a) (b)

Figure 5.16: The color plots of the velocity magnitude [m/s] at the symmetry plane generated by a) cfmesh (Mesh 1) and b) COMSOL mesh (Mesh 2)

The temperature comparison for both meshes, Mesh 1 and Mesh 2 is similar to the velocity comparison. It follows the pattern of flow dynamics. There is no significant difference between the temperature distribution obtained by the two meshes. This suggests the temperature in the furnace is highly dependent on the flow dynamics.

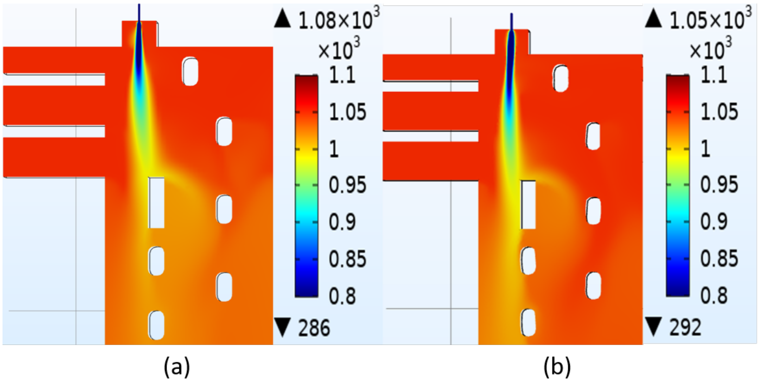

Figure 5.17: The color plots of the temperature [K] at the symmetry plane generated by a) cfmesh (Mesh 1) and b) COMSOL mesh (Mesh 2)

Further comparison of the turbulent viscosity ratio with the two meshing techniques is as shown in Figure 5.18 (a) and (b), respectively. It is important to analyse the turbulent quantities since the combustion modelling that follows from the turbulent flow modelling depends on the turbulence parameters. It can be observed that the turbulent viscosity ratio immediately near the fuel outlet is lower with the COMSOL mesh as compared to cfmesh. Moreover, the turbulent viscosity ratio starts dissipating with the COMSOL mesh. Both observations can be attributed to the higher numerical diffusion with the COMSOL mesh. Due to the dissipation with the COMSOL mesh, the flow dynamics in the downstream such as near the obstacle of the tie-brick are affected. Since, the NOx formation is restricted to this region, the changes in the flow dynamics are translated to thermal NOx formation phenomena as well.

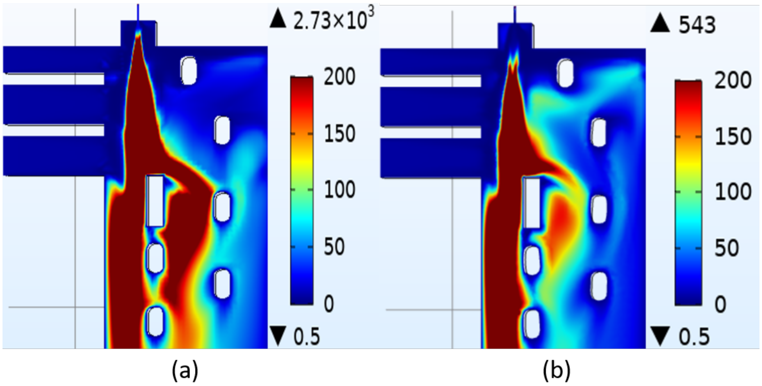

Figure 5.18: The color plots of the turbulent viscosity ratio at the symmetry plane generated by a) cfmesh (Mesh 1) and b) COMSOL mesh (Mesh 2)

COMPARISON OF MESH 1 AND MESH 3

The idea of local mesh refinement in the region of interest is well known. For the large models such as the industrial furnaces, it is important to identify the region which is sensitive to the flow dynamics. In the present study, such region lies beneath the fuel inlet. Therefore, in this section the sensitivity of the results on the local refinement in the region of jet development is studied. Two meshes with varying local refinement (Mesh 2 and Mesh 3) are generated by cfmesh software. The representation and description of these meshes is given in the Chapter 4 (Figure 4.12). The comparison of velocity magnitude and temperature with both meshes shows that the results do not differ significantly (Figure 5.19 and Figure 5.20). The width of the jet is slightly higher for Mesh 3 as compared to Mesh 2. This is due to the higher numerical diffusion introduced by Mesh 3.

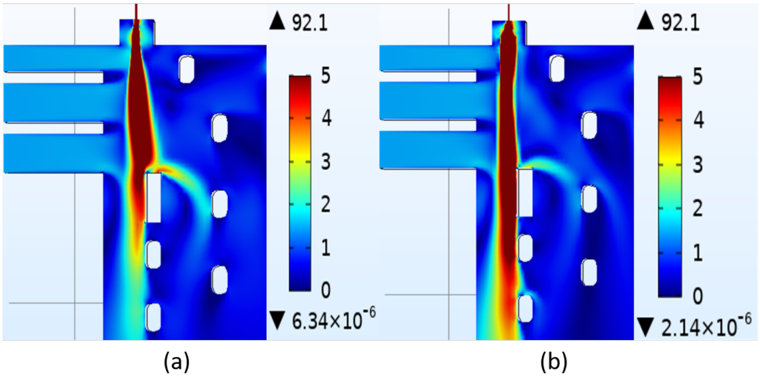

Figure 5.19: The color plots of the velocity magnitude [m/s] at the symmetry plane generated by cfmesh software a) with jet refinement (Mesh 1) and b) without jet refinement (Mesh 3)

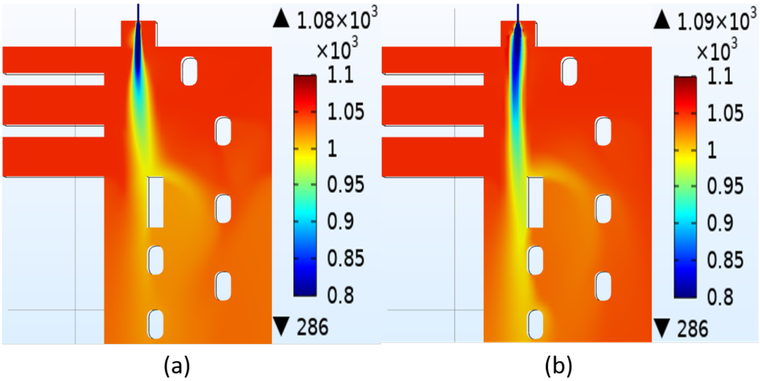

Figure 5.20: The color plots of the temperature [K] at the symmetry plane generated by cfmesh software a) with jet refinement (Mesh 1) and b) without jet refinement (Mesh 3)

However, the effect of such local refinement is prominent on the turbulent viscosity ratio as shown in Figure 5.21. For the mesh that does not have local refinement has lower turbulent viscosity ratio immediately near the fuel inlet as compared to the one with local refinement. The effect of turbulence are better captured with locally refined mesh. Therefore, the higher numerical diffusion for the mesh without local refinement has a major effect on the turbulent viscosity ratio. Studying such effects near the burner is important since this is the region where NOx is generated.

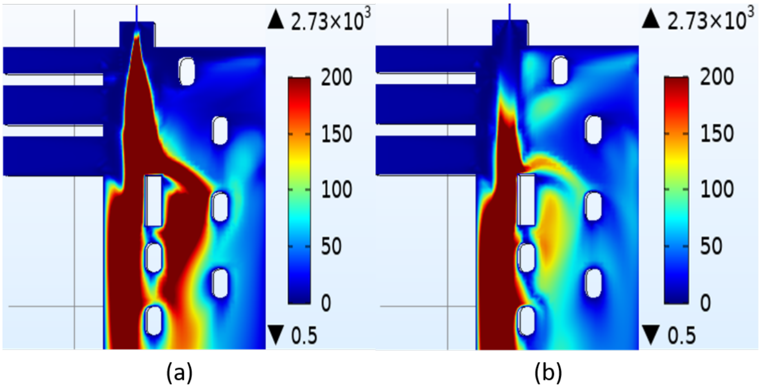

Figure 5.21: The color plots of the turbulent viscosity ratio at the symmetry plane generated with the mesh of cfmesh software a) with jet refinement (Mesh 1) and b) without jet refinement (Mesh 3)

EFFECT OF VARIATION OF FUEL VELOCITY

In an earlier section, the sensitivity of the flow dynamics in the furnace to the meshing structure and technique is elaborated. The results obtained by Mesh 1 are accurate as compared to Mesh 2 and Mesh 3. The flow dynamics in the furnace further depends on the mixing of the two streams namely, air and fuel. Due to the small magnitude of the air velocity, the flow dynamics depends highly on the velocity of the fuel injection.

Therefore, further analysis is carried out to understand the effect of increasing the fuel jet velocity.

Figure 5.22 shows the velocity magnitude at XY symmetry plane for increasing fuel jet velocity. It can be observed that with increasing velocity, the fuel jet penetrates deeper in the furnace. The jet at burner one is split due to the obstacle. This leads to a shorter jet at burner one as compared to burner two. Further comparison of the turbulent viscosity ratio for the increasing velocity shows the increasing turbulent behaviour as can be observed in Figure 5.23. The difference in the flow dynamics for the varying fuel jet velocity has an impact on the combustion in the furnace. The combustion further affects the NOx generation in the furnace. The effect of the higher turbulent viscosity ratio for higher velocity of fuel injection on NOx generation will be discussed in the following chapters.

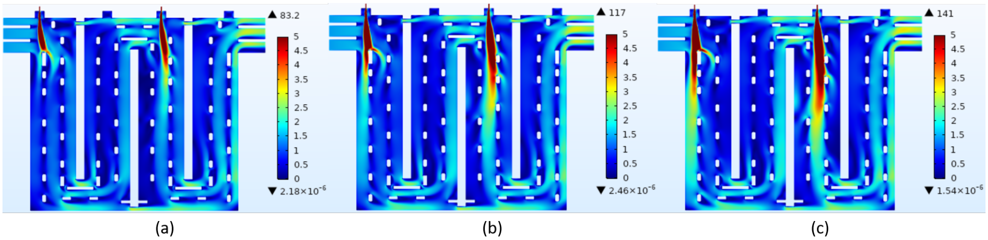

(a) (b) (c)

Figure 5.22: The color plots of the velocity magnitude [m/s] at the symmetry plane generated with the mesh of cfmesh software for fuel jet velocity of a) 50 m/s b) 74 m/s and (c) 90 m/s. The fuel pipe diameter is 9 mm for all three models.

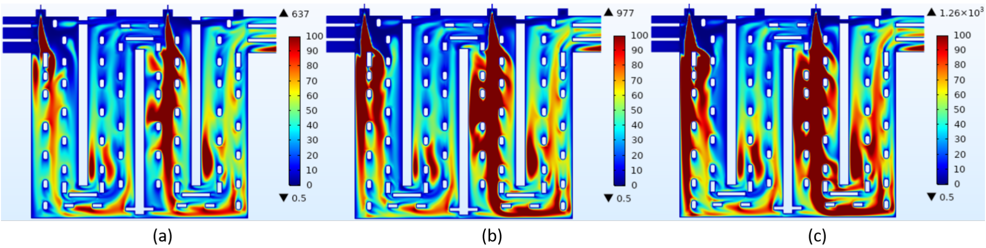

(a) (b) (c)

Figure 5.23: The color plots of the viscosity ratio at the symmetry plane generated with the mesh of cfmesh software for fuel jet velocity of a) 50 m/s b) 74 m/s and (c) 90 m/s. The fuel pipe diameter is 9 mm for all three models.

EFFECT OF INCREASING THE FUEL PIPE DIAMETER

In the earlier section, the effect of increasing the fuel inlet velocity is discussed. The mass flow rate of fuel increases with increasing the fuel inlet velocity. This leads to different air-fuel ratio in the furnace and therefore, has effect on the combustion. The mass flow rate of fuel can be kept constant while varying the fuel inlet velocity by changing the fuel pipe diameter. In this section, the effect of increasing the fuel pipe diameter on the flow dynamics is studied.

The comparison of the velocity magnitude at the XY symmetry plane for 9 mm and 13 mm diameter is carried out in Figure 5.24. The velocity for the 13 mm diameter fuel pipe model are decided based on the equivalent fuel mass flow rate from 9 mm diameter. Table 5.5 shows the values of velocities for the two fuel pipe diameters that yields equal mass flow rate of fuel injected in the furnace. As can be expected, for the larger diameter of fuel pipe, the injected fuel inlet velocity is lower. This further affects the flow dynamics in the furnace. Due to the smaller velocity for 13 mm fuel pipe diameter, the jet is shorter as compared to the 9 mm fuel pipe diameter. The further comparison of the turbulent viscosity ratio from Figure 5.25 shows that the turbulent viscosity ratio is higher for 9 mm diameter downstream of the jet for both burners. The higher turbulent viscosity ratio suggests higher mixing of two streams with 9 mm diameter. The effect of mixing on the combustion is explained in the following chapters.

Table 5.5: Values of fuel pipe diameters and velocities that have equivalent mass flow rate

Fuel mass flow rate [kg/s]	**Fuel pipe diameter [mm]**	**Fuel inlet velocity [m/s]**
0.0030	9	74
	13	35

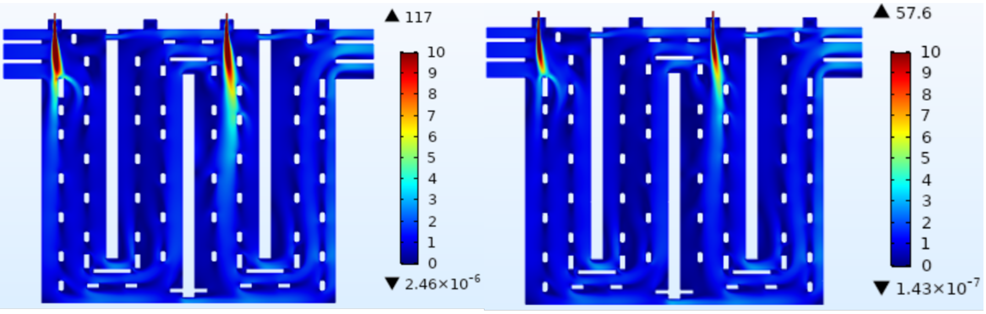

(a) (b)

Figure 5.24: Velocity magnitude [m/s] comparison at the symmetry plane with the fuel pipe diameter of (a) 9 mm and (b) 13 mm for fuel mass flow rate of 0.003 kg/s. The jet has penetrated deeper for the 9 mm fuel pipe diameter due to higher momentum.

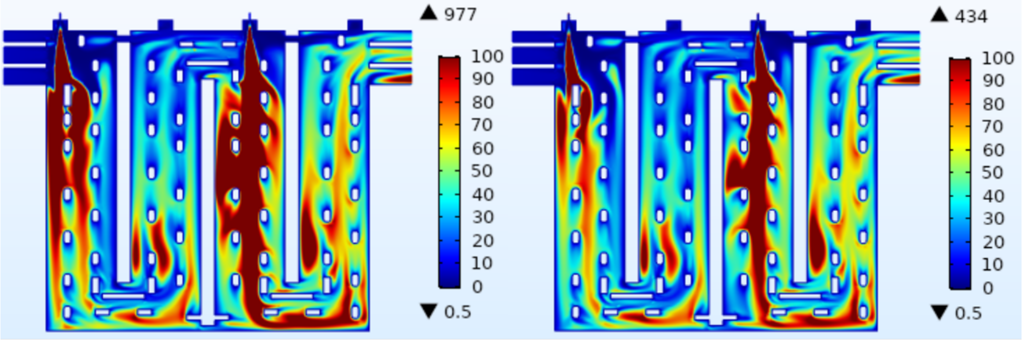

(a) (b)

Figure 5.25: Comparison of the turbulent viscosity ratio at the symmetry plane with the fuel pipe diameter of (a) 9 mm and (b) 13 mm for fuel mass flow rate of 0.003 kg/s. Higher turbulence is observed for the 9 mm fuel pipe diameter due to higher velocity magnitude.

5.2.3. REALIZABLE K-ϵ MODEL

The realizable k-ϵ model is the improved model of standard k-ϵ model in which the dependence of mean flow distortion on turbulent dissipation is accounted. The realizable k-ϵ model is known to provide well quantified results for the confined jets as compared to the standard k-ϵ model [95]. The predicted jet is expected to be less diffusive with the realizable model as compared to standard k-ϵ model. Moreover, Shih et. al. proposes that the new dissipation equation for the realizable model increases the numerical stability of the turbulent flow computations [96]. However, in the present study, the difficulties are observed for the convergence with the realizable k-ϵ model for a complex geometry such as anode baking furnace. The baseline model with Mesh 1 explained in the previous section fails to converge for the realizable k-ϵ model. In case of realizable k-ϵ model, more constraints are introduced which create instabilities for the mesh of the baseline model. There are several studies carried out to analyse these constraints which would provide techniques to achieve convergence with realizable k-ϵ model.

EFFECT OF NUMERICAL DIFFUSION

Convergence with the realizable k-ϵ model is obtained on the coarser meshes prepared by the COMSOL default mesher. In the earlier section, the results of this converged model are discussed. The results of this model compares well with IB-Raptor code for variables such as velocity and temperature. However, the turbulent properties are not correctly resolved on the mesh obtained by COMSOL default mesher. This suggest that the mesh prepared by the COMSOL mesher leads to more numerical diffusion. The larger numerical diffusion introduced by the mesh aids in convergence for this case. The effect of higher diffusion is tested by introducing artificial isotropic diffusion. COMSOL Multiphysics applies consistent and inconsistent stabilization techniques. The inconsistent stabilization technique introduces isotropic artificial diffusion to the equation. If the flow is convection dominated i.e. for the higher Peclet number, the numerical problem may become unstable. Isotropic diffusion in such respect may be used as a stabilization technique. The extent of the isotropic diffusion can be controlled by the stabilization parameter which ranges from 0 to 1. The stabilization parameter, that controls the extent of the artificial diffusion is varied and the effect on the convergence behavior is analysed. The addition of artificial diffusion results in convergence with realizable k-ϵ model with mesh for the baseline model which is prepared using cfMesh software. The equations governing the isotropic diffusion are presented by Equation 5.2 to 5.4.

Suppose Equation 5.2 is considered such as the flow is convection dominated.

$$\frac{\partial u}{\partial t} + \beta \cdot \nabla u = \nabla \cdot (c \nabla u) + F \tag{5.2}$$

The isotropic diffusion stabilization method adds an additional artificial diffusion given by Equation 5.3.

$$c_{\text{art}} = \delta_{\text{id}} h ||\beta|| \tag{5.3}$$

Equation 5.2 changes to Equation 5.4 after addition of diffusion coefficient.

$$\frac{\partial u}{\partial t} + \beta \cdot \nabla u = \nabla \cdot ((c + c_{\text{art}}) \nabla u) + F \tag{5.4}$$

Figure 5.26 shows the convergence plots with varying stabilization parameter δ_{id}. As the value of stabilization parameter decreases, the artificially added diffusion also decreases. As can be observed from Figure 5.26, this leads to difficulties in the convergence. For the $\delta_{\text{id}} = 0.2$, the convergence is achieved earlier than with the $\delta_{\text{id}} = 0.1$. Further decrease to $\delta_{\text{id}} = 0.05$ results in divergence.

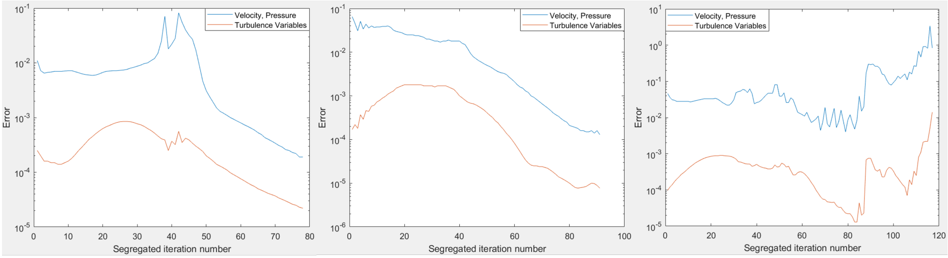

(a) (b) (c)

Figure 5.26: Convergence plots of incompressible flow model for varying stabilization parameters (a) $\delta_{\text{id}} = 0.2$, (b) $\delta_{\text{id}} = 0.1$, and (c) $\delta_{\text{id}} = 0.05$.

Figure 5.27 shows the turbulent viscosity ratio of realizable k-ϵ model with artificial diffusion and standard k-ϵ model without such diffusion. The analysis of converged results of realizable k-ϵ model shows that the model is more diffusive as compared to the standard k-ϵ model. Therefore, though the convergence is obtained with artificial diffusion, the realizable k-ϵ model does not provide the expected improved results compared to standard k-ϵ model.

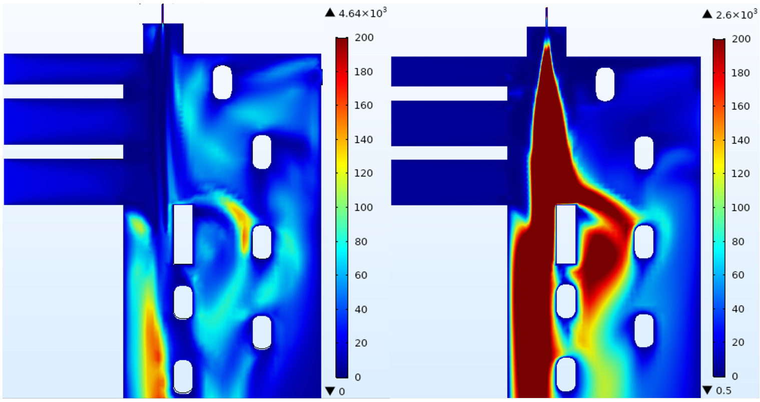

(a) (b)

Figure 5.27: Turbulent viscosity ratio at the XY symmetry plane with (a) realizable k-ϵ model ($\delta_{\mathrm{id}} = 0.1$) and (b) standard k-$\epsilon$ model.

Tuning equations to standard k-ϵ model

The standard k-ϵ model converges for the baseline model with mesh prepared by the cfMesh software. The difficulties occur when the realizable k-ϵ model is implemented. The two main differences between the standard and realizable k-ϵ models are the definition of C_μ and the production-destruction terms of the turbulent dissipation rate equation. These terms of the realizable k-ϵ model are modified such that they are similar to the standard k-ϵ model. The tests are carried out on the incompressible turbulent flow for simplification. The turbulent dissipation rate equation is modified as shown by Equation 5.5.

$$\rho(\mathbf{u}\cdot\nabla)\epsilon = \nabla\cdot\left[\left(\mu+\frac{\mu_t}{\sigma_\epsilon}\right)\nabla\epsilon\right] + C_1\rho S\epsilon - C_{\epsilon 2}\frac{\rho\epsilon^2}{k+\mathrm{Para1}\times\sqrt{\nu\epsilon}} \tag{5.5}$$

Where,

$$\mu_t = \rho C_\mu \frac{k^2}{\epsilon} \tag{5.6}$$

The equation for C_μ is modified as shown in Equation 5.7.

$$C_\mu = \frac{1}{A_0 + \mathrm{Para2}\times A_s U^{(*)}\frac{k}{\epsilon}} \tag{5.7}$$

When the values of parameters ‘Para1’ and ‘Para2’ are zero, the terms are equivalent to standard k-ϵ model with value of A_0 equal to inverse of the widely used value of 0.09 of C_μ. Figure 5.28 shows the convergence plots with varying value of these parameters. It can be observed that as the value of parameter approaches to 1 (for value of 0.7), the difficulties in the convergence starts occurring. For values close to 0, the model equations are similar to standard k-ϵ model and therefore, introduces higher diffusivity which facilitates the convergence.

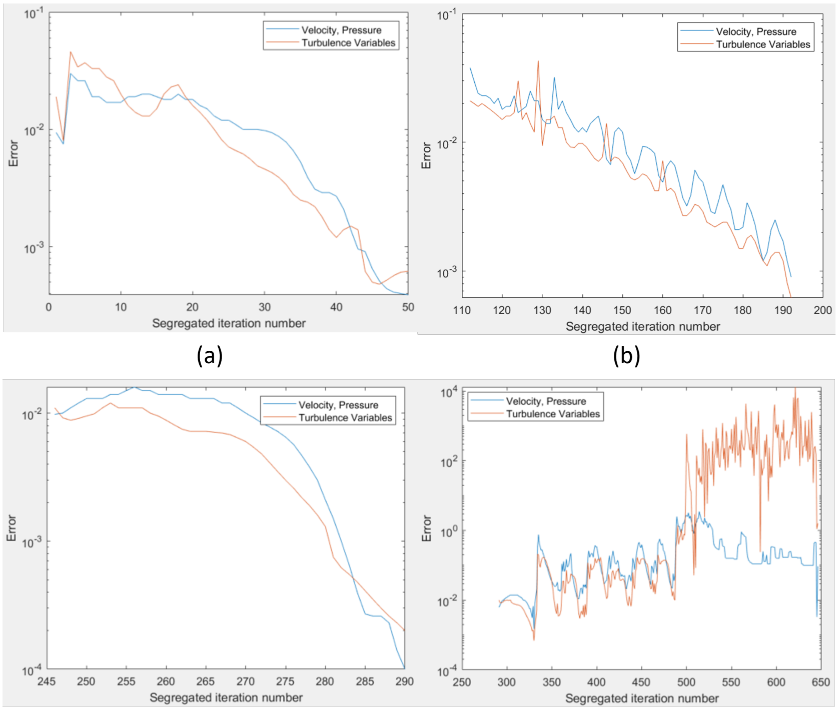

(a) (b)

(c) (d)

Figure 5.28: Convergence plots of incompressible turbulent flow with modified realizable k-ϵ model with varying parameters (a) Para1=0.0, Para2=0.0 (b) Para1=0.3, Para2=0.3 (c) Para1=0.6, Para2=0.6 and (d) Para1=0.7, Para2=0.7.

The parameters modify the values of C_μ. Figure 5.29 shows the surface plot of C_μ with varying parameters. For values of parameter equal to zero, the value of C_μ is constant corresponding to the value for standard k-ϵ model. As the values of the parameters increases, the value of C_μ starts depending on turbulent kinetic energy, k and, turbulent dissipation rate, ϵ. The value of C_μ and thus, turbulent viscosity is lower where the turbulent time scale (k/ϵ) is higher. As the dependence on the k/ϵ increases, the model becomes numerically unstable resulting in the divergence as shown in Figure 5.28 (d). Therefore, the corresponding surface plot of C_μ (Figure 5.29 (d)) shows undeveloped solution.

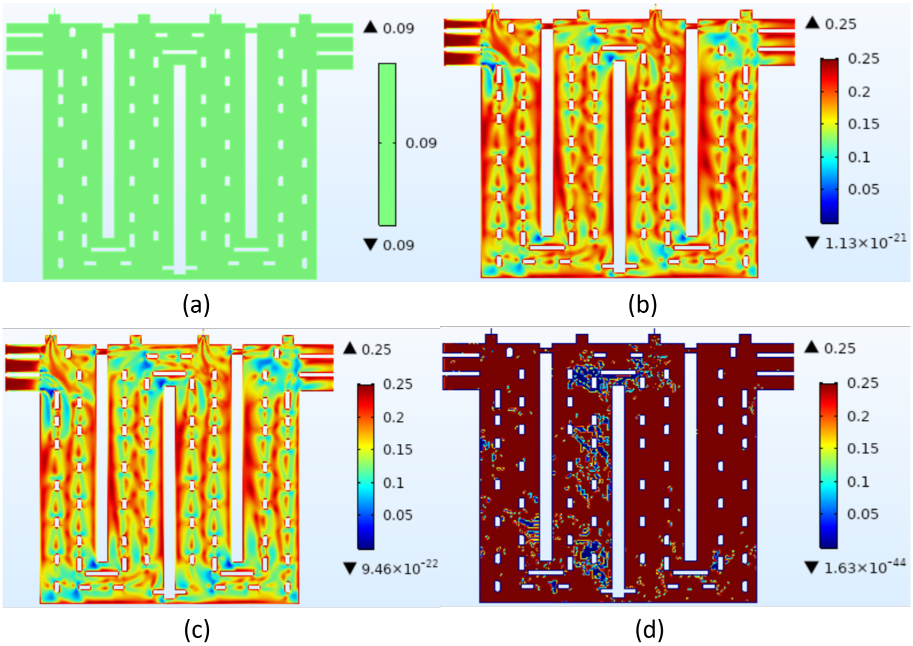

Figure 5.29: Surface plots of values of C_μ with modified realizable k-ϵ model with varying parameters (a) Para1=0.0, Para2=0.0 (b) Para1=0.3, Para2=0.3 (c) Para1=0.6, Para2=0.6 and (d) Para1=0.7, Para2=0.7.

EFFECT OF ACCURACY OF LINEAR SOLVER

The realizable k-ϵ model considers more constraints. With the increased constraints, the changes in the solver settings might be needed. The effect of the solver scheme on the non-convergence of the realizable k-ϵ model is elaborated in this section. The incompressible turbulent flow case is considered for simplification. The non-linear flow solver of COMSOL Multiphysics is described in the Chapter 3. One segregated step solves velocity and pressure whereas in the second segregated step, turbulent kinetic energy and turbulent dissipation rate are solved. The velocity and pressure are fully coupled in segregated step one. In the next stage, for each segregated step a non-linear solver is established. The convergence of the segregated solver is achieved when each non-linear segregated step is converged. Furthermore, for each non-linear segregated step, a damped Newton method is applied in which the solver assumes several linear steps. In order to understand the effect of the tolerance of the linear solver, a test case with simple rectangular channel is considered. The isothermal non-linear solver is ran for different tolerance of linear solver. Figure 5.30 shows the convergence behavior of the two segregated steps with different tolerance criteria of the linear solver. It can be observed that even with the more stringent tolerance criteria such as 10^{-14} of GMRES iterative linear solver, the convergence behavior is similar to more relaxed tolerance criteria of 10^{-2}. Moreover, the effect of direct linear solver on the convergence of the outer loop i.e. the non-linear solver is also similar to the GMRES iterative solver with algebraic multigrid as the preconditioner.

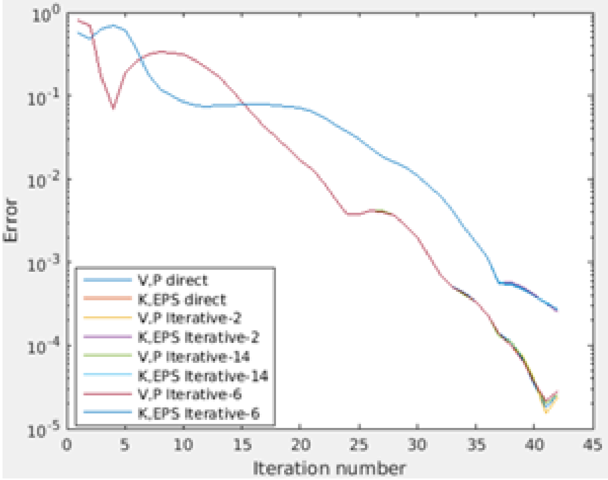

Figure 5.30: Convergence plots with varying tolerance of linear solvers for the isothermal turbulent flow test case.

EFFECT OF PSEUDO TIME STEPPING

As described in the earlier chapter (Chapter 3), the pseudo time stepping accelerates the convergence towards steady state by introducing a pseudo time step. The pseudo time step is related to the local CFL number and can be made more stringent with the PID regulator. If the flow has unsteadiness, the smaller pseudo time-step is expected to improve the convergence behavior of the steady-state solver. Since, one of the purposes of this section is to provide the possible solutions to the non-convergence problem in the realizable k- model, a case study to analyze the effect of pseudo time stepping parameter is provided. Table 5.6 shows the change in the parameters from the default settings to more stringent settings. Overall these parameters decrease the pseudo time step for each non-linear iteration.

Table 5.6: Stringent changes in the parameters of the PID controller

	Default values of parameters	**Stringent values of parameters**
Initial CFL number	1	0.001
PID controller k_P	0.65	0.065
PID controller k_I	0.05	0.005
PID controller k_D	0.05	0.005
Target Error estimate	0.1	0.001

A test case on a simpler geometry is carried out. It is observed that as compared to the default time step, the convergence with the smaller time steps is decreasing faster as shown in Figure 5.31. This suggests that it generates better initial guesses for the Newton iteration in the next time steps. However, the progress of the CFL ratio now becomes extremely slow. Due to this the overall simulation progress also hampers. Therefore, though the non-linear error decreases, the convergence does not improve significantly.

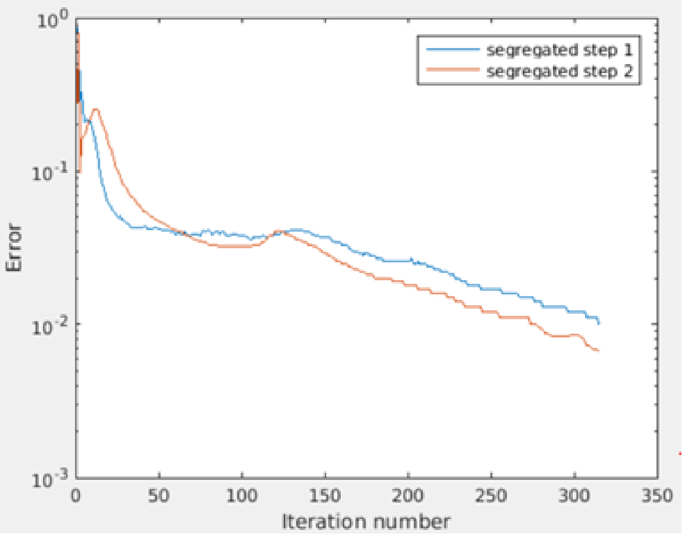

Figure 5.31: Convergence plot with stringent parameters of the PID controller.

5.3. CONCLUSION

In this chapter, the non-isothermal turbulent flow modeling in the heating section of anode baking furnace is discussed. The systematic development of the model is carried out by first elaborating the mixing pattern of air and fuel streams. The physical conditions in the heating section are established based on the existing conditions of the furnace. The major challenge in the development of non-isothermal turbulent flow modeling of the anode baking furnace geometry with COMSOL Multiphysics software has been the development of the appropriate mesh. The efficacy of the preliminary mesh developed by the COMSOL default mesher is analysed by comparing the results with another simulation environment, IB-Raptor code. The results of the COMSOL model are mesh sensitive but compare reasonably with IB-Raptor code for variables such as temperature and velocity. However, the inconsistency of the COMSOL mesh is realized by the comparison of the turbulent flow variables. This develops the requirement of more sophisticated meshing technique.

The cfMesh meshing tool is explored for meshing the complex geometry of anode baking furnace. The mesh with refinement in the jet development provides satisfactory results compared to the prior meshing techniques employed in the work. To generate the comparable results with the COMSOL default mesher, the number of elements required are eight times higher than the mesh generated by cfMesh. Therefore, the cfMesh meshing tool is proven to be more efficient in this study. Further, the baseline model is fixed with mesh generated with cfMesh meshing tool with the refinement in the jet development. The mesh provides satisfactory results even for the variables such as turbulent viscosity ratio that is more sensitive to the mesh. With fixing the appropriate mesh, the variations in the fuel jet velocity and fuel pipe diameter are studied. The effect of such variations on the mixing is recognized by analysing the turbulent viscosity ratio. It can be concluded that the intensity of mixing increases by increasing the fuel mass flow rate and decreasing the fuel pipe diameter. Such effects are important with respect to understanding the temperature and therefore, NOx emissions discussed in following chapters.

The attempts to improve the turbulent flow model from standard k-ϵ to realizable k-ϵ model are carried out. It can be concluded that the lower numerical diffusion poses difficulties in the convergence of realizable k-ϵ model. The additional constraints added in the realizable k-ϵ model for the definition of C_μ parameter and the destruction of turbulent dissipation rate needs calibration. This calibration is difficult to obtain without having control over software such as COMSOL Multiphysics.

6

MODELING OF COMBUSTION AND HEAT TRANSFER FOR NOX ANALYSIS

In this chapter, the combustion modeling of an industrial anode baking furnace is described. The combustion models of industrial furnaces can provide understanding of essential parameters. Identifying these parameters is important to test possibilities with which an effective combustion system can be generated. Such studies provide insights on changes required in the current conditions or design. In this chapter, the operational conditions such as air flow velocity, fuel flow velocity and fuel pipe diameter are varied and their effect on the combustion process are examined. The combustion modeling in COMSOL Multiphysics software consists of only eddy dissipation model. In this chapter, a workflow of more advanced mixture fraction/beta PDF model is developed and compared with the eddy dissipation model.

The heat released during the combustion reaction is modeled based on the enthalpy of heat formation in the reaction zone. The temperature in the furnace due to heat generated by combustion process is higher than 2000^{o}C in the reaction zone. Therefore, radiation modeling is included and the effect of adding radiation is analysed. The heat generated in the furnace is transferred to anodes via conduction through walls. The conjugate heat transfer through walls is modeled and this effect is examined. Studies of the radiation absorption coefficient with respect to conjugate heat transfer also provides interesting results as discussed further in this chapter.

The NOx in the anode baking furnace is generated due to high temperatures, referred as thermal NOx. Therefore, the NOx can be computed once the temperature distribution in the furnace is modeled. In the final part of this chapter, the analysis of NOx generation in the furnace is carried out.

Parts of this chapter have been published in [97]

6.1. COMBUSTION IN ANODE BAKING FURNACE

Among the various industrial processes, the anode baking process is carried out in combustion furnaces. Natural gas is utilized as the burning fuel. The combustion process occurs when preheated air mixes with natural gas. The turbulent flow of flue gas aids in the mixing of the two streams. The heat is generated as a result of the combustion process. The heat is transferred to anodes in the adjacent pits by conduction through walls. The fuel is injected into the anode baking furnace through burners. The design of the burner can be modified to control the combustion in the furnace. The various design parameters that affect the combustion in the furnace and effectively reduce the emissions have been described in Chapter 4. However, apart from the design of the burner, the arrangement of the furnace also has a significant impact on the combustion process. In this thesis work, the understanding of the combustion in the anode baking process of the Aluchemie furnace is developed.

The combustion modeling approach is chosen for developing the understanding of the process. The fuel mixes with the preheated air in the furnace. Therefore, a non-premixed combustion process is assumed. The anode baking process is a multi-physics phenomenon. Furthermore, the geometry of the furnace is complex. Due to necessary coupling between different physical phenomena in complex geometry, it is difficult to account for combustion with a detailed model. Therefore, relatively simple combustion models such as the eddy dissipation model and mixture fraction/PDF model have been studied in this thesis work. The aim of the study is to establish a model that provides comparative results with the measurements in the available computational and modeling resources.

6.2. EDDY DISSIPATION MODEL (EDM) WITHOUT RADIATION

Eddy dissipation is a turbulent-chemistry model that provides reaction source terms based on turbulent mixing. The reaction rate is determined by the dissipation of eddies that contain reactants and products [98]. The rate of reaction through reaction kinetics is assumed to be faster as compared to turbulent mixing. Therefore the mixing time scale is larger than the chemical time scale. The reaction source term in the eddy dissipation model is controlled by k and ϵ. Moreover, the two streams, namely of preheated air and fuel, are assumed to be mixed at ignition temperature. In other words, the combustion process occurs as soon as the two streams are mixed.

The eddy-dissipation model can be applied to a multi-step reaction mechanism. However, the rate of reaction for all reaction steps will be determined by turbulent mixing. Since the turbulent mixing parameters, k and ϵ are equal for all steps; the reaction rate is only varied by the species concentrations. This is physically inaccurate. Therefore, the eddy dissipation model is generally applied to one or two-step reaction mechanisms. In this work, a single step methane reaction with a total of five chemical species namely, CH_4, O_2, CO_2, H_2O and N_2 are considered for the base case model. The kinetic reaction rate is set such that the reaction occurs infinitely fast. The specific heat capacity of gases are defined by a temperature dependent analytical function. The parameters specific to a certain gas are obtained from NIST database [1]. The specific heat capacity for the

---

[1] https://webbook.nist.gov/

mixture of gases is then calculated considering the contribution of each of the gas.

The heat energy produced during the combustion process is accounted as a source term in the heat transfer equation. The heat energy can be quantified based on the extent of the reaction and the heat of the reaction. The heat of reaction is further calculated from the enthalpy of formation of the individual species. Table 6.1 presents the enthalpy of formation of the species considered in the system. The total enthalpy produced during the combustion reaction is calculated by multiplying the enthalpy of formation by the number of moles of individual species in the system.

Table 6.1: Enthalpy of formation of chemical species

Species	**Enthalpy of formation [KJ/mol]**
CH_4	-74.87
CO_2	-393.52
H_2O	-241.83
O_2	0
N_2	0

The combustion model is coupled with the turbulent flow modeling discussed in the previous chapter. The coupling parameter between the two physical phenomena as well as the mathematical formulations has been discussed in Chapters 2 and 3.

6.2.1. IMPLEMENTATION OF EDM ON THE BASE CASE MODEL

The base case model is formulated as an extension of the baseline turbulent flow model discussed in the previous chapter. The definition of base case model is defined in this section. After developing the initial flow results, the transport of chemical species is included in the model. The mass fractions at the inlet boundaries of the model are given in Table 6.2. The turbulent chemistry interaction is modeled by the eddy dissipation model. This model is based on the ‘mixed is burnt’ phenomenon. This can be observed from the mass fraction distribution of chemical species presented in Figure 6.1 and 6.2. The mass fraction distribution of CH_4 and O_2 (reactants) are shown in Figure 6.1. Whereas, the mass fraction distribution of CO_2 and H_2O (products) are shown in Figure 6.2. The mixing region of the fuel and oxidizer stream shows the sharp gradient of the chemical species. As the system consists of fuel-lean conditions, the CH_4 completely reacts with O_2 in the mixing region closer to the fuel outlets. The source term of the reaction in the eddy dissipation model is strongly related to the turbulence parameters that govern mixing. Therefore, the products CO_2 and H_2O appears in the mixing region which can also be referred as reaction zone. The fuel composition, in reality, consists of other hydrocarbons as well. However, as described earlier, the multiple reactions can not be modeled accurately with the eddy dissipation model. Therefore, for simplicity, the fuel composition is assumed to be as shown in Table 6.2. The effect of considering other hydrocarbons in the fuel is shown in section 6.2.5.

Table 6.2: Inlet boundary conditions for the chemical species

Species	**Mass fraction at Air inlet**	**Mass fraction at Fuel inlet**
CH_4	0	0.99
CO_2	0	0
H_2O	0	0
O_2	0.233	0
N_2	0.767	0.01

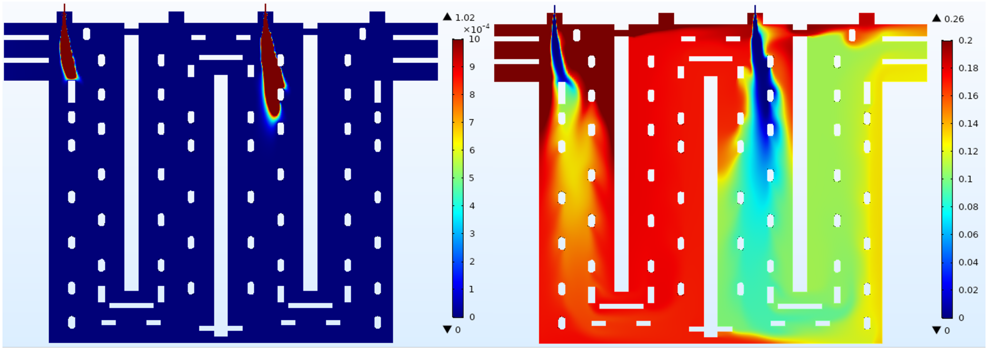

(a) (b)

Figure 6.1: Mass fraction distribution in the furnace with 9 mm fuel pipe diameter of chemical species (a) CH_4 and (b) O_2

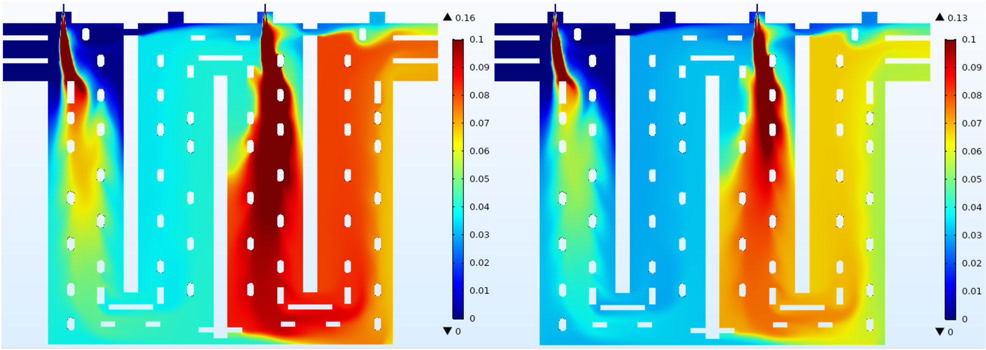

(a) (b)

Figure 6.2: Mass fraction distribution in the furnace with 9 mm fuel pipe diameter of (a) CO_2 and (b) H_2O

The combustion process is highly affected by the flow dynamics and air-fuel ratio in the furnace. The operation conditions at the boundaries are varied to understand their effect on the combustion process.

6.2.2. EFFECT OF VARIATIONS IN AIR FLOW CONDITION

The air flow conditions at the inlet for the base case model are calculated based on the existing values in the furnace at a given location. These calculations require temperature at the inlet locations. The temperature at the inlet location varies in a range of approximately 250°C. For the base case model, the average of the measured temperature is used. In this section, the air flow conditions computed by a lower range of measured temperature at the inlet are compared with the base case model. The reaction source term in eddy dissipation model is based on the turbulent eddy time scale, ϵ/k. Figure 6.3 shows the distribution of ϵ/k at the symmetry plane. It can be observed that the ϵ/k has a higher value for higher air flow inlet velocity near the jet and has a more bulgy shape.

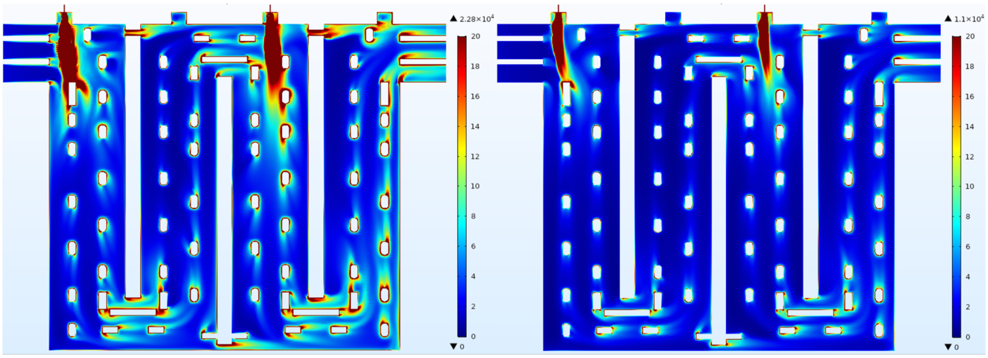

(a) (b)

Figure 6.3: The inverse of turbulent eddy time scale in EDM (ϵ/k) in the furnace with 9 mm fuel pipe diameter with air inlet velocity of (a) 1.90 m/s and (b) 1.45 m/s

Figure 6.4 and 6.5 show the comparison of mass fraction distribution with respect to the base case model of O_2 and CO_2, respectively. It can be observed that by lowering the air mass flow rate, the available O_2 for the combustion process decreases. The reason of such a decrease is associated with a decrease in the inverse of the turbulent eddy time scale. Moreover, the momentum of the air flow stream is not high enough to achieve complete mixing in the mixing region downstream to the fuel outlet. This results in a narrow streamline behaviour of O_2 in the case of a lower air inlet velocity. For the higher air inlet velocity, the mixing occurs evenly, and the combustion process is restricted to a smaller region near the fuel outlet from the burner. Therefore, the mass fraction distribution of O_2 is lower in only a small part of the furnace.

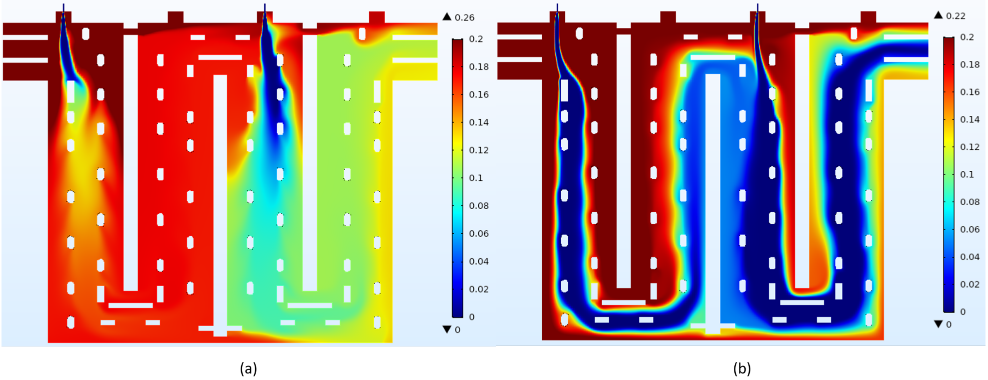

(a)

(b)

Figure 6.4: Mass fraction distribution of O_2 in the furnace with 9 mm fuel pipe diameter with air inlet velocity of (a) 1.90 m/s and (b) 1.45 m/s

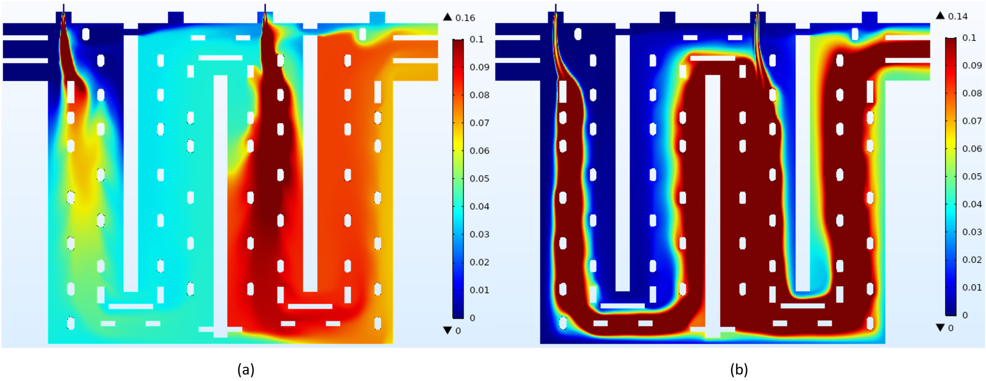

(a)

(b)

Figure 6.5: Mass fraction distribution of CO_2 in the furnace with 9 mm fuel pipe diameter with air inlet velocity of (a) 1.90 m/s and (b) 1.45 m/s

The mass fraction distribution of CO_2 for the lower air inlet velocity reflects the streamline behaviour similar to mass fraction distribution of O_2. The CO_2 appears in the streamline where the O_2 mass fraction is lower. For the higher inlet velocity, due to immediate higher mixing of streams, CO_2 appears in a smaller region of the reaction zone rather than a complete streamline.

The temperature is calculated based on the enthalpy and the extent of the reaction. Therefore, the higher temperature regions are formed based on the reaction zone itself. As per the earlier discussion, for the lower air inlet velocity, the streamline higher temperature zones are formed as shown in Figure 6.6. Whereas for the higher air inlet velocity, better mixing gets rid of the streamline behaviour, and higher temperature zone occur only downstream of the fuel outlet.

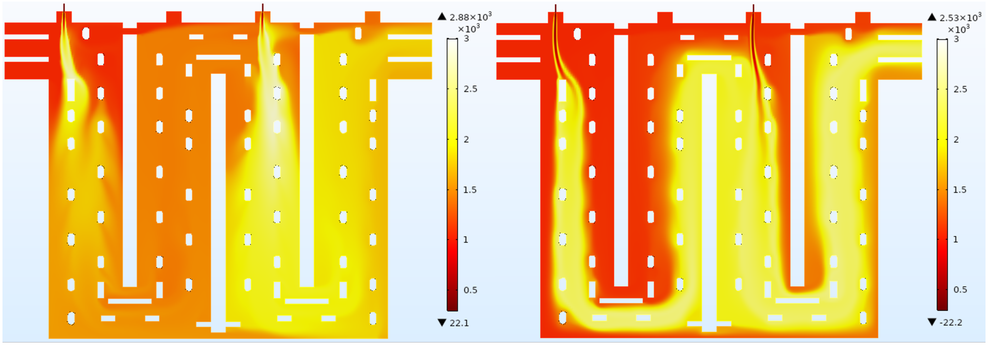

(a) (b)

Figure 6.6: Temperature distribution in [^{o}C] in the furnace with 9 mm fuel pipe diameter with air inlet velocity of (a) 1.90 m/s and (b) 1.45 m/s

Figure 6.7 shows the comparison of O_2 and CO_2 for two inlet air velocity values on the line Y=4.5 m at the XY symmetry plane. It can be observed that for the higher inlet velocity, the values of CO_2 are higher than that for lower air inlet velocity. This is attributed to higher extent of the combustion reaction.

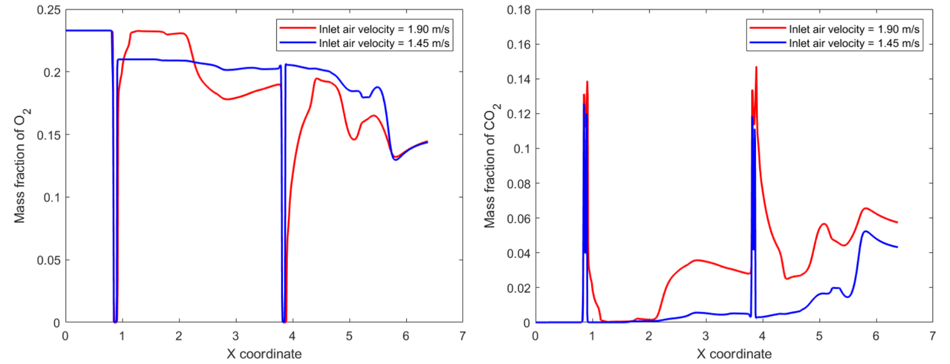

(a) (b)

Figure 6.7: Comparison with respect to different air inlet velocity at Y=4.5 m at XY symmetry plane for mass fraction of (a) O_2 and (b) CO_2

6.2.3. EFFECT OF VARIATIONS IN THE FUEL FLOW CONDITION

The mixing pattern of the air and fuel streams depends highly on the fuel jet velocity in an anode baking furnace due to its significantly higher value compared to the air inlet velocity. It has been discussed in the earlier section that the mixing behavior changes due to the variation of the air inlet velocity though values are relatively smaller compared to the fuel jet velocity. In this section, the effect of variation of the fuel jet velocity is studied. The fuel jet velocity for the base case model is 74 m/s. This value is calculated based on the operating pressure of the burner at Aluchemie. The effect of the fuel jet velocity is studied by choosing two more values (50 m/s and 90 m/s).

Figure 6.8 shows the distribution of ϵ/k at the symmetry plane with varying fuel jet velocity. It can be observed that with increasing fuel inlet velocity, the shape of ϵ/k near the jet extends deeper into the furnace. This shows the increase in the reaction source term.

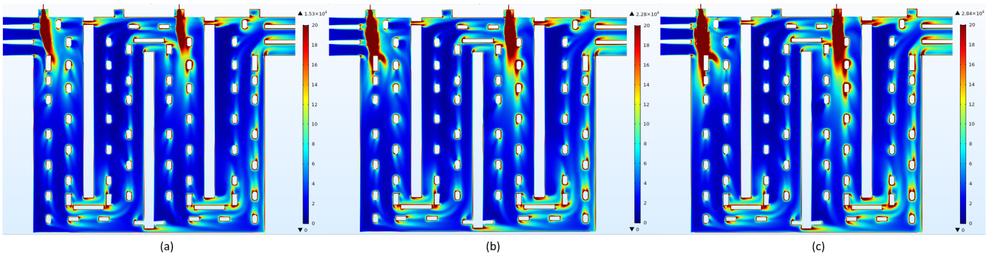

(a) (b) (c)

Figure 6.8: The inverse of turbulent eddy time scale in EDM (ϵ/k) at the symmetry plane for varying fuel inlet velocity of (a) 50 m/s (b) 74 m/s and (c) 90 m/s with 9 mm fuel pipe diameter

Figure 6.9 shows the mass fraction distribution of O_2 at the symmetry plane for varying fuel inlet velocities. It can be seen from the figure that for higher velocity (90 m/s), more combustion occurs in the furnace due to a higher reaction source term and the availability of more fuel. Therefore, the O_2 mass fraction at the outlet decreases with the increase in the fuel mass flow rate. Though overall combustion reaction increases, the reaction zone is widely spread in the case of higher fuel jet velocity. This can be attributed to the reduced mixing due to higher momentum. For a fixed diameter of a fuel pipe, the increase in velocity also accounts for the increase in the fuel quantity. For a fixed oxidizer concentration, it takes longer to consume all CH_4. Therefore, the length of the jet increases with an increase in velocity.

Figure 6.10 and 6.11 show the mass fraction distribution of CO_2 and the temperature at the symmetry plane for varying fuel inlet velocities. The observations of the combustion reaction zone are reflected in the surface distribution plots of CO_2 and the temperature as well. The amount of CO_2 produced in the case of higher fuel jet velocity is higher, leading to extended higher temperature zones in the second half of the furnace. Though the zone of higher temperature increases with the increase in fuel jet velocity, the observed maximum temperature for the model is lower compared to lower fuel jet velocity. This can be attributed to higher mixing in the restricted zone for lower jet velocity. The significant mixing occurs in a region closer to the fuel outlet for a lower jet velocity due to lower momentum. Therefore, the maximum temperature for the lower jet velocity is higher.

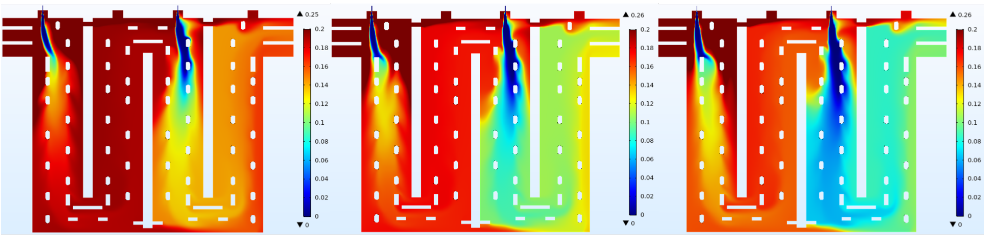

(a) (b) (c)

Figure 6.9: The O_2 mass fraction distribution at the symmetry plane for varying fuel inlet velocity of (a) 50 m/s (b) 74 m/s and (c) 90 m/s with 9 mm fuel pipe diameter

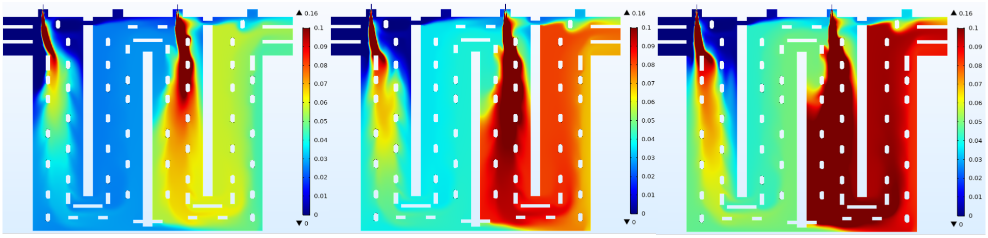

(a) (b) (c)

Figure 6.10: The CO_2 mass fraction distribution at the symmetry plane for varying fuel inlet velocity of (a) 50 m/s (b) 74 m/s and (c) 90 m/s with 9 mm fuel pipe diameter

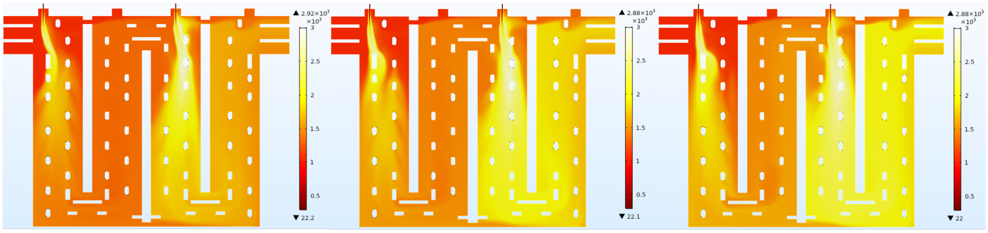

(a) (b) (c)

Figure 6.11: The temperature distribution in [^oC] at the symmetry plane for varying fuel inlet velocity of (a) 50 m/s (b) 74 m/s and (c) 90 m/s with 9 mm fuel pipe diameter

Figure 6.12 shows the comparison of O_2 and CO_2 for three inlet fuel jet velocity values on line Y=4.5 m at XY symmetry plane. It can be observed that the O_2 mass fraction decreases, and CO_2 mass fraction increases with the increase in the fuel jet velocity due to increased amount of combustion. The effect of reducing fuel jet velocity by reducing the operating pressure of the burners in one of the furnaces in Aluchemie confirms that the temperature decreases with decreasing the fuel jet velocity.

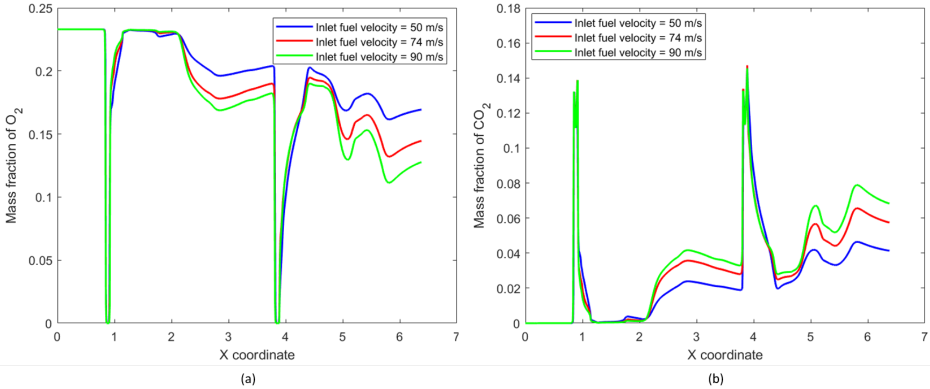

Figure 6.12: Comparison with respect to different fuel inlet velocity at Y=4.5 m at XY symmetry plane for mass fraction of (a) O_2 and (b) CO_2

6.2.4. EFFECT OF VARIATIONS IN THE FUEL PIPE DIAMETER

The change in the air or fuel jet velocity changes the air-fuel ratio in the furnace compared to the base case model. This leads to a variation in the combustion reaction due to the difference in the availability of the oxidizer or fuel. It is interesting to see the effect of flow dynamics on the combustion process. This can be achieved by changing the diameter of the fuel inlet in such a way that the fuel mass flow rate remains the same. In this section, the effects of change in the advection term are studied in such a way that the fuel amount remains the same. This is carried out by increasing the fuel pipe diameter. The diameter of the fuel burner pipe is increased from 9 mm to 13 mm. The velocity of the fuel inlet through a 13 mm fuel pipe is such that the mass flow rate of fuel is equal to that through a 9 mm diameter pipe. Table 6.3 shows the values of velocities for the two fuel pipe diameters that yield equal mass flow rate of fuel injected in the furnace. As can be expected, for the larger diameter of the fuel pipe, the injected fuel inlet velocity is lower. This implies that the advection term of the flow dynamics with two fuel pipe diameters is different. Moreover, in this comparison, the air/fuel ratio for a given mass flow rate of fuel is constant for the two fuel pipe diameters. Therefore, the difference in the results for the two fuel pipe diameters is governed by the difference in the flow dynamics.

Table 6.3: Values of fuel pipe diameters and velocities that have equivalent mass flow rate

Fuel mass flow rate [kg/s]	**Fuel pipe diameter [mm]**	**Fuel inlet velocity [m/s]**
0.0030	9	74
	13	35

Figure 6.13 shows the distribution of the inverse of the turbulent eddy time scale that provides a measure of reaction source term. The larger reaction source term region

under the fuel outlet is observed for the 9 mm case. This can be attributed to the higher momentum of the jet.

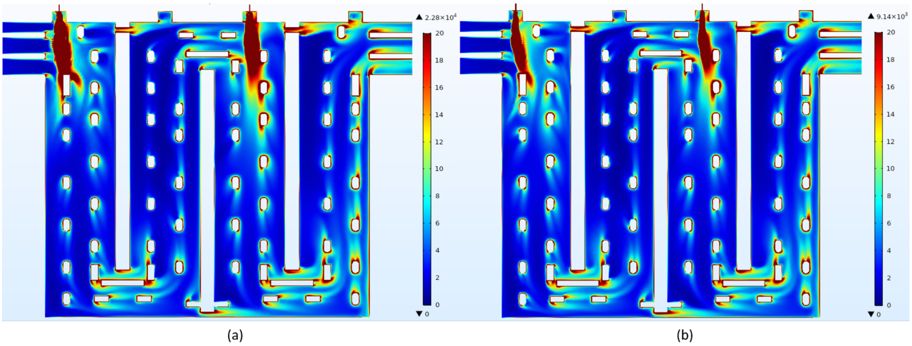

(a)

(b)

Figure 6.13: The inverse of the turbulent eddy time scale in EDM (ϵ/k) at the symmetry plane for a constant fuel mass flow rate but varying fuel pipe diameter of (a) 9 mm and (b) 13 mm

Figure 6.14 shows the mass fraction distribution of O_2 at the symmetry plane with the two fuel pipe diameters. It can be seen from the comparison that the reaction zone is smaller in the case of 9 mm diameter while the wider reaction zone is observed for 13 mm fuel diameter. This can be associated with larger ϵ/k for 9 mm case. The lower values of O_2 (dark blue color region) represents the reaction zone. This aligns with our expectation that due to higher turbulence O_2 reacts readily with the fuel in the case of the 9 mm diameter pipe. This further results in a higher combustion reaction restricted to a smaller region near the fuel inlet. This effect is translated into the mass fraction distribution of CO_2 as well. The higher mass fraction of CO_2 is spread wider in the 13 mm fuel pipe diameter as compared to the 9 mm fuel pipe diameter.

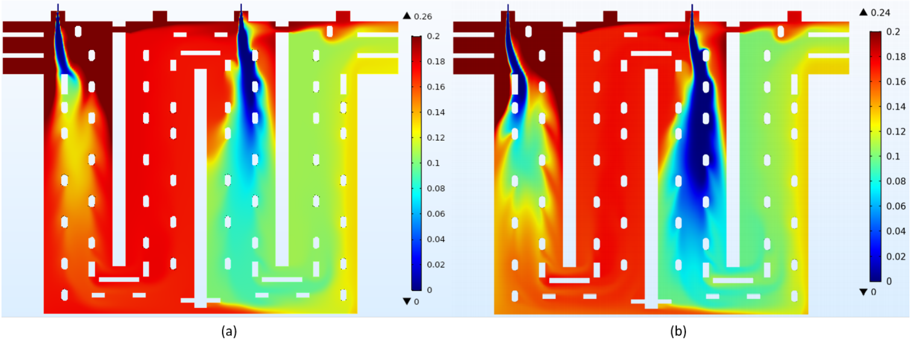

(a)

(b)

Figure 6.14: The O_2 mass fraction distribution at the symmetry plane for a constant fuel mass flow rate but varying fuel pipe diameter of (a) 9 mm and (b) 13 mm

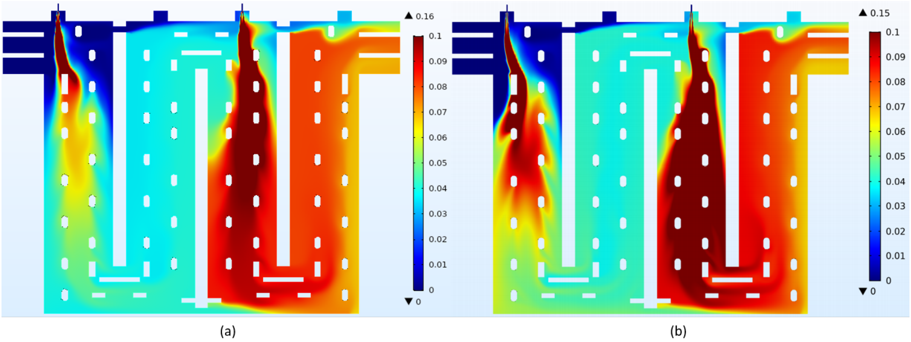

(a) (b)

Figure 6.15: The CO_2 mass fraction distribution at the symmetry plane for a constant fuel mass flow rate but varying fuel pipe diameter of (a) 9 mm and (b) 13 mm

The temperature distribution for the two cases is provided in Figure 6.16. The heat source of the reaction is defined in such a way that the heat generation occurs in the reaction zones. Therefore, the wider high-temperature zones for the two burners of 13 mm diameter are reflected in the figure. Furthermore, since the combustion process for the 9 mm diameter model is limited to a smaller region, the maximum temperature in the model is significantly higher compared to the 13 mm model. In the case of a 13 mm fuel pipe diameter, the temperature disperses in such a way that the maximum temperature is lowered.

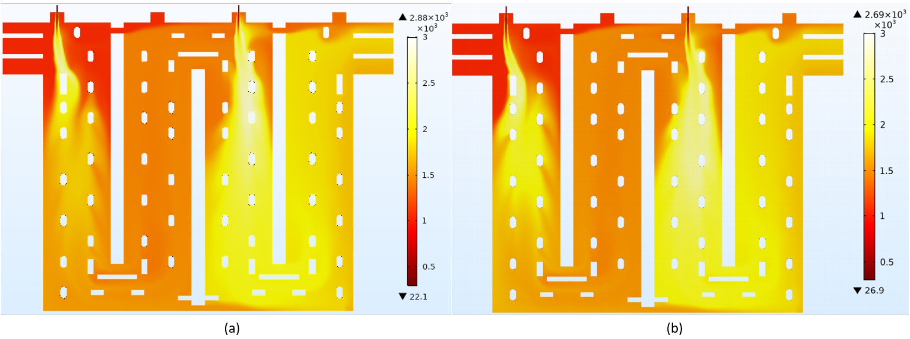

(a) (b)

Figure 6.16: The temperature distribution at the symmetry plane for a constant fuel mass flow rate but varying fuel pipe diameter of (a) 9 mm and (b) 13 mm

Figure 6.17 shows the comparison of mass fraction of O_2 and CO_2 on line Y=4.5 m at XY symmetry plane for two fuel pipe diameters. The values of both O_2 and CO_2 are similar at the outlet. The air-fuel ratio for both cases is the same. Therefore, the overall quantity of consumption of O_2 and production of CO_2 is equal. The same amount of CO_2 is produced, but the reaction zone differs for the two cases with different fuel pipe diameters. This observation is interesting since the combustion reaction for the two cases differs due to the flow dynamics.

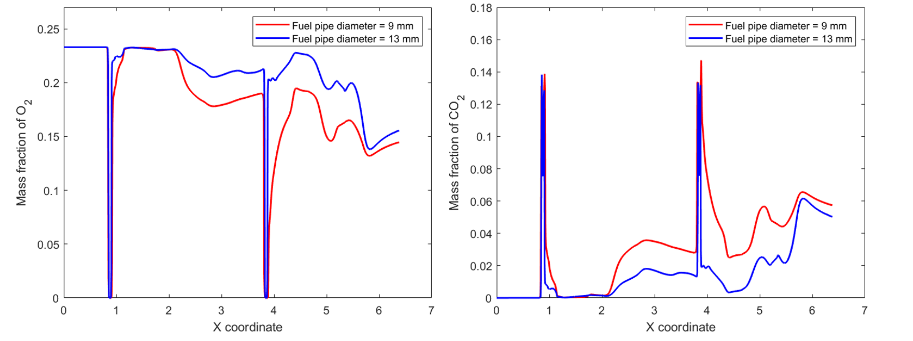

(a) (b)

Figure 6.17: Comparison with respect to different fuel pipe diameter at Y=4.5 m at XY symmetry plane for mass fraction of (a) O_2 and (b) CO_2

6.2.5. EFFECT OF FUEL COMPOSITION

The reaction rate of eddy dissipation model depends completely on the turbulent mixing parameters such as k and ϵ. The fuel composition for the base case model is assumed to be 99% CH_4 by mass since the eddy dissipation model is preferable only for single or two reactions. In this section, the effect of different fuel compositions is tested. In addition to CH_4, the fuel contains C_3H_8, C_4H_{10} and CO_2. Table 6.4 shows the new fuel composition for the model.

Table 6.4: Modified inlet boundary conditions for fuel inlet

Species	**Mass fraction at Fuel inlet**
CH_4	0.81
C_2H_6	0.10
C_3H_8	0.05
CO_2	0.02
H_2O	0
O_2	0
N_2	0.02

Figure 6.18 shows the distribution of the inverse of turbulent eddy time scale for the varying fuel composition. The flow conditions for both cases are exactly equal. The only difference is in the composition of fuel. Therefore, the distribution of ϵ/k for both cases is equivalent.

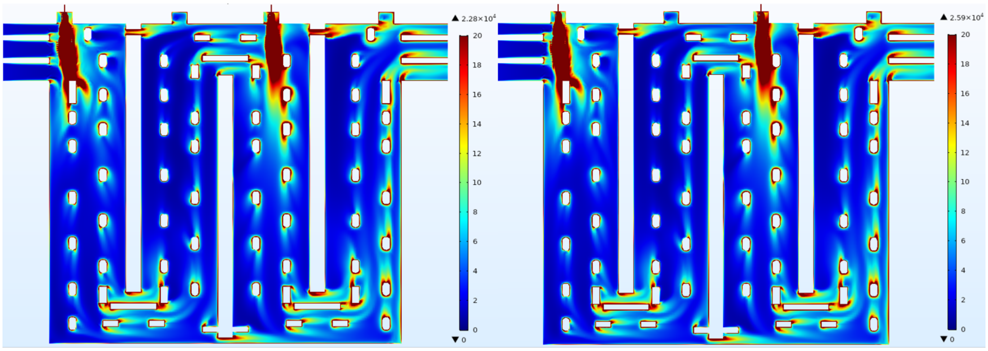

(a)

(b)

Figure 6.18: The inverse of the turbulent eddy time scale in EDM (ϵ/k) at the symmetry plane for varying fuel fuel composition with mass fraction of methane as (a) 0.99 and (b) 0.81

Figure 6.19 shows the comparison of O_2 with varying mass fraction of CH_4 in the fuel. The mass fraction of O_2 at the downstream of the second burner suggests that the reaction zone extends longer for the model in which the fuel has less amount of CH_4. The difference in the reaction zone is due to the different number of reactions occurring in both models. The amount of O_2 consumed by each reaction is different. The O_2 consumed by the multiple reactions is slightly higher than the model with a single reaction. This suggests that the higher combustion occurs in the case of the multiple reaction model.

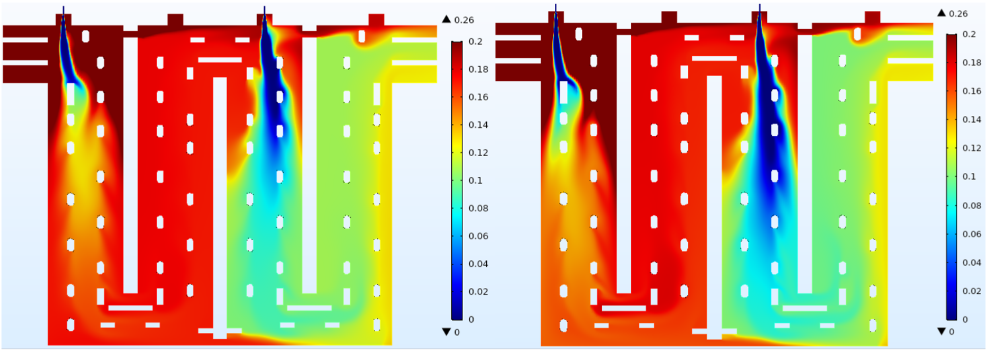

(a)

(b)

Figure 6.19: The O_2 mass fraction distribution at the symmetry plane for varying fuel composition with the mass fraction of methane as (a) 0.99 and (b) 0.81

The effect of the difference in reactions is also reflected in the mass fraction distribution of CO_2. The higher mass fraction of CO_2 slightly extends in the model where multiple reactions occur. The higher mass fraction of CO_2 downstream of the second burner also suggests that the extent of the combustion reaction is higher in the case of the model with multiple reactions.

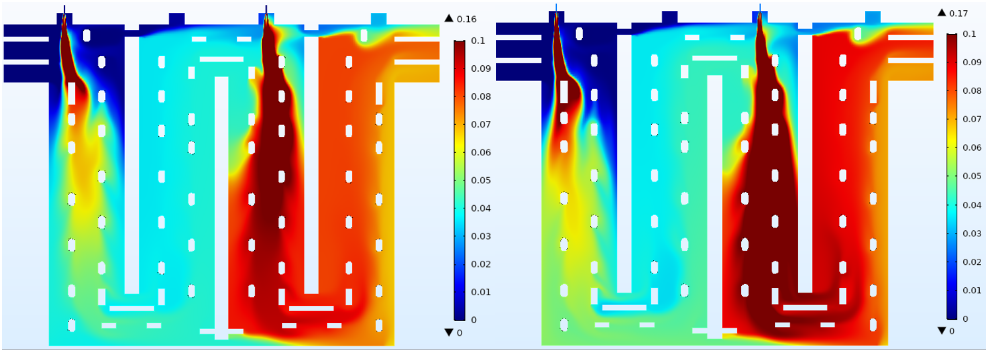

(a)

(b)

Figure 6.20: The CO_2 mass fraction distribution at the symmetry plane for varying fuel composition with mass fraction of methane as (a) 0.99 and (b) 0.81

The heat of combustion reaction is calculated as the sum of enthalpy of formation by the three reactions of CH_4, C_2H_6 and C_3H_8. The section of the furnace downstream of the second burner is slightly warmer in the case of a model with multiple reactions. The maximum temperature, however, is higher for the model with a single reaction. This can be attributed to the higher combustion reaction in smaller parts near the second fuel outlet. In the model with multiple reactions, there are competing reactions due to which the combustion reactions are distributed to a wider region. This results in overall high temperatures but lower maximum temperature.

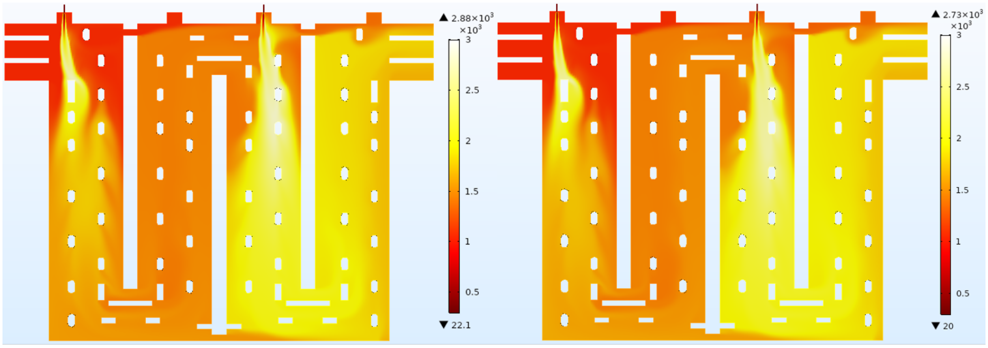

(a)

(b)

Figure 6.21: The temperature distribution [^{o}C] at the symmetry plane for varying fuel composition with mass fraction of methane as (a) 0.99 and (b) 0.81

The comparison on line Y=4.5 m at XY symmetry plane is carried out for the different fuel composition models. Figure 6.22 shows the comparison of mass fraction of O_2 and CO_2 for varying fuel compositions. It can be observed that the values are similar for the two models. The values of O_2 and CO_2 are slightly lower and higher respectively for the model with fuel stream containing multiple hydrocarbons. The modeling of multiple reactions with the eddy dissipation model itself introduces inaccuracies. Therefore, there is a compromise of accuracies in the results for both models.

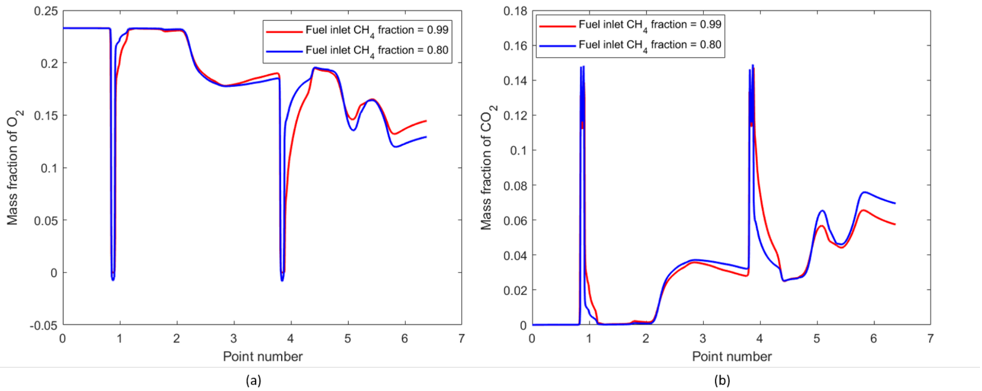

Figure 6.22: Comparison with respect to different fuel composition at line Y=4.5 m at XY symmetry plane for mass fraction of (a) O_2 and (b) CO_2

6.3. MIXTURE FRACTION-PDF MODEL WITHOUT RADIATION

The eddy dissipation model shows reasonable results for the given application of an anode baking furnace. Though the eddy dissipation model is the most simplistic combustion model, predicting trends with varying operating conditions provides significant insights. The eddy dissipation model is highly dependent on the turbulence parameters such as turbulent kinetic energy and turbulent dissipation rate. These parameters remain equal for all reactions. Therefore, the implementation of the eddy dissipation model is restricted for the single-step or two-step reactions. The results are inaccurate for the multi-step reaction mechanism with the eddy dissipation model. The accuracy of the turbulent model directly affects the combustion process. Furthermore, the eddy dissipation model does not require ignition since the combustion occurs as soon as the turbulent flow is generated.

Mixture fraction theory, along with the Probability Distribution Function (PDF), provides another way to define turbulent chemistry interaction. Authors studying anode baking furnace models have proven the improved results with this combustion model [31]. The theory is based on the assumption that the thermochemical state of the fluid is related to a conserved scalar quantity called mixture fraction. The chemical equilibrium assumption for the reactions provides the equilibrium species mass fraction at a given state of the mixture. The average values of the species mass fraction can then be obtained using the probability density function. Commercial softwares such as Ansys Fluent has inbuilt modules for implementing the non-premixed mixture fraction/PDF model. The COMSOL Multiphysics software is limited with respect to the available combustion models. In this thesis, an attempt is made to establish an adiabatic system model for a single burner stream with mixture fraction/PDF theory.

6.3.1. THEORY OF MIXTURE FRACTION/PDF MODEL

The COMSOL Multiphysics software does not provide the module for describing the turbulent chemistry interaction by mixture fraction-PDF theory. In this work, the workflow for defining the turbulent-chemistry interaction in terms of the mixture fraction and the probability density function is developed.

Figure 6.23 shows the workflow that is developed for the adiabatic case. There are three main components for the development of the model. In the first component (represented by yellow blocks), the transport equations of the mixture fraction and its variance are solved. The derivation of these equations and the underlying assumptions are provided later in this section. The probability density function is needed in the case of the turbulent flow for averaging the instantaneous fluctuations of the thermochemical state. The parameters α and β of the probability density function are calculated based on the mixture fraction and its variance. These parameters are defined in section 6.3.4 (Equation 6.6 and 6.7). At each location in the furnace, the shape of the probability density function can be obtained as a function of the mixture fraction based on these parameters. It has been observed that for the given application, the PDF shape approaches infinity at most of the location points. The necessary modifications to the PDF function, such as use of Cumulative Distribution Function (CDF), are explained later in the section. The next component is the equilibrium chemistry as a function of the mixture fraction to understand the instantaneous thermochemical state of the species. In the third component, the integration of the instantaneous equilibrium chemistry function and modified PDF over the complete range of mixture fraction is carried out to get the tables of average values of the scalar quantities as a function of mixture fraction and variance.

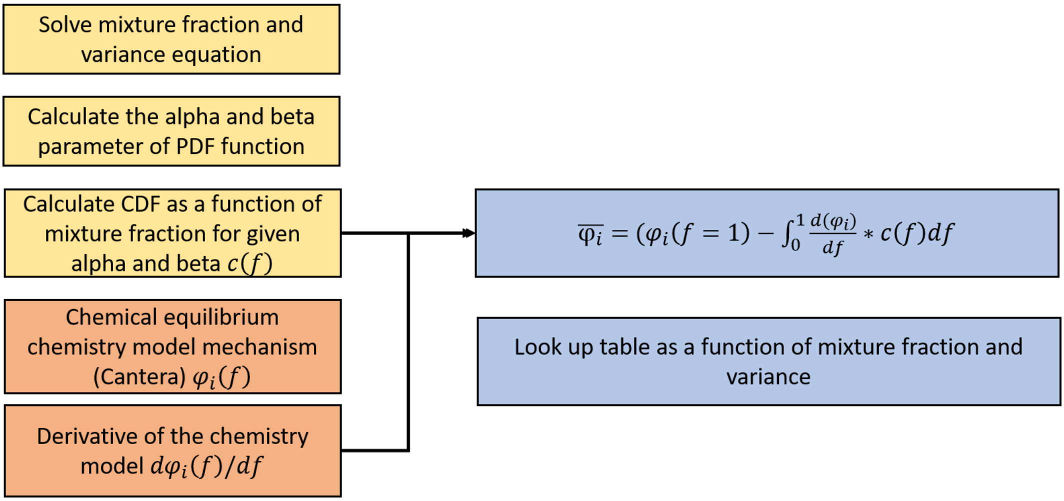

Figure 6.23: The workflow for the implementation of mixture fraction-PDF model to an adiabatic case.

6.3.2. MIXTURE FRACTION AND VARIANCE

The modeling of the source term in the transport equation of chemical species is difficult. The definition of the source term by the Arrhenius law introduces non-linearity in the equations. Solving such non-linear equations for detailed chemistry mechanisms is complicated. Therefore, models are developed in which the source term in the transport equation can be eliminated. The mixture fraction is a conserved scalar quantity that is defined based on the elemental mass fraction. Since the elements are conserved in a chemical reaction, the transport equation of the mixture fraction does not have a source term. The transport equations for fuel and oxidizer are combined by the appropriate treatments to a single transport equation of a mixture fraction under the following assumptions [99].

- All species have equal diffusivities
- The rate of fuel and oxidizer consumption occurs according to stoichiometric ratio

In the adiabatic system, there is no exchange of heat to and from the system. In this case, the transport equation for the enthalpy is similar to that of the mixture fraction. Therefore, the two quantities can be linearly related under the following assumptions instead of solving another transport equation for the enthalpy. With the adiabatic formulation, the average mass fraction of chemical species and temperature can be obtained by solving just two transport equations.

- Lewis number is unity
- Pressure work is negligible

The numerical equation of the mixture fraction and its variance is given by Equation 6.1 and 6.2, respectively [36].

$$\nabla \cdot (\overline{\rho u}\overline{f}) = \nabla \cdot (\frac{\mu_l + \mu_t}{\sigma_t} \nabla \overline{f}) \tag{6.1}$$

$$\nabla \cdot (\overline{\rho u}\overline{f'^2}) = \nabla \cdot (\frac{\mu_l + \mu_t}{\sigma_t} \nabla \overline{f'^2}) + C_g \mu_t \cdot (\nabla \overline{f})^2 - C_d \rho \frac{\epsilon}{k} \overline{f'^2} \tag{6.2}$$

The Dirichlet boundary conditions for the mixture fraction variable are specified at the air and fuel inlet. The mixture fraction variable is zero at the air inlet and unity at the fuel inlet. At the outlet, the diffusion flux is zero, whereas, at all other boundaries, the net flux is defined to be zero. The variance at both air and fuel inlets is defined as zero, whereas at all other boundaries, the net flux is defined to be zero.

The default values of the constants in Equation 6.1 and 6.2 are provided in Table 6.5. The effect of the diffusion coefficient of the transport of chemical species has a significant effect on the results in the case of the eddy dissipation model. The constant σ_t is used to control the diffusion in the mixture fraction and variance equation. The reactive flow model of COMSOL Multiphysics software couples the transport of chemical species with flow equations using Kays-Crawford model. The model computes the turbulent Schmidt number that governs the diffusion coefficient of the turbulent reactive flow with the eddy dissipation model. The value of σ_t is set as the value of the turbulent Schmidt number. It has been observed that the value of the turbulent Schmidt number is similar to the default value of $\sigma_t = 0.85$. The laminar molecular viscosity term in the diffusion coefficient is adjusted such that the term is similar to the eddy dissipation model with the reactive flow.

Table 6.5: Values of constants in mixture fraction and variance equations

Constant	**Value**
σ_t	0.85
C_g	2.86
C_d	2.00

6.3.3. CHEMISTRY MODEL

The chemistry model establishes a relationship between the thermochemical scalars such as mass fraction species, temperature, and density with the mixture fraction at chemical equilibrium. The unique correlation between these variables makes it possible to reduce the chemistry in the combustion modeling to the reduced number of transport equations. This relation is as presented in Equation 6.3 [36].

$$\phi_i = \phi_i(f) \tag{6.3}$$

The chemical equilibrium of the participating chemical species in a single or set of reactions at a given thermodynamic state is calculated by using the equilibrate function of the Cantera tool [2]. The thermodynamics data for the chemical species is accessed from the Cantera library. The equilibrate function of Cantera is based on the element potential method. The element potential method describes the equilibrium state based on the maximization of entropy. In this way, the method differs from the regular Gibbs free energy minimization technique. The primary advantage of using the element potential method over Gibbs free energy minimization is that it requires solving a number of equations equal to the number of atoms. Whereas in the Gibbs free energy minimization technique, the number of equations equals the number of species. In general, the number of atoms is smaller than the number of species, and therefore, the element potential method requires solving a lesser number of non-linear equations as compared to the Gibbs free energy minimization. More details on the element potential method algorithm are explained in [100]. The damped Newton method is used to solve the non-linear equations. The equilibrium conditions are achieved by fixing two thermodynamics states. In the adiabatic case, the constant enthalpy and pressure are used to solve the equilibrium. The initial state of the gas mixture is defined based on the initial mass fraction of CH_4, O_2 and N_2, initial temperature, and pressure. A MATLAB code has been developed to make tables of instantaneous thermochemical scalars as a function of the mixture fraction and is validated by comparing it with tables generated by Ansys Fluent. The comparison of the instantaneous scalar fields as a function of the mixture fraction computed by the in-house MATLAB code and the Fluent software is carried out for single step and GRI 3.0 chemistry mechanism. Figure 6.24 and Figure 6.25 show the comparison for the single-step and GRI 3.0 chemistry mechanism respectively. It can be observed from Figure 6.24 that the comparison of results with both programs is in good

---

[2] https://cantera.org/

agreement for the mole fraction of the chemical species. The temperature computed by the MATLAB in-house code is slightly higher than that computed by Fluent. The slight differences can be associated with the variation in the equilibrium method that is used by both programs.

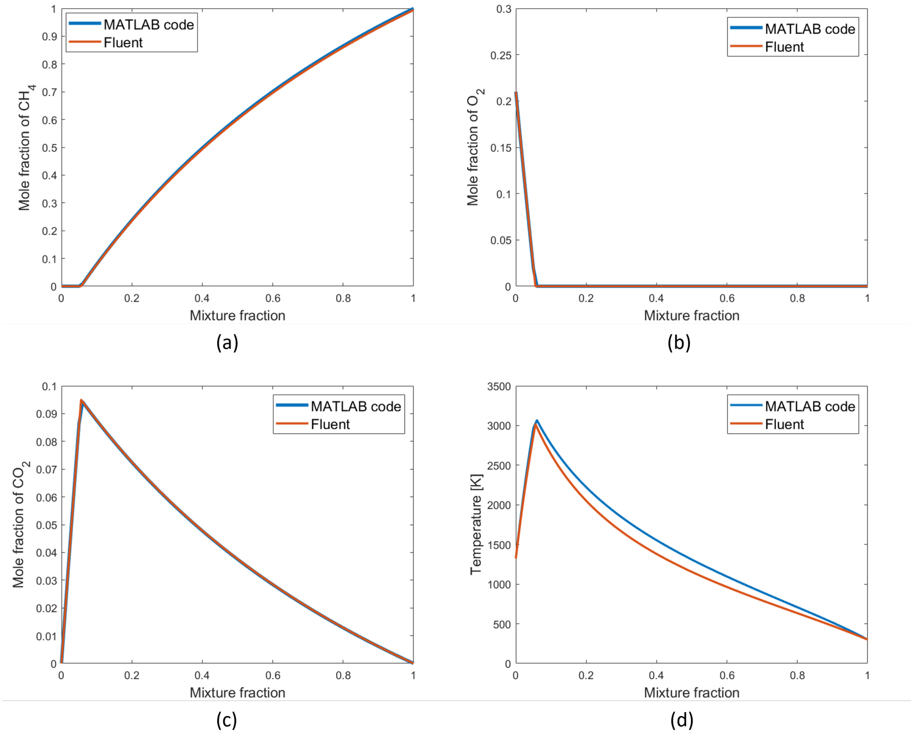

Figure 6.24: Comparison of instantaneous properties such as (a) mass fraction of CH_4, (b) mass fraction of O_2 (c) mass fraction of CO_2 and (d) temperature as a function of mixture fraction with in-house code in MATLAB and with fluent. Both programs use single step chemistry mechanism.

Similar to the single-step chemistry mechanism, the GRI 3.0 mechanism is also compared with the two programs. It can be observed that the reactant species such as CH_4 and O_2 compares well with the two programs in most of the mixture fraction space. For the product species, the CO_2 mole fraction is higher in the mixture fraction space after the stoichiometric mixture fraction. Whereas the temperature is higher with the MATLAB in-house code compared to Fluent in limited mixture fraction space after the stoichiometric mixture fraction. Despite these differences, the shape of the instantaneous mole fraction of species and temperature with mixture fraction is in close agreement. As mentioned for the single-step mechanism, the slight differences can be associated with the variation in the equilibrium method that is used by both programs.

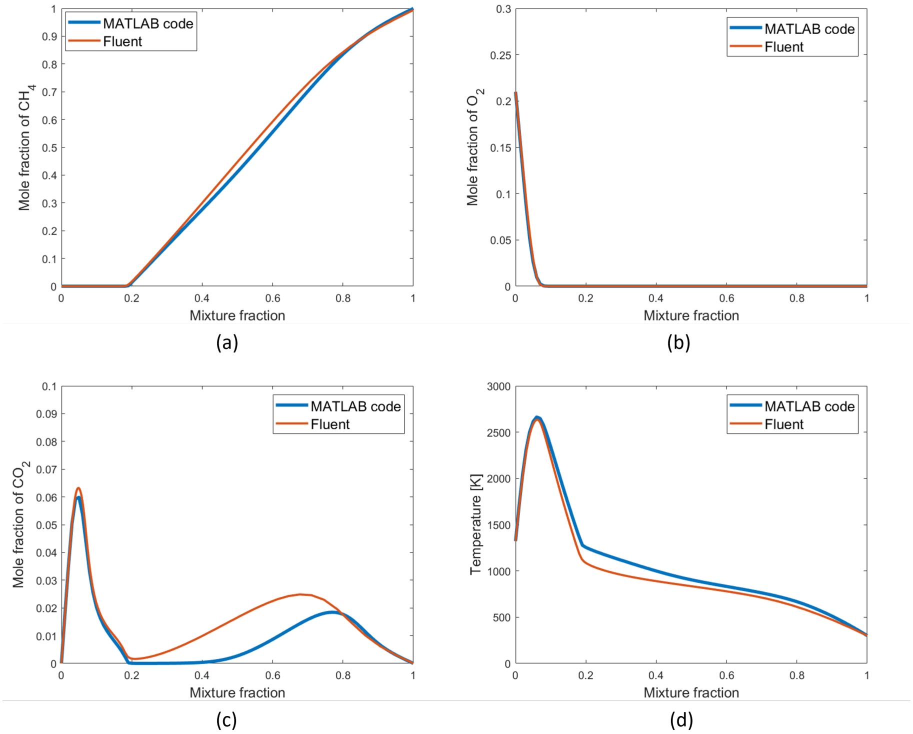

(a) (b)

(c) (d)

Figure 6.25: Comparison of instantaneous properties such as (a) mass fraction of CH_4, (b) mass fraction of O_2 (c) mass fraction of CO_2 and (d) temperature as a function of mixture fraction with in-house code in MATLAB and with fluent. Both programs use GRI 3.0 chemistry mechanism.

The instantaneous thermo-chemical scalars as a function of mixture fraction at chemical equilibrium are tabulated for different reaction mechanisms. Figure 6.26 shows the adiabatic flame temperature with respect to the mixture fraction for different chemical mechanisms. A smooth transition of adiabatic flame temperature at stoichiometric conditions occurs for the more detailed GRI 3.0 mechanism. It can be observed that the adiabatic flame temperature for the single-step mechanism is highest, and the one for GRI 3.0 mechanism is lowest. For a single-step mechanism, the intermediate reactions are not taken into account. These reactions being endothermic, absorb heat energy reducing the temperature. Therefore, as we go from the single-step mechanism to a more detailed chemistry mechanism, the temperature decreases. Moreover, the temperature change as a function of mixture fraction at the stoichiometry is smoother as the detailed chemistry mechanisms are used.

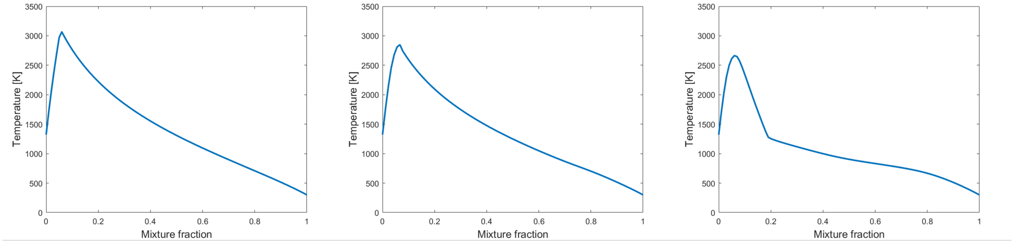

(a) (b) (c)

Figure 6.26: The adiabatic flame temperature with respect to the mixture fraction for different chemistry mechanisms such as (a) single step (b) two steps (c) GRI 3.0.

Figure 6.27 shows the instantaneous mass fraction as a function of the mixture fraction for varying chemical reaction mechanisms. The difference for the mass fraction of reactants such as CH_4 and O_2 does not vary significantly with the chemical reaction mechanism. However, the formation of the products such as CO_2 shows a significant difference for different mechanisms. A single maximum of CO_2 for a single-step mechanism curve shows that the formation of CO_2 occurs in a single step. Whereas, for two steps and GRI 3.0 mechanism, the formed CO_2 further dissociates in the intermediate reactions. Therefore, after the first maximum, the CO_2 concentration decreases. CO_2 being the product of the intermediate reactions, a second maximum appears at higher mixture fractions. This suggests that the chemical reaction mechanism has a significant impact on the overall combustion.

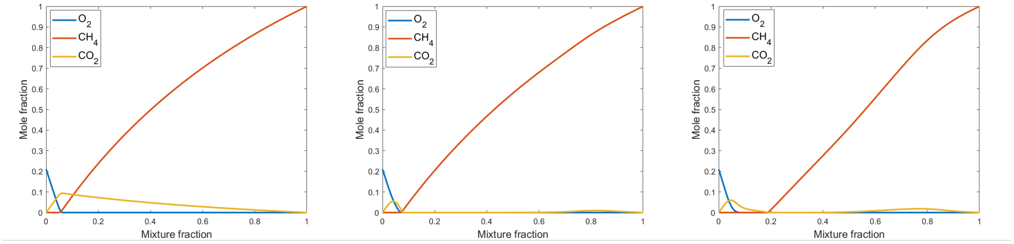

(a) (b) (c)

Figure 6.27: The mass fraction of chemical species with respect to the mixture fraction for different chemistry mechanisms such as (a) single step (b) two steps (c) GRI 3.0.

The chemistry model is validated by comparing with the data from Fluent software. The next step in the workflow explained in Figure 6.23 is the calculation of average quantities. The convolution of the instantaneous scalar quantities is required for obtaining the average quantities.

6.3.4. PROBABILITY DENSITY FUNCTION (PDF)

The chemistry model provides the instantaneous relation between species fraction and the conserved scalar quantity, i.e., mixture fraction. In the case of turbulent flow, the mean species mass fraction and temperature are of interest. The conversion of instantaneous relationship to an averaged quantity needs a statistical approach. The probability density function is used to convert the instantaneous relationship provided by the chemistry model to the mean values. The PDF is the fraction of time in which the fluid is in the vicinity of a particular thermodynamic state. Equation 6.4 presents the relation of the average quantity of the variable based on the instantaneous value provided by the chemistry model and PDF.

$$\overline{\phi_i} = \int_0^1 p(f)\phi_i(f)df \tag{6.4}$$

Among the various shapes of PDF, β-PDF is the most commonly used function in combustion modeling. The shape of β-PDF is defined by two parameters α and β as given by Equation 6.5.

$$p(f) = \frac{\Gamma(\alpha+\beta)}{\Gamma(\alpha)\Gamma(\beta)} f^{\alpha-1}(1-f)^{\beta-1} \tag{6.5}$$

The mixture fraction and the variance transport equations, 6.1 and 6.2, discussed in the earlier sections are required for defining the shape of β-PDF at different locations in the furnace. The parameters α and β are calculated using mixture fraction and variance as per the Equation 6.6 and 6.7, respectively.

$$\alpha = \overline{f}\left[\frac{\overline{f}(1-\overline{f})}{\overline{f'^2}} - 1\right] \tag{6.6}$$

$$\beta = (1-\overline{f})\left[\frac{\overline{f}(1-\overline{f})}{\overline{f'^2}} - 1\right] \tag{6.7}$$

Figure 6.28 shows a shape of β-PDF as a function of mixture fraction for various values of α and β. It can be observed from the figure that the singularity occurs near boundaries for α and β values less than one. Moreover, for higher values of α and β (say the value of 100), the PDF function has NaN and Inf values. Therefore, it is challenging to use β-PDF for the given application.

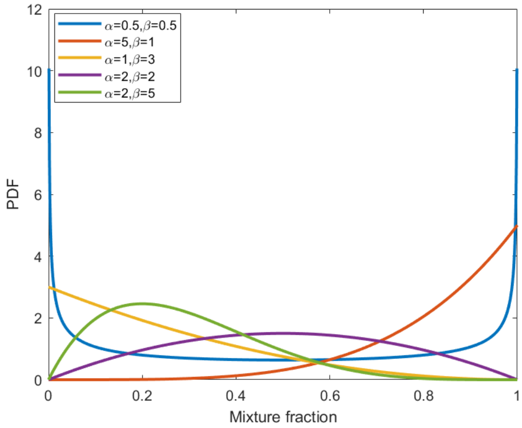

Figure 6.28: The PDF function for different α and β parameters

Among the various alternatives for treating the β-PDF, using the integrated form of PDF such as Cumulative Distribution Function (CDF) can be useful [101]. As opposed to β-PDF, the CDF is bounded between 0 and 1. The PDF function can be found by differentiating the CDF. If X is the continuous variable with PDF as f and CDF as F, the relation between f and F can be established using Equation 6.8.

$$f(x) = \frac{d}{dx}[F(x)] \tag{6.8}$$

Figure 6.29 shows the CDF as a function of mixture fraction for various values of α and β parameters. It can be observed that even for higher values, the CDF is calculated and bounded. Therefore, the function is more suitable for the case of anode baking furnace conditions as compared to PDF.

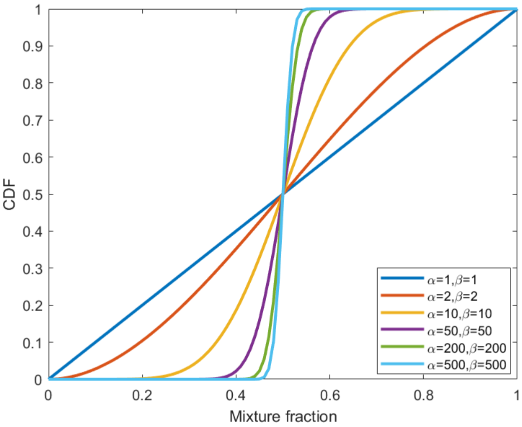

Figure 6.29: The CDF function for different α and β parameters

To use the CDF ($c(f)$) instead of PDF, Equation 6.4 is modified to Equation 6.9 using integration by parts. It can be observed from Equation 6.9 that the derivative of the function that relates the instantaneous quantities with mixture fraction is required for the calculation of average quantities.

$$\overline{\phi_i} = \phi(f=1) - \int_0^1 \frac{d(\phi_i)}{df} c(f) df \tag{6.9}$$

6.3.5. FORMULATION IN MATLAB

In the previous sections, the theory of combustion modeling in terms of mixture fraction-PDF theory with the chemical equilibrium chemistry model is explained in detail. Since COMSOL Multiphysics software does not provide the default module for this formulation, the tables of average quantities as a function of mixture fraction and variance are generated in MATLAB. These tables are then imported as interpolation functions in COMSOL. Finally, the surface plots at the XY symmetry planes are obtained by looking up at the interpolated tables for corresponding values of mixture fraction and variance at a particular location.

At present, the integration in Equation 6.9 is carried out by a rough technique. The integration is simply the summation of areas of rectangles over the range of the mixture fraction. The midpoint rule of numerical integration is implemented. This rough method tends to provide approximate results. Depending on the shape of the function for a particular quantity, the values are either underestimated or overestimated with this integration method.

6.3.6. 2D RECTANGULAR TEST CASE MODEL

A 2D rectangular test case is formulated as shown in Figure 6.30. The purpose of this model is to verify the implementation of mixture fraction/PDF model in COMSOL software. The boundaries are specified, as shown in Figure 6.30.

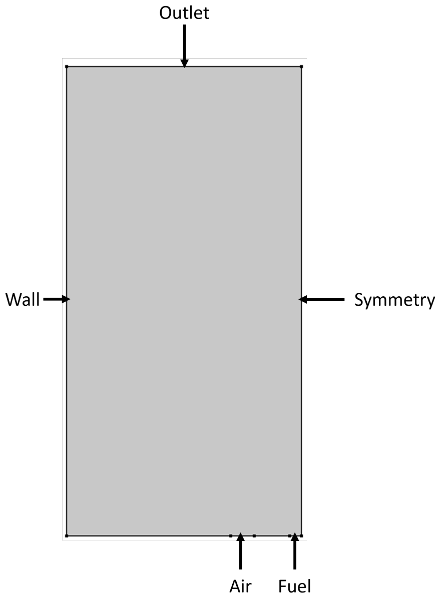

Figure 6.30: 2D test case simplified rectangular model geometry to establish mixture fraction/PDF module in COMSOL software.

The boundary conditions are as given in Table 6.6. These conditions are decided such that the equivalence ratio is higher than one to mimic lean fuel conditions in an anode baking furnace.

Table 6.6: Boundary conditions of 2D test case simplified rectangular model

Parameter	**Value**
Length of air inlet	0.1 [m]
Length of fuel inlet	0.05 [m]
Velocity of air	47 [m/s]
Velocity of fuel	5 [m/s]
Equivalence ratio	1.13

The mixture fraction and variance are computed on the simple rectangular geometry model. The details of the three meshes are given in table 6.7. The mesh sensitivity study shows that by refining the mesh, i.e., by increasing the number of elements by 23%, the change in the result of mixture fraction is within 7-8%. Figure 6.31 shows the comparison of mixture fraction calculated by transport Equation 6.1 for two meshes with different refinement. Therefore, the results are considered to be independent of the mesh.

Table 6.7: Details of the three meshes on simple rectangular test case model

Mesh	Number of elements	Average quality
Mesh 1	146422	0.95
Mesh 2	213102	0.95
Mesh 3	262723	0.94

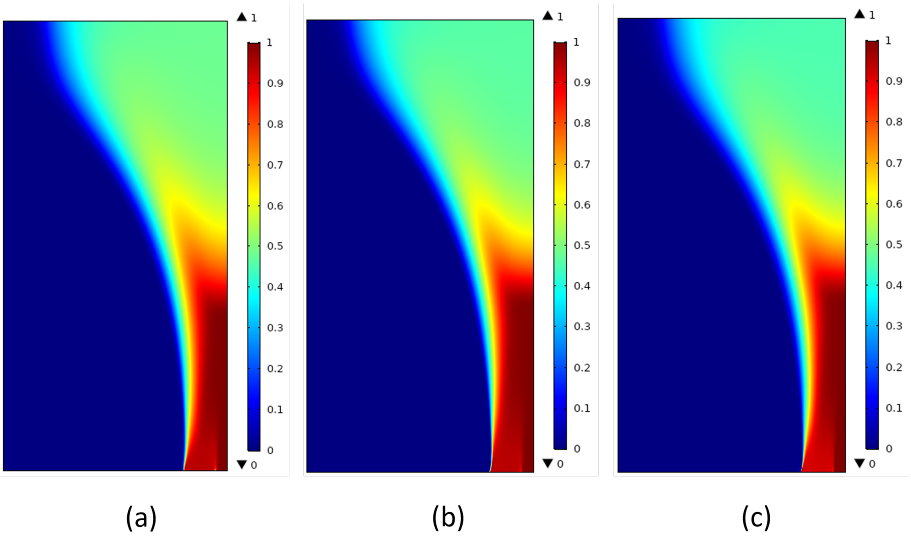

Figure 6.31: Comparison of mixture fraction computed by the transport equation of mixture fraction for (a) Mesh 1 (b) Mesh 2 and (c) Mesh 3.

For a given geometry, the reactive flow model is generated with an eddy dissipation model. The mixture fraction can be calculated using the final composition of the chemical mixture with Equation 6.10.

$$f_{\text{EDM}} = \frac{sY_{\text{fu}} - Y_{\text{ox}} + Y_{\text{ox},0}}{sY_{\text{fu},1} + Y_{\text{ox},0}} \tag{6.10}$$

where s is the stoichiometric oxygen/fuel mass ratio, Y_{fu} is the mass fraction of fuel, Y_{ox} is the mass fraction of oxygen, $Y_{\text{fu},1}$ is the mass fraction of fuel in fuel stream and $Y_{\text{ox},0}$ is the mass fraction of oxygen in the oxidizer stream. The mixture fraction computed with the transport equation as given by Equation 6.1 is compared with the mixture fraction calculated using the eddy dissipation model (Equation 6.10). Figure 6.32 shows the mixture fraction surface plot of the 2D rectangular model. It can be observed that there are slight differences in the results of the mixture fraction computed with different approaches downstream of the jet. However, these differences are less than 10%. The comparison of the two mixture fractions provides validation of the mixture fraction computed by the transport equation.

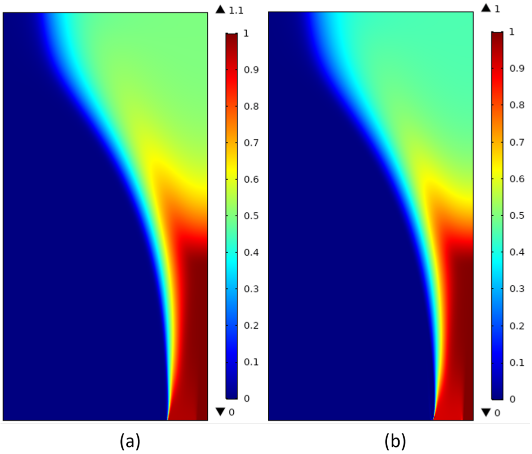

Figure 6.32: Comparison of mixture fraction computed by (a) the expression of final chemical species composition of eddy dissipation model and by (b) the transport equation of mixture fraction.

The α and β values are calculated for a model of simple rectangular case based on the mixture fraction and variance values solved by the transport equations 6.1 and 6.2, respectively. Figure 6.33 shows the corresponding alpha and beta parameter distribution at the XY symmetry plane. It can be observed that there are certain regions in the furnace where the α and β parameters are higher, and therefore, defining the shape of β-PDF for these regions is not possible.

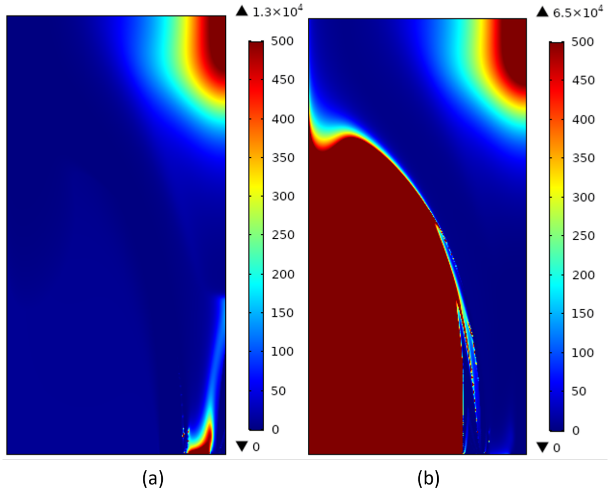

Figure 6.33: The α and β parameters at the symmetry plane of simple rectangular geometry

Figure 6.34 shows the three locations in the simple geometry case. The α and β parameters at these locations are calculated based on the corresponding mixture fraction and variance at these locations. Based on these parameters, an attempt is made to plot the corresponding PDF and CDF at those locations. It can be observed from Figure 6.34 that at points 1 and 2, the PDF is out of bound while CDF can still be calculated at these points.

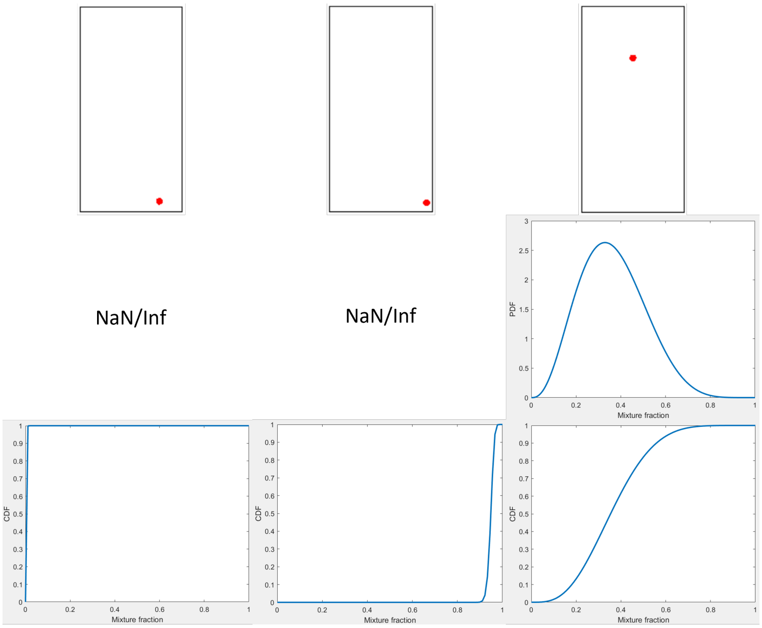

Figure 6.34: Three location points in the simple geometry and corresponding PDF and CDF calculated based on the α and β parameters at those points.

The 2D rectangular test case model confirms the parameters that can be used in the transport equation of mixture fraction and variance. Moreover, the results of this model motivates the use of the CDF approach for obtaining the average values from the instantaneous chemistry model values.

6.3.7. CHALLENGES

The development of the non-premixed mixture fraction/PDF model in COMSOL has several remaining challenges. The model is suitable for only primary streams. The addition of secondary streams requires further treatment to mixture fraction computation. Moreover, the current model does not account for the non-adiabatic conditions such as radiation or conjugate heat transfer. The non-adiabatic model requires solving one more transport equation for enthalpy. The improvement in the existing mixture fraction/PDF model is limited by the required information in the COMSOL software and methods for validation of the model. This development is out of scope for this thesis work. Therefore, the developed adiabatic model is tested with one burner anode baking furnace model.

6.4. COMBUSTION MODELING FOR ONE FUEL INLET IN ABF WITHOUT RADIATION

The model is modified by switching off the second burner inlet. The purpose of such a model is to test the improvement in the results to switch from the eddy dissipation model to the non-premixed mixture fraction model. Moreover, the effect of different chemistry mechanisms can also be tested with the non-premixed mixture fraction model. The eddy dissipation model is limited to a single-step mechanism. Figure 6.35 shows the model with one burner inlet. The model is adiabatic and therefore excludes the heat transfer through walls. The burner closer to the air inlet is activated, while the second burner fuel pipe is considered as a closed patch. The boundary condition for the model is similar to the base case model described earlier. The main purpose of the one burner anode baking furnace model is twofold.

- To check the effect of chemistry mechanism on the species and temperature in the anode baking furnace
- To compare the improvement in the model due to detailed chemistry mechanism with respect to the single-step chemistry of eddy dissipation model

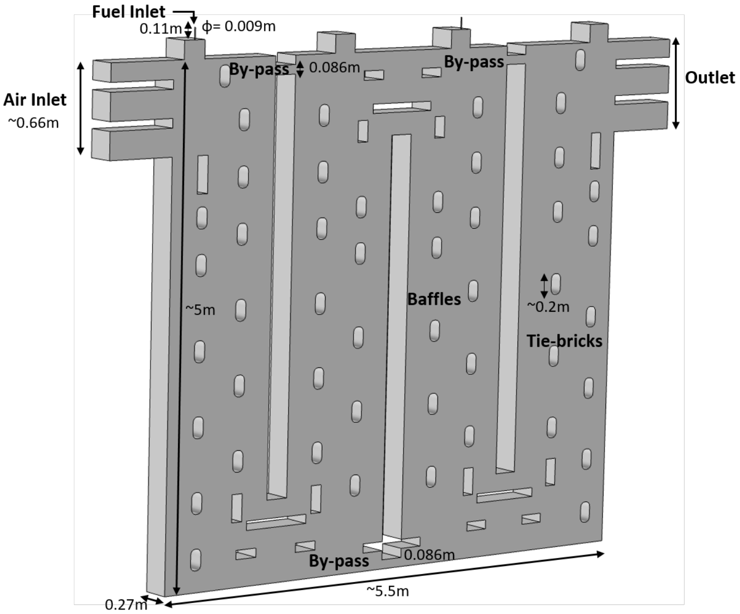

Figure 6.35: Anode baking furnace model with one activated burner

6.4.1. COMPARISON OF SINGLE STEP AND GRI 3.0 CHEMISTRY MECHANISMS

The non-premixed mixture fraction/PDF model is developed and compared for single step and GRI 3.0 chemistry mechanisms. Both models implement the non-premixed mixture fraction model developed in this work. The mass fraction distribution from Figure 6.36 shows that the amount of CO_2 formation for the GRI 3.0 mechanism model is lesser as compared to the single-step mechanism in the encircled region. This can be attributed to the presence of multiple species for the GRI 3.0 mechanism model. In the single-step mechanism model the conversion of CH_4 occurs completely into CO_2.

Whereas, for the GRI 3.0 mechanism model, there are competing reactions and the formation of other products.

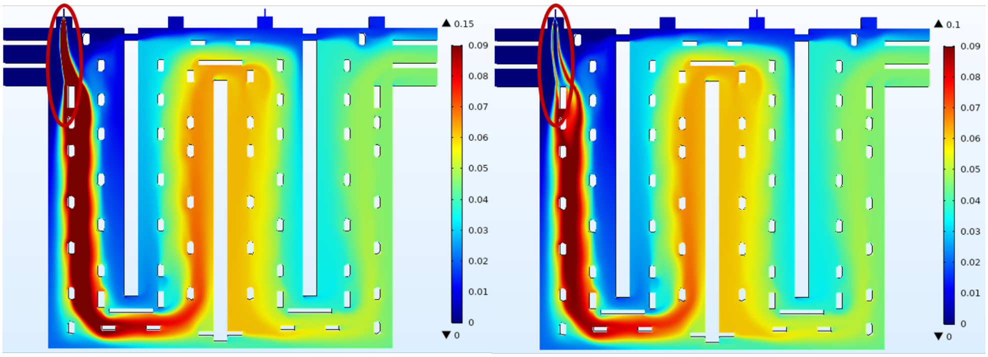

(a) (b)

Figure 6.36: Comparison of mass fraction of CO_2 at the symmetry plane obtained by non-premixed mixture fraction/PDF model with (a) single step chemistry mechanism and (b) GRI 3.0 chemistry mechanism

The effect of multiple chemical reactions for the GRI 3.0 mechanism is translated into the temperature distribution as well. The GRI 3.0 reaction mechanism consists of 325 chemical reactions. Some of these reactions are endothermic and absorb the energy released by other reactions. Due to the energy exchange among reactions, the overall heat of the combustion reaction is reduced. Therefore, the temperature in the furnace is lower for the GRI 3.0 mechanism model as compared to the single-step mechanism model, as can be observed from Figure 6.37.

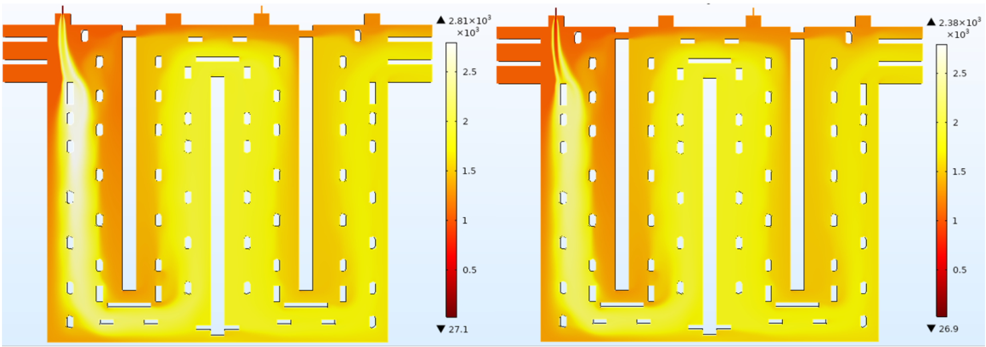

(a) (b)

Figure 6.37: Comparison of temperature in [^{o}C] at the symmetry plane obtained by non-premixed mixture fraction/PDF model with (a) single step chemistry mechanism and (b) GRI 3.0 chemistry mechanism

6.4.2. Comparison with eddy dissipation model

The eddy dissipation model is limited by the single-step chemistry mechanism. In this section, the adiabatic eddy dissipation model is compared with the non-premixed mixture fraction/PDF model with GRI 3.0 mechanism developed in this thesis. Figure 6.38 shows the comparison of mass fraction of CO_2 for both combustion models. The non-premixed mixture fraction model accounts for a detailed chemistry mechanism (325 chemical reactions of GRI 3.0 mechanism). Therefore, the CO_2 obtained by the non-premixed mixture fraction model is lower compared to the eddy dissipation model due to the presence of other chemical species.

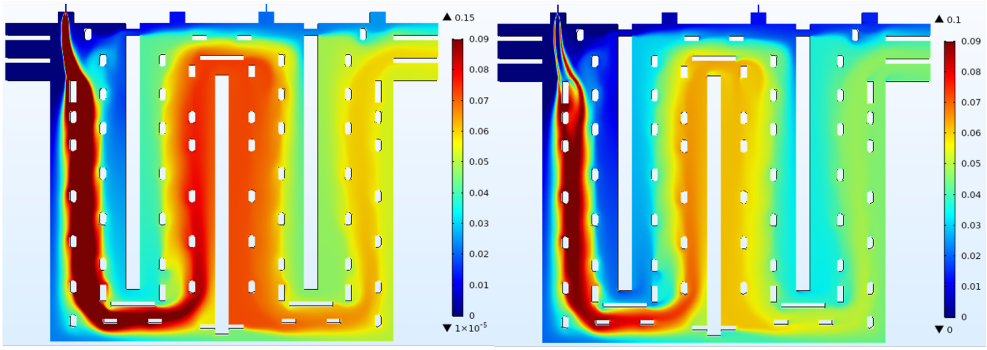

(a) (b)

Figure 6.38: Comparison of mass fraction of CO_2 at the symmetry plane obtained by (a) eddy dissipation model and (a) non-premixed mixture fraction/PDF model

6.5. HEAT TRANSFER BY RADIATION

Radiation, in the simplest terms, can be defined as the energy transfer in the form of high-speed particles or electromagnetic waves through a vacuum or medium. Generally, the radiation is more efficient through a gas medium. The emission of energy in the form of waves is possible only when the temperature of the emitting body is high enough. In the anode baking furnace, the temperatures are as high as 2000°C. Moreover, the medium in the furnace is gaseous. This favors the heat transfer in the form of radiation.

The radiation modeling involves solving a radiative transfer equation in the form of a radiation intensity field. The radiation intensity is a function of the location vector and the direction vector. The overall attenuation of the radiation intensity depends on gas emission as well as scattering in the medium in multiple directions. Furthermore, the radiation transfer equation accounts for the absorption of radiation intensity by the medium that contains gas molecules such as CO_2, H_2O which absorbs radiation intensity. The modeling of radiation is difficult due to the complex mathematics, uncertainties related to optical properties of the participating media, variability in the emissivity surfaces, and needs high computational power. As discussed earlier, the aim of this thesis work is to compute NOx generation. The generation of NOx is highly sensitive to temperature. Therefore, neglecting radiation modeling in the system like an anode baking furnace has a significant impact.

The difficulties in modeling radiation while maintaining accuracy in temperature computations can be balanced by the appropriate choice of the radiation model. There are different radiation models with varying levels of accuracy and complexity. The COMSOL Multiphysics software employed in this thesis work contains two in-built radiation models, namely, the P1 approximation model and the discrete ordinate method. Table 6.8 presents the degrees of freedom solved with these two models for a given mesh in an anode baking furnace. It can be observed that even with the S2 discrete ordinate method, which solves for a minimum number of radiation intensity rays in different directions, the degrees of freedom are much higher than the P1 approximation model. Moreover, the default solving approach for the discrete ordinate method employs the coupling of four rays in one step. The coupling of the rays inside one group leads to off-diagonal blocks with a large number of non-zero elements. The Jacobian per segregated group will thus be large and non-trivial to solve. This results in large memory requirements by the discrete ordinate method. Therefore, the P1 approximation model is chosen for the radiation modeling in this work.

Table 6.8: Degrees of freedom for different radiation models for a given mesh

Radiation model	**Degrees of freedom**
P1 approximation model	6.7M
Discrete ordinate method (S2)	37.7M

6.5.1. EFFECT OF ADDING RADIATION

The addition of radiation has a significant impact on the temperature distribution in the furnace. Due to the change in the temperature, the density of the flow field is affected, which in turn modifies the chemical species distribution. Figure 6.39 and 6.40 shows the effect of adding radiation on the mass fraction distribution of O_2 and temperature, respectively. The mass fraction distribution of O_2 downstream to both burners shows differences due to the changed density fields affecting the flow dynamics. The effect is significantly seen from the temperature distribution provided in Figure 6.40. It can be observed that the addition of radiation aids in heat transfer in the furnace resulting in a more uniform distribution of temperature. The higher temperature gradients are limited to the flame region after the addition of radiation modeling. Without radiation, the difference in the temperature distribution downstream of the first and second burner is higher. This difference decreases with the addition of radiation. Moreover, the addition of radiation lowers the maximum temperature recorded by the model due to enhanced heat transfer.

The effect of adding radiation is more prominent in the case of a lower air-flow rate. As discussed earlier in Section 6.2.2, reducing air flow velocity from 1.9 m/s to 1.45 m/s, the narrower streamline behaviour of the reaction zone is observed with higher gradients. Therefore, the addition of radiation affects the case of lower air flow velocity to higher extent, as shown in Figure 6.41. With the addition of radiation, the difference in the temperature distribution for the air flow velocity of 1.9 m/s and 1.45 m/s decreases.

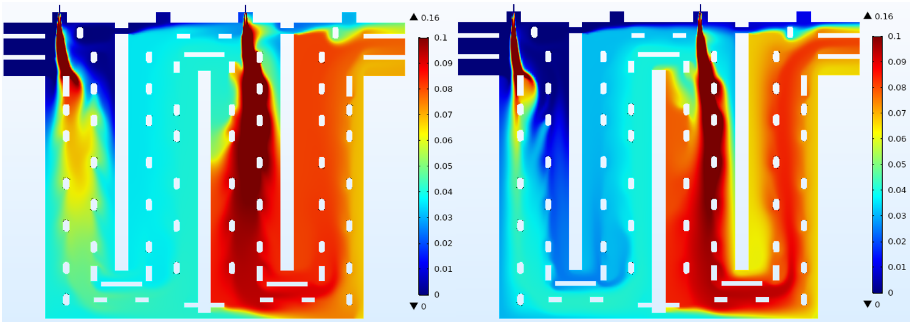

(a) (b)

Figure 6.39: The mass fraction distribution of O_2 at the symmetry plane (a) without radiation and (b) with radiation for air flow velocity of 1.9 m/s

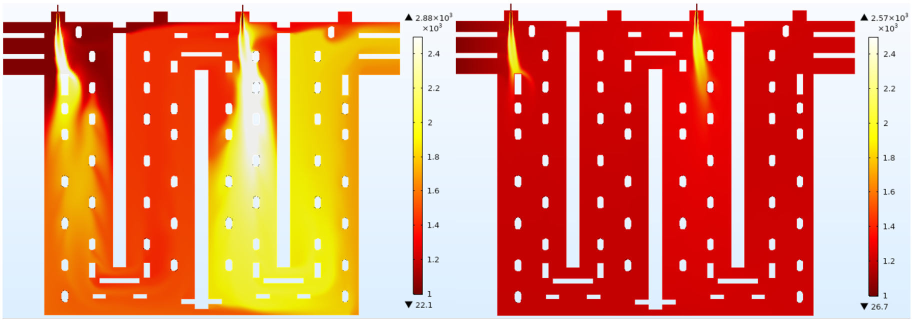

(a) (b)

Figure 6.40: The temperature distribution [^{o}C] at the symmetry plane (a) without radiation and (b) with radiation for air flow velocity of 1.9 m/s

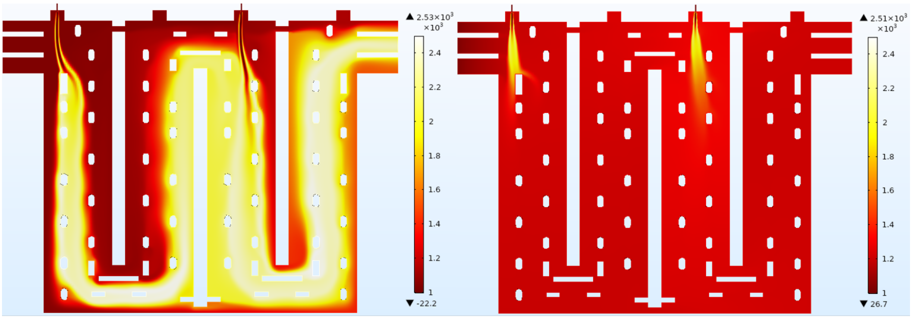

(a) (b)

Figure 6.41: The temperature distribution [^{o}C] at the symmetry plane (a) without radiation and (b) with radiation for air flow velocity of 1.45 m/s

6.5.2. MODELING OF ABSORPTION COEFFICIENT

The effect of adding radiation is explicitly described in the earlier section. However, in the earlier section, the radiation is modeled considering the constant value of the absorption coefficient. The gas medium in the anode baking furnace contains chemical species such as CO_2 and H_2O. These species are known to absorb radiation intensity due to the structure of their molecules. The absorption of radiation intensity by these molecules can be computed by analytical modeling. Among various models, Planck mean absorption coefficient is chosen for the relative simplicity in modeling without compensating for reasonable accuracy. The choice of the model is described in Chapter 2. The PMAC approach is based on the partial pressure of the radiation absorbing species and provides a more realistic modeling technique for accounting absorption coefficient. The results of the constant absorption coefficient model are compared with the radiation model with the PMAC approach. Figure 6.42 shows the temperature distribution at symmetry plane calculated with constant absorption coefficient (Figure 6.42 (a)) and with PMAC approach (Figure 6.42 (b)). It can be observed that the maximum flame temperature increases with the use of the PMAC approach. This suggests that the heat transfer by radiation has been reduced with the PMAC approach. It should be noted that the constant value of the absorption coefficient for the model is equivalent to the volume average of the absorption coefficient calculated by the PMAC approach.

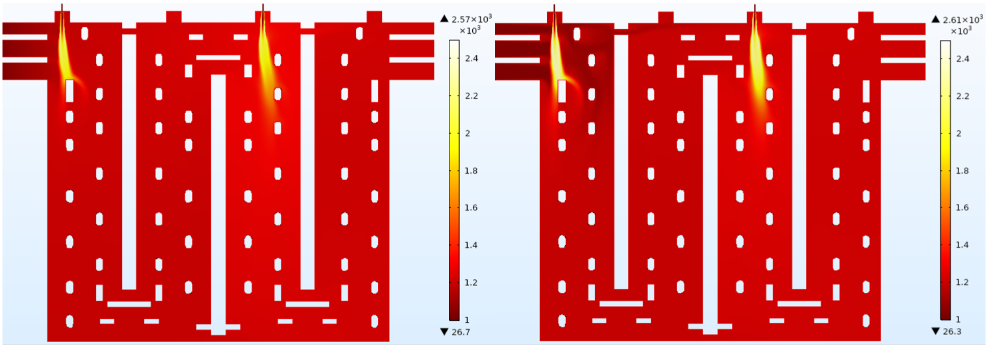

(a) (b)

Figure 6.42: The temperature distribution [^{o}C] at the XY symmetry plane with different absorption coefficients (a) constant absorption coefficient, 0.65 [1/m] and (b) absorption coefficient by PMAC

The difference between the results can be explained by the absorption coefficient plot of PMAC as shown in Figure 6.43. The plot shows that the absorption coefficient in the proximity of the flame for both burners is lesser than the average value. The absorption coefficient of CO_2 and H_2O are a function of temperature. At higher temperature, the value of absorption coefficient is lesser than average for both CO_2 and H_2O. Therefore, though their mole fraction values are higher in these regions, the absorption coefficient is lower. The lower absorption coefficient leads to the lesser absorption of radiation which results in the lower heat transfer by radiation. Therefore, the flame temperature for the model with the PMAC approach remains at a higher value compared to the constant absorption coefficient.

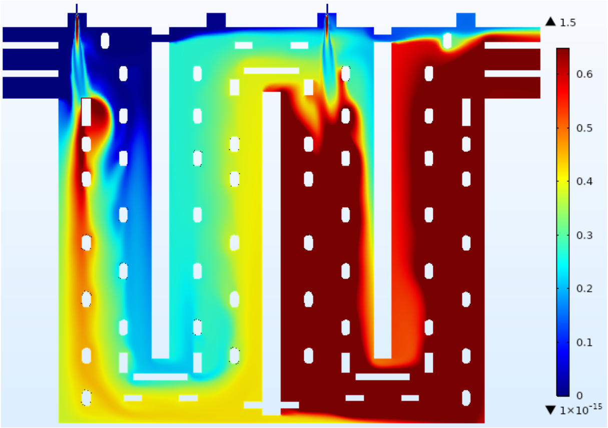

Figure 6.43: The absorption coefficient at the XY symmetry plane with the PMAC approach.

6.6. HEAT TRANSFER BY CONJUGATE HEAT TRANSFER (CHT)

The anode baking furnace consists of two phases. A furnace, referred to as flue wall, is the one in which a gaseous phase exists in the channel. The heat is generated in this channel by means of the combustion process of the natural gas. Another phase is the walls through which the heat generated in the flue channel is conducted to anodes. This phase is regarded as the solid phase. There are three layers of solid through which heat transfer occurs via conduction. The first layer is the wall that separates the flue channel and pits in which anodes are placed. The second layer is the packing coke in the pits that surround anodes to avoid heat loss in the surrounding. The third layer is of the anodes.

Figure 6.44 shows the geometry of the combined model of flue channel and three layers of solid. The thickness of the wall, packing coke, and the half anode is 0.11 m, 0.097 m, and 0.302 m, respectively.

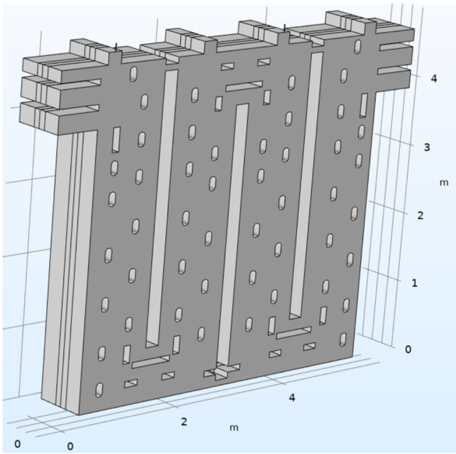

Figure 6.44: The geometry of the anode baking furnace with three layers of solid

In this study, the focus is on nitric oxide generation in the fluewall. Hence, we are primarily interested in the temperature distribution in the fluewall. The heat flux to the solid phase in the process has a significant effect on the temperature in the fluewall. The heat flux conducted to the solid phase can be calculated based on considering a single bricklayer. This results in the reduced computational domain allowing us to focus on the important region and physical phenomena. The temperature measurements are carried out at the opposite end of the brick wall, which is not in contact with the fluewall. This temperature is utilized as the Dirichlet boundary condition allowing to account for the heat flux leaving the fluewall to the solid phase. Therefore, the modified geometry of the combined model of gas and solid phase is reiterated as shown in Figure 6.45.

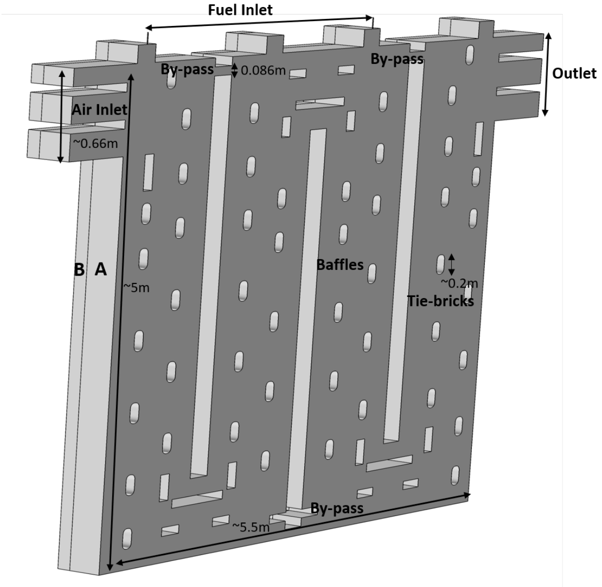

Figure 6.45: The geometry of the anode baking furnace with single brick layer representing the solid phase

The meshing of the geometry presented in Figure 6.45 is carried out using the extrusion feature of the OpenFOAM utility. The mesh of the fluewall is simply extended in the Z direction for the brick layer.

6.6.1. BOUNDARY CONDITION FOR THE SOLID

The boundary condition for the single solid layer is provided based on the measured temperature values at the bricklayer. Figure 6.46 shows the position of sixteen thermocouples. At each thermocouple, the maximum temperature recorded is extracted. The average of the maximum temperatures at these 16 thermocouples is specified as the Dirichlet boundary condition. This results in the boundary condition at the wall as 1145^{o}C. The deviation of minimum and maximum value from the average is 70^{o}C and 95^{o}C, respectively.

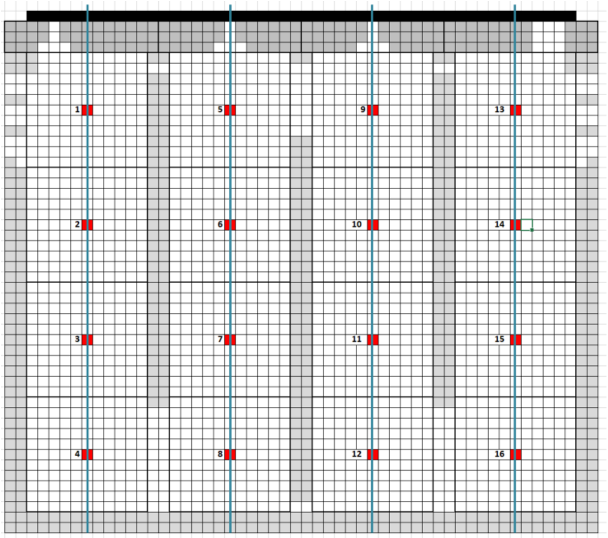

Figure 6.46: The geometry of the anode baking furnace with single brick layer representing the solid phase

6.6.2. THE COUPLED RADIATION AND CHT MODEL

The radiation and conjugate heat transfer are the major heat transfer phenomena in the anode baking furnace. The coupling of radiation and conjugate heat transfer model is carried out to understand the overall temperature distribution in the furnace. The temperature at the YZ planes passing through burner inlets is analysed. Figure 6.47 shows the temperature distribution at YZ planes through the first and second burner. It can be observed that the temperature in the furnace is lower as compared to the temperature in the solid wall in the proximity of the interface at the first burner. Whereas the temperature decreases continuously from the furnace to the wall for the second burner. This effect is visible from the line graph as shown in Figure 6.47 (c). The values of the line passing through the first burner increase at the interface and decrease from the interface in the solid domain. This effect is only slightly observed for the line through the second burner. Further analysis is carried out to understand the difference between the behaviour at the first and second burner.

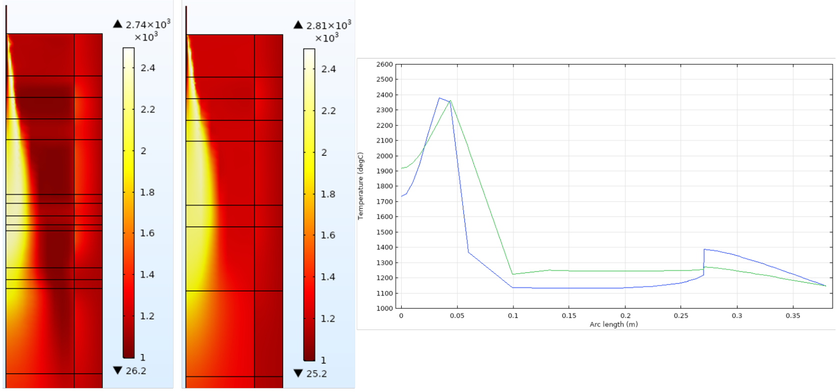

(a) (b) (c)

Figure 6.47: The temperature [^{o}C] distribution at the YZ plane by adding conjugate heat transfer through (a) first and (b) second burner (c) Line graph of temperature at Y= 4.5m at both YZ planes through first and second burner with PMAC absorption coefficient.

Figure 6.48 shows the radiation absorption coefficient at YZ planes passing through first and second burners calculated by the PMAC approach. It can be observed that the absorption coefficient at the furnace is significantly lower as compared to that near the solid wall at the proximity of the interface. The lower absorption coefficient absorbs less radiation, and therefore, the temperature in the region is lower. Whereas the conduction occurs through the solid at a faster rate, heating the region near the interface. This results in a higher temperature at the wall side as compared to the furnace side at the interface near the first burner. On the contrary, the radiation absorption coefficient at the second burner is higher. Therefore, the species absorbs higher energy increasing the temperature at the furnace side of the interface.

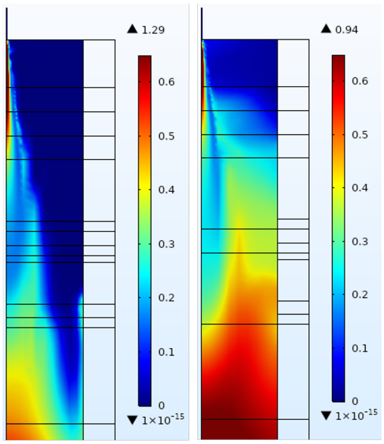

(a) (b)

Figure 6.48: The absorption coefficient calculated by PMAC approach at the YZ plane through (a) first and (b) second burner

The investigation on the effect of the radiation absorption coefficient is carried out by imposing a constant absorption coefficient in the furnace. Three values of absorption coefficients are chosen, and their effect on the temperature distribution at the YZ plane passing through the first burner is analysed. Figure 6.49 shows the temperature distribution across the YZ plane passing through the first burner for three constant absorption coefficients. It can be observed that the temperature in the furnace in the proximity of the interface increases with the increase in the absorption coefficient. With the increase in the absorption coefficient, the heat transfer in the furnace occurs faster as compared to the heat conduction through the solid wall. Therefore, the temperature drop at the furnace side disappears as the absorption coefficient value increases. Furthermore, the maximum temperature decreases with an increase in the absorption coefficient. This is the result of increased heat transfer with increasing radiation transport phenomena due to increased absorption coefficient.

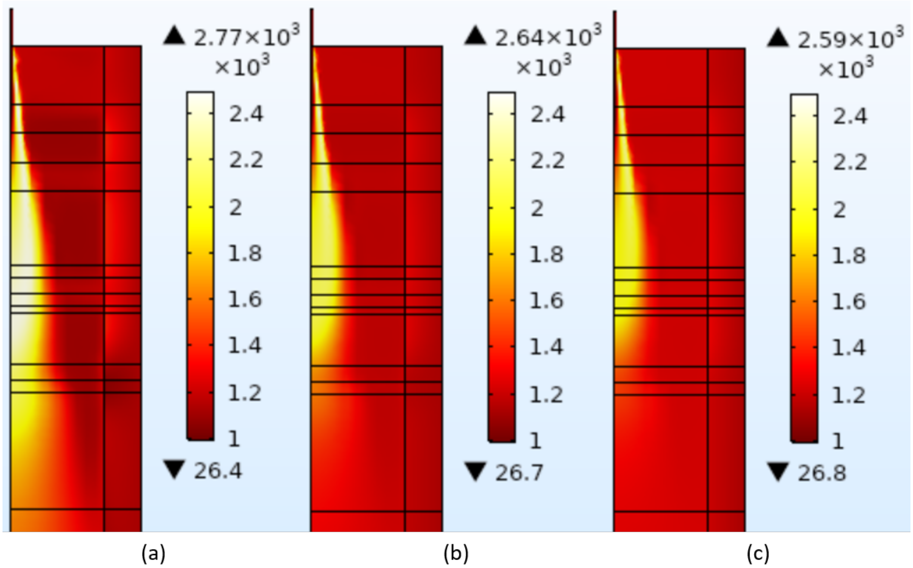

(a) (b) (c)

Figure 6.49: The temperature [^{o}C] distribution at the YZ plane by adding conjugate heat transfer through the first burner for constant absorption coefficient (a) 0.1 (b) 0.65 and (c) 1.2

This effect can be better visualized with Figure 6.50. The line graph shows the temperature [^{o}C] at the line Y= 4.5 m at the YZ plane through the first burner for three constant absorption coefficient values. As can be observed from Figure 6.50, the temperature drops for the absorption coefficient of 0.1 at the interface on the furnace side. The solid wall, in this case, is warmer. This effect disappears for the absorption coefficient of 0.65 and 1.2.

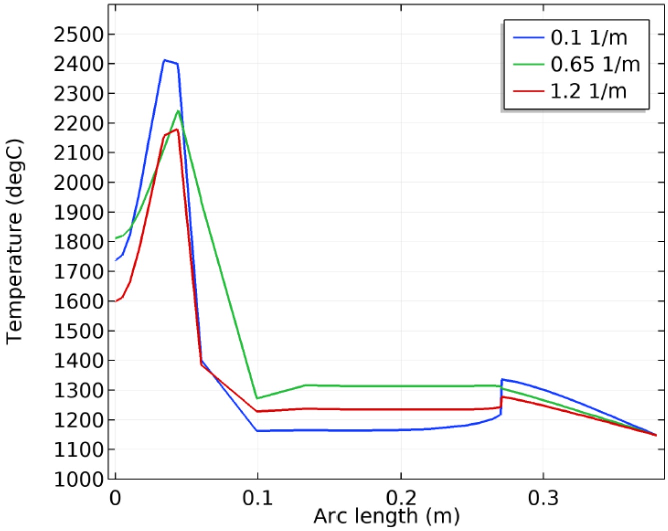

Figure 6.50: The temperature [^{o}C] at the line Y=4.5 m at the YZ plane through the first burner for three constant absorption coefficient values

EFFECT OF BOUNDARY CONDITIONS ON CONJUGATE HEAT TRANSFER FOR THREE LAYERS OF SOLID PHASE

As discussed in the geometry chapter, the solid phase consists of three layers such as bricks, packing coke, and anodes. In this section, the motivation for reducing the model from three layers to a single layer is discussed. Furthermore, the effect of the boundary condition at the interface of anodes is analysed based on the two cases. In both cases, the PMAC is used to define the radiation absorption coefficient. All other physical phenomena are also equal for both cases. In the first case, the Neumann boundary condition is specified at the interface of the anode. Whereas, for the second case, the Dirichlet boundary condition with 727^{o}C value is specified at the interface. Figure 6.51 shows the comparison of the temperature distribution at the YZ plane passing through the first and second burner for both cases. The comparison of the temperature in the fluewall shows that the temperature in the gas phase does not depend on the boundary condition at the interface. For both cases, the temperature distribution in the gas phase for the first burner is equal ((a) and (d)). Similarly, the temperature distribution in the gas phase for the second burner is equal for both cases ((b) and (e)). The difference in the temperature distribution is observed in all three layers of solids. For the Neumann boundary condition, the temperature in all three layers is equal while the temperature decreases for the first layer to the last layer for the Dirichlet boundary condition. The effect is observed prominently with the line graph of temperature plotted at Y= 4.5 m at the given YZ planes through the first and second burners. For both cases, the line graph of the first burner shows similar nature in the gas phase domain (till arc length of 0.27 m). Similarly, the line graph of the second burner shows comparable nature in the gas phase domain. However, the line graph becomes flat in the solid domain for the Neumann boundary condition and decreases for the Dirichlet boundary condition for both burners.

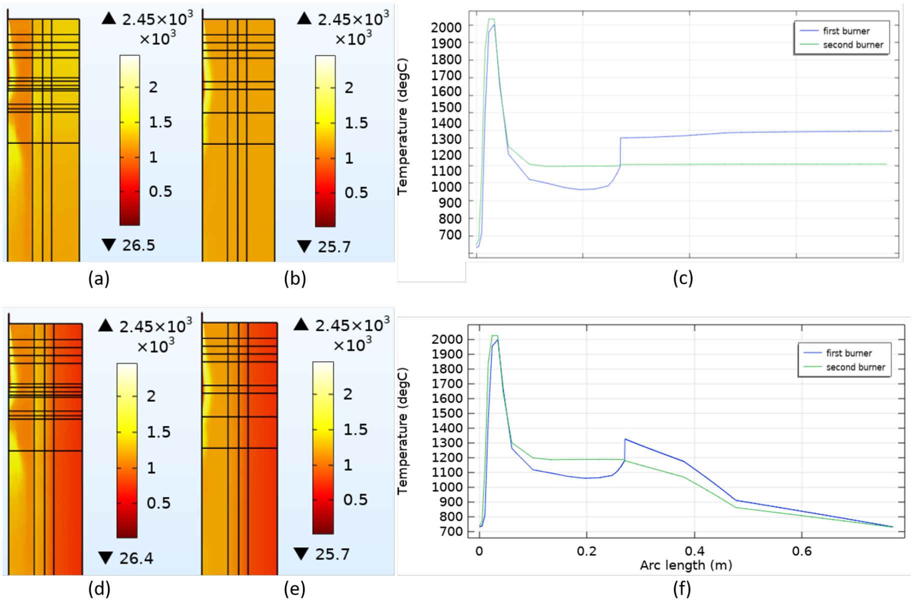

(a) (b) (c)

(d) (e) (f)

Figure 6.51: (a) Temperature distribution [^{0}C] at YZ plane passing through the first burner with Neumann boundary condition on the anode side (b) Temperature distribution [^{0}C] at YZ plane passing through the second burner with Neumann boundary condition on the anode side (c) Line graph of temperature [^{0}C] at Y= 4.5 m through YZ plane with Neumann boundary condition on the anode side (d) Temperature distribution [^{0}C] at YZ plane passing through the first burner with Dirichlet boundary condition on the anode side (e) Temperature distribution [^{0}C] at YZ plane passing through the second burner with Dirichlet boundary condition on the anode side (f) Line graph of temperature [^{0}C] at Y= 4.5 m through the YZ plane with Dirichlet boundary condition on the anode side

This analysis suggests that the effect of boundary conditions at the interface of the anodes does not have an impact on the temperature distribution in the gas domain. The temperature distribution in the solid domain is, however, highly dependent on the boundary condition at the interface. With a steady-state assumption, the constant temperature distribution with the Neumann boundary condition is justifiable. Moreover, the decrease in the temperature from bricklayer to anode layer with the Dirichlet boundary condition is also expected. In reality, the temperature decreases from the bricklayer to the anode layer. But the temperature at the middle plane of the anode interface is difficult to measure. The temperature measurements are carried out at the bricklayer with 16 thermo-couples. The average temperature can be provided as the input for the Dirichlet boundary condition for the model. As discussed earlier, this does not have a significant effect on the gas domain. Moreover, with this, the computational domain can be reduced. Since the objective is not to understand the temperature in the anodes, this treatment suffices to predict the correct temperature distribution in the gas domain.

6.7. ANALYSIS OF NOX GENERATION

The turbulent flow, combustion of natural gas, radiation, and conjugate heat transfer are the major physics involved in the anode baking furnace. The combined model, including all these physics, provides a temperature distribution in a flue wall. The thermal NOx in the furnace is dependent on this temperature distribution. Therefore, the NOx is computed by employing the Zeldovich mechanism in the post-processing stage.

6.7.1. NOX COMPUTATION FOR THE BASE CASE MODEL

Figure 6.52 shows the NOx generated in the furnace for the base case model boundary conditions. The definition of the base case model and the corresponding boundary conditions have been described in the section 6.2.1. The figure shows that the NOx generation is higher in the reaction zone underneath both burners. The NOx is higher in the second U shape of the furnace compared to the first since the temperature in the region is comparatively higher. The NOx model is extremely sensitive to temperature. Therefore, even a slight difference in the temperature affects the NOx generation to a great extent.

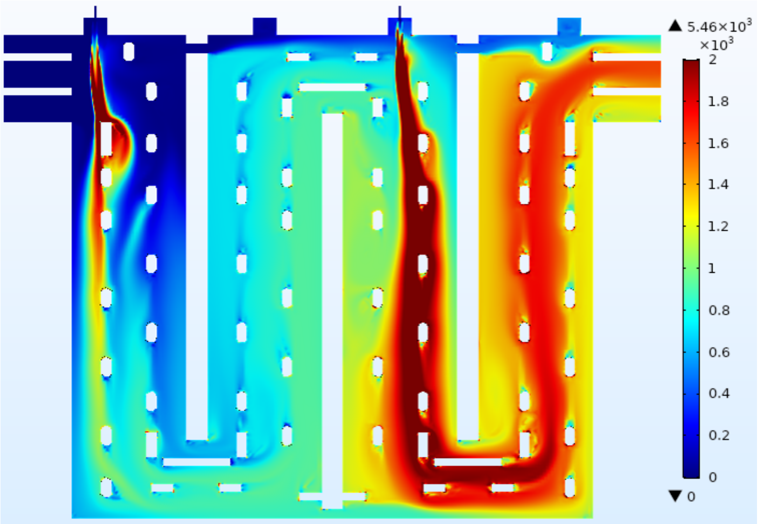

Figure 6.52: The NOx mass fraction in ppm at the symmetry plane for the base case model

6.7.2. NOX VARIATION WITH CHANGE IN AIR FLOW

The change in the inlet conditions influences the flow dynamics in the furnace. This leads to variations in the extent of reaction as well as the location of the reaction zone. In this section, the effect of an increase in the air flow rate is examined. It has been observed that the decrease in the air flow rate limits the availability of O_2 which leads to narrow streamline behaviour of the reaction zone. Moreover, the lesser O_2 results in lower extent of reaction. Therefore, the temperature in the furnace is decreased. Since the NOx generation depends on the temperature, a decrease in the temperature lowers the formation of NOx, as can be observed from Figure 6.53. Further comparison is carried out by plotting the NOx values on line Y=4.5 m at the XY symmetry plane. Figure 6.54 shows this comparison. Two peaks are observed for both models underneath the burners. The values of lower air inlet velocity are lower in most of the locations due to lower temperature values.

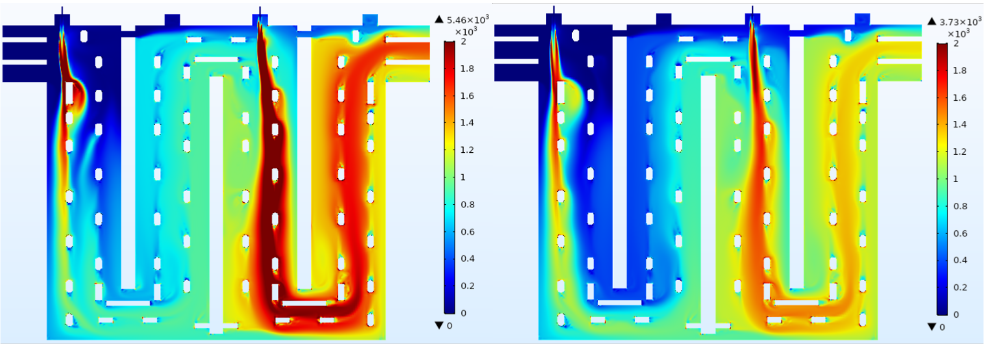

(a)

(b)

Figure 6.53: Mass fraction distribution of NOx in ppm at the symmetry plane with 9 mm fuel pipe diameter with inlet air velocity of (a) 1.90 m/s and (b) 1.45 m/s

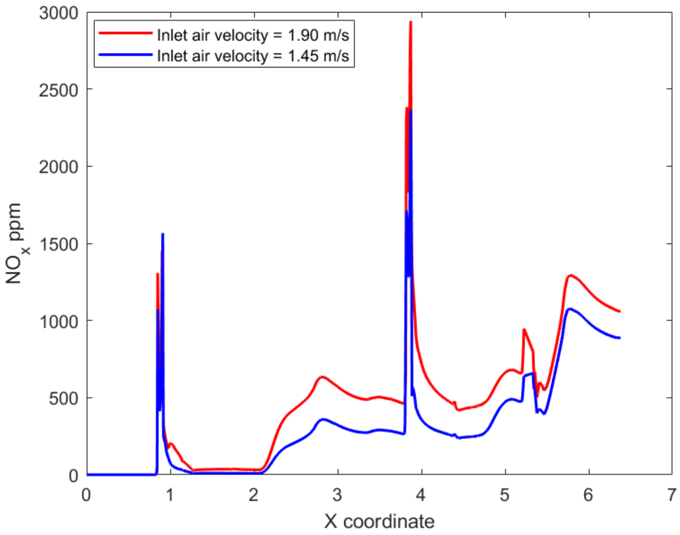

Figure 6.54: Comparison with respect to different air inlet velocity at a line Y=4.5 m on the XY symmetry plane (Z=0.27 m) for mass fraction of NOx in ppm

6.7.3. NOX VARIATION WITH CHANGE IN FUEL FLOW

The fuel jet inlet velocity is significantly higher than the air inlet flow velocity. The results in the previous section suggest variations in flow dynamics due to change in air inlet velocity. This encourages examining the effect of fuel jet velocity. Figure 6.55 shows the NOx formation at the symmetry plane for fuel jet velocities of 50 m/s, 74 m/s and 90 m/s for a fixed value of air flow velocity (1.9 m/s). The increase in the fuel jet velocity changes the flow dynamics in the furnace. Moreover, with an increase in the fuel jet velocity, more fuel amount is injected into the furnace that increases the overall reaction in the furnace. Due to higher heat generation, the temperature in the furnace increase resulting in higher NOx formation for 90 m/s. A better comparison is obtained by plotting the NOx values on line Y=4.5 m at the XY symmetry plane as shown in Figure 6.56. The NOx values increase with an increase in the fuel jet velocity.

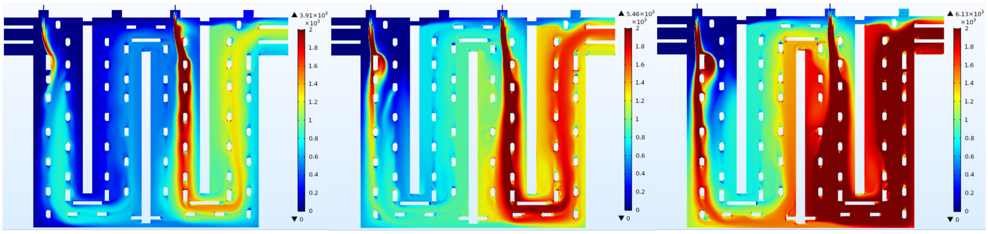

(a) (b) (c)

Figure 6.55: The NOx mass fraction distribution in ppm at the symmetry plane for varying fuel inlet velocity of (a) 50 m/s (b) 74 m/s and (c) 90 m/s with 9 mm fuel pipe diameter

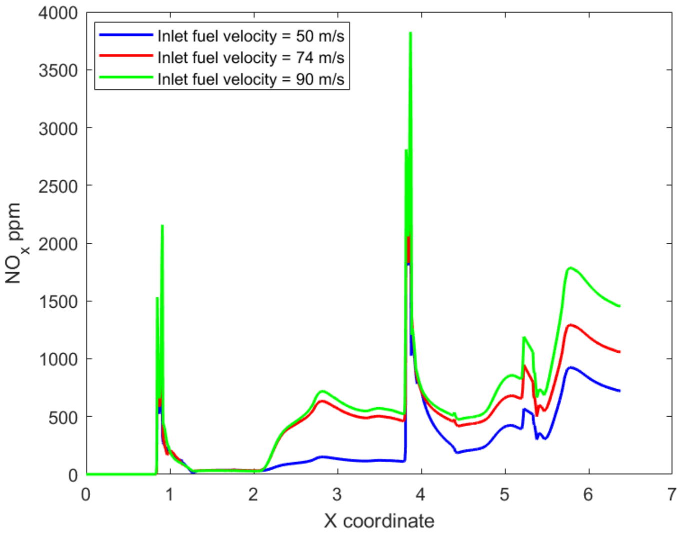

Figure 6.56: Comparison with respect to different fuel inlet velocity at a line Y=4.5 m on the XY symmetry plane (Z=0.27 m) for mass fraction of NOx in ppm

6.7.4. NOX VARIATION WITH CHANGE IN FUEL PIPE DIAMETER

The change in the air-fuel ratio by varying the air or fuel mass flow rate changes the overall enthalpy of heat formation in the furnace. The flow dynamics can be changed without changing the air-fuel ratio by varying the fuel pipe diameter. Figure 6.57 shows the NOx generation at the symmetry plane for fuel pipe diameters of 9 mm and 13 mm. In both cases, the mass flow rate of air and fuel is kept constant. The increase in the fuel pipe diameter to 13 mm decreases the fuel inlet velocity to keep the mass flow rate equal. The decrease in the fuel jet velocity lowers the turbulence in the furnace, which results in a wider reaction zone. Therefore, lower temperature zones are formed in comparison to the 9 mm diameter model. Therefore, NOx formation decreases with an increase in the fuel pipe diameter. Figure 6.58 shows the comparison of NOx plotted on line Y=4.5 m at XY symmetry plane. In general, the NOx values for 13 mm fuel pipe diameter are lesser than that of 9 mm. Underneath the second burner, the value for the 13 mm model seems to be higher at one coordinate. This might be due to local high temperatures occurring under the burner.

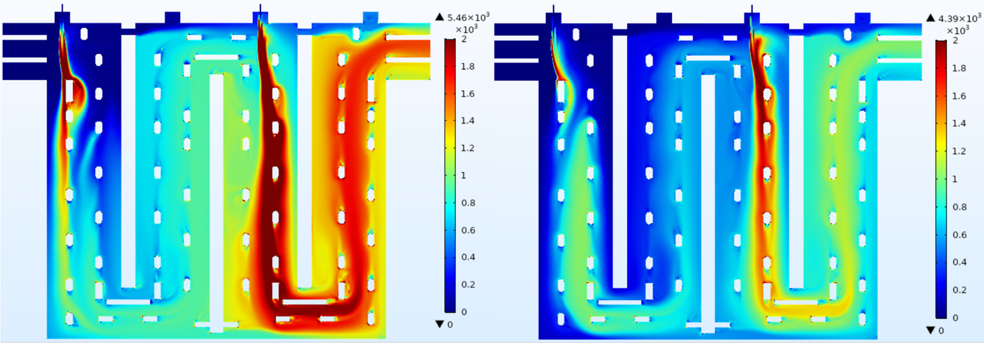

(a) (b)

Figure 6.57: The NOx mass fraction distribution in ppm at the symmetry plane for a constant fuel mass flow rate but varying fuel pipe diameter of (a) 9 mm and (b) 13 mm

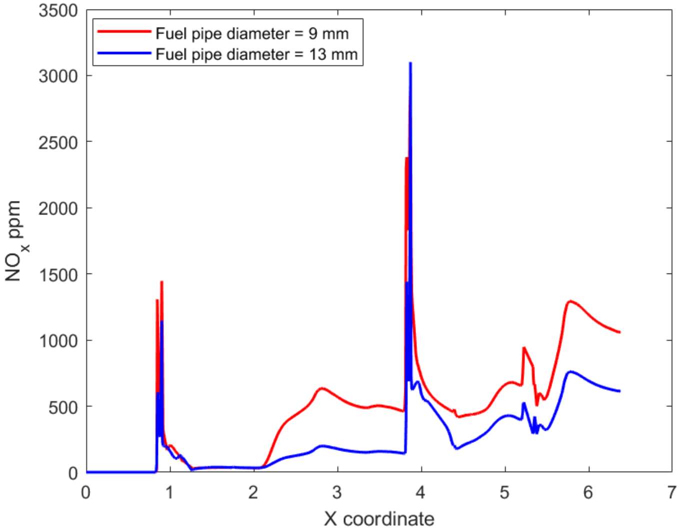

Figure 6.58: Comparison with respect to different fuel pipe diameter at a line Y=4.5 m on the XY symmetry plane (Z=0.27 m) for mass fraction of NOx in ppm

6.7.5. NOX VARIATION WITH CHANGE IN FUEL COMPOSITION

The Dutch natural gas contains around 0.81 mass fraction of CH_4. There are other two major hydrocarbons namely C_2H_6 and C_3H_8 in the fuel stream. However, the eddy dissipation model assumes that reaction rates of all reactions are based on turbulent mixing. This leads to inaccuracies with respect to the combustion process. However, assuming fuel stream to contain all CH_4 and then considering single reaction with eddy dissipation model is also imprecise. Therefore, in this section, both cases are compared. Earlier in section 6.2.5, the mass fraction of O_2 and CO_2 are compared for these cases. There are no significant differences in that comparison for the two cases. Figure 6.59 shows the comparison of NOx generation at the XY symmetry plane. It can be observed that the NOx increases significantly when multiple hydrocarbons are considered in the fuel stream.

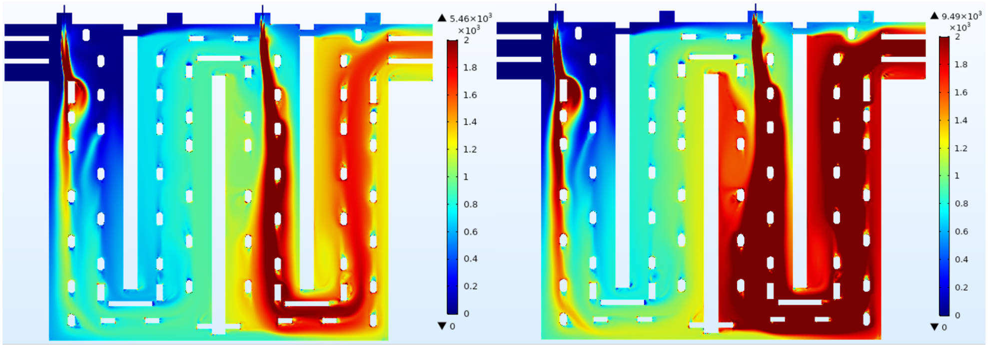

(a) (b)

Figure 6.59: The NOx mass fraction distribution in ppm at the symmetry plane for varying fuel composition with mass fraction of CH_4 as (a) 0.99 and (b) 0.81

The results are plotted on the line to have a more quantitative comparison. The line closer to fuel injection (Y=4.5 m) shows that the NOx generation for the case in which mass fraction of CH_4 is 0.81 has higher NOx. The overall analysis suggests that though the extent of the combustion reaction is equal for both cases, the heat released during the combustion process increases. This results in higher NOx formation.

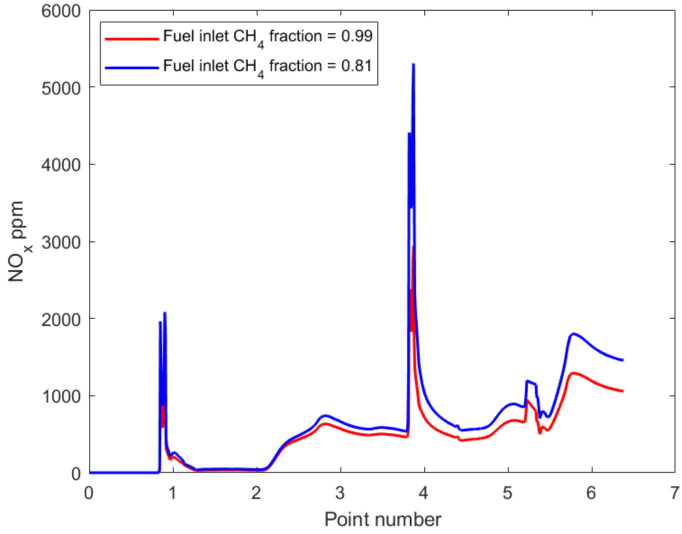

Figure 6.60: Comparison with respect to different fuel composition at a line Y=4.5 m on the XY symmetry plane (Z=0.27 m) for mass fraction of NOx in ppm

6.8. CONCLUSION

The combustion modeling in an anode baking furnace is described in the first part of this chapter. The complexity of the anode baking furnace geometry and the necessary coupling between multiple physical phenomena limits the use of a complicated combustion model for this application. In this thesis work, the simplistic eddy dissipation model is used as a combustion model. In the anode baking furnace, the combustion process is governed by turbulent flow. Therefore, the implementation of the eddy dissipation model is a reasonable approximation.

The trends of mass fraction of chemical species with varying operating conditions in the anode baking furnace are analyzed. The air flow velocity, fuel jet velocity, fuel pipe diameter, and fuel composition are varied, and their effect on combustion are examined. The decrease in the air flow velocity changes the flow dynamics in the furnace. The narrow streamline reaction zones are observed by lowering the air flow velocity. The overall production of CO_2 remains similar due to excess air in both cases. However, due to the availability of higher O_2 near the fuel outlet in the case of higher air flow rate, higher mixing occurs, leading to higher temperature zones. Similarly, an increase in the fuel jet velocity increases the combustion reaction source term in the furnace. This leads to the higher CO_2 production and higher temperature. This observation is confirmed by tests in Aluchemie furnace as well. With the lowering of fuel pressure (which leads to lowering of fuel jet velocity), lower temperature zones are observed in the furnace. Furthermore, the effect of keeping the air-fuel ratio constant but varying the flow dynamics is tested by changing the fuel pipe diameter. It has been observed that by increasing the fuel pipe diameter, the fuel injection velocity has to be decreased to maintain an equal flow rate. This leads to lower momentum of the jet, resulting in a wider reaction zone. Such flow dynamics decrease the maximum temperature in the furnace as the flame is stretched. Another analysis is carried out to compare the effect of the varying fuel composition. In reality, the fuel consists of significant percentage of C_2H_6 and C_3H_8. The addition of these reactions does not change the species distribution. The temperature in the section after the second burner is relatively lower when multiple reactions are considered. However, with the eddy dissipation model, the inaccuracies increases for multiple reaction rates. Therefore, it is difficult to conclude which of the two models with different fuel compositions is more accurate.

The multiple reaction mechanisms can be handled precisely by selecting another combustion model. The non-premixed mixture fraction/PDF model provides a better framework to account for multiple reaction mechanisms. The COMSOL Multiphysics software has limited inbuilt combustion models. In this thesis work, a module for the non-premixed mixture fraction/PDF model for an adiabatic case is developed. The models confirm that the temperature in the furnace decreases when multiple reaction mechanisms (such as GRI 3.0) are considered. Therefore, the existing anode baking furnace model can be improved by developing the non-premixed mixture fraction/PDF model for the non-adiabatic case. Such development is out of the scope for this thesis work.

After careful examination of combustion modeling, the model is improved by adding heat transfer phenomena. The radiation and conjugate heat transfer to the wall are the major components of the heat transfer modeling. The P1 approximation radiation model is implemented due to its relative simplicity and reasonable accuracy. The enormous (six times as that of the P1 approximation model) increase in degrees of freedom with the discrete ordinate method and the default coupled solver approach for the group of radiation intensity rays demands for high computational power. Therefore, the P1 approximation model is applied. The addition of radiation and conjugate heat transfer to solid distributes the temperature in the furnace uniformly. Moreover, the mass fraction distribution changes due to varying flow dynamics associated with the temperature-dependent density field.

The Planck mean absorption coefficient (PMAC) is calculated for the radiation absorbing species such as CO_2 and H_2O. The overall absorption coefficient of the gaseous mixture is based on the mole fraction average of the individual PMAC of chemical species CO_2 and H_2O. It has been observed that the absorption coefficient computed by the PMAC approach is lower than the average value in the region underneath both burners. This is due to the dependency of PMAC on temperature. With higher temperatures, the radiation absorption by chemical species decreases. Therefore, though the mole fraction of CO_2 and H_2O are higher in the region of flame, the absorption coefficient is lower. The varying absorption coefficient distributes the temperature based on the radiation absorption capacity. Whereas for the constant absorption coefficient, the radiation absorption is equal. Therefore, the non-uniform and more realistic temperature distribution is obtained by the PMAC model.

The coupling of radiation and conjugate heat transfer shows the temperature dip at the interface of the wall on the furnace side. Usually, a continuous decrease in the temperature would be expected. This temperature dip is associated with a lower absorption coefficient in the region. The dip is lower for the second burner due to the higher radiation absorption coefficient. A study of three constant absorption coefficients confirms that for a lower absorption coefficient higher temperature dip in the furnace occurs at the interface.

Finally, the NOx computation is carried out in the post-processing stage. The NOx generation is highly sensitive to the temperature in the furnace. The formation occurs in the high-temperature reaction zones. The NOx formation with varying air inlet velocity, fuel inlet velocity, fuel pipe diameter and fuel composition is examined. The increase in air flow velocity and fuel flow velocity increases the NOx generation due to higher combustion and subsequently higher temperatures. Whereas an increase in the fuel pipe diameter decreases the NOx generation due to the spread-out reaction zone. The effect of fuel composition on NOx generation is difficult to judge due to the higher inaccuracies with multiple reactions in the eddy dissipation model.

7

MEASUREMENT IN THE ANODE BAKING FURNACE

In this chapter, the model approximations are compared with experimental results from the anode baking furnace of Aluchemie. The measurement of chemical species and temperature is carried out at locations that are easily accessible. The measurement techniques are described, followed by their comparison with the model values. In most industrial applications, the approximate solutions of model provide extensive insights that are otherwise not possible to obtain with experiments. Since multiple approximations are involved in numerical modeling, it is essential to validate these models. Therefore, measurement proves to be important in the validation process.

7.1. MEASUREMENT TECHNIQUES

The anode baking furnace of Aluchemie is situated in Rotterdam, The Netherlands. Due to collaboration with the company, the furnace is accessible for performing measurement drives. For the validation of the model, the possible measurement values from the furnace are obtained for chemical species such as O_2, CO_2 and NOx. Moreover, the values of temperatures are also measured at certain locations. It should be noted that the measured values are not extracted from the lab scale environment. The values are from the actual furnace of Aluchemie.

7.1.1. MEASUREMENT OF TEMPERATURE

The company has a FLIR P640 12^o, FLIR infrared imaging camera. The infrared energy (radiation) is detected by these cameras and converted into an electronic signal. This signal is then processed to produce a thermal image which can be used to predict temperatures in heating chambers [102]. Since the camera is not inserted inside the furnace, the picture can be taken through all four top openings of the section. For the two openings, the burners are removed, and pictures are taken from the top. While, for the other two openings, the floor plates are removed to take pictures. Figure 7.1 shows a picture taken through the camera through the four top openings. It can be observed that temperatures underneath both burners are higher compared to the temperatures recorded through the other two openings. Moreover, temperature increases while going through the first burner to the second burner due to the combustion of pre-heated air under the second burner. Moreover, the temperature measured at the opening after the first burner is slightly cooler than the temperature measured at the opening after the second burner.

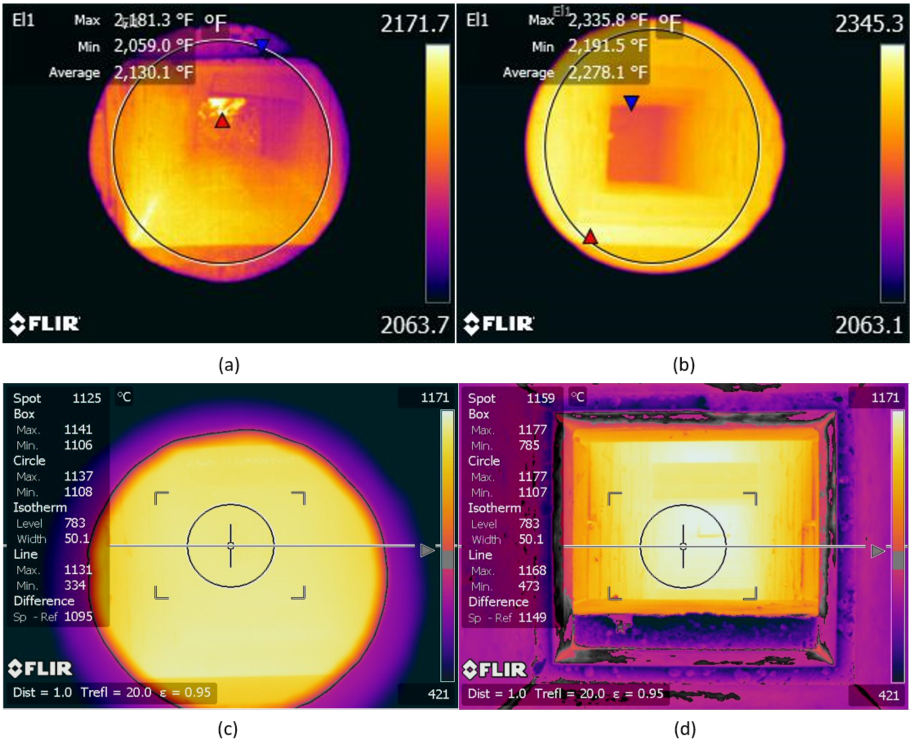

(a) (b)

(c) (d)

Figure 7.1: Pictures obtained by the Flir Infrared camera through removing (a) first burner (b) second burner (c) floor plate of second top opening and (d) floor plate of second top opening

7.1.2. MEASUREMENT OF CHEMICAL SPECIES

The company has a Testo 350 flue gas analyser for the measurement of chemical species [103]. The device consists of two main parts, namely, the control unit and the analyser unit. The control system provides a list of settings to control the analyser unit. The analyser unit consists of the probes for different chemical species with sensor technology. The probe can be inserted into the furnace, and the automatic recording of chemical species is carried out. The number of chemical species measured depends on the activated probes. Figure 7.2 shows the locations at which three species namely O_2, CO_2 and NOx are measured from the anode baking furnace. The probe is sensitive to a higher temperature and may get damaged if exposed to high temperatures (> 1800°C). Such high temperatures are expected only in the region where fuel is injected. Therefore, the location points shown in Figure 7.2 are chosen such that the measurement points are away from the flame under burners. As can be seen from Figure 7.2, three points are chosen after the first burner while three more points are chosen after the second burner. Moreover, first three-point locations are varied by keeping the y-coordinate same, while for the remaining three points, the x-coordinate is kept constant. It should be noted that these locations are only approximate. Therefore, the comparison can not be claimed to be very accurate. The comparisons, however, help to understand the range in which the values of various chemical species should reside.

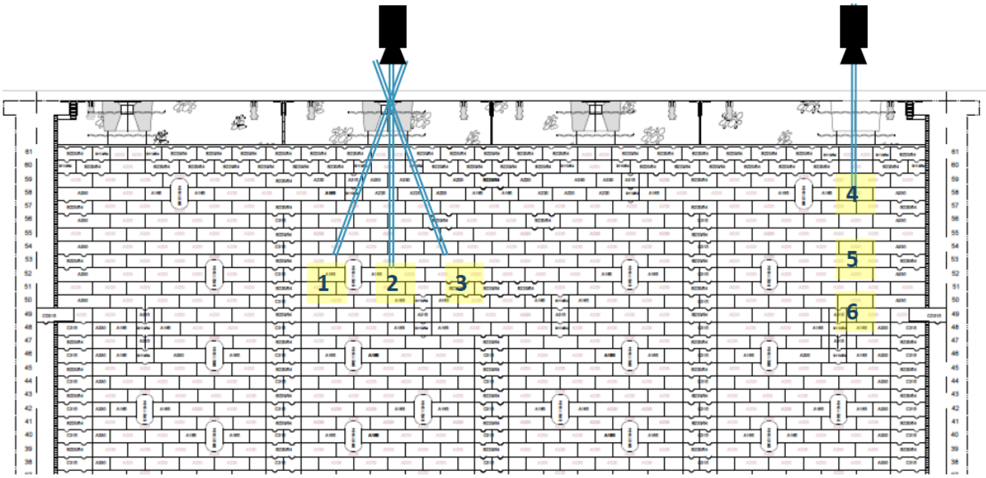

Figure 7.2: Location of the measurement points in the furnace

The probes are inserted by removing the floor plate. Figure 7.3 shows some of the pictures when the probe is inserted in the furnace by removing the plate. The height of the probe is adjusted based on the location point. At each location, the values are measured for five minutes at a frequency of one measurement per second. The probe is cooled down to room temperature before inserting at a new location to avoid measurement errors at the next location point.

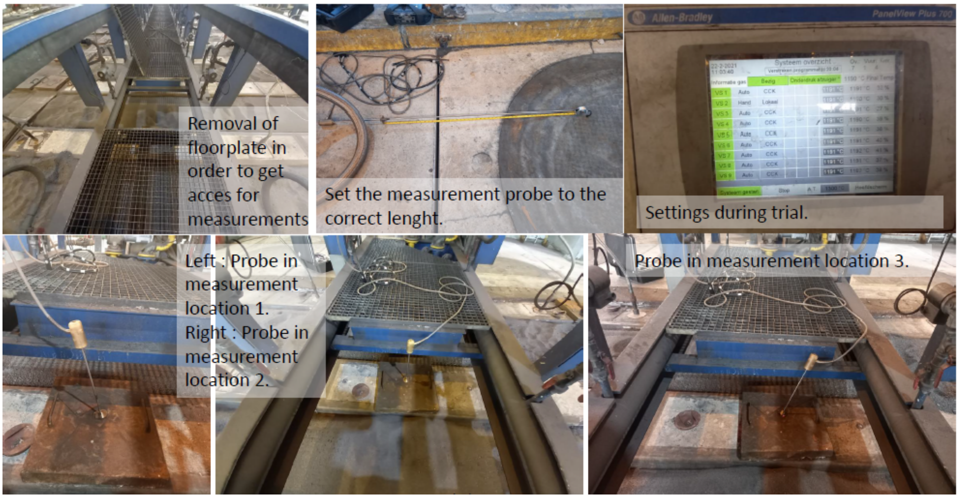

Figure 7.3: Real pictures while setting the probe in the furnace during the measurement drive

7.2. COMPARISON OF MEASURED TEMPERATURE WITH MODEL

The images captured by the camera are shown in Figure 7.1. In this section, the temperature given by the camera after processing the image is compared with the model values. The pointers in the pictures of the camera approximately show the depth at which the temperature is processed. For all images taken through top holes, the temperature is computed at the bottom side of the furnace, which is comparatively stable with respect to dynamics. The lines as shown in Figure 7.4 (a) are drawn at YZ planes passing through each top hole. The measured values by the camera provide the temperature at one of the points on these lines. The temperature at these lines is plotted as shown in Figure 7.4 (b). The temperature plots of the model data show that the values do not change significantly on lines that are not underneath burners. There is a slight increase in the temperatures for lines that are underneath burners, especially for the second burner. Therefore, the average of the values at these lines can be compared with the values from the measurement. Table 7.1 presents the average temperature of the model and the measured temperatures by the camera. The comparison shows that for each part of the section, the temperature computed by the model is higher than the measured values. It should be noted that values compared in the table are approximate since the exact location of the measurement is not known. However, the relative differences between the model and measured values are within 10%. The trends predicted by the model are similar to those of measured values. The temperature under the second burner is higher than that of the first burner for both data of model and measurements. Consequently, the region after the second burner has a higher temperature than that of the region after the first burner for both data of model and measurements.

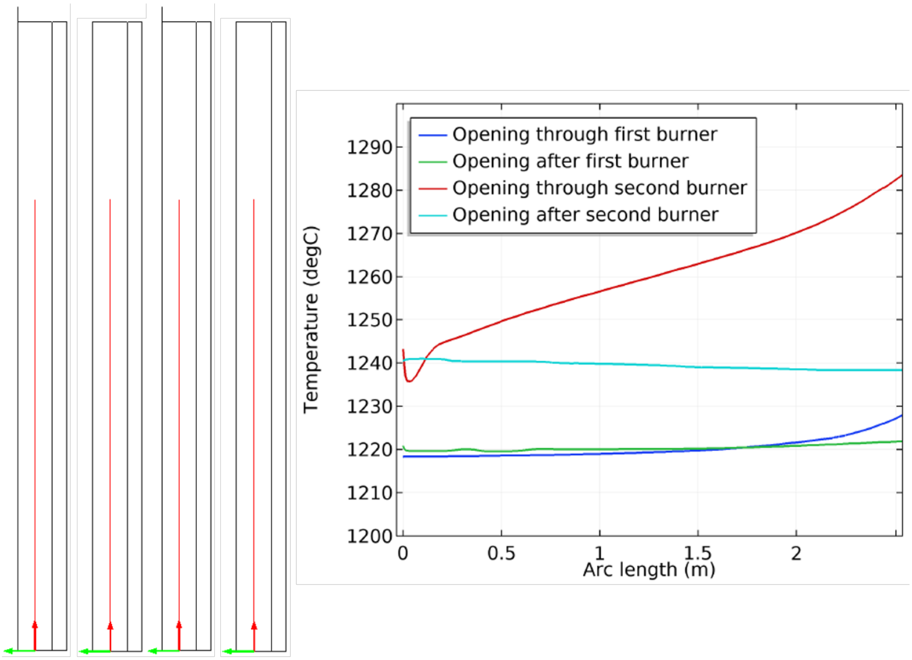

(a) (b)

Figure 7.4: (a) The average temperature is computed at these Lines on YZ plane cutting through the center point of the top four openings. The regions shown by these lines are assumed to be visible through top four openings of the furnace (b) Temperature calculated at these lines with model

Table 7.1: Comparison of temperature computed by model and predicted by Flir infrared camera

Location	**Measurement [^{o}C]**	**Model [^{o}C]**	**% overprediction**
Opening through first burner	1165	1224	5.1
Opening after first burner	1125	1220	8.4
Opening through second burner	1250	1265	1.2
Opening after second burner	1159	1240	7.0

7.3. COMPARISON OF MEASURED CHEMICAL SPECIES WITH MODEL

The approximate locations of the measurement points are shown in Figure 7.2. Based on the length of the inserted probe and the angle of insertion, approximate coordinates of the measured points are calculated. The values computed at these coordinates are compared with the measured values. The boundary conditions for the test case model described in the earlier chapter (Chapter 6) are based on the known values from measurements at the boundaries. Therefore, the values of the test case model are compared with the measured values.

Figure 7.5 and 7.6 shows the comparison of volume % of O_2 and CO_2 at six locations computed by the model and measurement by the analyser. The Testo 350 flue gas analyser is assumed to have a machine error of 15%. The error bars over the measured data account for this machine error. The results show that the test case model provides good comparison with the measured values for O_2 and CO_2. The trends such as the decrease in O_2 for the set of three points in the second part of the furnace compared to the first part of the furnace are correctly predicted. Results of the comparison suggest that the combustion is slightly over predicted at the second burner compared to the measured values.

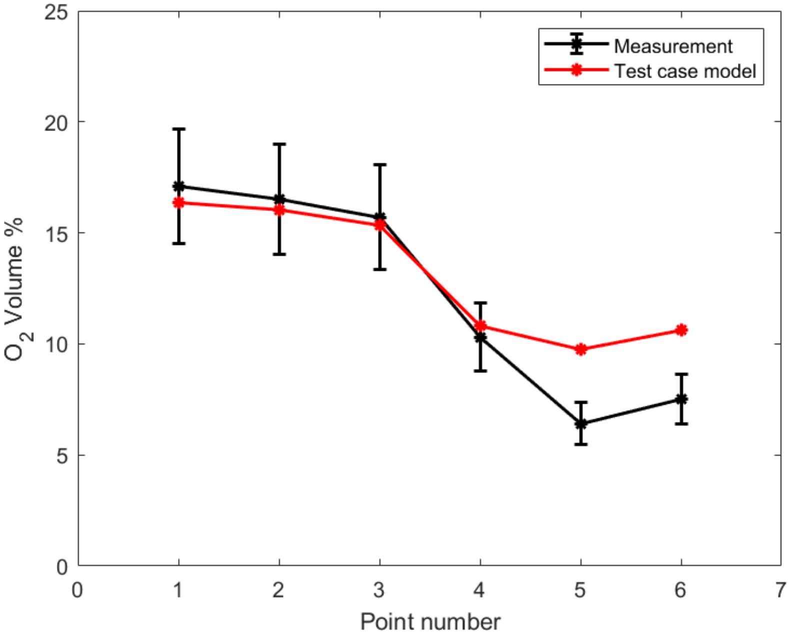

Figure 7.5: Comparison of model values and measured values in volume % at six locations for the chemical species O_2

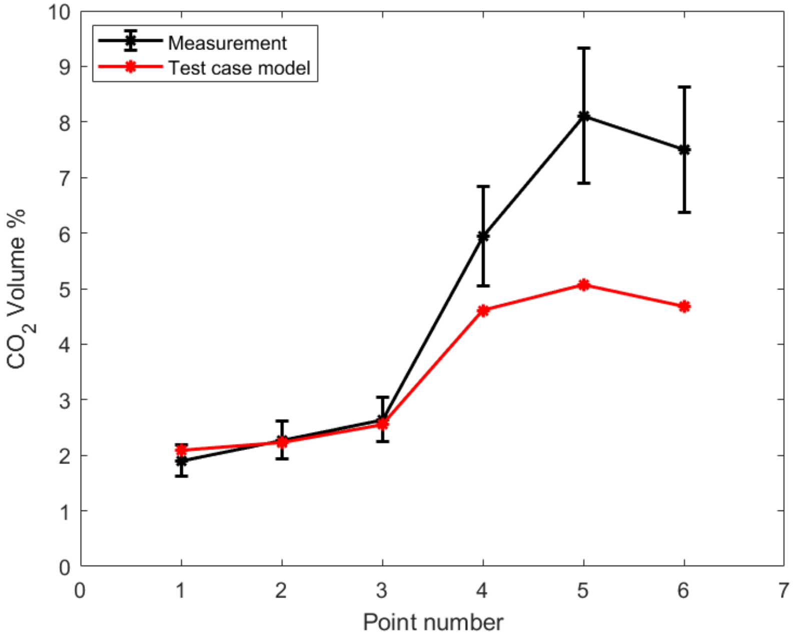

Figure 7.6: Comparison of model values and measured values in volume % at six locations for the chemical species CO_2

The analyser also measures the NOx from the furnace. Figure 7.7 shows the comparison of NOx at six location points measured in the furnace with that of the model values. Unlike the comparison of O_2 and CO_2, the NOx values computed by the model are significantly higher than the measured values. The over prediction of NOx by the model can be attributed to various factors. The difference in the values is higher, especially for the three points in the second part of the section. As seen from the comparison plots of CO_2, the overall combustion modeled in this part is over predicted. This increases the temperature in the furnace. Since the NOx is sensitive to the temperature, even a slight difference in the temperature results in a higher difference in NOx. In reality, the fuel injection is carried out in pulses. This reduces the NOx formation in the furnace compared to the continuous injection case. Therefore, though the mass flow rate for a given pulse utilized in the furnace is equivalent to the boundary condition for the model, the amount of fuel injection changes. We varied different conditions at the boundaries of the model to examine their effect of the comparison with measurements. As mentioned earlier, the boundary conditions are calculated based on known values from the furnace. These computations of boundary conditions from the known values involve considering various assumptions. Therefore, varying conditions at boundaries and comparing them with measurements can provide more insights about conditions in the furnace.

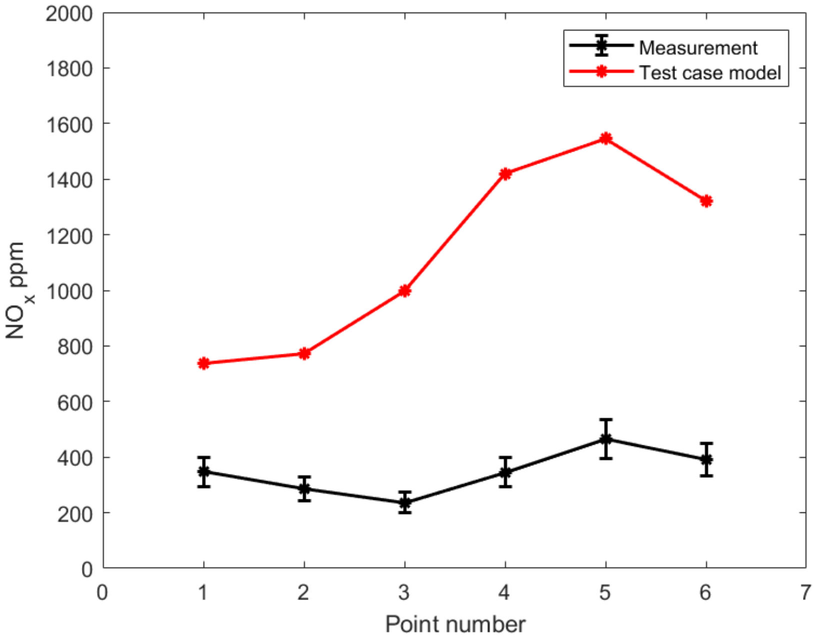

Figure 7.7: Comparison of model values and measured values in volume % at six locations for the chemical species NOx

7.3.1. AIR FLOW RATE VARIATIONS

The velocity boundary condition at the air inlet is calculated using measured values of flow rate. The temperature at the inlet is required to compute density at the inlet. The thermocouple data at the inlet provides a range of temperatures calculated over time. The boundary condition for the test case model is based on the average temperature of the given range. In this section, the results of the test case model (1.9 m/s) are compared with lower air inlet velocity calculated considering the minimum temperature of the thermocouple range. Figure 7.8 shows the comparison of volume % of O_2 and CO_2 for two models and set of measured values. For the initial three points, the test case model compares well with the measured values. For the last three points, the measured values are between those of the two models. The last three points are after both burners are activated. Therefore, the values at these points would depend a lot on the combustion process. Moreover, the figure shows that the values of O_2 are higher at all points for a higher velocity model. While, the CO_2 is lower for a higher velocity model.

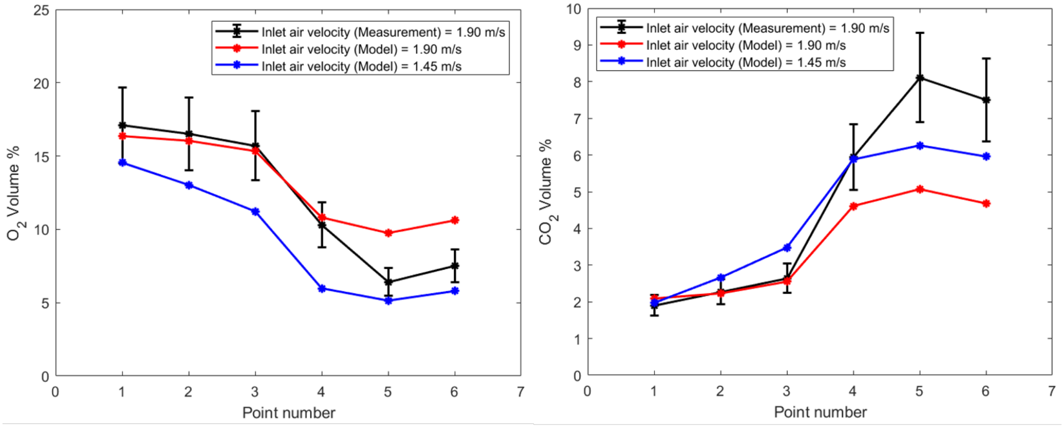

(a) (b)

Figure 7.8: Comparison of model values and measured values in volume % at six locations for the chemical species (a) O_2 and (b) CO_2 for varying values of air inlet velocity

Figure 7.9 shows the NOx comparison at six locations for the two models of varying air inlet velocity and measurement. The NOx is overestimated with both models compared to measurement. The NOx values for higher air inlet velocity are higher due to an increase in the temperature through a higher combustion process. The overestimation with respect to measurements is due to the relatively high temperature from the model, as discussed earlier.

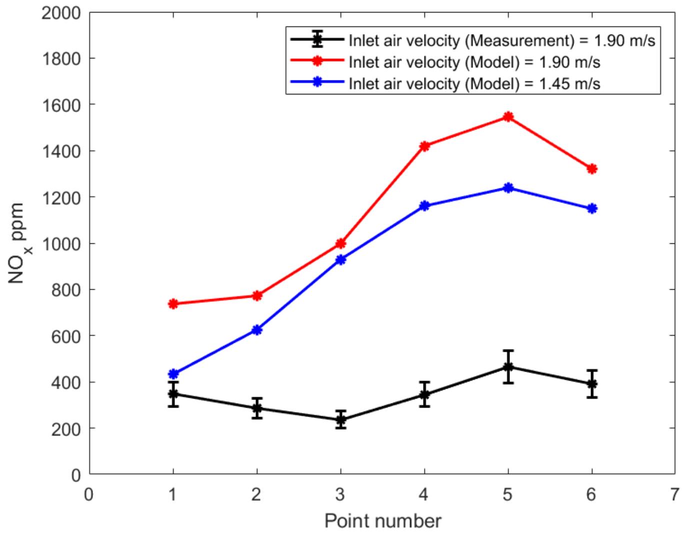

Figure 7.9: Comparison of model values and measured values in volume % at six locations for the NOx with varying values of air inlet velocity

7.3.2. FUEL FLOW RATE VARIATIONS

The fuel injection in the Aluchemie furnace occurs in pulses. A time-dependent model is required for modeling this behaviour which is out of scope for this work. In this section, the fuel injection velocity is varied, and the values are compared at six measurement locations. Figure 7.10 shows the comparison of volume % of O_2 and CO_2 for models with varying fuel inlet velocity and measurements. The measured values of O_2 compare well with the test case model at most of the points. The measured values of CO_2 at the last three points are higher than all models. Comparison of only model values suggests that with an increase in fuel injection, the extent of the combustion process increases.

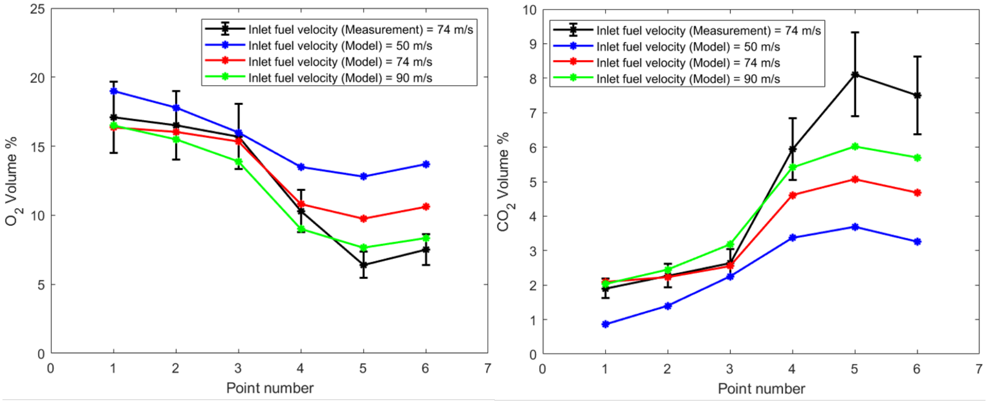

(a)

(b)

Figure 7.10: Comparison of model values and measured values in volume % at six locations for the chemical species (a) O_2 and (b) CO_2 for varying values of fuel inlet velocity

Figure 7.11 shows the comparison of NOx for models with varying fuel inlet velocity and measurements. All models overestimate the NOx compared to measurements due to overestimation of the temperature. The increase in fuel inlet velocity results in a further increase of NOx.

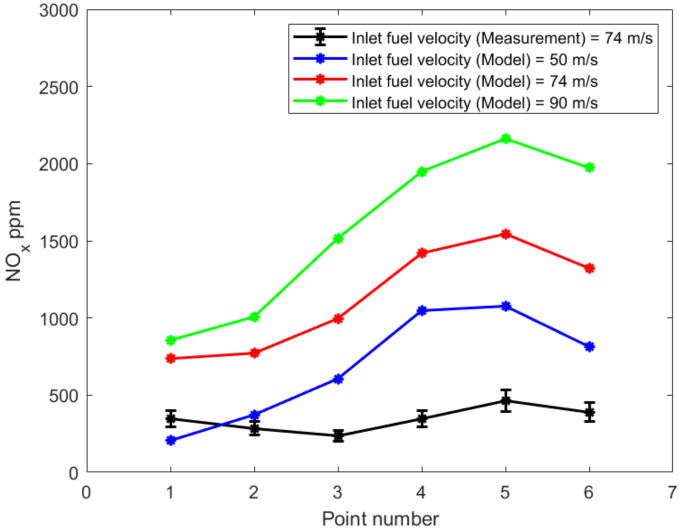

Figure 7.11: Comparison of model values and measured values in volume % at six locations for the NOx with varying values of the fuel inlet velocity

7.3.3. FUEL COMPOSITION VARIATIONS

The mass fraction of CH_4 in the fuel stream is varied. The eddy dissipation model is generally used for a single reaction. Multiple reactions can be implemented with the eddy dissipation model but they increase inaccuracies in the reaction rates. Therefore, a compromise is made by either considering an inaccurate assumption or fuel stream comprising of only CH_4. Figure 7.12 shows the comparison of O_2 and CO_2 for models with varying fuel composition. It can be observed that with both models results do not vary significantly for O_2 and CO_2.

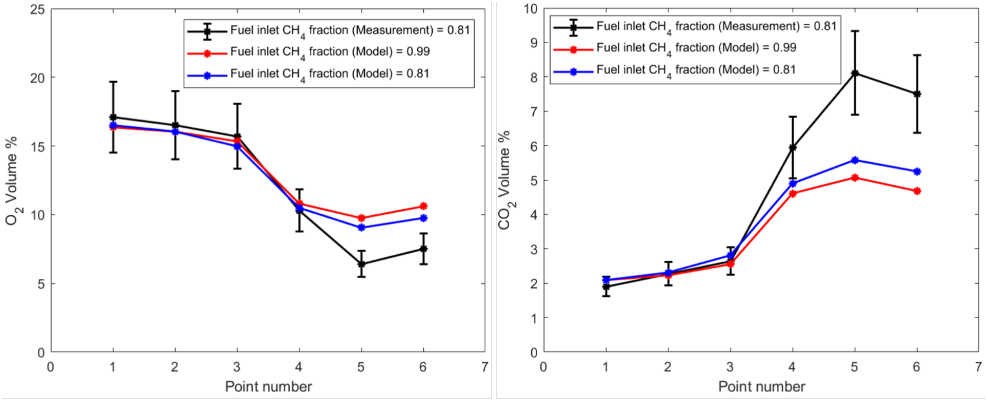

(a) (b)

Figure 7.12: Comparison of model values and measured values in volume % at six locations for the chemical species (a) O_2 and (b) CO_2 for mass fraction of CH_4 in the fuel

Figure 7.13 shows the comparison of NOx for models with varying fuel composition. From the comparison of O_2 and CO_2 it can be seen that an almost equivalent extent of combustion reaction occurs. However, the enthalpies of the reaction are different, leading to different temperature profiles. This results in a difference in NOx formation. In both models, the NOx is overestimated compared to measured values due to overestimation in temperature.

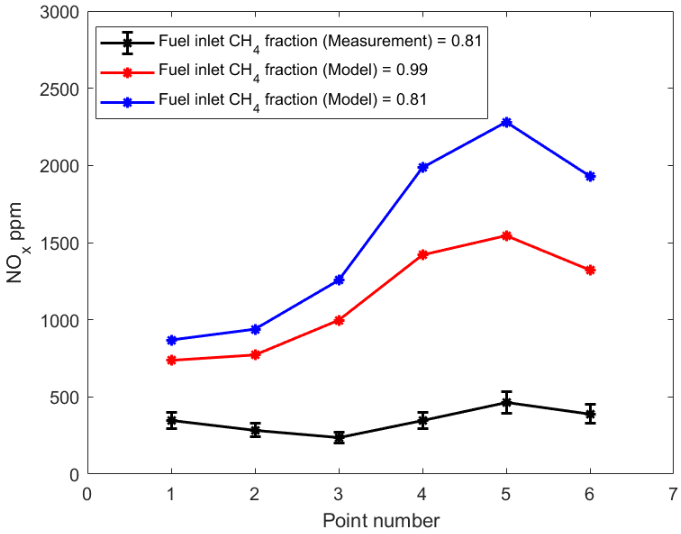

Figure 7.13: Comparison of model values and measured values in volume % at six locations for the NOx with varying values of mass fraction of CH_4 in the fuel

7.4. CHALLENGES

There are certain limitations associated with the measurement values. The measurement of chemical species is possible only at the top part of the furnace. Most often, if the probe is too hot, the probe starts melting down, leading to errors. For the same reason, the probe can not be inserted at locations below fuel injection. Most of the dynamics occur in the region below burners. However, measuring at these locations to validate the model is difficult. In the given measurement drive, the probe was cooled after measuring at each location to avoid errors. Also, the location points were chosen in the region where the fluid dynamics are relatively stable.

The limitations occur for the measurement of the temperature as well. With the thermal camera image, it is difficult to identify the height at which the temperature is measured. Due to the high temperature in the furnace, the camera is held at a height. It is difficult to cut off noise from the image that corresponds to the surrounding undesirable part of the image.

Due to these limitations, the use of measurements is limited to understanding the range of values and trends. The model compares well within such a range of measured values and provides expected trends.

7.5. CONCLUSION

The model developed in this thesis work is validated by comparing with measured values at the furnace of Aluchemie. The measurements are carried out for the temperature and concentration of chemical species. The FLIR infrared thermal camera and Testo 350 flue gas analysers are used for the measurements.

The temperature values are computed by post-processing the image captured by the camera with the software provided by Flir. The pictures are obtained at four locations through each of the top openings of the furnace. The approximate location is identified based on the surrounding walls, and the temperature at these regions is extracted from the model. It is observed that the pointer in the image gives the temperature at the bottom of the furnace. Therefore, average values at the bottom are computed by plotting values at lines in the region that can be in the line of sight from the openings. The temperature is overpredicted by the model. But the difference is within 10% compared to the measurements. The trends of the temperature computed by the models match the measured values.

The concentration of chemical species is measured at six locations that are accessible from the openings of the furnace. The Testo 350 flue gas analysers give concentration of O_2, CO_2 and NOx. The approximate coordinates of the measurement locations are calculated based on the length of the probe and the angle of insertion. The model values at these positions are compared with the measured values. The comparison of species concentration from the model at the points after the first burner is in good agreement with the measured values. Whereas, the model values of O_2 and CO_2 compared to measured values are higher and lower, respectively. However, the values are within the accepted range and differ due to the simplistic combustion model.

8

CONCLUSIONS AND RECOMMENDATIONS

8.1. CONCLUSIONS AND DISCUSSION

The NOx generation in the anode baking furnace is addressed in this thesis work. In order to make this possible the combustion process and its numerical simulation has been addressed. The numerical model of the heating section of anode baking furnace is developed in COMSOL Multiphysics software. The important physical phenomena in the heating section of the furnace are identified. The modeling approaches available for each of these physical phenomena are discussed (Chapter 2). The choice of models such as standard k-ϵ turbulent flow model with RANS approach, eddy dissipation combustion model, P1 approximation radiation model and Zeldovich mechanism for modeling NOx source term are justified. The COMSOL Multiphysics software is based on finite element method and has multiple solver approaches. The suitable solver approach for the model with different complexities is discussed in chapter 3. The combination of coupled and segregated solver approach provides reasonable balance between robustness and required computational power.

The meshing is one of the important part of the finite element modeling. The meshing techniques are varied and their effects on the variables such as velocity, temperature, turbulent viscosity ratio are examined. The meshing approaches are varied in terms of the meshing software and the refinement under the jet. The properties such as turbulent viscosity ratio, turbulent kinetic energy and turbulent dissipation rate are more sensitive to the mesh as compared to the properties such as velocity and temperature. The meshing approach is chosen based on the analysis of the sensitive variables such that the physically plausible results are obtained. The mesh obtained by the cfMesh software with appropriate refinement under the jet region provides such results.

The analysis of jet through two burners shows that the boundary conditions of both air and fuel inflow have effect on the flow dynamics. Moreover, the behaviour of jets through two burners are different due to varied placement of obstacles underneath the burners. The first jet is obstructed due to the impact on the tie-brick whereas, such obstruction does not happen for the second jet. Eventually this affects the combustion process. The investigation on improving the turbulent flow model from standard to realizable k-ϵ model is carried out. The analysis shows that the realizable k-ϵ model fails to converge when the numerical diffusion is not sufficient. The effect of addition of numerical diffusion shows the nonphysical results of properties such as turbulent viscosity ratio in the region of jet development. Multiple tests with adjusting solver approach such as using more computationally intensive direct solver and reducing pseudo time step fails to provide convergence. Therefore, it can be concluded that the module of realizable k-ϵ model of COMSOL Multiphysics software for a given mesh is incapable and further treatment is needed for achieving convergence.

The adequate resolution of flow dynamics in the furnace are carried out due to their significant effect on the combustion process. The complexity of the real time geometry of industrial furnace and the involvement of multiple physical phenomena limits the use of intricate combustion model in the furnace. The observations in the furnace suggests the facilitation of combustion process with variations in flow conditions. Moreover, the limitations of the COMSOL Multiphysics software with combustion modeling facilitates the use of eddy dissipation model. The coupled combustion model with turbulent flow shows that the effect of flow dynamics has significant impact. The variations in operational conditions such as air flow velocity, fuel flow velocity and fuel pipe diameter are tested. These models are developed without considering radiation phenomena to primarily gain insights of combustion model. With the decrease in velocity, the available O_2 in the air stream decreases. This results in narrow reaction zone. Consequently, the streamline behaviour of the chemical species is observed. In real furnace, the radiation phenomena changes such behaviour. The increase in heat transfer affects the density resulting in different flow dynamics. Therefore, the narrow streamline behaviour changes and relatively wider reaction zone is observed. The effect of increasing fuel flow velocity is higher than the air flow velocity due to its higher magnitude. The higher fuel velocity creates higher turbulence under the jets, especially the second jet. Moreover, due to lean conditions there is enough oxidizer to burn more fuel. This results in higher extent of combustion reaction and higher temperature in the furnace. The examination of increasing fuel pipe diameter by keeping the air-fuel ratio constant shows that the flow dynamics changes under the burners. The increase in fuel pipe diameter has longer flame due to relatively slower mixing. This leads to lower temperature in the furnace. In reality, the fuel composition consists of other hydrocarbons apart from CH_4. However, the inaccuracies increases with two or more reactions while using eddy dissipation model. Therefore, there are inaccuracies involved in both approaches; assuming fuel with complete CH_4 and considering fuel with other hydrocarbons. In this thesis, the assumption of fuel with complete CH_4 is considered.

The importance of adding radiation is especially realized by the test on varying air flow velocity. The radiation modeling by discrete ordinate method for the complex geometry such as anode baking furnace requires solving approximately six times of degrees of freedom compared to the P1 approximation model. The limitation of computational power motivates the use of P1 approximation model. The coupling of radiation with the reactive flow model shows significant impact on flow variables, chemical species as well as temperature. The distribution of heat changes the density leading to more diffused flow dynamics. The local overheating observed in the models without radiation disappears with the addition of radiation. This lowers the maximum temperature observed in the furnace. The gas medium in the furnace contains radiation absorbing species such as CO_2 and H_2O. The Planck mean absorption coefficient (PMAC) model is employed to calculate absorption coefficient of the gas mixture. The more realistic temperature distribution is observed with PMAC approach compared to the average constant value. The heat transfer to the wall is accounted by adding a layer of solid in the model. The PMAC approach suggests that at higher temperatures the radiation absorption capacity of CO_2 and H_2O is less. Since near the burner, the temperatures are always higher, the radiation absorption coefficient is always less. It has been observed that the temperature dip occurs in the fluid domain near the burners at the interface of fluid and solid domains. This dip is due to the lower radiation absorption coefficient. Our industrial partner, Aluchemie confirms occurrence of such dip.

The model developed in the work is validated by comparing with the measured values from the furnace. The measurement of temperature is carried out by obtaining images with FLIR infrared camera through four top openings. The comparison with model values show an overestimation by maximum 8.5% with the measured values. Moreover, the measurement of chemical species such as O_2 CO_2 and NOx are carried out at six locations using Testo 350 gas analyser. A good comparison is obtained for O_2, CO_2 with the measured values. The NOx values computed from the model are overestimated due to overestimation in temperature. The difference of NOx values from model and measurement shows that the thermal NOx is extremely sensitive to temperature. Therefore, difference of approximately 80^{o}C in the temperature results in overestimation of NOx by almost 1.5 times compared to measurement.

It can be concluded that the model developed in this work closely mimics the real time conditions in the furnace. The accuracy of the model is achieved by focusing on improving the mesh of the model. Therefore, even with basic models for individual physics, a good comparison is obtained with the measurement values.

8.2. SCIENTIFIC CONTRIBUTIONS

The following scientific contributions are obtained during this thesis work.

- Numerical model of realistic representation of furnace by industrial partner and comparison with measurements

- Mesh generation by external software (cfMesh) and the conversion tool to convert mesh from FOAM to Nastran format

- Development of mixture fraction beta-pdf combustion model in COMSOL Multiphysics software

The scientific articles provided in the list of publication provides further insights on the scientific contribution.

8.3. RECOMMENDATIONS

In this thesis work, the modeling of the anode baking furnace is carried out in COMSOL Multiphysics software. The modeling of combustion in the package is limited. The package contains the choice of only eddy dissipation model. The eddy dissipation model is not compatible to account for the detailed chemistry mechanism. This limits considering the correct fuel composition resulting in inaccuracies. The adiabatic mixture fraction beta-pdf model with GRI 3.0 mechanism is developed in this work. The extension to non-adiabatic model is required such that the radiation and conjugate heat transfer can be modeled. With execution of this model the accurate fuel composition can be considered. Moreover, for the NOx computation, the PDF averaging of NOx can then be obtained to avoid influence of fluctuations. The model can further be improved with accounting combustion model such as flamelet generated manifold.

The radiation modeling for the participating media needs input of absorption coefficient. The models for the absorption coefficient such as weighted sum of gray gas (WSSG) model are not available in the COMSOL package. COMSOL Multiphysics software also has inadequacy in meshing capability for the complex geometry especially for making the Cartesian mesh. The more advanced software for the meshing capabilities, modeling of turbulent, combustion and radiation will be advantageous for the further study. One such modeling attempt is carried out in converge CFD software. The converge CFD software is advanced in meshing techniques. The software requires minimum input from the user for the adaptive mesh refinement. Moreover, the package is advanced with combustion modeling such as an option of flamelet generated manifold model. Another attempt is carried out to obtain a model in OpenFOAM software [104]. Since the software is open source, it can further be explored with more advanced models for turbulent flow, combustion and radiation.

The fuel injection through burners of Aluchemie furnace happens in a pulsating manner. To account for the pulses in fuel injection, a time-dependent model is needed. The steady state assumption overestimates the fuel input in the furnace resulting in higher extent of combustion reaction. We observed that the NOx values obtained from the model are overestimated compared to the measured values. Accounting for the pulses for fuel injection will provide more control on the fuel input boundary conditions.

To summarize, following developments can be carried out with the advanced software package.

- Developing a mixture fraction beta PDF for a non-adiabatic system. This would allow NOx computation with PDF averaging
- Improving the radiative properties from Planck mean absorption coefficient to WSSG
- Combustion chemistry can further be improved from equilibrium assumed PDF model to flamelet assumed PDF model
- Extending the model to unsteady operation (fuel injection pulsation)
- Improving turbulence model from two-equation modeling to full Reynolds stress modeling

- Improving NOx model from short to extended Zeldovich mechanism (including OH) model
- Improving radiation model from P1 approximation to discrete ordinate model
- Improving radiation model by adding spectral effect in the radiative transfer equation

The local overheating near the fuel injection primarily results in NOx generation. The design of burner plays an important role in controlling the NOx formation at the source. The pre-mixing of fuel and oxidizer helps in avoiding the local overheating near the fuel injection. The nature of such pre-mixing depends on the various parameters such as air inlets of the burner that provides air for pre-mixing, the length of mixing region, the nozzle diameter etc. Therefore, considering the detailed burner geometry instead of a simple pipe will have impact on NOx calculations. The bottleneck for using such burner geometry for this work occurred at the meshing stage. With the appropriate software package, resolving such limitation should be possible.

Due to limitation of computational resources, only one heating section of the anode baking furnace is studied in this work. In real furnace, consecutive three such sections are present. All these sections have fuel injection through burners similar to the one section considered in this work. This implies that all three sections are the source of NOx generation. It has been observed in this study that the jet of the second burner is different from that of the first burner due to different placement of obstacles for the two burners. The air available for combustion for the second burner is at higher temperature due to passage through first burner. Moreover, this air contains less concentration of O_2. This results in different combustion at the second burner compared to the first burner. This suggests that the combustion under each burner of the following sections would be different. Therefore, extrapolating NOx generation in the furnace based on a single section is not possible. Therefore, modeling three consecutive heating sections will provide better understanding of NOx generation.

The recommendations discussed above are for improving the model of the current operation. However, to reduce NOx, improvements in the furnace are also required. The use of pre-heated air in the anode baking furnace is the main cause of high NOx. This can be improved by using flameless combustion configurations (FLOX). This leads to dilution of the air stream with product gases. Tajik et.al. have shown in their study that diluting the stream of oxidizer reduces NOx in the furnace [28]. However, in this study, the model considers elevated oxidizer temperature. There are studies for glass furnaces in which the recirculated flue gas is at a lower temperature. The results by Giese et.al. [105] show a 50% reduction in NOx using FLOX configuration. However, this requires recirculated flue gas at a lower temperature. The pre-heating sections of the anode baking furnace elevate the temperature of the flue gas before it enters the heating section. Therefore, the feasibility of dilution after the pre-heating section needs to be assessed in the anode baking furnace.

ACKNOWLEDGEMENTS

First of all I would like to thank my supervisor Dr. Domenico Lahaye. You were my professor during one of the courses in master program. Little did I know that a casual discussion in the Christmas dinner of the department would change my career path to such an extent. I met you at the dinner and I mentioned my interest in the applied mathematics. I was looking for an internship opportunity back then. You asked me to meet again and from there the discussion on the Aluchemie project started. The journey of just a possibility of internship to a Ph.D. position at the company had many hurdles. But you made it possible to cross every hurdle with ease. I am really thankful for that. You were supportive at each step of my Ph.D. right from the first day. I appreciate all opportunities you provided me in last four years such as conferences, presentations at different meetings, company visits etc. You always enhanced my confidence by appreciating even the smallest achievement. When things were not falling in place back at home in India, you always supported me. I am really thankful to you for letting me work from India for such a long time and helping me with all arrangements around that. I cannot imagine to be at the final phase of my Ph.D. without you. I would always be grateful to you.

Then I would like to thank my promotor Kees Vuik. Kees, you have always supported me with the required resources and feedback at important milestones. I really appreciate your efforts on correcting all my scientific papers and chapters of my thesis out of your busy schedule. You have always encouraged me to focus on requirements for finishing the Ph.D. Your asking of specific tasks such as literature review after the first year, graduate course credits have helped me during the final phase. Thanks a lot for all such advices. I would like to thank my committee member Arnold Heemink for always being there during the milestone meetings. Your questions and advices during these meetings have always been helpful. I would like to thank my other two committee members Dirk Roekarts and Arvind Gangoli Rao who have seen the development of results time to time during combustion meetings. Dirk, thank you for your questions and suggestions after each presentation delivered in the combustion meeting. Your questions not only to me but for everyone have always increased my knowledgebase in the field. Arvind, Thanks for all your questions to me as well. The recent meeting with you really provided me lot of insights for the thesis structuring. I would not have been able to structure few chapters the way they are right now, had you not provided your suggestions. Thanks for being proactive for knowing more about the work.

I would like to thank my other committee members Chris Budd and Benedicte Cuenot. Chris, thank you for your very first suggestions when you had arrived in TU Delft. I really appreciate the invitation for giving talk at AIMS seminar in Bath university. Thanks for reviewing my thesis. Benedicte, thank you for accepting my invitation as a speaker in SIAM annual day of delft chapter. Your presentation provided us with new combustion modeming techniques used in Cerfacs. Thanks also for reviewing my thesis.

I would also like to thank Rene Pecnic for accepting to be part of my committee and reviewing my thesis through all chapters. The support from Aluchemie for this thesis work was enormous. The first contact from Aluchemie was my manager Annimieke Groen. I am really thankful to her and Brenda for arranging all resources for the Ph.D. from Aluchemie side. The senior process engineer Guillaume Vergowen was the most important from Aluchemie for this project. Guillaume, I can't thank you enough for all your support during the work. You not only provided with the data required for this thesis but also posed logical and practical questions for building strong foundation to this thesis. I can't forget your support during the my stay in India last year. You made that journey possible without any hurdles. I really appreciate all your efforts. Another important personality who helped me in this thesis work is Marco Talice. Marco, thank you for all your support during this Ph.D. thesis. Your intelligent questions always helped me to think more conceptually about the problem. You were always with your solution box for my problems. I appreciate all your efforts in this work. Franjo Juretic from the principle developer at creative fields entertained my queries related to the cfMesh software personally. Franjo, thank you for your time in your busy schedule. You made enormous efforts for customizing the tool for my project. You were always kind and patient with me. I am grateful to you. I would also like to thank support team from COMSOL software, especially Paul and Sander. Thank you for your quick response to my queries. You always made it possible to provide more details on the software. Some of the important work in this thesis was carried out with the help of master students. I would like to thank Alberto Martinez Gonzale and Chaitanya Bhatraju for contributing to this thesis project. Alberto, thank you for helping me in developing a mixture fraction model. Your work indeed formed the basis for the further development of the model. Chaitanya, thank you for helping me gaining more insights on developing a mesh for the detailed burner geometry. The numerical analysis group has been the fun group since the start. I would like to thank everyone in the group who some or the other way helped me. You all supported me with your contribution for my initiative on Mask for India. I am really grateful to all of you for showing confidence on me. Alice, I have no words to express my gratitude. You have been a go to person for me in the department since day one. You have always been extremely helpful to me. You always made me feel part of the group. All your postcards, gifts, supporting texts have made me come to this point of Ph.D. journey. You always picked up all my work when I was in India, always arranged things for me, made my SIAM journey easier and the list just goes on. I am going to miss the awesome cakes you baked for me, the most authentic Chinese food you cooked for me. I am glad that I could enjoy some nice restaurants and my first ever high tea with you. Thanks a lot for everything. Roel, thanks for all your most logical and practical words. You were an awesome office mate to have. You have shared the wise words that has always given me more clear path to go ahead in the Ph.D. journey. Thanks for that. Mohamed, you were the first one I talked to in the group. Thanks for you advices at the start of the Ph.D. I have always come to you with my complaints and you have always listened to me patiently. So really thankful for that. Vandana, I know we could share the office talks for only limited time. But the similarities in our cultures have always made you understand my struggles. Thanks for checking on me time to time. I really appreciate all our discussions. Marieke, Jochen and Mousa, thanks for being the supportive office mates. Unfortunately we couldn't work more consistently on Optimath but that definitely helped me learn a bit about machine learning. So thanks for that. Anne, thank you for your warm hospitality during one of our meet-ups. Merel, it has been my pleasure knowing you. Xiu shan, you are really sweet. Thank you for all gifts that you got us from China. Gabie, I have known you for a very short time. But you always helped me to integrate with the group. So thank you for that. Thanks to Jiao, Bailja, elisa, Jinqiang, Linlin, hugo, Thomas, Reinaldo, Amey as well for being a wonderful company in the department.

Apart from the people related to my academic career there have been enormous support from my family and friend circle to make this Ph.D. possible. I would like to thank them all as well. Arjun, I would have been in India already, leaving this Ph.D., if I had not have you around. Little did I know that sharing a house with you will have such a positive impact in my life. During past four years you have closely seen all my phases. You are the first person to experience super happy me, super sad me, super depressed me, super annoying me, super enthusiastic me. And I am really really grateful to you for your unique support to all those emotions. Thanks a lot Arjun. Raj, I remember your constant encouragement about taking up this Ph.D. Thank you for pushing me to take that decision when I was vulnerable. The journey from there to the moment when you said that 'the Ph.D. title is looking good on your CV' was not possible without you. You have always motivated me to be ambitious by constantly supplying me with confidence. Life couldn't have been this better without you. Thanks a lot. Kshiteej, you have been my constant mentor since I started this Ph.D. You have always shown me my positive side and made me realize my worth. Thank you for all interesting discussions. Many of them made me feel good about myself and boost my confidence. I am really thankful to you for sticking by my side in all ups and downs. Your constant checking on me always make me feel that I have a go to person in close proximity. Thanks for all your efforts to make me feel comfortable here in Netherlands. Snigdha, I am so happy to have you so close to my life again. I can't thank you enough for always checking on me and always understanding my feelings. You have literally gone out of your comfort zone to make my moments special and encouraged me to push my limits. Thank you for sharing all your learnings in the Ph.D. journey and providing me confidence to finish. Sakshi, thanks for being around in some of the crucial times of my Ph.D. Thanks for making me feel comfortable to talk about my insecurities and providing new perspectives. All of you have seen my crying face multiple times during this Ph.D. Thanks for making a transition from there to a happy face. Daware, thank you for showing confidence in me more than I had on myself. I would never forget you fighting for me with the HR of the company emphasizing that I am the perfect candidate. That was extremely sweet of you. I am really thankful for taking all those confidence boosting sessions. Nilaya, I could have never able to finish masters with honors without you. You have no idea but small things that I learnt from you during masters have helped me in Ph.D. as well. Unknowingly you always impart new perspectives and I am really thankful for that. Rucha, I remember from day 1 of this Ph.D. how you appreciated my decision. You always regarded me higher for taking up this Ph.D. That really meant a lot. Thanks a lot Ruche. I really appreciate how clear and sorted things are for you, something I always try to learn from you. Poornima, thanks a lot for being around at times when I needed you and kshiteej. There have been times when you went out of the way to make me feel comfortable. I am really grateful for that. Smriti, I really appreciate all your efforts to make some of the special moments of my life memorable. Thanks a lot sunny for always being in my team. Srinidhi, thanks for being around especially at the last phase of my Ph.D. You have no idea but you have given me company in some of my most crucial moments of Ph.D. Thanks a lot.

Well, I am lucky to be surrounded by some great friends who have made this journey possible. I had never thought that I would find my life partner in one of my best friend. Parag, I remember the arguments at the start of this Ph.D. and a possible long commitment of four years. The path looked difficult and it happened to be challenging as we expected. But once you decided to support my decision you never looked back. I know you had to suffer as much as I did during this Ph.D. journey. But I am really grateful to you for your constant support, your efforts to change your career path based on mine, your encouraging words, your constant efforts to distress me by making me live in the present instead of thinking way ahead. As I always say, you are the best thing that has ever happened to me. Thanks a lot for everything.

The credit of completion of this Ph.D. majorly goes to my family for providing all opportunities to make it happen. Dada, I don't say this enough but your constant support on everything provides me a great relief. I have never been sorted in my life and of course that makes me anxious. But I always know back of my mind that if something goes wrong I can always rely on you. Thanks dada. Shweta, thanks for being an amazing sister-in-law you are. I am proud of you for managing studies with a kid. It really has inspired me in this Ph.D. journey. Oju, you are too small to understand this right now. But you have been source of motivation as well. In low times, watching your videos have worked like a therapy. Aatu loves you a lot. Last but not the least I am extremely grateful to my parents. Both of them are so unique in their own ways and have constantly supported me. Aai, I have always respected your ambitious nature. I know how hard you have worked to be at the position where you are. I think part of me that motivates me to work hard to achieve those ambitious goals are inherited from you. Thanks for all your support aai. Pappa, I know how hard it is for you to go against the conventional routes. Even in that case you have wholeheartedly supported me to go against conventions in all respect. Your calm and patient nature has always surprised me. All my friends appreciate my patience and I know where this quality of mine comes from. Thanks a lot for being so patient with me.

REFERENCES

[1] S. Naimoli and S. Ladislaw, *Decarbonizing heavy industry,* CSIS Briefs (2020).

[2] D. Brough and H. Jouhara, *The aluminium industry: A review on state-of-the-art technologies, environmental impacts and possibilities for waste heat recovery,* International Journal of Thermofluids **1**, 100007 (2020).

[3] R. Bui, A. Charette, and T. Bourgeois, *Simulating the process of carbon anode baking used in the aluminum industry,* Metallurgical Transactions B **15**, 487 (1984).

[4] E. Dernedde, M. Thibault, R. Bui, and A. Charette, *Simulating the dynamics of the anode baking ring furnace,* in *Journal of Metals,* Vol. 36 (1984) pp. 95–95.

[5] R. Bui, A. Charette, T. Bourgeois, and E. Dernedde, *Performance analysis of the ring furnace used for baking industrial carbon electrodes,* The Canadian Journal of Chemical Engineering **65**, 96 (1987).

[6] R. Bui, S. Peter, A. Charette, A. Tomsett, and V. Potocnik, *Modelling of heat transfer and gas flow in the vertical flue anode baking furnace,* Light Metals 1995 , 663 (1995).

[7] S. Peter, A. Charette, R. Bui, A. Tomsett, and V. Potocnik, *An extended two-dimensional mathematical model of vertical ring furnaces,* Metallurgical and Materials Transactions B **27**, 297 (1996).

[8] M. Jacobsen and M. C. Melaaen, *Numerical simulation of the baking of porous anode carbon in a vertical flue ring furnace,* Numerical Heat Transfer, Part A Applications **34**, 571 (1998).

[9] Y. Kocaefe, E. Dernedde, D. Kocaefe, R. Ouellet, Q. Jiao, and W. Crowell, *A 3D mathematical model for the horizontal anode baking furnace*, Tech. Rep. (Minerals, Metals and Materials Society, Warrendale, PA (United States), 1996).

[10] L. Zhang, C. Zheng, and M. Xu, *Simulating the heat transfer process of horizontal anode baking furnace,* Developments in Chemical Engineering and Mineral Processing **13**, 447 (2005).

[11] J. A. Johnson, A. V. Rozin, and A. P. Skibin, *A simplified baking furnace model for improving flue wall design,* in *Light Metals-Warrendale-Proceedings* (TMS, 2004) pp. 547–552.

[12] D. S. Severo, V. Gusberti, and E. C. Pinto, *Advanced 3D modelling for anode baking furnaces,* Light metals **2005**, 697 (2005).

[13] D. S. Severo, V. Gusberti, P. O. Sulger, F. Keller, and M. W. Meier, *Recent developments in anode baking furnace design,* in *Light Metals 2011* (Springer, 2011) pp. 853–858.

[14] N. Oumarou, D. Kocaefe, Y. S. Kocaefe, B. Morais, and J. Chabot, *A dynamic process model for simulating horizontal anode baking furnaces,* (2013).

[15] D. S. Severo and V. Gusberti, *User-friendly software for simulation of anode baking furnaces,* Proceeding of 10th Australisian (2011).

[16] M. Baiteche, Y. S. Kocaefe, D. Kocaefe, B. Morais, and J. Lafrance, *A 3D mathematical model of a horizontal anode baking furnace as a design tool,* (2013).

[17] Y. Kocaefe, N. Oumarou, M. Baiteche, D. Kocaefe, B. Morais, and M. Gagnon, *Use of mathematical modelling to study the behavior of a horizontal anode baking furnace,* in *Light Metals 2013* (Springer, 2016) pp. 1139–1144.

[18] M. Baiteche, D. Kocaefe, Y. Kocaefe, D. Marceau, B. Morais, and J. Lafrance, *Description and applications of a 3D mathematical model for horizontal anode baking furnaces,* in *Light Metals 2015* (Springer, 2015) pp. 1115–1120.

[19] N. Oumarou, Y. Kocaefe, D. Kocaefe, B. Morais, and J. Lafrance, *A dynamic process model for predicting the performance of horizontal anode baking furnaces,* in *Light Metals 2015* (Springer, 2015) pp. 1081–1086.

[20] N. Oumarou, D. Kocaefe, Y. Kocaefe, and B. Morais, *Transient process model of open anode baking furnace,* Applied Thermal Engineering **107**, 1253 (2016).

[21] N. Oumarou, D. Kocaefe, and Y. Kocaefe, *An advanced dynamic process model for industrial horizontal anode baking furnace,* Applied Mathematical Modelling **53**, 384 (2018).

[22] A. R. Tajik, T. Shamim, M. Zaidani, and R. K. A. Al-Rub, *The effects of flue-wall design modifications on combustion and flow characteristics of an aluminum anode baking furnace-cfd modeling,* Applied Energy **230**, 207 (2018).

[23] M. Zaidani, R. Abu Al-Rub, A. R. Tajik, and T. Shamim, *Computational modeling of the effect of flue-wall deformation on the carbon anode quality for aluminum production,* in *Heat Transfer Summer Conference*, Vol. 57885 (American Society of Mechanical Engineers, 2017) p. V001T02A010.

[24] A. R. Tajik, R. K. A. Al-Rub, M. Zaidani, and T. Shamim, *Numerical investigation of turbulent diffusion flame in the aluminum anode baking furnace employing presumed pdf,* Energy Procedia **142**, 4157 (2017).

[25] M. Zaidani, R. A. Al-Rub, A. R. Tajik, and T. Shamim, *3D multiphysics model of the effect of flue-wall deformation on the anode baking homogeneity in horizontal flue carbon furnace,* Energy Procedia **142**, 3982 (2017).

[26] A. R. Tajik, T. Shamim, R. K. A. Al-Rub, and M. Zaidani, *Two dimensional cfd simulations of a flue-wall in the anode baking furnace for aluminum production,* Energy Procedia **105**, 5134 (2017).

[27] M. Zaidani, A. R. Tajik, Z. A. Qureshi, T. Shamim, and R. K. A. Al-Rub, *Investigating the flue-wall deformation effects on performance characteristics of an open-top aluminum anode baking furnace,* Applied Energy **231**, 1033 (2018).

[28] A. R. Tajik, T. Shamim, A. F. Ghoniem, and R. K. Abu Al-Rub, *CFD modelling of NOx and soot formation in aluminum anode baking furnace,* in *ASME International Mechanical Engineering Congress and Exposition*, Vol. 52118 (American Society of Mechanical Engineers, 2018) p. V08AT10A016.

[29] A. Bourgier, S. Besson, and J.-P. Schneider, *3d transient modelling of a complete fire line for anode baking furnace design and optimization,* in *TMS Annual Meeting & Exhibition* (Springer, 2018) pp. 1373–1378.

[30] F. Grégoire, L. Gosselin, and H. Alamdari, *Combustion in anode baking furnaces: Comparison of two modeling approaches to predict variability,* Combustion (2013).

[31] F. Grégoire and L. Gosselin, *Comparison of three combustion models for simulating anode baking furnaces,* International Journal of Thermal Sciences **129**, 532 (2018).

[32] T. L. Bergman, F. P. Incropera, D. P. De Witt, and A. S. Lavine, *Fundamentals of heat and mass transfer* (John Wiley & Sons, 2011).

[33] H. K. Versteeg and W. Malalasekera, *An introduction to computational fluid dynamics: the finite volume method* (Pearson education, 2007).

[34] L. Zhou, *Theory and modeling of dispersed multiphase turbulent reacting flows* (Butterworth-Heinemann, 2018).

[35] Y. Zhiyin, *Large-eddy simulation: Past, present and the future,* Chinese journal of Aeronautics **28**, 11 (2015).

[36] Ansys, *Modeling of Turbulent Flows,* Fluent user guide , 49 (2006).

[37] W. Frei, *Which Turbulence Model Should I Choose for my CFD Application?* COMSOL Blog , 1 (2013).

[38] *CFD Module User 's Guide,* COMSOL Multiphysics , 598 (2019).

[39] H. Grotjans and F. R. Menter, *Wall functions for general application CFD codes,* Computational fluid dynamics'98 , 1112 (1998).

[40] *Turbulent Flow over a Backward - Facing Step,* COMSOL Multiphysics software (2020).

[41] A. Gaba and S. F. Iordache, *Reduction of air pollution by combustion processes,* The Impact of Air Pollution on Health, Economy, Environment and Agricultural Sources , 119 (2011).

[42] J. Warnatz, U. Maas, and R. W. Dibble, *Physical and chemical fundamentals, modeling and simulation, experiments, pollutant formation* (Springer, 1990).

[43] S. R. Turns, *An Introduction to Combustion: Concepts and Applications* (McGraw-Hill Companies New York, NY, USA, 2012).

[44] I. Glassman and R. Yetter, *Combustion* (Elsevier Science and Technology, 2008).

[45] K. K. Kuo, *Principles of combustion* (John Wiley, 2005).

[46] C. K. Law, *Combustion physics* (Cambridge university press, 2010).

[47] N. Peters, *Turbulent combustion* (Cambridge University Press, 2001).

[48] *Industrial Combustion Technology Roadmap: A Technology Roadmap by and for the Industrial Combustion Community*, Tech. Rep.

[49] T. Poinsot and D. Veynante, *Theoretical and numerical combustion* (RT Edwards, Inc., 2001).

[50] *Methane / air combustion cantera database online,* Cantera , 1 (2017).

[51] L. Wang, Z. Liu, S. Chen, and C. Zheng, *Comparison of different global combustion mechanisms under hot and diluted oxidation conditions,* Combustion Science and Technology **184**, 259 (2012).

[52] A. H. Kadar, *Modelling Turbulent Non-Premixed Combustion in Industrial Furnaces Using the Open Source Toolbox OpenFOAM,* TU Delft repository , 1 (2015).

[53] T. Echekki and E. Mastorakos, *Turbulent combustion modeling: Advances, new trends and perspectives,* Vol. 95 (Springer Science & Business Media, 2010).

[54] B. F. Magnussen and B. H. Hjertager, *On mathematical modeling of turbulent combustion with special emphasis on soot formation and combustion,* in *Symposium (international) on Combustion*, Vol. 16 (Elsevier, 1977) pp. 719–729.

[55] *Chemical Reaction Engineering Module User 's Guide,* COMSOL Multiphysics **9**, 1 (2016).

[56] *Syngas Combustion in a Round-Jet,* COMSOL Multiphysics software (2020).

[57] R. Barlow, G. Fiechtner, C. Carter, and M. Flury, *Sandia/ETH-Zurich CO/H2/N2 flame data-release 1.1,* Sandia National Laboratories , 1 (2002).

[58] J. van Oijen and L. de Goey, *Modelling of premixed laminar flames using flamelet-generated manifolds,* Combustion Science and Technology **161**, 113 (2000).

[59] L. Ma and D. Roekaerts, *Modeling of spray jet flame under mild condition with non-adiabatic fgm and a new conditional droplet injection model,* Combustion and Flame **165**, 402 (2016).

[60] M. Ren, S. Wang, N. Romero-Anton, J. Zhao, C. Zou, and D. Roekaerts, *Numerical study of a turbulent co-axial non-premixed flame for methanol hydrothermal combustion: Comparison of the edc and fgm models,* The Journal of Supercritical Fluids **169**, 105132 (2021).

[61] H. Pitsch and N. Peters, *A consistent flamelet formulation for non-premixed combustion considering differential diffusion effects,* Combustion and flame **114**, 26 (1998).

[62] *Heat Transfer Module User 's Guide,* COMSOL Multiphysics **9**, 1 (2016).

[63] M. Darwish and F. Moukalled, *The Finite Volume Method in Computational Fluid Dynamics: An Advanced Introduction with OpenFOAM® and Matlab®* (Springer, 2021).

[64] W. M. Kays, *Turbulent Prandtl number. where are we?* ASME Transactions Journal of Heat Transfer **116**, 284 (1994).

[65] G. Montambaux, *Generalized Stefan–Boltzmann law,* Foundations of Physics **48**, 395 (2018).

[66] M. Chmielewski and M. Gieras, *Planck mean absorption coefficients of H2O, CO2, CO and NO for radiation numerical modeling in combusting flows,* Journal of Power Technologies **95**, 97 (2015).

[67] S. Silvestri, D. Roekaerts, and R. Pecnik, *Modelling turbulent heat flux accounting for turbulence-radiation interactions,* International Journal of Heat and Fluid Flow **89**, 108728 (2021).

[68] P. Coelho, M. Mancini, and D. Roekaerts, *Thermal radiation,* in *ERCOFTAC Best Practice Guidelines-Computational Fluid Dynamics of Turbulent Combustion* (Ercoftac, 2016) pp. 77–143.

[69] A. Perpignan and A. G. Rao, *Effects of chemical reaction mechanism and nox formation pathways on an inter-turbine burner,* The Aeronautical Journal **123**, 1898 (2019).

[70] A. A. Perpignan, R. Sampat, and A. Gangoli Rao, *Modeling pollutant emissions of flameless combustion with a joint cfd and chemical reactor network approach,* Frontiers in Mechanical Engineering **5**, 63 (2019).

[71] P. Nakate, *Mathematical modeling of combustion reactions in turbulent flow of anode baking process,* DIAM report , 17 (2017).

[72] S. C. Brenner and L. R. Scott, *The mathematical theory of finite element methods,* Vol. 3 (Springer, 2008).

[73] C. Johnson, *Numerical solution of partial differential equations by the finite element method* (Courier Corporation, 2012).

[74] *Detailed explanation of the finite element method (fem),* COMSOL Multiphysics (2020).

[75] Wikipedia contributors, *Hilbert space — Wikipedia, the free encyclopedia,* (2021), [Online; accessed 13-July-2021].

[76] P. Deuflhard, *A modified Newton method for the solution of ill-conditioned systems of nonlinear equations with application to multiple shooting,* Numerische Mathematik **22**, 289 (1974).

[77] *Comsol reference manual version 5.4,* COMSOL Multiphysics (2019).

[78] J. Donea and A. Huerta, *Finite element methods for flow problems* (John Wiley & Sons, 2003).

[79] O. C. Zienkiewicz and R. L. Taylor, *The finite element method for solid and structural mechanics* (Elsevier, 2005).

[80] R. Codina, *Comparison of some finite element methods for solving the diffusion-convection-reaction equation,* Computer methods in applied mechanics and engineering **156**, 185 (1998).

[81] T. J. Hughes, L. P. Franca, and M. Balestra, *A new finite element formulation for computational fluid dynamics: V. circumventing the Babuška-Brezzi condition: A stable Petrov-Galerkin formulation of the stokes problem accommodating equal-order interpolations,* Computer Methods in Applied Mechanics and Engineering **59**, 85 (1986).

[82] G. P. Carver, M. P. Heap, G. B. Martin, D. W. Pershing, D. P. Rees, D. M. Zallen, *et al.*, *Low emissions process and burner,* (1983), US Patent 4,381,718.

[83] R. S. Tuthill, I. W. T. Bechtel, J. A. Benoit, S. H. Black, R. J. Bland, G. W. DeLeonardo, S. M. Meyer, J. C. Taura, and J. L. Battaglioli, *Swozzle based burner tube premixer including inlet air conditioner for low emissions combustion,* (2002), US Patent 6,438,961.

[84] J. T. Kelly, *Temperature controlled low emissions burner,* (1996), US Patent 5,542,839.

[85] C. Bhatraju, *Aspects of mesh generation for the burner optimization of an anode baking furnace,* `http://resolver.tudelft.nl/uuid:7adcb3c8-6038-4d3b-86f2-c047e27b3516` (2020).

[86] S. Besson, S. Bache, A. Bourgier, J.-P. Schneider, and T. Conte, *Modelling of gas injection on anode baking furnace and application to operations,* in *Light Metals 2020* (Springer, 2020) pp. 1196–1202.

[87] W. Jeong and J. Seong, *Comparison of effects on technical variances of computational fluid dynamics (CFD) software based on finite element and finite volume methods,* International Journal of Mechanical Sciences **78**, 19 (2014).

[88] R. Biswas and R. C. Strawn, *Tetrahedral and hexahedral mesh adaptation for CFD problems,* Applied Numerical Mathematics **26**, 135 (1998).

[89] F. Juretic, *cfMesh version 1.1 users guide,* `http://cfMesh.com/wp-content/uploads/2015/09/User_GuidecfMesh_v1.1.pdf` (2015).

[90] M. Staten and N. L. Jones, *Local refinement of three-dimensional finite element meshes,* Engineering with Computers **13**, 165 (1997).

[91] P. Nakate, D. Lahaye, C. Vuik, and M. Talice, *Systematic development and mesh sensitivity analysis of a mathematical model for an anode baking furnace,* in *Fluids Engineering Division Summer Meeting,* Vol. 51562 (2018) p. V002T09A010.

[92] P. Nakate, D. Lahaye, C. Vuik, and M. Talice, *Computational study of the anode baking industrial furnace,* in *Industrial Combustion Symposium; The American Flame Research Committee (AFRC): Lakewood Ranch, FL, USA* (2019).

[93] P. Nakate, D. Lahaye, C. Vuik, and M. Talice, *Analysis of the aerodynamics in the heating section of an anode baking furnace using non-linear finite element simulations,* Fluids **6**, 46 (2021).

[94] G. Iaccarino and R. Verzicco, *Immersed boundary technique for turbulent flow simulations,* Appl. Mech. Rev. **56**, 331 (2003).

[95] T.-H. Shih, J. Zhu, and J. L. Lumley, *A new Reynolds stress algebraic equation model,* Computer methods in applied mechanics and engineering **125**, 287 (1995).

[96] T. Shih, W. Liou, A. Shabbir, Z. Yang, and J. Zhu, *A new k-ϵ eddy viscosity model for high Reynolds number turbulent flows-model development and validation,* NASA TM **106721** (1994).

[97] P. Nakate, D. Lahaye, and C. Vuik, *The nitric oxide formation in anode baking furnace through numerical modeling,* International Journal of thermofluids (2021).

[98] E. Vasquez and T. Eldredge, *Process modeling for hydrocarbon fuel conversion,* in *Advances in Clean Hydrocarbon Fuel Processing* (Elsevier, 2011) pp. 509–545.

[99] H. K. Versteeg and W. Malalasekera, *An introduction to computational fluid dynamics: the finite volume method* (Pearson education, 2007).

[100] A. M. González, P. Nakate, and D. Lahaye, *Presumed β-pdf model for the prediction of the nox and co emissions in combustion chambers,* Excerpt from the Proceedings of the 2019 COMSOL Conference in Cambridge, UK (2019).

[101] I. Langella and N. Swaminathan, *Unstrained and strained flamelets for les of premixed combustion,* Combustion Theory and Modelling **20**, 410 (2016).

[102] *Flir p640 12^o, the high performance infrared inspection system,* `https://www.flir.com/` (2009).

[103] *Testo 350 - analysis box for exhaust gas analysis systems,* `https://static-int.testo.com/media/d1/56/d4836ea87dd7/testo-350-Instruction-Manual.pdf` (2012).

[104] D. Lahaye, P. Nakate, C. Vuik, F. Juretic, and M. Talice, *Modeling conjugate heat transfer in an anode baking furnace using openfoam,* Fluids (2022).

[105] A. Giese, U. Konold, A. AI-Halbouni, and K. Görner, *Application of flameless oxidation in glass melting furnaces-GlasFLOX,* in *7th Imternational Symposium on High Temperature Air Combustion and Gasification* (2008).

CURRICULUM VITÆ

Prajakta NAKATE

11-09-1991	Born in Aurangabad, India.

EDUCATION

2017–2021	Ph.D. in Applied Mathematics (TU Delft, Netherlands) Supervisor: Dr. D.J.P. Lahaye Promoter: Prof. dr. ir. C. Vuik
2015–2017	Master of Science in Chemical Engineering (TU Delft, Netherlands) Thesis: in molecular dynamics (MD) simulation of non-ideal diffusion behaviour. Completed masters with honors certificate
2010–2014	Bachelor of Technology in Chemical Engineering (VNIT, Nagpur, India)

WORK EXPERIENCE

2017–2021	Aluminium and Chemie Rotterdam B.V. (Aluchemie) Industrial researcher in collaboration with TU Delft

INTERNSHIPS AND PROJECTS

2016–2017	TATA Steel, The Netherlands Honours programme project
2016–2017	Royal Dutch Shell, The Netherlands Honours programme project
2014–2015	National Chemical Laboratory, India Project assistant

PUBLICATIONS

JOURNAL PUBLICATIONS

1. **P. Nakate**, **D.J.P Lahaye**, **C. Vuik**, **M. Talice** *Analysis of the aerodynamics in the heating section of an anode baking furnace using non-linear finite element simulations*, Fluids **6**, 46 (2021).
2. **P. Nakate**, **D.J.P Lahaye**, **C. Vuik** *The nitric oxide formation in anode baking furnace through numerical modeling*, International Journal of thermofluids , (2021).
3. **D.J.P Lahaye**, **P. Nakate**, **C. Vuik**, **F. Juretic**, **M. Talice** *Modeling conjugate heat transfer in an anode baking furnace using OpenFoam*, Fluids , (2022).

CONFERENCE PROCEEDINGS

1. **P. Nakate**, **D.J.P Lahaye**, **C. Vuik**, **M. Talice** *Systematic development and mesh sensitivity analysis of a mathematical model for an anode baking furnace*, 5TH Joint US-European Fluids Engineering Division Summer Meeting, ASME, Montreal, Canada (2018).
2. **P. Nakate**, **W. V. De**, **D.J.P Lahaye**, **C. Vuik**, **M. Talice** *Numerical modeling of anode baking process with COMSOL® Multiphysics*, Excerpt from the Proceedings of the 2018 COMSOL Conference in Lausanne, Switzerland , (2018).
3. **P. Nakate**, **D.J.P Lahaye**, **C. Vuik** *Reactive turbulent flow model of anode baking furnace to estimate NOx through Zeldovich mechanism*, in Proceedings of the 5th World Congress on Mechanical, Chemical and Material Engineering (MCM'19), Lisbon, Portugal , (2019).
4. **A. Martínez González**, **P. Nakate**, **D.J.P Lahaye** *Presumed β-PDF model for the prediction of the NOx and CO emissions in combustion chambers*, Excerpt from the Proceedings of the 2019 COMSOL Conference in Cambridge, UK , (2019).
5. **P. Nakate**, **D.J.P Lahaye**, **C. Vuik**, **M. Talice** *Computational study of the anode baking industrial furnace*, in Proceedings of the American Flame Research Committee (AFRC 2019), Hawaii, USA , (2019).